Some patterns of shape change controlled by eigenstrain architectures

Sébastien Turcaud

UNIVERSITÉ DE GRENOBLE

THÈSE

Pour obtenir le grade de

DOCTEUR DE L'UNIVERSITÉ DE GRENOBLE

Spécialité : **Ingénierie-matériaux mécanique énergétique environnement procédés production**

Arrêté ministériel : 7 août 2006

Présentée par

Sébastien TURCAUD

Thèse dirigée par **Yves Bréchet** et codirigée par **Peter Fratzl**

préparée au sein du **Laboratoire de Biomatériaux de l'Institut Max-Planck de Colloïdes et Interfaces (Potsdam, Allemagne)** dans **l'École Doctorale I-MEP2**

Motifs de changement de forme contrôlés par des architectures de gonflement

Thèse soutenue publiquement le **6 février 2015**
devant le jury composé de :

M. Yves Bréchet
Directeur de thèse, SiMap (membre)
M. Peter Fratzl
Co-directeur de thèse, MPIKG (membre)
M. John Dunlop
Encadrant de thèse, MPIKG (membre)
M. Denis Favier
Professeur, UJF (président)
M. Samuel Forest
Professeur, Centre des matériaux (rapporteur)
M. Benoit Roman
Professeur, ESPCI (rapporteur)
M. Claudia Fleck
Professeur, Technische Universität (membre)

Max Planck Institute of Colloids and Interfaces
Department of Biomaterials, Potsdam Germany

Materials and Processes
Science and Engineering Laboratory
Grenoble, France

Some Patterns of Shape Change controlled by Eigenstrain Architectures

PhD Thesis

presented by

Sébastien Turcaud

Director : *Peter Fratzl*
co-Director : *Yves Bréchet*
Supervisor : *John Dunlop*

To my family
my friends
Sissy

Acknowledgements

So many people paved the way to where I am. Three periods are determining : my childhood, my studies and my research time. As there is no good reason to start from one end or the other, I will start from the middle, my studies.

During my engineering studies at École des Ponts in Paris, I spend most of my time with two amazing people which I'd like to thank here. Anders Thorin, with whom being smart became a cool thing. At the beginning of the second year, we were told to quit half of the courses we joined, because according to the secretary it was at least twice as much as the usual schedule and would have been impossible to follow. We kept only the hardest and most obscure courses. Not sure if I got it all, but it was definitely a vaccine against complexity. In our graduating year, we both followed the same research master on micro-mechanics of materials and structures, and Anders is now officially a doctor and a specialist in modeling the piano key control with non-smooth dynamics. The second is Pierre Guérold, who despite of his content for useless researches still tolerates me. He is the smartest guy I know. When I was working one year as a structural engineer at Bollinger & Grohmann in 2009, I met Dimitry Demin, a "crazy" architect and my favorite Cosak friend, who introduced me to the world of soap bubbles, which triggered my interest for natural structures. I'd also like to thanks Manfred Grohmann and Klaus Bollinger for employing me, thus allowing me to discover the concept of integrated design in Architecture and the capabilities of three-dimensional drawing softwares.

During my childhood, I want to thank Carlos Marques, who got me into scientific studies in the first place and who connected me to the world of research when I was searching for a PhD thesis during my last year of studies. His patience and calm when approaching new knowledge still impress me and I have a long way ahead before I reach his level. Amongst the numerous teachers I had in school, I want to thank my math teacher Madame Leclerc, who believed I could achieve a lot if I only wanted to.

During my PhD-thesis, I especially want to thank Yves Bréchet, whom I first met casually at the "Brasserie le Luco" near le Jardin du Luxembourg in Paris. He gave me his trust and confidence all along my thesis and every meeting we had—at random times and arbitrary locations—is a special moment I keep in my memory. He put me in contact with Peter Fratzl, who I want to thank intensely, for giving me the chance to do my thesis in the Biomaterials department at the Max Planck Institute in Golm and for supporting me and giving me a second chance to finish it when I was struggling during my last year. A very special thanks goes to John Dunlop, who supervised me on a daily basis and gave me all kinds of support and advice in good and bad times. John, I owe you. In the research environment, I met tons of interesting people, some of which I want to thank here. Inside the institute, I want to thank Ingo Burgert, Lorenzo Guiducci, Felix Repp, Khashayar Razghandi and Friedericke Saxe for discussions and collaborations. Outside the institute, I want to thank Leonid Ionov and his team at the Leibniz Institute for Polymer research in Dresden for sharing with me their amazing experiments and allowing me to collaborate to their research. From my engineering school, I want to thank Alain Ehrlacher, who allowed me to supervise the student project of Fanny Chouteau, Madge Martin and Alan le Goallec. Also, thank you Justin Dirrenberger, Arthur Lebée and Andrew McCormick for many discussions on

architectured materials, mechanics and shape changes. Thank you Etienne Reyssat, for showing me around your lab and pointing me to Elite double for doing prestrain models. Thank you Ailyn Bornmüller, for helping me in preparing these prestrained experiments. Thank you René Genz, for lending me a laptop when mine crashed during the redaction of the thesis. Thank you computer store owner in Potsdam, for recovering my hard drive (twice). I don't know your name, but you saved me. Thank you also Garrett for the intense time in Potsdam and for the many scientific and philosophical discussions we had, you're a friend for life.

Last but not least, I want to thank my family—Louis-Marie, Beate, Aurélie, Madeleine and Matthias—for supporting me until the end and never giving up on me.

I surely forgot a lot of names and did not mention the friends I made along the way, so thank you all !

Abstract

Nature provides an unlimited source of inspiration for engineers, either by exhibiting new solutions to existing problems or by challenging them to develop systems displaying new functionalities. Recent advances in the characterization and modeling of natural systems reveal new design principles, which can be increasingly mimicked by engineers thanks to the progress in the production and modeling of man-made materials.

In this thesis, we are inspired by biological actuators (e.g. pine cone) which change their shape under an external fluctuating stimulus as a result of their material architecture. Our goal is to explore the design space of the *morphing* of solid objects controlled by an imposed distribution of inelastic strain (*eigenstrain*). We focus on elongated and thin objects where one dimension is either much bigger or much smaller than the other two (rods and sheets) and restrict ourselves to the framework of linear elasticity. Patterns of shape change are usually induced by large transformations, which requires considering a nonlinear dependency between strain and displacements. This requires the use of numerical methods in order to predict the *morphing* patterns. We looked at relaxation of springs, energy minimization and finite-elements. These patterns were also illustrated using experimental methods such as pre-straining, thermal expansion and swelling.

In the context of rod-like objects, two fundamental *morphers* are studied displaying bending and twisting respectively : *benders* and *twisters*. The standard mirror-symmetric bilayer *eigenstrain* architecture of *benders* can be smoothened in order to lower interfacial stress and modified in order to produce longitudinally graded or helical *benders*. By stacking *benders* in a honeycomb like manner, the relatively small mid-deflection of *benders* is geometrically amplified and produces relatively large displacements. According to finite-element simulations, the proposed rotationally-symmetric *eigenstrain* architecture of *twisters* displays a stretching-twisting instability, which is analyzed using energetical arguments. Similarly to *benders*, twisting can be varied along the longitudinal direction by grading the material properties along the *twister*. By combining *benders* and *twisters*, an arbitrary configuration of a rod can be obtained. In the context of sheets, we focus on diffusion-driven *morphing*, where the *eigenstrain* is applied progressively instead of instantaneously as motivated by experiments on thermo-responsive polymer bilayers. This leads to long-side rolling of rectangular shapes (instead of the standard short-side rolling of *benders*) and reveals a complex multi-step *morphing* process in the case of star shapes, where the edges wrinkle and bend and the initially flat star eventually folds into a three-dimensional structures (e.g. pyramid). With the progress in designing new materials, the *morphers* presented in this thesis could be used in different fields, including the design of macroscopic structures for Architecture.

Résumé

La nature fournit une source d'inspiration intarissable pour les ingénieurs, soit en exhibant de nouvelles solutions à des problèmes d'ingénierie existants ou en les mettant au défi de développer des systèmes possédant de nouvelles fonctionnalités. Les progrès récents dans la caractérisation et la modélisation des systèmes naturels révèlent de nouveaux principes de conception, qui peuvent être de plus en plus imité par les ingénieurs grâce aux progrès dans la production et la modélisation de matériaux synthétiques.

Dans cette thèse, nous sommes inspirés par des actuateurs biologiques (par exemple la pomme de pin) qui changent de forme en présence d'un stimulus externe variable en raison de leur architecture matérielle. Notre objectif est d'explorer l'espace de conception du morphing d'objets solides contrôlées par une distribution imposée des déformations inélastiques (eigenstrain). Nous nous concentrons sur des objets allongés ou minces pour lesquels une dimension est soit prédominante ou négligeable devant les deux autres (tiges et feuilles) et nous nous limitons au cadre de l'élasticité linéaire. Les motifs de changement de forme correspondent généralement à de grandes transformations, ce qui requiert de considérer une dépendance non-linéaire entre les déformations et les déplacements. L'utilisation de méthodes numériques permet de prédire ces motifs de morphing. Nous avons examiné la relaxation de ressorts, la minimisation d'énergie et les éléments finis. Ces motifs ont également été illustrés à l'aide des méthodes expérimentales telles que la pré-déformation, la dilatation thermique et le gonflement.

Dans le contexte des tiges, deux morphers fondamentaux sont étudiés qui démontre la flexion et la torsion : flexeurs et torseurs. L'architecture d'eigenstrain standard du bilame à symétrie miroir peut être lissée afin de réduire la contrainte interfaciale d'un flexeur et modifiée afin de produire des flexeurs à gradient longitudinal ou hélicoïdaux. En assemblant des flexeurs en forme de nid d'abeille, la déflection relativement petite est amplifiée géométriquement et produit de relativement grands déplacements. Des simulations aux éléments finis démontre que l'architecture d'eigenstrain à symétrie de révolution proposée pour les torseurs induit une instabilité extension-torsion, laquelle est analysée en utilisant une approche énergétique. De même que pour les flexeurs, la torsion peut être variée longitudinalement en introduisant un gradient de propriétés le long du torseur. En combinant flexeurs et torseurs, une configuration arbitraire d'une tige peut être obtenue. Dans le contexte de feuilles, nous nous concentrons sur le morphing contrôlé par la diffusion, où l'eigenstrain est appliquée progressivement au lieu de instantanément, motivé par des résultats expérimentaux sur de bi-couches en polymères qui gonflent différemment en fonction de la température. Cela démontre l'enroulement selon le long côté de formes rectangulaires (au lieu de roulement côté court des flexeurs) et révèle un processus de morphing complexe en plusieurs étapes dans le cas de formes étoilés, où les bords rides et s'enroulent et l'étoile initialement plate prend un configuration trois-dimensionnelle (par exemple pyramidale). Grâce aux progrès récents dans la conception de nouveaux matériaux, les morphers présentés dans cette thèse peuvent être utilisés dans une pluralité de domaines, y compris la conception de structures macroscopiques en Architecture.

Résumé étendu

Les motifs de changement de forme des systèmes naturels ont depuis longtemps intéressés les scientifiques avec les contributions modernes commençant par Darwin (C. Darwin and F. Darwin 1897). La diversité de ces motifs est large comme remarquablement illustré par les travaux d'Ernst Haeckel (Haeckel 2013). Dans son livre pionnier (Thompson et al. 1942), D'Arcy Thompson a commencé l'explication de formes naturelles à l'aide de lois physiques. Depuis lors, les efforts pour expliquer la morphogénèse—création de forme—ou le changement de forme par le biais de mécanismes physiques s'intensifie. Ces modèles combinent géométrie, mécanique et une force motrice, qui peut être due soit à la croissance, soit à un *eigenstrain* (déformation inélastique telle que le gonflement).

Cette thèse explore l'espace de conception d'objets solides, qui changent de forme en réponse à une fluctuation d'un stimulus extérieur. Nous appelons ces objets *morphers* et les considérons comme constitués d'un matériau élastique linéaire. L'objectif est d'identifier des architectures d'*eigenstrain*, qui conduisent à des motifs spécifiques de changement de forme. L'accent est mis sur des objets élancés qui possède une dimension plus petite ou plus grande que les deux autres—tiges et feuilles. Pour cela, le cadre théorique de la mécanique des milieux continus est utilisé lequel est exploré à l'aide de méthodes numériques et expérimentales.

Les sections suivantes donne un bref résumé des différents chapitres de la thèse pour le lecteur francophone.

De la recherche biomimétique à l'Architecture bioinspirée

Chapter 1 fait le lien entre les leçons tirés de l'étude de *morphers* biologiques et les applications potentielles dans le domaine de l'Architecture. Un designer nécessite une source d'inspiration pour créer. Section 1.1 argumente que les connaissances scientifiques précisent la vision du monde des designers, en démontrant ce qui est possible et en dressant les limites de ce qui ne l'est pas. À l'intérieur des limites dictés par la science, la technologie et les contraintes programmatiques du projet en question, les designer peuvent s'inspirer de la Nature. Une pratique existante consiste alors à copier l'apparence de systèmes naturels, comme par exemple les bulles de savons. Section 1.2 propose d'aller plus loin, en copiant les principes fonctionnels de systèmes naturels. En effet, les plantes sont capables de générer des contraintes internes et de modifier leur forme grâce à leur architecture matérielle (fig. 1.2). Dans le cas de systèmes passifs (comme la pomme de pin), le changement de forme est la conséquence de l'interaction de cette architecture matérielle avec un stimulus extérieur (par exemple l'humidité). Ce principe peut être copié en Architecture pour créer des structures mouvantes.

Bref aperçu de motifs de changement de forme

Chapter 2 donne un aperçu de quelques motifs typiques de changement de forme décrits dans la littérature. Ces motifs sont décrits d'un point de vue géométrique indépendamment des causes qui mènent au *morphing* (croissance ou *eigenstrain*). Section 2.1 présente quelques motifs de *morphing* typiques de tiges (fig. 2.1). Du fait de sa nature uni-dimensionnelle, une tige possède des motifs fondamentaux de *morphing* découplés : élongation, flexion et torsion. Une combinaison de ces trois modes conduit à une morphologie hélicoïdale. En présence de contraintes extérieures (champ gravitationnel, contraintes géométriques), ces motifs de *morphing* se diversifient souvent à cause d'une instabilité des modes fondamentaux: flambement d'Euler, perversion hélicoïdale, instabilité de Michell, ondulations fractales .... Section 2.2 présente un aperçu quelques motifs de *morphing* typiques de feuilles (fig. 2.5). À l'inverse des tiges, les motifs de *morphing* fondamentaux des feuilles (élongation, flexion simple, flexion double) ne sont pas découplés en raison du théorème remarquable de Gauss. Ceci suffit à générer une pluralité de motifs de *morphing*: dômes, selles de cheval, configuration bi-stable, ...

Description théorique du *morphing*

Chapter 3 décrit le cadre théorique qui sert à modéliser le processus de *morphing*. Les concepts fondamentaux de la mécanique des milieux continus sont rappeler dans appendix A (déformation, contrainte, énergie). Les motifs de *morphing* correspondent souvent à des grandes transformations (déplacements et rotations), ce qui justifie d'utiliser des modèles non-linéaires du point de vue de la géométrie. Section 3.1 présente le modèle de tige non-linéaire—poutre de Cosserat—qui consiste en une courbe spatiale à laquelle sont attachés des repères orthonormés locaux qui décrivent l'orientation des sections de la tige. Dans ce formalisme, les motifs de *morphing* de tiges sont décrits par les courbures matérielles (deux de flexion et une de torsion). Section 3.2 introduit la notion d'*eigenstrain*, qui permet de modéliser toutes déformations inélastique du matériau (gonflement, expansion thermique, ...) sans pour autant modifier les caractéristiques élastiques du matériau.

Méthodes numériques

Chapter 4 présente les méthodes numériques ainsi que les logiciels utilisées pour simuler les motifs de *morphing*: relaxation de ressorts (section 4.1), minimisation de l'énergie (section 4.2) et la méthode des éléments finis (section 4.3).

Méthodes expérimentales

Chapter 5 présente les méthodes expérimentales utilisées pour illustrer les motifs de *morphing*: pré-déformation (section 5.1), dilatation thermique (section 5.2) et gonflement (section 5.3).

Flexeurs

Chapter 6 étend la solution classique du bilame de Timoshenko à des flexeurs en montrant que la contrainte interfaciale est réduite en lissant la distribution d'*eigenstrain* (section 6.1), que les flexeurs peuvent être gradués longitudinalement ou modifiés pour obtenir des morphologies hélicoïdales (section 6.2) et que la flèche d'un flexeur est amplifié géométriquement en les

empilant en nid d'abeille (section 6.3).

Torseurs

Chapter 7 propose une nouvelle architecture d'*eigenstrain* par analogie avec les flexeurs qui produit de la torsion—torseurs. Le *morphing* de torseurs consiste en une instabilité extension-torsion ainsi que confirmé par la méthode des éléments finis et modéliser analytiquement (section 7.1). En combinant flexeurs et torseurs, on obtient une configuration arbitraire d'une tige (section 7.2).

Morphing controllé par la diffusion en 2D

Chapter 8 examine des bicouches à deux dimensions—feuilles—pour lesquels l'*eigenstrain* est appliqué progressivement au lieu de instantanément. Cela conduit à l'enroulement inattendu de formes rectangulaires selon le long côté (section 8.1) et au processus de *morphing* complexe de forme étoilés menant à des configurations tri-dimensionnelles (section 8.2).

Conclusion et perspectives

Les *morphers* représentent un domaine de recherche florissant dans lequel il reste beaucoup à faire. Les trois *morpher* présentés dans cette thèse (flexeurs, torseurs et feuilles bicouches) sont trois éléments qui enrichissent les possibilité de *morphing* que nous montre la Nature. Le fait de contrôler le changement de forme en imposant une architecture d'*eigenstrain* donnée par le couple "stimulus-proprieté" ouvre de nouvelles perspectives en termes de structures passives potentiellement intéressantes en Architecture.

Contents

List of Figures

List of Tables

List of Notations

(M)	Mirror plane number.
(R_n)	Rotation axis of order n.
α	Microfibrilar angle.
α, β	Greek letters run over two indices ($\{\alpha, \beta\} \in \{1, 2\}$).
α_T	Coefficient of thermal expansion.
Δx	Spatial or temporal difference of the quantity x.
δ	Mid-deflection of a bilayer.
Δ_L	Laplace operator.
$\delta_{..}$	Kronecker's symbol.
Γ	Smooth-curve living in 3D space.
κ	Curvature.
κ_i^*	Natural curvatures of a rod.
κ_i	Material curvatures of a rod.
κ_α	Principal curvatures along a surface.
λ	Wavelength.
$[\![A]\!]_x$	Jump of the quantity A at location x.
$\vee$	Symbol for the disjunction **or** derived from the latin word *vel*.
$\mathcal{C}_{ijkl}$	Components of the stiffness tensor.
$\mathcal{E}$	Elastic energy.
$\mathcal{R}$	Rod-like object.
$\mathcal{S}_{ijkl}$	Components of the compliance tensor.
$\mathcal{X}$	Rank-four tensor quantity.
$\mathcal{X} : \boldsymbol{y}$	Double contraction between rank-four tensor $\mathcal{X}$ and rank-two tensor $\boldsymbol{y}$.
$\nabla \cdot \boldsymbol{X}$	Divergence of the tensor $\boldsymbol{X}$.
$\|\boldsymbol{x}\|$	Norm of $\boldsymbol{x}$.
ν	Poisson ratio.
Ω	Initial configuration.
Ω'	Final configuration.
Ω^*	Natural configuration.
ρ	Weight density.
σ	Surface tension.
τ	Characteristic time.
$\boldsymbol{\epsilon}$	Total strain tensor.
$\boldsymbol{\epsilon}^*$	Eigenstrain tensor.
$\boldsymbol{\epsilon}_I^*$	*Impotent eigenstrain.*
$\boldsymbol{\epsilon}_N^*$	*Nilpotent eigenstrain.*
$\boldsymbol{\epsilon}^{el}$	Elastic strain tensor.
$\boldsymbol{\sigma}$	Stress tensor.
$\boldsymbol{X}$	Rank-two tensor quantity.
θ	Angle.
$\boldsymbol{b}$	Binormal spatial vector.
$\boldsymbol{d}_1$	First material vector.
$\boldsymbol{d}_2$	Second material vector.
$\boldsymbol{d}_3$	Tangent material vector.
$\boldsymbol{e}_i$	Cartesian reference frame.
$\boldsymbol{n}$	Normal spatial vector.
$\boldsymbol{r}$	Position vector.
$\boldsymbol{t}$	Tangent spatial vector.
$\boldsymbol{u}$	Displacement vector.
$\boldsymbol{w}^g$	Geometrical Darboux vector.
$\boldsymbol{w}^m$	Material Darboux vector.
$\boldsymbol{x}$	Vector quantity.
$\boldsymbol{x}'(s)$	Derivation of $\boldsymbol{x}$ with respect to s.
$\boldsymbol{x} \cdot \boldsymbol{y}$	Scalar product between vectors $\boldsymbol{x}$ and $\boldsymbol{y}$.
$\boldsymbol{x} \times \boldsymbol{y}$	Cross-product of $\boldsymbol{x}$ and $\boldsymbol{y}$.
$\boldsymbol{x}_i$	i component of $\boldsymbol{x}$.
A	Amplitude.
A	Area of cross-section.
a	Side-length of the *core* of a *twister*.
b	Depth of boundary layer.
D	Diffusion constant.
d	Diffusion depth.
E	Young modulus.
F	Fractal dimension.
f	Force exerted by a spring.
H	Mean curvature.
I	Moment of inertia.
i, j, k	Latin letters run over three indices ($\{i, j, k\} \in \{1, 2, 3\}$).
K	Gaussian curvature.
k	Spring stiffness.

L	Length.
l	Actual length of a spring.
l_0	Initial length of a spring.
M	Bending moment.
m	Mass.
N	Axial force.
O_N	Total opening of N bender cells.
p	Pressure.
R	Radius.
r	Radius of circular cross-section.
R_B	Bending rigidity.
R_i	Principal radius of curvature.
R_T	Twisting rigidity.
s	Arc-length.
T	Final temperature.
T	Twisting moment.
t	Thickness.
T_0	Initial temperature.
W	Width of a sheet.
w	Width of a beam.
x	Scalar quantity.
x, y, z	Components of $\boldsymbol{r}$.
$X_{,j}$	Partial derivation $\delta X/\delta x_j$.

Introduction

"All the branches of a tree at every stage of its height when put together are equal in thickness to the trunk [below them]."—Leonardo da Vinci *(Bell and Richter 1970)*

Patterns of shape change of natural systems have long interested scientists with modern contributions beginning with Darwin (C. Darwin and F. Darwin 1897). The diversity of these patterns is broad as remarkably illustrated by Ernst Haeckel (Haeckel 2013). In his pioneering book (Thompson et al. 1942), D'Arcy Thompson started the explanation of shape by means of physical laws and mechanisms. Since then, efforts to explain morphogenesis—creation of shape— or shape change by means of physical models have been growing. Such models combine geometry, mechanics and a driving force, which can be due to growth or to an *eigenstrain*[1].

This thesis explores the design space of solid objects, which change their shape upon interaction with an external stimulus. We call these objects *morphers* and model them as linear elastic bodies. Our goal is to identify specific architectures of *eigenstrain* that lead to specific patterns of shape change. For this, we use the theoretical framework of continuum mechanics, which we address using numerical and experimental methods.

Part I starts with an introductory chapter which aims at drawing a connection between insights gained from the study of biological *morphers* and potential applications in the field of man-made Architecture (chapter 1). Chapter 2 reviews some typical patterns of shape change that have been described in the literature.

Part II addresses the materials and methods used to explore the design space of *morphers*. Chapter 3 recalls fundamental concepts of continuum mechanics—such as strain, stress and energy—in the three-dimensional (appendix A) and one-dimensional setting and specify the role taken by *eigenstrain*. Chapter 4 presents the three numerical methods used to simulate *morphers*: relaxation of springs, energy minimization and the finite-element method. Chapter 5 describes the experimental methods used to illustrate *morphers*: prestraining, thermal expansion and swelling.

Part III presents the results of the thesis. Chapter 6 expands Timoshenko's classical solution of the bending of bilayer to *benders* by showing: how interfacial stress is lowered by smoothening the differential *eigenstrain*, how *benders* can be longitudinally graded or modified into helical morphologies and how the deflection of *benders* is geometrically amplified by a honey-comb like stacking. Chapter 7 proposes a new *eigenstrain* architecture in analogy with *benders*, that leads to twisting—*twisters*. By combining *benders* and *twisters*, arbitrary configurations of an elongated object can be achieved. Finally, chapter 8 discusses bilayer sheets, where the *eigenstrain* is applied progressively instead of instantaneously. This leads to unexpected long-side rolling of rectangular shapes and to complex multi-step folding of star shapes.

1. We use the word *eigenstrain* to refer to an imposed inelastic strain field (e.g. due to swelling, thermal expansion) (see chapter 3).

Part I

State of the Art

Chapter 1

From Biomimetic Research to Bioinspired Architecture

Contents

What is the connection between architectural [1] design and biomimetic research? An architect needs a source of inspiration in order to create. On the other hand, biomimetic research reveals new design principles drawn from Nature. This chapter proposes the latter as a source of inspiration for the former [2].

Section 1.1 tackles the question of inspiration in architectural design. Scientific knowledge both enriches and constrains the worldview of designers [3] (subsection 1.1.1). The bounds of the design space where creativity can be inspired by biomimetic research in the architectural design process can be defined and implemented using modern digital softwares (subsection 1.1.2). Subsection 1.1.3 gives an example of Architecture mimicking the shape of a natural system—soap bubbles. Section 1.2 proposes the *morphing* of plants as a new inspiration for designers. More specifically, the *structure-function relationship* which enables plant *morphing* (subsection 1.2.1) can serve as a potential source for bioinspired *morphing* in Architecture (subsection 1.2.2).

1. Throughout this thesis, we use the word "architecture" to refer either to the mesoscopic architecture of a material or to an architecture (distribution) of *eigenstrain*. In this chapter, we shall use "Architecture" with an upper case first letter or "architectural design" when referring to macroscopic Architecture.

2. It's a difficult task to argue why architects should be inspired by Nature rather than something else. However, it seems even harder to argue that they should not. History provides enough examples where this proved to be successful (i.e. Leonardo da Vinci or Antoni Gaudi).

3. We use the word designer to refer to both engineers and architects.

1.1 Inspiration in Architectural Design

We do not want to dwell on trying to define inspiration properly, but simply state that it has to do with creativity. First, subsection 1.1.1 argues that scientific knowledge both enriches and constrains the worldview [4] of designers. Then, subsection 1.1.2 defines where creativity has room for expression within the architectural design process. Finally, subsection 1.1.3 gives an example of Architecture mimicking the shape of a natural system—soap bubbles.

1.1.1 Scientific knowledge enriches and constrains the worldview of designers

The worldview of designers is on one hand enriched by scientific knowledge which increases the resolution at which they see the world and the other hand is constrained by providing the limits of what's physically possible.

> "I have a friend who's an artist and has sometimes taken a view which I don't agree with very well. He'll hold up a flower and say "look how beautiful it is" and I'll agree. Then he says "I as an artist can see how beautiful this is but you as a scientist take this all apart and it becomes a dull thing" and I think that he's kind of nutty. First of all, the beauty that he sees is available to other people and to me too, I believe. Although I may not be quite as refined aesthetically as he is ... I can appreciate the beauty of a flower. At the same time, I see much more about the flower than he sees. I could imagine the cells in there, the complicated actions inside, which also have a beauty. I mean it's not just beauty this dimension, at one centimeter; there's also beauty at smaller dimensions, the inner structure, also the processes. The fact that the colors in the flower evolved in order to attract insects to pollinate it is interesting; it means that insects can see the color. It adds a question: does this aesthetic sense also exist in the lower forms? Why is it aesthetic? All kinds of interesting questions which the science knowledge only adds to the excitement the mystery and the awe of flower. It only adds. I don't understand how it subtracts." (Feynman 1981)

What Richard Feynman highlights in this citation is that scientific knowledge does not subtract anything to the "beauty in the world". On the contrary, it adds to it. The main reason is simply that it reveals more things in the world around us—from the nanometer scale of particles to the light-year scale of the universe. In a world seen in increased resolution, there is a lot more to see than in a blurry environment. One can thus assume that the chance to find beauty (or perhaps something else?) is increased [5]. Like the *flâneur* popularized by Charles Baudelaire or Walter Benjamin in the 19$^{\text{th}}$ century, scientists have the capability to enjoy perambulating in the world [6]. For a scientific mind, everything that exists potentially triggers myriads of questions related to "*how it is made?*" and "*how does it work?*".

Structural engineers will restrict their worldview to structures in the mechanical sense. They will look at cities and man-made constructions with a much more informed view than the layman and recognize static schemes underlying buildings, bridges or skyscrapers, look how connection

4. The term "worldview" is a calque of the German word "Weltanschauung".

5. This skepticism to scientifically unravel world secrets may have had religious roots, probably because it threatened the religious explanation of the world. Friederich Nietzsche, who grappled a lot with religion has this quote about science, which may be categorized as misogynous today, but shows that skepticism against science was still around even after "God was dead": "All rightful women find science goes against their modesty. They feel as if one wanted to look under their skin - even worse! under their dress and make-up.". We translated this from the German original: "Allen rechten Frauen geht Wissenschaft wider die Scham. Es ist ihnen dabei zu Muthe, als ob man damit ihnen unter die Haut, - schlimmer noch! unter Kleid und Putz gucken wolle." (Nietzsche 1886).

6. This approach should not be confused with *hypothesis-free research* as we assume that the world behaves according to existing theoretical models. This is clearly debatable in biology, but reasonable in the context of structural mechanics. We are thus still under the umbrella of *hypothesis-driven research*.

details are solved and imagine forces flowing through structures. The human-built world is their oyster. In fact, they do not have to limit their interest to human constructions, but can extend their curiosity to natural systems such as animals and plants, which may reveal new design principles (Vincent, Currey, et al. 1980). Egyptians recognized the pyramid as being a stable and scalable form more than $\sim$ 4000 years ago and the Gizeh pyramids challenged builders for millennia. Greeks followed by Romans managed to built impressive constructions (temples, aqueducts) using Aristotelean physics principles and thorough surveying techniques (Dijksterhuis, Dikshoorn, and Knorr 1987; Pollio 1914). During the middle-age, new cathedrals where replicas of previous ones with only small variations in the design and progress was made slowly through trial and error (Follett 1989). One had to wait the 17^{th} century for Galileo Galilei (Galileo, Crew, and Salvio 1914), Robert Hooke (Hooke 1678) and Isaac Newton (Newton 1934) to lay the foundations of the science of strength of material and structural mechanics. The treatment of the cracks in Brunelleschi's Dome in Florence are often referred to as the first real-world application of this "new science", where—based on force calculations and material strength assumptions—steel rings were added at the base of the dome to bear the tensile forces (Ottoni, Coïsson, and Blasi 2010). Unfortunately, this lead to a separation of tasks within the building process between architects responsible of the design and engineers responsible of the structural integrity. Schematically, architects seek to express their *creativity*, while engineers need to compel to the *principle of reality*. This opposition between two aspects of the design process is questionable [7]. Indeed, the work-flow of an architect "drawing something pretty" and of an engineer "doing their best to fix it afterwards" has some obvious drawbacks: the actual construction often does not meet the expectancy of the architect and is irrational from the viewpoint of the engineer. Would it not be better if architects where creating within the realm of what's possible in the first place? [8] Indeed, not only does structural mechanics reveal if a construction works in the real world, it also define the limits of the design space containing what's physically possible.

1.1.2 Where is creativity needed in the Architectural design process?

This subsection gives a brief description of today's digital modeling tools before emphasizing the decision space where creativity has room to express itself in the architectural design process.

Computer aided design Using modern theoretical models describing the behavior of materials and structures, architects and engineers are now capable of exploring new designs, which can be drastically different from any existing constructions. Thanks to three-dimensional drawing programs, it is possible to create willingly complex free-form geometries—blobs—using non-uniform basis spline (NURBS) (subsection 4.1.1). Free forms are then usually decomposed into a set of ruled surfaces, a step called rationalization or paneling (Pottmann 2007). So-called digital materials that do not correspond to any real material, but take into account various other constraints (e.g. ease of fabrication or aesthetics) can help to reveal original designs (Piker 2014). The resulting shape is then often approximated regarding what is technically and economically feasible. The limit is thus not set by what can be drawn anymore, but by what can be built. However, this freedom in the design of the shape can lead to a pitfall, which is illustrated by the following citation by Nikola Tesla's replacing the word "scientists" with "architects", "mathematics" with "computer aided design" and "equation" with "design":

> "Today's scientists have substituted mathematics for experiments, and they wander

7. In today's French school system, this opposition is reflected by the separation between scientific education and humanities.

8. The philosophy of the Bauhaus, founded by Walter Gropius at the beginning of the 20^{th} century in Germany, aims at reconciling these two aspects of the design process.

> off through equation after equation, and eventually build a structure which has no relation to reality." (Tesla 1934)

Constraint driven design Beyond the potential improvement in time efficiency, the prospect of creativity expressing itself within the limits fixed by knowledge, technology and finance results in more efficient designs [9]. One critic of this approach is the argument that creativity only works in an unconstrained environment. This is obviously wrong, as musicians for example are able to express their creativity within the bounds of what their instrument is capable of—it just needs more preliminary work. Nevertheless, this remains a complex task as the constraints with which the architect must comply are numerous. Apart from programmatic constraints fixed by the investor (e.g. budget, location, program), logistic constraints (e.g. size of trucks, number of cranes), available manufacturing techniques (prefabrication or on-site assembly facilities), structures must obey principles of structural design (Bruno et al. 2010). The approach which consists in considering all the constraints during the design process—also referred to as integrated or constraint-driven design (Kilian 2006)—starts to be implemented in software programs under the common name "building information modeling (BIM)". Even within the bounds of what's physically possible and limited by what's technically doable or accessible, architects need a source of inspiration to draw their construct. Imagination can come from many sources and it seems impossible to present them consistently. However, two obvious sources of inspiration for architects are:

1. Human constructions ($\lesssim 200\,000$ years);
2. Natural constructions ($\lesssim 3.5$ Myears).

As Nature has a much longer experience in building things than humans do, it would be very surprising if designers could not learn something from it. This is where creativity can be inspired by biological research.

1.1.3 Mimicking the appearance of Nature

Copying Nature is a very old idea and has a long history in arts, culture, music and Architecture [10]. This subsection presents soap bubbles as an example of a natural system that has successfully inspired architects by starting to recall some of the physical principles underlying their formation and by giving some examples of architectural designs inspired by them.

The physics of soap bubbles Soap bubbles fascinate not only children, but also scientists, engineers and architects. A lot of observations on soap bubbles [11] can be found in the work of Isenberg (Isenberg 1978). At equilibrium, a cluster of soap bubbles consist of portions of entirely smooth surfaces with constant curvature and have two remarkable properties [12]:

1. Soap films always meet in three along an edge at an angle of 120°C;
2. These edges meet in four at a vertex at an angle of ~ 109°C (tetrahedral angle).

9. Carola Zwick's work from the Bild-Wissen-Gestaltung cluster is based on this approach.

10. Poetically speaking, the first houses can be seen as reconstructions of caves and the first bridges as trees thrown over rivers. Greek columns are similar to trunks of tall trees and traditional roofs can be seen as replicas of canopies in the forest. A lot of decorations are clearly inspired by vegetation such as flowers and leafs, and mimicking the appearance of natural shapes certainly has a good chance to please the human eye.

11. Observations include the description of their molecular structure, of their macroscopic properties such as varying light diffraction as a function of their thickness, and their use in solving physical problems such as the motorway problem or minimum area solutions.

12. These phenomenological laws—also referred to as Plateau's law—were found by Joseph Plateau in the end of the 19^{th} century.

The Young-Laplace-Gauss equation [13] describes how the geometry of a soap film accommodates pressure differences:

$$\Delta p = \sigma * 2H = \sigma * (\kappa_1 + \kappa_2) = \sigma * (\frac{1}{R_1} + \frac{1}{R_2}), \tag{1.1}$$

where Δp is the pressure difference across the soap film, σ the surface tension of the film and H the mean curvature of the film with κ_α and R_α ($\alpha \in \{1, 2\}$) the principal curvatures and radi of curvature of the film surface respectively. Energetically speaking, soap films minimize their energy which scales linearly with its area and so take a minimal surface between imposed edge boundaries.

Architectural designs inspired by soap bubbles Many architectural designs are based on the physics of soap bubbles and films. So-called minimal structures minimize the amount of material needed under some fixed boundary conditions similarly to how soap films behave. One way to design minimal structures is to use catenaries, which is the curve produced by a hanging chain under its own weight. The design of the Sagrada Familia in Barcelona by Gaudi is probably the most famous example of such a structure [14] (fig. 1.1a-c). The roof of the Munich Olympic stadium by Frei Otto also mimics the shape of a soap film [15] (fig. 1.1d). Soap bubbles can also inspire architectural designs. Using Surface Evolver [16] (Brakke 1992), one can calculate soap bubble clusters made of $2, 3, ..., n$ intersecting bubbles, which can serve as a draft for the design of "bubble-houses" (Demin and Turcaud 2009) (fig. 1.1e). Quite recently, the facade of the Beijing watercube strikingly mimics a soap bubble cluster (fig. 1.1f).

1.2 Biomimetic *Morphing* in Architecture?

The study of natural systems reveals *structure-function relationships*, which link a specific material architecture to a specific behavior of the system (Fratzl 2007). In the context of Architecture, one can mimic these relationships instead of mimicking the appearance of natural systems. They can be used by architects in two ways, either by providing them with an interesting solution to an existing problem [17], or by challenging them to find new applications for this existing solution. Subsection 1.2.1 describes the *structure-function relationship* enabling plant movement and subsection 1.2.2 addresses the question where bioinspired *morphing* can be used in Architecture.

1.2.1 The structure-function relationship of plant *morphing*

Unlike animals, plants do not need bones as they possess a stiff cell wall which—among other functions—ensures their structural integrity [18]. If differences occur between different species

13. This equation bears three names as it results from the unification by Johann Carl Friedrich Gauss in the beginning of the 19th century of the qualitative description of soap films by Thomas Young with their corresponding mathematical theory by Simon Laplace.

14. The computer program called CADenary by Axel Kilian allows to play with such catenaries. The program is available free of charge (CADenary).

15. For the anecdote, Frei Otto allegedly came to the meeting with the investors carrying a cranky construction made out of wire, which he then poured in soap water to show the design.

16. Surface Evolver is a computer program written by Kenneth Brakke twenty years ago, which minimizes a surfaces energy (e.g. surface tension, gravity) subjected to constraints similarly to how soap bubbles work. The program is available free of charge (surface evolver).

17. The self-healing capabilities of the byssal thread due to the rebounding of sacrificial bounds (Krauss et al. 2013) could inspire new solutions for the self-repairing of construction materials. A solution based on the use of bacterias is heading towards this direction (Jonkers et al. 2010).

18. Structural integrity is thus localized in animals, whereas it is distributed in plants. A similar distribution of resources is found in the mechano-sensing of spiders (Fratzl and Barth 2009).

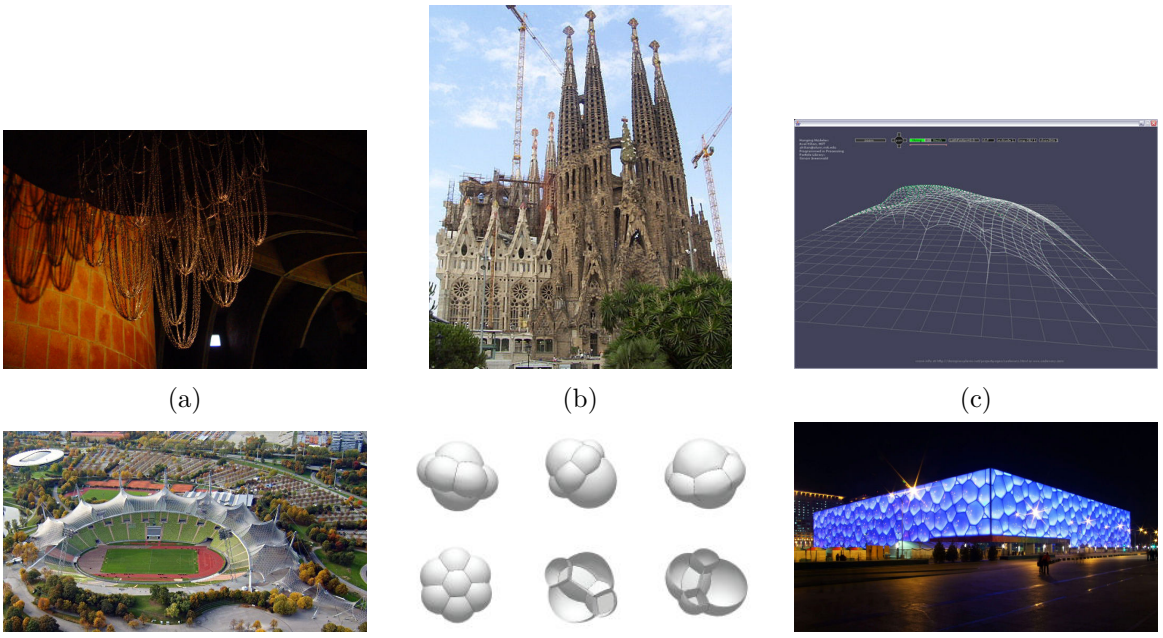

(a) (b) (c)

(d) (e) (f)

Figure 1.1 – (a) Gaudi's original hanging chain models used to determine the shape of the vaults of the Sagrada Familia in Barcelona. (b) Sagrada Familia in Barcelona still in construction planned to be finished in 2026. (c) Example of a minimal structure based on catenaries using the CADenary software by Axel Kilian. (d) The roof of the Munich Olympic stadium mimics the shape of a soap film. (e) Simulated clusters of soap-bubble clusters. (f) The facade of the Beijing watercube mimics a soap bubble cluster.

and types, many plants are organized in a similar hierarchical way (Niklas 1994). This enables us to describe these common principles taking a reductionist view without referring to any specific plant. The following describes the hierarchical ordering of the constitutive material of the structural cells in plants and discusses how the *eigenstrain* can be tuned in plants simply by changing the microfibrilar angle of the cells.

The hierarchical material architecture of plants The constitutive material of many plants is organized across three hierarchical scales [19]. It is organized like a cellular solid composed of individual plant cells, where the cell wall of each cell is itself a laminate composite. This composite material consists of a matrix of hemicelluloses and lignin reinforced by cellulose microfibrils [20]. These microfibrils are roughly parallel and wind around the cell in a helical manner at an angle called the microfibrilar angle (MFA) which is denoted by α [21].

Tuning the expansion/contraction of a plant cell through microfibrilar angle [22] The cellulose microfibrils are stiff and impermeable to water, whereas the matrix is soft and highly swellable. For a given *eigenstrain* of the matrix (ϵ^*), the longitudinal elongation of the cell is

19. For a detailed description of the hierarchical material architecture of plants, see (Fratzl and Weinkamer 2007).

20. The composition of this composite material varies across the different layers of the cell wall. This description focuses on the secondary cell wall, which is the thickest and predominant for load bearing.

21. We do not use the notation μ for the MFA, as we already use it to denote the first Lamé coefficient of an isotropic material (appendix A.2.4).

22. Here, only the behavior of "dead" cells is discussed. In the case of "living" cells, the expansion/contraction is controlled by turgor pressure.

a function of the MFA [23] (fig. 1.2). When the fibers are parallel to the cell-axis ($\alpha = 0°$), the longitudinal *eigenstrain* of the cell is nearly zero ($\epsilon^*_{zz} \approx 0$). When the fibers are perpendicular to the cell-axis ($\alpha = 90°$), the longitudinal *eigenstrain* of the cell is equal to the imposed *eigenstrain* ($\epsilon^*_{zz} \approx \epsilon^*$). Interestingly, the intermediate values of MFA ($0° < \alpha < 90°$) do not lead to an intermediate longitudinal *eigenstrain* of the cell, but there is a window of MFA ($11° < \alpha < 43°$) for which the cell shrinks longitudinally [24]. This simple model of the plant cell wall shows how plants are able to tune the longitudinal *eigenstrain* across their cross-section by tuning the microfibrilar angle.

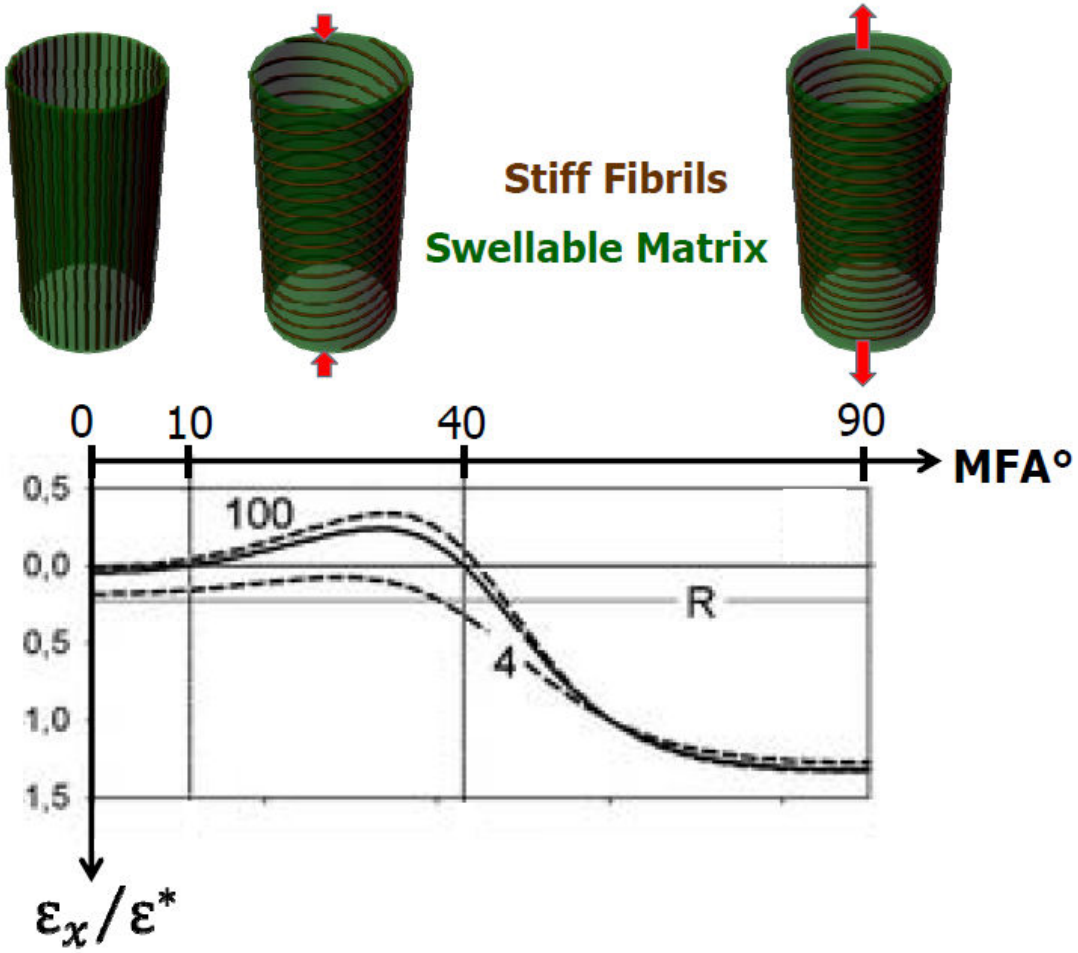

Figure 1.2 – For a given *eigenstrain* of the matrix (ϵ^*), the longitudinal swelling of the cell (ϵ_x) is zero when the fibers are parallel ($\alpha = 0°$) to the cell axis, and equal to the imposed *eigenstrain* when the fibers are perpendicular ($\alpha = 90°$) to the cell axis. For a sufficiently high stiffness contrast between the fibrils and the matrix, there exist a range of microfibrilar angles ($11° < \alpha < 43°$) for which the cell shrinks longitudinally. Modified and reproduced from (Fratzl, Elbaum, and Burgert 2008) by permission of The Royal Society of Chemistry.

23. For a detailed discussion of how the MFA tunes the swelling (and stiffness) of a cell in the longitudinal direction, see (Fratzl, Elbaum, and Burgert 2008).

24. Longitudinal shrinking occurs for a stiffness ratio of the microfibrils compared to the matrix higher than 20 (Fratzl, Elbaum, and Burgert 2008).

1.2.2 *Morphing* in Architectural design

This subsection describes how the *structure-function relationship* underlying plant *morphing* can inspire architects either to add smaller hierarchical scales to their designs or to potentially create *morphing* Architectures.

The concept of hierarchy in Architecture Architects are already familiar with the idea of hierarchy found in all natural systems at different degrees of refinement, except that they start at larger length scales [25]. A skyscraper for example is composed of floors and columns, which consists of a variety of connected beams and sheets with different profiles (lattice structures), which in turn can be analyzed in terms of singular elements with specific micro-structures. All Nature does, is going several more steps down towards smaller length scales [26]. In the context of steel construction, introducing a supplementary length scale between the micro-structure and the macroscopic profile diversifies the macroscopic properties of the object, thus potentially filling new holes in material space (Dunlop and Bréchet 2009; Bouaziz, Bréchet, and Embury 2008; Bréchet and Embury 2013).

Potential areas where *morphing* can be used in Architecture Currently, areas related to movement in Architecture are limited to openings (e.g. doors, facades) and to convertible structure (e.g. roofs, bridges) [27]. Existing realization of such moving structures includes in no specific order:

1. the expandable structures by Chuck Hoberman [28] across the world (Hoberman 2014b);
2. the facade of the Institut du Monde Arabe by Jean Nouvel in Paris [29];
3. the kinetic facade of one of the main buildings at the EXPO in Yeosu, South Korea, by Jan Knippers.

These are impressive realization, but they are all actuated by means of electrically-driven motors and sensors (see footnote 29). As sustainability is one of the main issues of our generation, one would wish to be able to farm the surrounding energy mimicking natural actuators. Also, even if the resulting *morphing* patterns can be quite elegant—such as the kinetic facade of Knippers based on a lateral-torsion instability inspired by the bird-of-paradise flower (Schleicher et al. 2011)—their driving force is discrete. In this thesis, we are interested in distributed actuation—*morphing*—driven by external fluctuating fields (such as humidity or temperature). To our knowledge, only two such realizations exist:

1. the hygroscopic structures by Achim Menges exposed at the Centre Pompidou in Paris;
2. the bimetallic structures by Doris Kim Sung (Kim Sung 2014).

Even if these structures are still more sculptures than buildings, this is a promising start. It would be interesting to realize more of these construction, especially trying out new *eigenstrain* architectures such as the *twisters* presented in chapter 7. Letting our creativity run free, an interesting question is "where else can movement be used in Architecture?". This opens a whole new paradigm in Architecture that yet needs a vision before it really start to grow [30].

25. Realization of architects are typically bigger than the biological *morphers* proposed for inspiration (e.g. pine cone).

26. Man-made structures can be analyzed at arbitrary small length scales, but contrary to natural systems, order disappears for sufficiently small length scales. Nature acts like a sculptor that arranges elements not only at the macroscopic scale, but also at very small length scales.

27. This list is most probably not exhaustive.

28. Chuck Hoberman is also known for his expandable toys (Hoberman 2014a).

29. Upon visiting the Institute, I was told that the facade only moved during the opening ceremony.

30. Neri Oxman seems to be an adequate person to formulate such a vision. The aesthetics of such a *morphing* city could be inspired by Hundertwasser.

Conclusions

This chapter describes how biological research can potentially inspire architectural design. First, the role of inspiration within the architectural design process is discussed. Scientific knowledge both enriches and constrains the worldview of a designer. Within the design space of what's possible to build, creativity can draw inspiration from biomimetic research in the architectural design process. Mimicking the shape of natural systems—such as soap bubbles—already inspires Architectural designs. Instead of copying the appearance of Nature, one can draw inspiration from the *structure-function relationship* of natural systems. As such, plant *morphing* can inspire new Architectures which *morph* in response to energy fluctuations in their environment.

References

Bouaziz, Olivier, Yves JM Bréchet, and J David Embury (2008). « Heterogeneous and architectured materials: a possible strategy for design of structural materials ». In: *Advanced Engineering Materials* 10.1-2, pp. 24–36.

Brakke, Kenneth A (1992). « The surface evolver ». In: *Experimental mathematics* 1.2, pp. 141–165.

Bréchet, Yves JM and J David Embury (2013). « Architectured materials: Expanding materials space ». In: *Scripta Materialia* 68.1, pp. 1–3.

Bruno, Andrea et al. (2010). *Featuring Steel*.

Demin, Dimitry and Sébastien Turcaud (2009). « Geometrical solutions of soap bubble clusters ». In: *Design Modeling Symposium 2009*. Ed. by Berlin Universität der Künste.

Dijksterhuis, Eduard Jan, Carry Dikshoorn, and Wilbur Richard Knorr (1987). *Archimedes*. Princeton University Press Princeton.

Dunlop, John WC and Yves JM Bréchet (2009). « Architectured structural materials: a parallel between nature and engineering ». In: *MRS Proceedings*. Vol. 1188. Cambridge Univ Press, pp. 1188–LL09.

Feynman, Richard (1981). *The pleasure of finding things out*. BBC Horizon. URL: `http://www.youtube.com/watch?v=FXiOg5-l3fk`.

Follett, Ken (1989). *The pillars of the earth*. Pan.

Fratzl, Peter (2007). « Biomimetic materials research: what can we really learn from nature's structural materials? » In: *Journal of the Royal Society Interface* 4.15, pp. 637–642.

Fratzl, Peter and Friedrich G Barth (2009). « Biomaterial systems for mechanosensing and actuation ». In: *Nature* 462.7272, pp. 442–448.

Fratzl, Peter, Rivka Elbaum, and Ingo Burgert (2008). « Cellulose fibrils direct plant organ movements ». In: *Faraday discussions* 139, pp. 275–282.

Fratzl, Peter and Richard Weinkamer (2007). « Nature's hierarchical materials ». In: *Progress in Materials Science* 52.8, pp. 1263–1334.

Galileo, G, H Crew, and A de Salvio (1914). *Discourses and Mathematical Demonstrations Relating to Two New Sciences (1638)*.

Hoberman, Chuck (2014a). *Toys*. URL: `http://www.hoberman.com/fold/main/index.htm`.

— (2014b). *Transformable design*. URL: `http://www.hoberman.com/`.

Hooke, Robert (1678). « Lectures de potentia restitutiva, or of spring explaining the power of springing bodies ». In: *Printed for John Martyn printer to the Royal Society, Bell in St. Paul's church-yard*.

Isenberg, Cyril (1978). *The science of soap films and soap bubbles*. Courier Dover Publications.

Jonkers, Henk M et al. (2010). « Application of bacteria as self-healing agent for the development of sustainable concrete ». In: *Ecological engineering* 36.2, pp. 230–235.

Kilian, Axel (2006). « Design exploration through bidirectional modeling of constraints ». In:

Kim Sung, Doris (2014). *Metal that breathes*. URL: `http://www.ted.com/talks/doris_kim_sung_metal_that_breathes`.

Krauss, Stefanie et al. (2013). « Self-repair of a biological fiber guided by an ordered elastic framework ». In: *Biomacromolecules* 14.5, pp. 1520–1528.

Newton, I (1934). *Philosophiae Naturalis Principia Mathematica (1687), translated and reprinted by Cambridge Univ.*

Nietzsche, Friedrich Wilhelm (1886). *Jenseits von Gut und Böse*. Vol. 1988.

Niklas, Karl J (1994). *Plant allometry: the scaling of form and process*. University of Chicago Press.

Ottoni, Federica, Eva Coïsson, and Carlo Blasi (2010). « The Crack Pattern in Brunelleschi's Dome in Florence: Damage Evolution from Historical to Modern Monitoring System Analysis ». In: *Advanced Materials Research* 133, pp. 53–64.

Piker, Daniel (2014). *Space Symmetry Structure*. URL: `http://spacesymmetrystructure.wordpress.com/`.

Pollio, Vitruvius (1914). *Vitruvius: The Ten Books on Architecture*. Harvard university press.

Pottmann, Helmut (2007). *Architectural geometry*. Vol. 10. Bentley Institute Press.

Schleicher, S et al. (2011). « Bio-inspired kinematics of adaptive shading systems for free form facades ». In: *Proceedings of the IABSE-IASS Symposium, Taller Longer Lighter, London, UK*. Vol. 9.

Tesla, Nikola (1934). *Radio Power Will Revolutionize the World*. Modern Mechanix. URL: `http://blog.modernmechanix.com/radio-power-will-revolutionize-the-world/`.

Vincent, Julian FV, John D Currey, et al. (1980). *The mechanical properties of biological materials*. Cambridge University Press.

Chapter 2

A Short Review of Patterns of Shape Change

Contents

Patterns of shape change is a subject of increasing interest as suggested by multiple recent reviews on non-euclidean plates (Sharon and Efrati 2010), morphological instabilities and surface wrinkling of soft materials (Li et al. 2012), stimuli-responsive polymer films (Gracias 2013), swelling or shrinking of hydrogels (Liu, Swaddiwudhipong, and W. Hong 2013; Ionov 2013), finite elasticity (Nardinocchi, Teresi, and Varano 2013), reconfigurable matter (Studart and Erb 2014) and foldable origami (Peraza-Hernandez et al. 2014) [1]. They emerge from the interplay of geometry, elasticity and *eigenstrain*, and can often be illustrated using simple toy models.

This chapter reviews some typical patterns of shape change, which can be found in natural and man-made systems. The main focus is on shape changes controlled by an architecture of *eigenstrain*, but some examples of growth or externally-induced shape changes are also covered when relevant. This approach reveals similarities between *morphers* stemming from apparently unrelated fields such as growing natural materials, swelling polymers or heated metals. A systematic approach of shape changes follows both the dimensionality of the shape and the dimensionality in which the shape change occurs [2]. This enable to establish a non-exhaustive taxonomy of patterns of shape change, which is used throughout this thesis. The shape of an object, which has two dimensions much smaller or much larger than the third [3], can be regarded as a line or a surface respectively. A line may deform on a line (stretching), in a plane (bending) or in space (twisting), whereas a surface may only deform on a surface (stretching) or in space (bending). The following discusses patterns of shape changes of one-dimensional objects (rods

1. This list is far from being exhaustive, as they have been many recents reviews on this growing topic.
2. The dimensionality in which the shape change occurs is equal to the dimensionality of the *final* configuration of the shape.
3. Volumetric *morphers* seems to be rare in nature.

and ribbons in section 2.1) and of two-dimensional objects (plates and shells in section 2.2) based on the dimensionality of the *morphing* space.

2.1 Rods and ribbons

An object which has two dimensions much smaller than the third ($a, b \ll L$) can be regarded as a line. As presented in section 3.1, such an object can be described by rod theory, where a rod is represented by a spatial curve with attached orthonormal frames giving the orientation of the cross-sections (subsection 3.1.1). In subsection 2.1.1, we discuss the three fundamental *morphing* modes of rods [4]: stretching (subsubsection 3.1.2.1), bending (subsubsection 3.1.2.2) and twisting (subsubsection 3.1.2.3). Locally, a combination of these modes leads to coiling [5] as illustrated by the ubiquitous helical patterns found in nature (Galloway 2002). In subsection 2.1.2, we discuss the *morphing* patterns of rods which appear under external or topological constraints. Due to the presence of constraints, a rod might buckle from one *morphing* mode into the other or show localized morphologies such as perversions and kinks. When increasing the external torque for example, a rod will super-coil and might display local over-coiling also called plectoneme as in the case of DNA (Yang, Tobias, and Olson 1993). Finally, rod models also help to understand differential edge-growth which constitutes a transition to the patterns of shape change described in section 2.2. An overview of these *morphing* patterns is given in fig. 2.1.

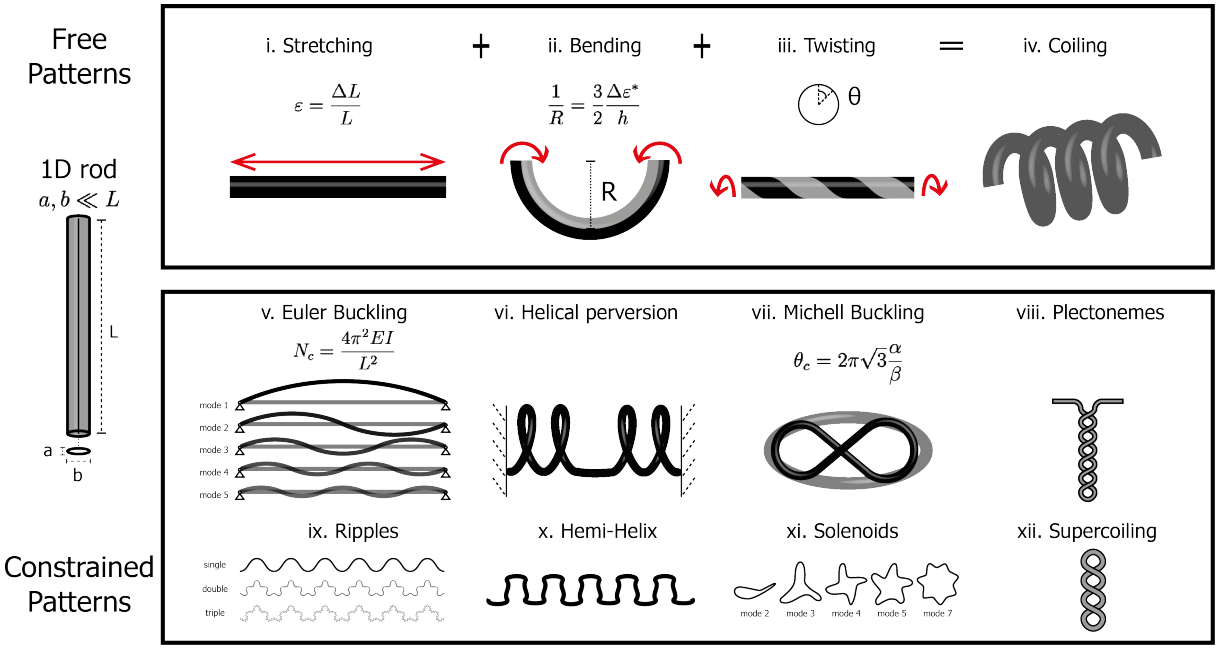

Figure 2.1 – Some shape changing patterns of rods. (i-iv) Free modes displaying changes in length—stretching (i), changes in curvature—bending (ii) and change in torsion—twisting (iii). A combination of these three modes leads to a local helical configuration—coiling (iv). (v-xii) Constrained patterns displaying stretching to bending instability under external (v) and geometrical constraint (ix), curvature to writhe instability under external constraint (vi, x), twisting to bending instability under topological constraint (vii, xi) and local (viii) or global (xii) overcoiling.

4. This is discussed in more details in subsection 3.1.2
5. The word curling could be used equivalently to coiling.

2.1.1 Free modes

In this subsection, we present the free *morphing* modes of rods analyzed in subsection 3.1.2, along with some examples of natural *morphers*. Due to the one-dimensional nature of rods, these modes are uncoupled [6] and constitute thus the basis in which all *morphing* patterns of rods can be expressed.

Stretching Free growing or expanding rods are probably the simplest systems to start with (fig. 2.1i). As analyzed in subsubsection 3.1.2.1, stretching corresponds to a uniform distribution of the longitudinal strain across the cross-section (see also fig. 7.17a). Without external or topological constraints, homogeneous tip growth or bulk growth [7] will lead to simple extension of the rod with no internal stresses. Interestingly, exponential tip growth leads to a linear increase of the rod length for a constant tip length (Goriely and Moulton 2011).

Bending Bending is ubiquitous in rod-like objects (fig. 2.1ii). As analyzed in subsubsection 3.1.2.2 and extensively discussed in section 6.1, bending corresponds to a transversal distribution of the longitudinal strain across the cross-section (see also fig. 7.17b). The seminal paper of Timoshenko on bi-metal thermostats (Timoshenko et al. 1925) paved the way to the understanding and controlling of many bilayer systems: from nano-architectured bilayers using lattice misfit (M. Huang et al. 2005), to biological actuators using differential swelling such as pine cones (Harlow, Cote, and Day 1964; Dawson, Vincent, and Rocca 1997), wheat awns (Elbaum, Zaltzman, et al. 2007; Elbaum, Gorb, and Fratzl 2008) and ice plant seed capsules (Harrington et al. 2011). The way transversal variations of expansion generate curvature is best illustrated by simple paper-plastic bilayers (Reyssat and Mahadevan 2009) or simply by a piece a paper placed on water (Reyssat and Mahadevan 2011). The distribution of eigenstrain can be smoothened by increasing the number of layers (Vasudevan and Johnson 1961), which will decrease the intersurfacial stress for the same curvature generation. A perfectly graded distribution will not produce any stress, as it is the actual distribution of elastic strain when a bar is bended (subsection 6.1.2).

Twisting Rods can also twist as their cross-section rotate around their straight middle-line (fig. 2.1iii). As analyzed in subsubsection 3.1.2.3, twisting corresponds to a radial gradient of shear strain across the cross-section (see also fig. 7.17c). Pure twist is quite rare in natural system [8] and usually occurs in combination with bending to produce coiling.

Coiling A mixture of the free *morphing* modes of a rod—coiling, produces a helical morphology (fig. 2.1iv). As initiated by Kirchhoff (Kirchhoff 1859), it can be proven that helical configurations constitute a rich family of solutions to the rod model (Chouaieb, Goriely, and Maddocks 2006), thereby underlying its frequent occurrence in nature. Among biological actuators, the stork's bill awn show an interesting example of coiling serving two purposes: the ballistic detachment from the mother plant (Evangelista, Hotton, and Dumais 2011) and the self-burial mechanism (Stamp 1984). Recently, it was shown that the coiling pattern is produced by a tilted microfibrilar helicoidal arrangement at the cell-wall level [9], which results in intrinsic coiling (Abraham et al. 2012). The intrinsic curvature and twist associated with this particular material architecture can be calculated using a non-linear rod model (Aharoni et al. 2012).

6. This is an approximation as there might be some coupling between bending and twisting in the case of anisotropic materials or thin-walled cross-sections.

7. For a review of plant cell growth, see Geitmann and Ortega 2009.

8. I couldn't find any natural actuator that displays pure twisting.

9. See subsection 1.2.1 for a description of the cell-wall architecture.

2.1.2 Constrained modes

Morphing patterns of rod-like objects become more diverse in the presence of external or topological constraints. We separated the constraints into global constraints due to self-weight (subsubsection 2.1.2.1), confinements (subsubsection 2.1.2.2), end constraints (subsubsection 2.1.2.3) and side constraints (subsubsection 2.1.2.4).

2.1.2.1 Global constraint: self-weight

In the presence of an external field such as gravity, the *morphing* patterns achieved through *eigenstrain* will be forced into an intermediate configuration, which minimizes both their elastic energy as well as their potential energy of interaction with this field.

Growing rod under self-weight For sufficient expansion, a straight growing rod of length L will finally buckle under its own weight at a critical length $L_c = \sqrt{7,837EI/\rho}$, where E is the Young modulus of the material, I the moment of inertia of the cross-section and p the weight per unit length of the rod (Greenhill 1881). For a given volume of material, shape of cross-section and Young modulus, one finds that the shape which yields the tallest column stable against buckling is a paraboloid shape [10], which can be approximately twice as tall as a cylindrical column (Niordson and J. Keller 1966). Allometric studies of trees suggest that this plays a role in the maximum observed height of trees (McMahon 1975; Niklas 1994) even though water-transport is another huge constraint whose predominance is still debated (King et al. 2009).

Curved hair under gravity In the presence of gravity, a naturally curved rod such as a hair will display an intermediate equilibrium configuration between its *natural* curved configuration, which minimizes its elastic energy, and the straight down configuration, which minimizes its potential energy (Bertails et al. 2006). For a relatively moderate weight compared to the bending rigidity of the rod, the curls will be localized near the end of the hair (fig. 2.2).

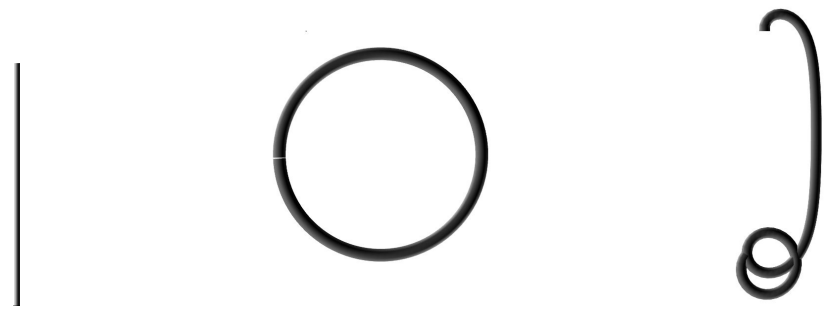

(a) (b) (c)

Figure 2.2 – (Left) Initial straight configuration. (Middle) Natural curved configuration. (Right) Final configuration under gravity. This images were produced using the energy-minimization approach presented in section 4.2.

10. Greek columns posses a slightly paraboloid shape, even though there are also thinner at their base.

2.1.2.2 Confinement

A growing rod in confined space will switch from one *morphing* mode to another in order to release some of its stretching energy [11].

Euler Take a one-dimensional wire growing between two stiff boundaries. Its stretching energy scales like $t\,\varepsilon^{*2}$, while its bending energy scales as $t^3\,\kappa^2$, where t is the thickness, ϵ^* the *eigenstrain* and κ the curvature. For sufficiently thin wire or sufficiently large eigenstrain, the bended configuration becomes more favorable than the straight configuration [12]. This is equivalent to Euler buckling (Euler 1952) with the well-known critical load $N_c = \pi^2 EI/L^2$, where E is the Young modulus, I the moment of inertia and L the length of the rod.

Michell Analogous to Euler buckling, a rod shaped as a circular ring will buckle out of plane into an eight-shape for a sufficient intrinsic twist [13] (fig. 2.1vii). The critical twist is a function of the ratio $a = R_B/R_T$ of flexural to torsional rigidity: $T_c = 2\pi\sqrt{3}/a$. The eight-shape is actually a metastable state, since work has to be done on the ring in order to return to the circular shape (Charitat and Fourcade 1998).

Crumpling Take a one-dimensional wire growing in a two-dimensional space such as a circular disk [14]. As the relative confinement space gets smaller, the wire starts to bend, comes in contact with the confinement and self-contacts until a jammed configuration of rearranging loops emerges. Self-contact and high packing densities require considering plasticity and friction as additional ingredients besides geometry and elasticity. Different global morphologies of crumpling can be achieved depending on the static wire friction as well as their elastic yield curvature (N Stoop, Wittel, and Herrmann 2008). High friction produces a symmetric cascade of loop, whereas low friction leads to asymmetric spiral morphology. Plasticity induces even more symmetry loss and results in an visually chaotic cascade of loops, which was also observed in (Gomes et al. 2008). Locally, the morphology of crumpling can be decomposed into S- and C-shaped curves (Boué et al. 2006), where the maximum curvature is inversely proportional to numbers of layers in contact $\kappa_{max} \sim 1/N$, where N is the number of layers (Spears and Alben 2008). The crumpled morphology of the wire can be analyzed using statistical analysis. This reveals a simple mass-size relation $m \sim R^F$, where m is the mass of wire, R the radius of the confining disk. The exponent F is close to the fractal dimension as determined by the box-counting method (Mandelbrot 1983) ($F = 1.8 \pm 0.2$) [15]: $F = 1.9 \pm 0.2$ (Donato, Gomes, and Souza 2003), and $F = 1.85$ (high friction) or $F = 1.75$ (plastic) (Gomes et al. 2008).

2.1.2.3 End constraints

Another way to produce *morphing* patterns, is to subject the rod to end constraints such as torques or displacements. This reveals a regular triangular buckling pattern, local or staggered

11. Such a bifurcation between *morphing* modes is called buckling in the context of structures.

12. Even though the bended configuration is characterized by a supplementary bending strain, it is longer than the straight configuration and thus the stored stretching energy is smaller.

13. This problem was discussed as early as 1889 by Michell (Michell 1889), then rediscovered in the context of submarine cables (Zajac 1962) and derived a third time twice independently in the DNA community (Benham 1989; Le Bret 1984) until credit was given back to Michell recently (Goriely 2006).

14. This can be achieved either by pushing a long wire into a small circular disk of constant size (Donato, Gomes, and Souza 2002), by reducing the size of the disk around a wire of constant length (Spears and Alben 2008) or by using a cylindrical sheet shaped into a conical shape and pulled through a circular hole (Boué et al. 2006)

15. The fact that $F \approx 2$ shows that crumpled morphology is close to filling the two-dimensional confinement space.

perversions and plectoneme or supercoils.

Triangular buckling When a thin strip is twisted between its end points under a sufficiently high tension, one observes, at some critical load, a buckling of the strip into a regular triangular pattern (Korte, Starostin, and Heijden 2010).

Perversion and hemi-helix Tendril perversion already fascinated Darwin (Darwin 1865; Darwin 1888) and remains ubiquitous in telephone cords. A first modeling of perversion was given by Keller (J. B. Keller 1980) and a n extensive review on the subject can be found in (McMillen, Goriely, et al. 2002). A perversion is a junction of two helices with opposite handiness (fig. 2.1vi). Once the growing tendril attaches to a support after circumnutation, it generates intrinsic curvature in order to increase its rigidity and toughness. As the attachments cannot rotate, the net twist has to stay zero, which leads to a perverted morphology. The change in morphology is thus a curvature-to-writhe instability (Goriely and Tabor 1998), where the symmetry breaking is constrained by a topological invariant (Pieranski, Baranska, and Skjeltorp 2004). In a recent paper (Gerbode et al. 2012), the counterintuitive over-winding of the tendril when pulled apart was explained by a large bending stiffness compared to its twisting stiffness. This behavior was reproduced using physical models of prestrained rubber strips and confirmed by a mathematical model. Another morphological pattern can emerge if one slowly releases the tension at the end of a bi-strip where one of the strips was initially prestrained. A staggering of perversion also called hemi-helix (fig. 2.1x) appears [16]. Interestingly, this hemi-helix also appears when one end of the helix is free to rotate indicating that this configuration is a stable minimum. However, this is a local minimum (metastable) as the helical configuration displays a lower elastic energy (global minimum) at the cost of overcoming an energy barrier.

Plectoneme and supercoiling When the ends of a twisted straight rod are brought together, a local twisted loop—plectoneme—will appear (fig. 2.1viii). The same morphology is achieved by twisting the ends of a rod in the presence of gravity (Bergou et al. 2008; Martin et al. 2010). If instead a twisted ring is twisted further, supercoiling morphologies appear (fig. 2.1xii) as studied extensively in the DNA community (Tobias and Olson 1993). A supercoiled morphology can also be demonstrated using a simple elastic band rotated at its ends (fig. 2.3).

2.1.2.4 Side constraints

Yet another way to enrich the *morphing* patterns of rods, is to attach them to a *passive* element along their length [17]. This reveals two types of *morphing* patterns: loops and ripples.

Looping When a growing rod is attached to an elastic sheet along its side, it will buckle into a looping morphology reminiscent of the hemi-helix mentioned above. The characteristics of this looping pattern (wavelength and amplitude), which is present in the guts of vertebrate, can be determined as a mere function of the geometrical, mechanical and *eigenstrain* characteristics measured experimentally on different guts (Savin et al. 2011).

Rippling The extending edge of a flat sheet will buckle into a multi-scale ripple (fig. 2.1ix). This morphological pattern can be observed in several natural and man-made systems, as for example along the edge of torn plastic sheets (Sharon, Roman, Michael Marder, et al. 2002)

16. The hemi-helix morphology was first reported in (El-Shiekh, Bogdan, and Gupta 1971a; El-Shiekh, Bogdan, and Gupta 1971b) among the textile literature and rediscovered recently in (J. Huang et al. 2012).

17. This substrate can have finite rigidity as in the case of loops or infinite rigidity as in the case of ripples.

(a) (b) (c)

Figure 2.3 – (Left) Initially configuration of an elastic band attached to a support and straightened by a hanging weight. (Middle) After a sufficient rotation of the bottom point, the elastic band displays a helical morphology. (Right) When the bottom point is rotated further, the helical band starts to coil into a helix.

(see fig. 2.4 were we reproduced the experiment by tearing a plastic bag [18])), along the edges of leafs (M Marder 2003) or simply in the design of clothes [19]. The excessive edge-length is either due to the irreversible plastic deformations along the edges of the crack produced by the high stress near the crack tip, the differential edge-growth or the geometry of the assembled fabric. As the bending rigidity of a sheet is much smaller than its stretching rigidity, the excessive edge-length will relax into a cascade of ripples in order to lower its elastic energy. The ripples in (Sharon, Roman, Michael Marder, et al. 2002) show 6 levels of self-similar waveform with a scaling factor of 3.2, while their amplitude stays proportional to their wavelength $A = 0.15\lambda$. This is thus an experimental realization [20] of a fractal, which spans 2.5 orders of magnitude and stop at a very small length scale (only 6.5 times the sheet's thickness). Generally speaking, the associated geometric problem consists in studying the embedding of non-euclidean surfaces (in this case hyperbolic) in 3D Cartesian space. The existence of such embeddings remains an open question and existing solutions are often far from unique (Spivak 1975). In this particular case, an explicit embedding of the hyperbolic surface resulting from edge-activation can be constructed—a "surface à godets" or "gored surface", which features the multi-scale ripple (Nechaev and Voituriez 2001). On top of this geometrical approach, elastic theory can be used to try to predict the observed morphological change. In first approximation, one can only model the distended edge by an elastic strip with appropriate boundary conditions instead of the entire sheet (Audoly and Boudaoud 2002; M Marder 2003; M Marder et al. 2003). When cut from the bulk, the distended edge relaxes into its *natural* configuration: a ring which curls on itself like a Slinky®. When the ends of the Slinky® are pulled apart, the ring becomes a helix which progressively unloops as the pulling force increases. Now the Slinky® is constrained to the bulk and therefore cannot overwind. In other words its linking number must be zero, which can only be accomplished by a combination of bending and twisting. The resulting rippled shape consists of a staggered perversion reminiscent of the hemi-helix. In more details, one can study the self-similarity of the ripples using elastic plate theory (Landau and Lifshitz 1959), thus finding a theoretical scaling factor close to the one observed experimentally (Audoly and Boudaoud 2003; Sharon, Roman, and Swinney 2007).

18. For the anecdote, we asked the cleaning ladies to borrow some samples of their trash bags.

19. A purely geometric approach to this pattern was apparently introduced as early as 1878 in Paris by the Russian mathematician Chebyshev (Chebyshev 1878), but his works remains unpublished (traces of it can be found in (McLachlan 2014)).

20. A mathematical fractal spans an infinite order of magnitude.

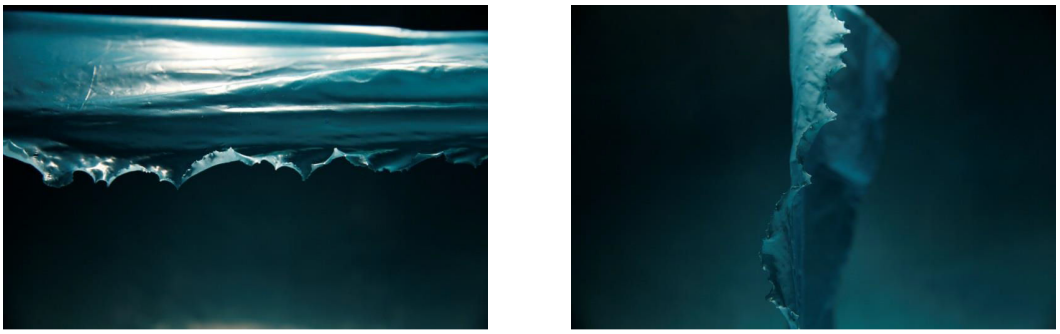

(a) (b)

Figure 2.4 – (Left) Multi-scaled ripples along the edge of a torn plastic sheet. (Right) This view of the ripples looks similar to the edge of a leaf, whose morphology follows the same principles.

2.2 Plates and shells

Sheets [21] have one dimension much smaller than the two others and can thus be assimilated to a surface. Deformation of a surface can be decomposed into bending and stretching deformation. While stretching energy scales linearly with the thickness ($\sim t$), bending energy scales with the third power of the thickness ($\sim t^3$). For sufficiently thin plates, the energy of isometric deformations [22] is thus much lower than deformations involving significant stretching of the center surface [23]. The variety of *morphing* patterns of sheets is huge and we only review a small number of them (fig. 2.5).

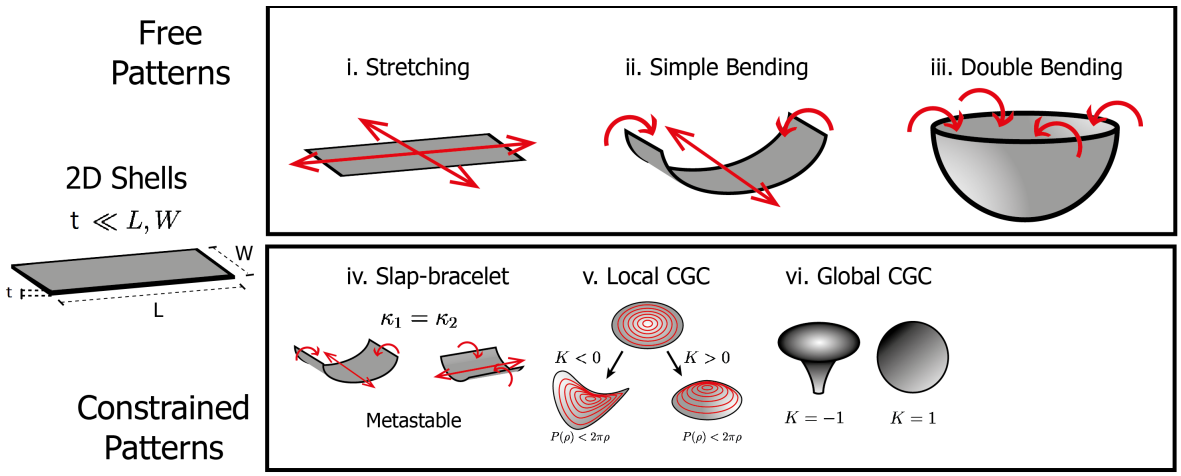

Figure 2.5 – Some shape changing patterns of shells. (i-iii) Free modes displaying uni- or bi-axial stretching (i), single bending in one direction (ii) or double bending (iii). (iv-vi) Constrained patterns displaying bi-stability (iv) local Gaussian curvature (v) and global Gaussian curvature (vi) constraints.

21. We use the word sheets to refer both to plates and shells.
22. Per definition, isometric transformations don't affect the distances.
23. This is an accordance with Gauss *theorema egregium* (see footnote 13 of chapter 8).

2.2.1 Stretching and single bending

In the case of stretching (fig. 2.5i) or single bending (fig. 2.5ii), the analyzes of the morphology can be done using the same theoretical framework as for rod-like objects (subsection 2.1.1). One only has to use a two-dimensional theoretical framework when both stretching and single bending are present at the same time, or in the presence of double bending.

2.2.2 Disks and annuli

Take a flat disk/annuli with a radial gradient in *eigenstrain*. Depending on the direction of the gradient—decreasing or increasing from inside to outside—the *eigenstrain* will impose a positive ($K > 0$) or negative ($K < 0$) Gaussian curvature respectively (fig. 2.5v) [24]. Embedding the elliptic plane ($K > 0$) in Euclidean space results in an axisymmetric dome shape, which minimizes its bending energy with almost no stretching energy through local accommodation of the prescribed Gaussian curvature. On the other hand, embedding the hyperbolic plane ($K < 0$) in Euclidean space is far less trivial (Han and J.-X. Hong 2006) and leads to a wavy structure [25] that breaks axial symmetry as was reviewed by (Gemmer and Venkataramani 2013). This azimuthally oscillating morphology only meets the target Gaussian curvature in average and the wrinkled configuration minimizes both stretching and bending energy. This was observed in (Klein, Efrati, and Sharon 2007; Efrati et al. 2007), where they used NIPA gels (see subsection 5.3.3) with changing monomer concentrations to locally tune the swelling rate. Interesting morphologies can also be achieved by considering an anisotropic *eigenstrain* in the radial and circumferential direction (Dervaux and Amar 2008). Radial growth leads to an axially symmetric conic shape, while circumferential growth leads to a saddle shape with two oscillations—e(xcessive)-cone [26]. This two morphologies strongly resembles two of the stages in the growing pattern of the algae *Acetabularia acetabulum* during its development (Serikawa and Mandoli 1998). Actually, n-fold saddle shapes are also stable such that the two-fold saddle shape could flip spontaneously to higher order folds in case as the circumferential growth increases (Müller, Amar, and Guven 2008; Santangelo 2009). Another possibility would be for the disk to stay in this two-fold configuration upon growth until it starts to form a skewed cone after self-contact occurs (Norbert Stoop et al. 2010). More generally, one can solve for the inverse problem of determining the two-dimensional *eigenstrain* which will lead to a given three dimensional axisymmetric shape (Dias, Hanna, and Santangelo 2011).

2.2.3 Bi-stability

Sheets can possess more than one equilibrium configuration upon *morphing*. As we discuss in section 8.1, the actual *morphing* pattern may depend on the history of activation. In the following, we present two examples of *morphers* which possess two stable configuration: the Venus fly-trap and the slap-bracelet.

The Venus fly-trap The Venus fly-trap is probably the most known carnivorous plant. It is also the best example of a natural bi-stable system [27]. When triggered by an adequate pray [28],

24. For an decreasing radial *eigenstrain*, the *natural* configuration would like to be "longer" inside, whereas for an increasing radial *eigenstrain*, it would like to be "longer" outside.

25. This is similar to the ripples discussed in subsubsection 2.1.2.4.

26. A related morphology to this e-cone is the d-cone where deformations are localized in the case of crumpling (Cerda et al. 1999).

27. The Venus fly-trap—a living system—is triggered by turgor pressure instead of passive swelling (see footnote 22 of chapter 1).

28. The trap is set free by stimulating at least two separate hairs, which ensures that the pray is not too small.

it closes suddenly ($\tau_c \approx 100ms$), making it one of the fastest movements in the plant kingdom (Skotheim and Mahadevan 2005). The open configuration is curved outward (convex), while the closed configuration is curved inward (concave). Upon snapping, both the Gaussian and the mean curvature of the leaf change suddenly. According to (Forterre et al. 2005), the elastic energy of the leaf displays a region of bi-stability for sufficiently large curved leafs. However, this buckling scenario is "too fast" as the inertial time is hundred times less than the snapping time, but can be adjusted by adding a viscous term due to the fluid flow inside the leaf which triggers the instability.

The slap-bracelet A famous example of a man-made bi-stable system is the slap-bracelet (fig. 2.5iv). A slap-bracelet is a bilayer where each layer is prestrained in a perpendicular direction (fig. 6.11). When the bilayer is sufficiently narrow or thick, it has a unique saddle equilibrium shape, while it displays two metastable cylindrical equilibrium shapes with the same curvature if wide or thin enough. The stability is controlled by two dimensionless parameters, which depend on mechanical properties, geometrical dimensions and the surface stress exerted by each layer on the intermediate strip [29] (Chen et al. 2012).

2.2.4 Flowers, fruits and leaves

Last but not least, *morphing* patterns can be found in profusion amongst flowers, fruits and leaves. Looking at their shape, one can try to guess the architecture of *eigenstrain* which tuned their *morphing* process. In the following, we discuss some general ideas underlying the *morphing* of flowers, fruits and leaves.

Flowers By changing the natural distance between points on a surface or by differential growth across a surface, growth acts either as a source of Gaussian or mean curvature in the case of two-dimensional shapes. At equilibrium, shapes minimize their elastic energy and accommodate both curvatures if possible. In case where no such surface exists, sufficiently thin shapes will usually nullify their stretching energy by accommodating their Gaussian curvature while minimizing their bending energy by playing with their mean curvature. The morphology of bell-shaped sympetalous flowers with approximate constant Gaussian curvature can be understood in this context. Examples of surfaces with constant Gaussian curvature are the sphere [30] ($K = 1$) and the pseudo-sphere [31] ($K = -1$) (fig. 2.5vi). Amongst many, we can cite the *brugmansia* ("Angel's trumpet") and the *surfinia* as examples of flowers which resemble an ideal piecewise sphere or pseudo-sphere separated by a number of veins (Amar, Müller, and Trejo 2012).

Fruits A lot of fruits display undulating surface morphologies—ridges. Generally speaking, these ridges appear because the skin grows faster than the core, which puts the skin under compression. When reaching a critical compressive stress, the skin starts to buckle and ridges appear. In the presence of anisotropic growth of the skin, such core/skin models can explain some global feature of fruits (Yin et al. 2008).

29. In Chen et al. (2012), they bonded two prestreched rubber sheets to a thick elastic strip, which they then analyzed using classic continuum theory. It would be interesting to see if one could apply their approach in the absence of this intermediate layer.

30. Other examples are the spindle ("rugby ball" with two cupsidal singularities) and the bulge (a sphere cut by two planes symmetrically resulting in two opposite circular singularities).

31. Equivalent variations to the ones described in footnote 30 exist also for the pseudo-sphere.

Leaves Long leaves often display a typical morphology with a saddle-like mid-surface and rippled edges [32]. The morphology of these leafs is often controlled by the profile of longitudinal growth across the leaf (Liang and Mahadevan 2009). This profile is often increasing towards the edge. As they illustrated by pulling on the edges of a rectangular foam past its yield point, an inhomogeneous profile of plastic strains [33] leads to saddle-shape configurations in case of moderate strains ($\epsilon^* \sim 5\%$) or to edge ripples for larger strains ($\epsilon^* \sim 20\%$). Returning to flowers, a similar mechanism is responsible for the blooming of asiatic lily *Lilium casablanca* (Liang and Mahadevan 2011). This approach illuminates the analogy of Goethe, who argued that flower petals are analogous to leafs physiologically (Goethe 1790).

32. See for example the leafs of the plantain lily *Hosta lancifolia* as studied in Liang and Mahadevan (2009).
33. The plastic strains being residual strain, they can act as an *eigenstrain*.

Conclusions

Patterns of shape changes are ubiquitous in natural systems. They can be found in biological actuators, which change shape upon interaction with some external stimulus, be the result of growth or simply demonstrated using experimental systems. Using arguments of geometry and elasticity, one can explain (sometimes even predict) these patterns. The richness of these patterns is huge, including bends, curls, crumples, perversions, loops and ripples.

References

Abraham, Yael et al. (2012). « Tilted cellulose arrangement as a novel mechanism for hygroscopic coiling in the stork's bill awn ». In: *Journal of The Royal Society Interface* 9.69, pp. 640–647.

Aharoni, Hillel et al. (2012). « Emergence of spontaneous twist and curvature in non-euclidean rods: application to Erodium plant cells ». In: *Physical review letters* 108.23, p. 238106.

Amar, Martine Ben, Martin Michael Müller, and Miguel Trejo (2012). « Petal shapes of sympetalous flowers: the interplay between growth, geometry and elasticity ». In: *New Journal of Physics* 14.8, p. 085014.

Audoly, Basile and Arezki Boudaoud (2002). « Ruban à godets: an elastic model for ripples in plant leaves ». In: *Comptes Rendus Mecanique* 330.12, pp. 831–836.

— (2003). « Self-similar structures near boundaries in strained systems ». In: *Physical review letters* 91.8, p. 086105.

Benham, Craig J (1989). « Onset of writhing in circular elastic polymers ». In: *Physical Review A* 39.5, p. 2582.

Bergou, Miklós et al. (2008). « Discrete elastic rods ». In: *ACM Transactions on Graphics (TOG)* 27.3, p. 63.

Bertails, Florence et al. (2006). « Super-helices for predicting the dynamics of natural hair ». In: *ACM Transactions on Graphics (TOG)*. Vol. 25. 3. ACM, pp. 1180–1187.

Boué, L et al. (2006). « Spiral patterns in the packing of flexible structures ». In: *Physical review letters* 97.16, p. 166104.

Cerda, Enrique et al. (1999). « Conical dislocations in crumpling ». In: *Nature* 401.6748, pp. 46–49.

Charitat, Thierry and Bertrand Fourcade (1998). « Metastability of a circular o-ring due to intrinsic curvature ». In: *The European Physical Journal B-Condensed Matter and Complex Systems* 1.3, pp. 333–336.

Chebyshev, Pafnouti L (1878). « On the cut of clothes ». unpublished.

Chen, Zi et al. (2012). « Nonlinear geometric effects in mechanical bistable morphing structures ». In: *Physical review letters* 109.11, p. 114302.

Chouaieb, Nadia, Alain Goriely, and John H Maddocks (2006). « Helices ». In: *Proceedings of the National Academy of Sciences* 103.25, pp. 9398–9403.

Darwin, Charles (1865). « On the movements and habits of climbing plants. » In: *Journal of the Linnean Society of London, Botany* 9.33-34, pp. 1–118.

— (1888). *The movements and habits of climbing plants*. J. Murray.

Dawson, Colin, Julian FV Vincent, and Anne-Marie Rocca (1997). « How pine cones open ». In: *Nature* 390.6661, pp. 668–668.

Dervaux, Julien and Martine Ben Amar (2008). « Morphogenesis of growing soft tissues ». In: *Physical review letters* 101.6, p. 068101.

Dias, Marcelo A, James A Hanna, and Christian D Santangelo (2011). « Programmed buckling by controlled lateral swelling in a thin elastic sheet ». In: *Physical Review E* 84.3, p. 036603.

Donato, Cassia C, Marcelo AF Gomes, and Ricardo E de Souza (2002). « Crumpled wires in two dimensions ». In: *Physical Review E* 66.1, p. 015102.

— (2003). « Scaling properties in the packing of crumpled wires ». In: *Physical Review E* 67.2, p. 026110.

Efrati, Efi et al. (2007). « Spontaneous buckling of elastic sheets with a prescribed non-Euclidean metric ». In: *Physica D: Nonlinear Phenomena* 235.1, pp. 29–32.

Elbaum, Rivka, Stanislav Gorb, and Peter Fratzl (2008). « Structures in the cell wall that enable hygroscopic movement of wheat awns ». In: *Journal of structural biology* 164.1, pp. 101–107.

Elbaum, Rivka, Liron Zaltzman, et al. (2007). « The role of wheat awns in the seed dispersal unit ». In: *Science* 316.5826, pp. 884–886.

Euler, Leonhard (1952). *Methodus inveniendi lineas curvas maximi minimive proprietate gaudentes sive solutio problematis isoperimetrici latissimo sensu accepti*. Vol. 24. Springer.

Evangelista, Dennis, Scott Hotton, and Jacques Dumais (2011). « The mechanics of explosive dispersal and self-burial in the seeds of the filaree, Erodium cicutarium (Geraniaceae) ». In: *The Journal of experimental biology* 214.4, pp. 521–529.

Forterre, Yoël et al. (2005). « How the Venus flytrap snaps ». In: *Nature* 433.7024, pp. 421–425.

Galloway, John (2002). « Helical imperative: paradigm of form and function ». In: *eLS*.

Geitmann, Anja and Joseph KE Ortega (2009). « Mechanics and modeling of plant cell growth ». In: *Trends in plant science* 14.9, pp. 467–478.

Gemmer, John and Shankar C Venkataramani (2013). « Shape transitions in hyperbolic non-Euclidean plates ». In: *Soft Matter* 9.34, pp. 8151–8161.

Gerbode, Sharon J et al. (2012). « How the cucumber tendril coils and overwinds ». In: *Science* 337.6098, pp. 1087–1091.

Goethe, Johann Wolfgang (1790). « Die Metamorphose der Pflanzen ». In: *Goethes Naturwissenschaftliche Schriften* 6.

Gomes, Marcelo AF et al. (2008). « Plastic deformation of 2D crumpled wires ». In: *Journal of Physics D: Applied Physics* 41.23, p. 235408.

Goriely, Alain (2006). « Twisted elastic rings and the rediscoveries of Michell's instability ». In: *Journal of Elasticity* 84.3, pp. 281–299.

Goriely, Alain and Derek Moulton (2011). « Morphoelasticity: A theory of elastic growth ». In: *New Trends in the Physics and Mechanics of Biological Systems: Lecture Notes of the Les Houches Summer School: Volume 92, July 2009* 92, p. 153.

Goriely, Alain and Michael Tabor (1998). « Spontaneous helix hand reversal and tendril perversion in climbing plants ». In: *Physical Review Letters* 80.7, p. 1564.

Gracias, David H (2013). « Stimuli responsive self-folding using thin polymer films ». In: *Current Opinion in Chemical Engineering* 2.1, pp. 112–119.

Greenhill, A George (1881). *Determination of the greatest height consistent with stability that a vertical pole or mast can be made, and of the greatest height to which a tree of given proportions can grow*.

Han, Qing and Jia-Xing Hong (2006). *Isometric embedding of Riemannian manifolds in Euclidean spaces*. Vol. 130. American Mathematical Society.

Harlow, William M, WA Cote, and AC Day (1964). « The opening mechanism of pine cone scales ». In: *Journal of Forestry* 62.8, pp. 538–540.

Harrington, Matthew J et al. (2011). « Origami-like unfolding of hydro-actuated ice plant seed capsules ». In: *Nature communications* 2, p. 337.

Huang, Jiangshui et al. (2012). « Spontaneous and deterministic three-dimensional curling of pre-strained elastomeric bi-strips ». In: *Soft Matter* 8.23, pp. 6291–6300.

Huang, Minghuang et al. (2005). « Nanomechanical architecture of strained bilayer thin films: from design principles to experimental fabrication ». In: *Advanced Materials* 17.23, pp. 2860–2864.

Ionov, Leonid (2013). « Biomimetic Hydrogel-Based Actuating Systems ». In: *Advanced Functional Materials* 23.36, pp. 4555–4570.

Keller, Joseph B (1980). « Tendril shape and lichen growth ». In: *Lect. Math. Life Sci* 30, pp. 257–274.

King, David A et al. (2009). « Trees approach gravitational limits to height in tall lowland forests of Malaysia ». In: *Functional Ecology* 23.2, pp. 284–291.

Kirchhoff, Gustav (1859). « Ueber das Gleichgewicht und die Bewegung eines unendlich dünnen elastischen Stabes. » In: *Journal für die reine und angewandte Mathematik* 56, pp. 285–313.

Klein, Yael, Efi Efrati, and Eran Sharon (2007). « Shaping of elastic sheets by prescription of non-Euclidean metrics ». In: *Science* 315.5815, pp. 1116–1120.

Korte, AP, EL Starostin, and GHM van der Heijden (2010). « Triangular buckling patterns of twisted inextensible strips ». In: *Proceedings of the Royal Society A: Mathematical, Physical and Engineering Science*, rspa20100200.

Landau, Lev Davidovich and Eugin M Lifshitz (1959). *Course of Theoretical Physics Vol 7: Theory and Elasticity*. Pergamon Press.

Le Bret, Marc (1984). « Twist and writhing in short circular DNAs according to first-order elasticity ». In: *Biopolymers* 23.10, pp. 1835–1867.

Li, Bo et al. (2012). « Mechanics of morphological instabilities and surface wrinkling in soft materials: a review ». In: *Soft Matter* 8.21, pp. 5728–5745.

Liang, Haiyi and L Mahadevan (2009). « The shape of a long leaf ». In: *Proceedings of the National Academy of Sciences* 106.52, pp. 22049–22054.

— (2011). « Growth, geometry, and mechanics of a blooming lily ». In: *Proceedings of the National Academy of Sciences* 108.14, pp. 5516–5521.

Liu, Zishun, Somsak Swaddiwudhipong, and Wei Hong (2013). « Pattern formation in plants via instability theory of hydrogels ». In: *Soft Matter* 9.2, pp. 577–587.

Mandelbrot, Benoit B (1983). *The fractal geometry of nature*. Vol. 173. Macmillan.

Marder, M (2003). « The shape of the edge of a leaf ». In: *Foundations of Physics* 33.12, pp. 1743–1768.

Marder, M et al. (2003). « Theory of edges of leaves ». In: *EPL (Europhysics Letters)* 62.4, p. 498.

Martin, Sebastian et al. (2010). *Unified simulation of elastic rods, shells, and solids*. Vol. 29. 4. ACM.

McLachlan, Robert (2014). *On the cut of clothes, by P. L. Tchebychef*. URL: `http://www.massey.ac.nz/~rmclachl/pseudosphere/tchebyshev.html`.

McMahon, Thomas A (1975). « The mechanical design of trees ». In: *Scientific American* 233, pp. 92–102.

McMillen, Tyler, Alain Goriely, et al. (2002). « Tendril perversion in intrinsically curved rods ». In: *Journal of Nonlinear Science* 12.3, pp. 241–281.

Michell, JH (1889). « On the stability of a bent and twisted wire ». In: *Messenger Math.* 11, pp. 181–184.

Müller, Martin Michael, Martine Ben Amar, and Jemal Guven (2008). « Conical defects in growing sheets ». In: *Physical review letters* 101.15, p. 156104.

Nardinocchi, P, L Teresi, and V Varano (2013). « The elastic metric: a review of elasticity with large distortions ». In: *International Journal of Non-Linear Mechanics* 56, pp. 34–42.

Nechaev, Sergei and Raphaël Voituriez (2001). « On the plant leaf's boundary,jupe à godets' and conformal embeddings ». In: *Journal of Physics A: Mathematical and General* 34.49, p. 11069.

Niklas, Karl J (1994). *Plant allometry: the scaling of form and process*. University of Chicago Press.

Niordson, FI and JB Keller (1966). « The tallest column ». In: *J. Math. Mech* 16, pp. 433–446.

Peraza-Hernandez, Edwin A et al. (2014). « Origami-inspired active structures: a synthesis and review ». In: *Smart Materials and Structures* 23.9, p. 094001.

Pieranski, Piotr, Justyna Baranska, and Arne Skjeltorp (2004). « Tendril perversion-a physical implication of the topological conservation law ». In: *European journal of physics* 25.5, p. 613.

Reyssat, E and L Mahadevan (2009). « Hygromorphs: from pine cones to biomimetic bilayers ». In: *Journal of The Royal Society Interface* 6.39, pp. 951–957.

— (2011). « How wet paper curls ». In: *EPL (Europhysics Letters)* 93.5, p. 54001.

Santangelo, Christian D (2009). « Buckling thin disks and ribbons with non-Euclidean metrics ». In: *EPL (Europhysics Letters)* 86.3, p. 34003.

Savin, Thierry et al. (2011). « On the growth and form of the gut ». In: *Nature* 476.7358, pp. 57–62.

Serikawa, Kyle A and Dina F Mandoli (1998). « An analysis of morphogenesis of the reproductive whorl of Acetabularia acetabulum ». In: *Planta* 207.1, pp. 96–104.

Sharon, Eran and Efi Efrati (2010). « The mechanics of non-Euclidean plates ». In: *Soft Matter* 6.22, pp. 5693–5704.

Sharon, Eran, Benoit Roman, Michael Marder, et al. (2002). « Buckling cascades in free sheets ». In: *Nature* 419.5, pp. 579–579.

Sharon, Eran, Benoit Roman, and Harry L Swinney (2007). « Geometrically driven wrinkling observed in free plastic sheets and leaves ». In: *Physical Review E* 75.4, p. 046211.

El-Shiekh, Aly, JF Bogdan, and RK Gupta (1971a). « The Mechanics of Bicomponent Fibers Part I: Theoretical Analysis ». In: *Textile Research Journal* 41.4, pp. 281–297.

— (1971b). « The Mechanics of Bicomponent Fibers Part II: Experimental Investigation ». In: *Textile Research Journal* 41.11, pp. 916–922.

Skotheim, Jan M and L Mahadevan (2005). « Physical limits and design principles for plant and fungal movements ». In: *Science* 308.5726, pp. 1308–1310.

Spears, Kevin and Silas Alben (2008). « A cascade of length scales in elastic rings under confinement ». In: *Chaos* 18.4, p. 41109.

Spivak, Michael (1975). « Differential Geometry, volume 1–5 ». In: *Publish or Perish, Berkeley*.

Stamp, Nancy E (1984). « Self-burial behaviour of Erodium cicutarium seeds ». In: *The Journal of Ecology*, pp. 611–620.

Stoop, N, Falk K Wittel, and HJ Herrmann (2008). « Morphological phases of crumpled wire ». In: *Physical review letters* 101.9, p. 094101.

Stoop, Norbert et al. (2010). « Self-contact and instabilities in the anisotropic growth of elastic membranes ». In: *Physical review letters* 105.6, p. 068101.

Studart, André R and Randall M Erb (2014). « Bioinspired materials that self-shape through programmed microstructures ». In: *Soft matter* 10.9, pp. 1284–1294.

Timoshenko, S et al. (1925). « Analysis of bi-metal thermostats ». In: *J. Opt. Soc. Am* 11.3, pp. 233–255.

Tobias, Irwin and Wilma K Olson (1993). « The effect of intrinsic curvature on supercoiling: predictions of elasticity theory ». In: *Biopolymers* 33.4, pp. 639–646.

Vasudevan, M and W Johnson (1961). « On multi-metal thermostats ». In: *Applied Scientific Research, Section B* 9.6, pp. 420–430.

Yang, Yang, Irwin Tobias, and Wilma K Olson (1993). « Finite element analysis of DNA supercoiling ». In: *The Journal of chemical physics* 98.2, pp. 1673–1686.

Yin, Jie et al. (2008). « Stress-driven buckling patterns in spheroidal core/shell structures ». In: *Proceedings of the National Academy of Sciences* 105.49, pp. 19132–19135.

Zajac, EE (1962). « Stability of two planar loop elasticas ». In: *Journal of Applied Mechanics* 29.1, pp. 136–142.

Part II

Materials and Methods

Chapter 3

Theory of *morphers*

Contents

> *"All linear problems are trivial, all non-linear problems are impossible."*
>
> —Rainer von Sachs *(Berkeley, 1970)*

A *morpher* is an object that changes its shape in response to some external energy fluctuation. The *morphing*[1] process can be theoretically described using the traditional framework of continuum mechanics and its theory of elasticity. In classical structural mechanics, shape changes and internal stresses usually results from external forces or moments applied to the boundary of an object[2]. Inspired by biological *morphers*, we are instead interested in *morphing* caused by an internal (potentially heterogeneous) inelastic strain field (which we refer to as *eigenstrain*). Such *eigenstrain* can be imposed by a variety of physical phenomena inducing inelastic volume changes (amongst others we can cite thermal expansion, swelling and phase transformation).

The fundamental concepts of the three-dimensional theory of elasticity are recalled in appendix A: the concepts of strain (appendix A.1), stress (appendix A.2), constitutive law (appendix A.2.4), mechanical equilibrium (appendix A.3) as well as elastic energy (appendix A.4). One complication that arises naturally in the description of *morphing* comes from the fact that substantial shape changes (large transformations) need to be considered instead of the usual assumption of small displacements. In a three-dimensional setting, large transformations usually induce finite strains which require considering the adequate material law and bring along a quite heavy formalism.

However, in the case of elongated objects where one dimension is either much bigger (rod) or much smaller (shell) than the other two, it is possible to obtain large transformations (dis-

1. We introduce the new word *morphing* to refer to what is sometimes known as distributed actuation.
2. Shape changes and internal stresses resulting from the interaction with an external (often homogeneous) field such as the gravitational- or a magnetic field can also be seen as a cause for *morphing*

placements and rotations) while still having small material strains. This is convenient for a theoretical approach as most materials possess a linear elastic behavior when experiencing small strains (Hooke's law) and so we only have one source of nonlinearity: *geometric nonlinearity*. This complication is unavoidable and justifies using a nonlinear rod model instead of the standard beam theory (section 3.1). Subsection 3.1.1 presents the kinematics of such a Cosserat rod and describe its fundamental modes of deformation (subsection 3.1.2): extension (subsubsection 3.1.2.1), bending (subsubsection 3.1.2.2) and twisting (subsubsection 3.1.2.3).

Section 3.2 closes the theoretical framework by introducing the concept of *eigenstrain* in the three-dimensional and one-dimensional case (subsection 3.2.1). Subsection 3.2.2 discusses how an arbitrary *eigenstrain* can be decomposed into two types of *eigenstrains*, *impotent eigenstrains*, which produces strain and no stress and *nilpotent eigenstrains*, which produces stress and no strain (subsection 3.2.2). Finally, subsection 3.2.3 describes how an *eigenstrain* can be applied progressively instead of instantaneously using a diffusion equation.

3.1 One-dimensional rods

For objects which have one dimension much larger than its other two, one would like to look at a simplified reduced one-dimensional model [3]. Classical beam theory is such an example and its knowledge is mandatory among structural engineers. However, such a beam theory usually rests on the assumption of small displacements (see appendix A.1.9) and so its use is limited in the case of *morphing* which implies large transformations. A nonlinear theory of elastic rods was pioneered by Euler's Elastica in two dimensions and completed by Kirchhoff in the three-dimensional case. It is based on differential geometry and imposes no restriction on the behavior of the rod. Such a rod-object, also called a *Cosserat* rod, is a one-dimensional example of a micropolar medium [4]. Subsection 3.1.1 presents the kinematics of such a rod and subsection 3.1.2 describes its fundamental modes of deformation. Finally, the elastic energy of such a rod is given in subsection 3.1.3.

3.1.1 Kinematics

A rod $\mathcal{R}$ is defined by a spatial curve Γ living in Euclidean space and the surrounding cross-section, which orientation is described by a field local material frames attached to the curve. Instead of using global Cartesian coordinates, spatial curves are best described using a intrinsic approach. This is done through a field of local orthonormal frames that follows the geometry of the curve [5]. Subsubsection 3.1.1.1 defines the geometrical and material frames attached to a rod, which are used to parametrize its configuration (subsubsection 3.1.1.2).

3.1.1.1 Geometrical and material frames attached to a space curve

Let Γ be a smooth curve living in three-dimensional Euclidean space. The position vector field spanning Γ is $\boldsymbol{r}(s)$ where s is the arc-length ($0 \leq s \leq L$) [6]. The projections $x(s)$, $y(s)$, $z(s)$ of $\boldsymbol{r}(s)$ on the fixed reference frame $(\boldsymbol{e_x}, \boldsymbol{e_y}, \boldsymbol{e_z})$ are its Cartesian coordinates. In the following,

3. In a one-dimensional model, all unknowns (stress and strain) depend only one degree of freedom: the longitudinal coordinate along the long direction of the object.

4. As opposed to a Cauchy medium where every point in space has three degrees of freedom, a micropolar medium adds a directionality to every point, thus possessing three more degrees of freedom.

5. The geometrical and material frames are related (see fig. 3.2).

6. In the context of rods, the actual configuration is directly parameterized by s and we use the prime notation $\boldsymbol{r}'(s)$ to denotes the derivation with respect to s. When needed, the *initial* configuration is denoted with a subscript x_0, where x is the quantity considered.

two local orthonormal frames attached to Γ are defined, which are useful to describe both the geometry of the curve Γ and the mechanical state of the rod $\mathcal{R}$.

Geometrical frame The geometrical frame (also called the Serret-Frénet frame) is a local orthonormal frame that arises naturally from the geometry of Γ. It is defined by the three vectors $\boldsymbol{t}(s)$, $\boldsymbol{n}(s)$, $\boldsymbol{b}(s)$ such that:

$$\begin{cases} \boldsymbol{t}(s) = \boldsymbol{r}'(s), \\ \boldsymbol{n}(s) = \boldsymbol{t}'(s)/\|\boldsymbol{t}'(s)\|, \\ \boldsymbol{b}(s) = \boldsymbol{t}(s) \times \boldsymbol{n}(s), \end{cases} \tag{3.1}$$

where $\boldsymbol{t}(s)$ is called the tangent vector, $\boldsymbol{n}(s)$ the normal vector and $\boldsymbol{b}(s)$ the binormal vector (see fig. 3.1). Since we chose an arc-length parametrization, the tangent vector $\boldsymbol{t}(s)$ is unitary ($\|\boldsymbol{t}(s) = 1\|$). From the tangent vector field $\boldsymbol{t}(s)$, the curve Γ can be recovered by integrating the first equation in eq. 3.1. The curvature of the curve is given by $\kappa(s) = \|\boldsymbol{t}'(s)\|$ and expresses the rate of rotation of $\boldsymbol{t}(s)$ and $\boldsymbol{n}(s)$ around $\boldsymbol{b}(s)$. For $\kappa(s) \neq 0$, the second line of eq. 3.1 can be rewritten $\boldsymbol{n}(s) = \boldsymbol{t}'(s)/\kappa(s) = R(s)\,\boldsymbol{t}'(s)$, where $R(s) = 1/\kappa(s)$ is the radius of the osculating circle [7] also called radius of curvature. The torsion of the curve is given by $\tau(s) = \boldsymbol{n}'(s) \cdot \boldsymbol{b}(s)$ and expresses the rate of rotation of $\boldsymbol{n}(s)$ and $\boldsymbol{b}(s)$ around $\boldsymbol{t}(s)$. Introducing the geometrical Darboux vector $\boldsymbol{\omega}^g(s) = \tau(s)\,\boldsymbol{t}(s) + \kappa(s)\,\boldsymbol{b}(s)$, the rate of change of the geometrical frame along the curve is then given by:

$$\boldsymbol{t}'(s) = \boldsymbol{\omega}^g(s) \times \boldsymbol{t}(s), \quad \boldsymbol{n}'(s) = \boldsymbol{\omega}^g(s) \times \boldsymbol{n}(s), \quad \boldsymbol{b}'(s) = \boldsymbol{\omega}^g(s) \times \boldsymbol{b}(s). \tag{3.2}$$

In matrix notation, this is expressed by:

$$\begin{pmatrix} \boldsymbol{t}'(s) \\ \boldsymbol{n}'(s) \\ \boldsymbol{b}'(s) \end{pmatrix} = \begin{pmatrix} 0 & \kappa(s) & 0 \\ -\kappa(s) & 0 & \tau(s) \\ 0 & -\tau(s) & 0 \end{pmatrix} \begin{pmatrix} \boldsymbol{t}(s) \\ \boldsymbol{n}(s) \\ \boldsymbol{b}(s) \end{pmatrix}. \tag{3.3}$$

The two scalar functions $\kappa(s)$ and $\tau(s)$ entirely define the curve Γ as long as $\kappa(s) = \|\boldsymbol{t}'(s)\| \neq 0$. This means that whenever the curve is straight (locally in the case of an inflexion point or globally when the curve is straight or has straight portions), the geometrical frame is ill-defined. This is why this frame that appears naturally in the analysis of mathematical curves is not well suited for building a rod model.

Material frame The material frame (also called the Darboux frame) is a local orthonormal frame attached to Γ that follows the material of the rod upon deformation. It is defined by the three vectors $\boldsymbol{d}_1(s)$, $\boldsymbol{d}_2(s)$, $\boldsymbol{d}_3(s)$ such that $\boldsymbol{d}_3(s)$ is tangent to the curve ($\boldsymbol{d}_3(s) = \boldsymbol{t}(s)$) and $\boldsymbol{d}_2(s)$, $\boldsymbol{d}_3(s)$ span the principal axis of the cross-section [8]. By assumption, we consider that the triad $(\boldsymbol{d}_1(s), \boldsymbol{d}_2(s), \boldsymbol{d}_3(s))$ remains approximately orthonormal [9]. Now for a unitary vector $\boldsymbol{d}_i(s)$, we have by definition $\|\boldsymbol{d}_i(s)\|^2 = 1$. By computing the derivate of this constant quantity with respect to s, one obtains $(\|\boldsymbol{d}_i(s)\|^2)' = 2\,\boldsymbol{d}_i'(s) \cdot \boldsymbol{d}_i(s) = 0$. This means that the derivative of a unitary vector yields a vector that is perpendicular to it. In particular, there exist three scalar functions $\kappa_1, \kappa_2, \kappa_3$ for which:

$$\begin{pmatrix} \boldsymbol{d}_1'(s) \\ \boldsymbol{d}_2'(s) \\ \boldsymbol{d}_3'(s) \end{pmatrix} = \begin{pmatrix} 0 & \kappa_3 & -\kappa_2 \\ \kappa_3 & 0 & \kappa_1 \\ \kappa_2 & -\kappa_1 & 0 \end{pmatrix} \begin{pmatrix} \boldsymbol{d}_1(s) \\ \boldsymbol{d}_2(s) \\ \boldsymbol{d}_3(s) \end{pmatrix}. \tag{3.4}$$

7. The best circle that approximates the curve at s. This circle is obviously degenerate for a straight line, thus the condition $\kappa(s) \neq 0$.

8. The principal axis of a cross-section are defined as the two perpendicular directions where the second moments of inertia a minimum and maximum respectively.

9. This is also known as the Euler-Bernoulli kinematical hypothesis, which means that in the small strain approximation, we can neglect the shear deformations between those three material vectors (see eq. A.19).

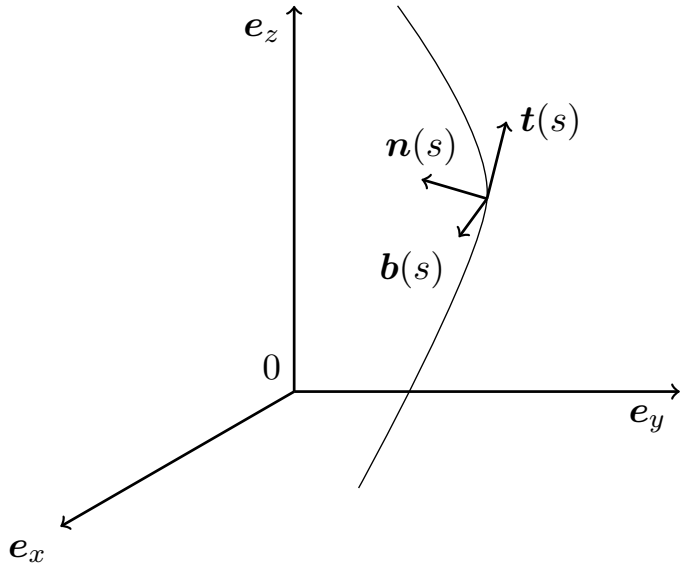

Figure 3.1 – Geometrical frame along a spatial curve given by the tangent vector $\boldsymbol{t}(s)$, the normal vector $\boldsymbol{n}(s)$ and the binormal vector $\boldsymbol{b}(s)$.

Introducing the material Darboux vector $\boldsymbol{\omega}^m(s) = \kappa_1 \boldsymbol{d}_1(s) + \kappa_2 \boldsymbol{d}_2(s) + \kappa_3 \boldsymbol{d}_3(s) = \kappa_i \boldsymbol{d}_i(s)$, we have: $\boldsymbol{d}_i'(s) = \boldsymbol{\omega}^m(s) \times \boldsymbol{d}_i(s)$. The components κ_i of the material Darboux vector express the rate of rotation of the material frame around the directions given by $\boldsymbol{d}_i(s)$. The numbers κ_1 and κ_2 are called the material curvatures (as opposed to the geometric curvature) and the κ_3 is called the material twist (as opposed to the geometric torsion). The material Darboux vector is different while related to the geometrical Darboux vector expressing the rate of rotation of the geometrical frame introduced previously. Indeed, one can pass from the geometrical frame to the material frame through a rotation of angle θ about the tangent vector $\boldsymbol{d}_3(s) = \boldsymbol{t}(s)$ (see fig. 3.2). The relations between $(\kappa_1, \kappa_2, \kappa_3)$ and (κ, τ, θ) are:

$$\begin{aligned} \kappa &= \sqrt{(\kappa_1)^2 + (\kappa_2)^2}, \\ \kappa_3 &= \tau + \frac{\mathrm{d}\theta}{\mathrm{d}s}. \end{aligned} \tag{3.5}$$

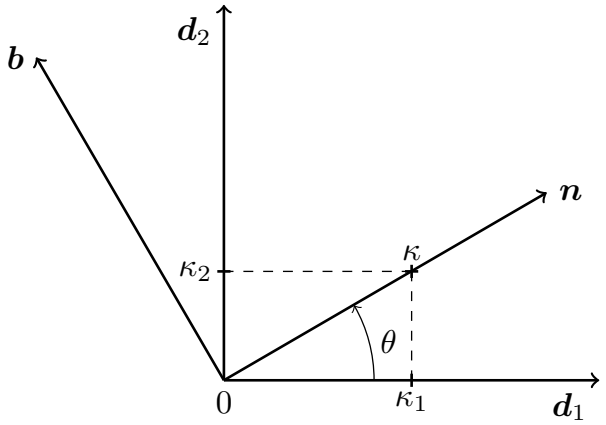

Figure 3.2 – The geometrical frame and the material frame are related by a rotation of angle θ about the tangent vector $\boldsymbol{d}_3(s) = \boldsymbol{t}(s)$. The dependence of all quantities on s is implicit.

3.1.1.2 Parametrization of the rod

Using the previously defined material frame, the rod can be parametrized as:

$$\boldsymbol{r}(x, y, z) = x\,\boldsymbol{d}_1(z) + y\,\boldsymbol{d}_2(z) + z\,\boldsymbol{d}_3(z), \tag{3.6}$$

where x and y span the cross-section of the rod [10]. The configuration of the rod is then entirely characterized by the orientation of the material vectors ($\boldsymbol{d}_i(s)$), which evolution along the rod is given by the material Darboux vector ($\boldsymbol{\omega}^m(s) = \kappa_i \boldsymbol{d}_i(s)$) through eq. 3.4 and can be concisely written as:

$$\boldsymbol{d}_i'(s) = \boldsymbol{\omega}^m(s)\boldsymbol{d}_i(s). \tag{3.7}$$

The components (κ_i) of the material Darboux vector are the measures of strain of the rod (κ_1 and κ_2 are the material curvatures and κ_3 is the material twist) [11].

3.1.2 Fundamental modes

Due to its one-dimensional nature, the rod model display uncoupled fundamental modes of deformation [12], which appear in the geometric description of a rod-object: the rod can change its length (subsubsection 3.1.2.1), bend (subsubsection 3.1.2.2) or twist (subsubsection 3.1.2.3). In general, these modes can vary along the length of the rod, in which case the one-dimensional strain measures (κ_i) and the corresponding three-dimensional strain et stress state become functions of the curvilinear abscissa (s). As long as the characteristic length of variation is larger than the characteristic thickness of the cross-section, the following analysis of uniform (translationally invariant) modes of deformation still applies.

3.1.2.1 Extension

Extensions or contractions corresponds to a re-parametrization of the curve Γ [13]. The new parametrization of the curve is given by:

$$\hat{s} = \lambda s, \tag{3.8}$$

where $\lambda - 1$ is the rate of extension of the rod similarly to what is discussed in eq. A.42. Using our analysis of traction (see appendix A.2.4), the three-dimensional strain state under extension is given by:

$$\epsilon_{zz} = \lambda, \qquad \epsilon_{xx} = \epsilon_{yy} = -\nu\,\lambda, \tag{3.9}$$

where all the non-diagonal strain components are zero by symmetry ($\epsilon_{ij} = 0,\ i \neq j$). As shown on the right side of the above equations, extension leads to a contraction of the cross-section according to Poisson effect. Using Hooke's law (eq. A.73), the three-dimensional stress state under extension is given by:

$$\sigma_{zz} = E\epsilon_{zz} = E\lambda, \tag{3.10}$$

where all the other stress components are zero.

10. $-a/2 \leq x, y \leq a/2$ for a square cross-section of side a.

11. The components of the material Darboux vector are the one-dimensional measures of strain, but should not be confused with the three-dimensional strain as defined in eq. A.11.

12. Classical rod models capture either extension effects, or bending and twisting effects. In Audoly and Pomeau 2010, chapter 3, it is argued that rod models should illustrate one of those effects, but not both, as they don't occur together. In our case, however, as deformations are imposed from within, it is possible to have both large extensions and bending/twisting effects.

13. This re-parametrization can a priori be non-uniform and vary along the length of the rod.

3.1.2.2 Bending

Bending corresponds to a change of the material curvature κ_1 and κ_2. The material Darboux vector describing the configuration of the rod is given by $\boldsymbol{\omega}^m(s) = \kappa_1 \boldsymbol{d}_1 + \kappa_2 \boldsymbol{d}_2$. Assuming that every straight filament in the *initial* configuration undergoes a traction along z in an amount proportional to the material curvatures of the rod, one can use the previous analysis of extension (subsubsection 3.1.2.1) in order to write the three-dimensional strain state under bending:

$$\epsilon_{zz}(x, y) = \kappa_1 x + \kappa_2 y, \qquad \epsilon_{xx}(x, y) = \epsilon_{yy}(x, y) = -\nu\, \epsilon_{zz}(x, y). \tag{3.11}$$

As in the case of extension, bending leads to a contraction (resp. extension) of the cross-section according to Poisson effect [14]. It can be shown that this strain field is compatible [15] and that this is indeed the strain state under bending. Using Hooke's law (eq. A.73), the three-dimensional stress state under bending is given by:

$$\sigma_{zz} = E\, \epsilon_{zz}, \tag{3.12}$$

while all the other stress components are zero. This stress field satisfies equilibrium ($\delta\sigma_{zz}/\delta z = 0$).

3.1.2.3 Twisting

Twisting corresponds to a change of the material twist κ_3. The material Darboux vector describing the configuration of the rod is given by $\boldsymbol{\omega}^m(s) = \kappa_3 \boldsymbol{d}_3$. In the case of twisting, the strain field can not be guessed immediately [16] and one has to solve the complete equation of elasticity (eq. A.77). The three-dimensional strain state actually depends on the shape of the cross-section and can be determined by solving a two-dimensional Poisson equation. In general, the solution is quite complex and involves warping [17]. In the case of a circular cross-section, the resulting strain state is quite and is given by:

$$\epsilon_{xz} = \epsilon_{yz} = \frac{\kappa_3\, r}{2}, \tag{3.13}$$

where r is the radius of the cross-section and all the other strain components are zero. Using Hooke's law (eq. A.73), the three-dimensional stress state under twisting is given by:

$$\sigma_{xz} = \sigma_{yz} = \frac{E}{2(1+\nu)} \kappa_3\, r, \tag{3.14}$$

while all the other stress components are zero [18].

3.1.3 Elastic energy

In the case of rods, the elastic energy given by eq. A.80 becomes:

$$\mathcal{E}_{rod} = \frac{1}{2} \int \left(EA(\lambda - 1)^2 + EI^{(1)}\kappa_1^2 + EI^{(2)}\kappa_2^2 + \mu J^{(\tau)}\kappa_3^2 \right) \mathrm{d}s \tag{3.15}$$

14. The upper filaments ($x, y > 0$) are extended, while the bottom filaments ($x, y < 0$) are contracted. Due to Poisson effect, the upper cross-section is contracted, while the bottom cross-section is extended (for $\nu > 0$).

15. To prove that this strain field is compatible, one would need to write the displacement field describing bending from which it derives.

16. It is no coincidence that twist was solved lastly historically as rotations are in general more confusing than translations.

17. Warping stands for out of plane deformation.

18. The coefficient $G = E/(2(1+\nu))$ is referred to as shear modulus.

where E is the Young modulus and μ is the shear modulus (see eq. A.74). A is the area and I_1 and I_2 are the principal moments of inertia of the cross-section. Section 4.2 explains how this energy can be minimized using a code written in python in order to calculate *morphing* patterns of rods.

3.2 Tuning *morphing* through *eigenstrain*

Appendix A recalls some of the fundamental concepts at the heart of the three-dimensional theory of elasticity, which were particularized in the case of elongated objects in section 3.1. This section adds one more concept to the theoretical framework describing the *morphing* of solid objects. Instead of applying external loads in order to trigger shape changes, one can impose an internal inelastic strain field, so called *eigenstrain* inspired from the biological *morphers* reviewed in chapter 2. Subsection 3.2.1 presents the concept of *eigenstrain* and describe its role in the three-dimensional and one-dimensional theoretical framework. Subsection 3.2.2 discusses an interesting distinction between two types of *eigenstrain*, which produce strain or stress exclusively. Finally, subsection 3.2.3 considers the case of a progressively applied *eigenstrain*, which accounts for the diffusion-driven *morphing* discussed in chapter 8.

3.2.1 The concept of *eigenstrain*

The concept of eigenstress was introduced as early as 1931 by Reissner to account for auto-equilibrated internal stress field in an elastic bodies (Reissner 1931) [19]. Such eigenstresses will emerge naturally in the presence of an internal strain field that can result from thermal dilatations or be due to dislocations and cracks. This concept was taken further by Eshelby, who famously solved for the elastic field around an ellipsoidal inclusion or inhomogeneity by a sequence of "imaginary cutting, straining and welding operations" (Eshelby 1957). His seminal work help to lay the foundations of the emerging field of micro-mechanics that deals with the analysis of heterogeneous materials especially regarding problems related to inclusions and dislocations at the microscopic scale of the material. The term *eigenstrain* [20] was later coined by Mura (Mura 1987) as a generic name to describe any nonelastic or stress-free strain that can arise from multiple causes such as thermal expansion, phase transformation, *initial* strains, plastic strains, misfit strains, photo-induced strains, ... This was formalized into the *eigenstrain* method, which despite its potential generality is mainly used for the static shape control of macroscopic structures. The main idea of shape control is to actively tune the internal *eigenstrain* field (i.e. by embedded piezoelectric actuators) in order to nullify all shape changes due to external causes. Based on this idea, intelligent structures for aerospace (such as satellites or telescopes) have been studied and designed in the recent years (Loewy 1997, Chopra 2002). In the spirit of Eshelby, let us introduce an auxiliary configuration, which represent the state of the object once all its stressed parts have been cut out and allowed relaxing into their desired state. Contrary to the *initial* and *final* configuration, the *natural* configuration is not a physical state of the object, but an imaginary configuration that helps to write down the mechanical equations of a solid body subjected to an *eigenstrain* distribution. By definition, it is stress-free and can be seen as the new reference configuration of the object from which elastic strains are to be measured.

Natural configuration Let Ω^* be the *natural* state of the object. In general, the *natural* configuration is not a connected domain in Euclidean space, but corresponds to a collection of

19. In the engineering literature, the term *residual stress* is used to describe such an auto-equilibrated internal stresses.

20. Sometimes the word *inherent strain* is used equivalently see (Ueda et al. 1975).

unstressed (potentially infinitesimal) domains.

Total strain The total strain $\boldsymbol{\epsilon}(\boldsymbol{r})$ is defined by the transformation between the *initial* configuration Ω and the *final* configuration Ω'. The total strain must fulfill the compatibility equations (see appendix A.1.11). This means that there exist a displacement vector field $\boldsymbol{u}(\boldsymbol{r})$ from which $\boldsymbol{\epsilon}(\boldsymbol{r})$ derives (see eq. A.11).

Eigenstrain The *eigenstrain* $\boldsymbol{\epsilon}^*(\boldsymbol{r})$ is defined by the transformation between the *initial* configuration Ω and the *natural* configuration Ω^*. The *eigenstrain* can be chosen arbitrarily. This means that there might not exist a displacement vector field from which it derives.

Elastic strain The elastic strain $\boldsymbol{\epsilon}^{el}(\boldsymbol{r})$ [21] is defined by the transformation between the virtual configuration Ω^* and the *final* configuration Ω'. Elastic strains arises whenever the *eigenstrain* is incompatible, i.e. in order to ensure the compatibility of the total strain.

Additive decomposition of strain In the context of small strains (eq. A.24), the total strain is given by the sum of the *eigenstrain* and the elastic strain:

$$\boldsymbol{\epsilon}(\boldsymbol{r}) = \boldsymbol{\epsilon}^{el}(\boldsymbol{r}) + \boldsymbol{\epsilon}^*(\boldsymbol{r}). \tag{3.16}$$

Hooke's law in the presence of *eigenstrain* By construction, only the elastic strain generates stresses. In the presence of *eigenstrain*, Hooke's law in term of the Lamé coefficients (eq. A.72) becomes:

$$\sigma_{ij}(\boldsymbol{r}) = 2\mu \left(\epsilon_{ij}(\boldsymbol{r}) - \epsilon^*_{ij}(\boldsymbol{r})\right) + \lambda\Big(\epsilon_{kk}(\boldsymbol{r}) - \epsilon^*_{kk}(\boldsymbol{r})\Big)\,\delta_{ij}. \tag{3.17}$$

In terms of the Young modulus and Poisson ratio (eq. A.73), one obtains:

$$\sigma_{ij}(\boldsymbol{r}) = \frac{E}{1+\nu}\left(\left(\epsilon_{ij}(\boldsymbol{r}) - \epsilon^*_{ij}(\boldsymbol{r})\right) + \frac{\nu}{1-2\nu}\left(\epsilon_{kk}(\boldsymbol{r}) - \epsilon^*_{kk}(\boldsymbol{r})\right)\delta_{ij}\right), \tag{3.18}$$

which can be written in a concise form as:

$$\sigma_{ij}(\boldsymbol{r}) = \mathcal{C}_{ijkl} : (\epsilon_{kl}(\boldsymbol{r}) - \epsilon^*_{kl}(\boldsymbol{r}))\,, \qquad \epsilon_{ij}(\boldsymbol{r}) - \epsilon^*_{ij}(\boldsymbol{r}) = \mathcal{S}_{ijkl} : \sigma_{kl}(\boldsymbol{r}), \tag{3.19}$$

where $\mathcal{C}$ and $\mathcal{S} = \mathcal{C}^{-1}$ are the stiffness and compliance rank-four tensors respectively. This means that the change in material properties as it is subjected to *eigenstrain* is disregarded [22].

Equilibrium By substituting Hooke's law in the presence of *eigenstrain* (eq. 3.19) into the equation of equilibrium in the absence of body forces (eq. A.71), one obtains [23]:

$$\left[\mathcal{C}_{ijkl} : (\epsilon_{kl}(\boldsymbol{r}) - \epsilon^*_{kl}(\boldsymbol{r}))\right]_{,j} = 0. \tag{3.20}$$

Assuming that the material is homogeneous, the stiffness tensor $\mathcal{C}_{ijkl}$ does not depend on position $\boldsymbol{r}$ and can be taken out from the partial derivative:

$$\mathcal{C}_{ijkl} : \epsilon_{kl,j}(\boldsymbol{r}) - \mathcal{C}_{ijkl} : \epsilon^*_{kl,j}(\boldsymbol{r}) = 0. \tag{3.21}$$

21. One should be careful to express $\boldsymbol{r}$ in the *initial* configuration.
22. This approximation seems reasonable as long as the *eigenstrain* is relatively small.
23. Here we use the comma derivative notation to write the partial derivation $\delta/\delta x_j$.

Comparing eq. 3.21 with eq. A.70, the contribution of the *eigenstrain* to the equation of equilibrium appears to play a similar role as a volumic force $-\mathcal{C}_{ijkl} : \epsilon^*_{kl,j}(\boldsymbol{r})$ [24]. The boundary condition for the free external boundary becomes:

$$\boldsymbol{\sigma} \cdot \boldsymbol{n} = 0 \implies \mathcal{C}_{ijkl} : \epsilon_{kl}(\boldsymbol{r})\, n_j = \mathcal{C}_{ijkl} : \epsilon^*_{kl}(\boldsymbol{r})\, n_j, \tag{3.22}$$

which shows that the effect of the *eigenstrain* is that of a surface force $\mathcal{C}_{ijkl} : \epsilon^*_{kl}(\boldsymbol{r})\, n_j$ acting on the boundary.

Eigenstrain mechanical problem Similarly to appendix A.3, let's write all the equation describing the static equilibrium of a continuous elastic medium subjected to an *eigenstrain* field and in the absence of (other) volumic forces nor imposed external forces and displacements in a concise form (the dependence on $\boldsymbol{r}$ is implicit):

$$\textbf{(SF)}^* \begin{cases} \nabla \cdot \boldsymbol{\sigma} = \mathbf{0} & \text{in } \Omega, \\ \boldsymbol{\sigma} = \mathcal{C} : \boldsymbol{\epsilon}^{el} & \text{in } \Omega, \\ \boldsymbol{\epsilon} = \boldsymbol{\epsilon}^* + \boldsymbol{\epsilon}^{el} = \frac{1}{2}(\nabla \boldsymbol{u} + \nabla^t \boldsymbol{u}) + \frac{1}{2}(\nabla \boldsymbol{u} \cdot \nabla^t \boldsymbol{u}) & \text{in } \Omega, \\ \boldsymbol{\sigma} \cdot \boldsymbol{n} = \mathbf{0} & \text{on } \delta\Omega. \end{cases} \tag{3.23}$$

Remark (On the inapplicability of the *eigenstrain* method)**.** *The above eigenstrain problem appears in (Mura 1987) and constitute the basis of the eigenstrain method. The next step consists in finding solutions to eq. 3.21 by using Fourier series, which enable to express arbitrary eigenstrain distribution. However, this approach is based on the superposition principle, which only holds when using the linearized strain tensor. To our knowledge, an analytical solution in the nonlinear case is not known.*

Elastic energy in the presence of *eigenstrain* Correspondingly, the elastic energy of a continuous elastic media in the presence of *eigenstrain* becomes (see eq. A.80):

$$\mathcal{E}_{el} = \frac{1}{2} \iiint_V \sigma_{ij} \left[\left(\epsilon_{ij}(\boldsymbol{r}) - \epsilon^*_{ij}(\boldsymbol{r}) \right) \right] \left(\epsilon_{ij}(\boldsymbol{r}) - \epsilon^*_{ij}(\boldsymbol{r}) \right) \mathrm{d}V. \tag{3.24}$$

Energy of a rod with *natural* curvatures The elastic energy of a rod with *natural* curvatures is given by:

$$\mathcal{E}_{rod} = \frac{1}{2} \int \left(EA \left(\epsilon - \epsilon^* \right)^2 + EI^{(1)} \left(\kappa_1 - \kappa_1^* \right)^2 + EI^{(2)} \left(\kappa_2 - \kappa_2^* \right)^2 + \mu J \left(\kappa_3 - \kappa_3^* \right)^2 \right) \mathrm{d}s \tag{3.25}$$

where κ_i^* are the *natural* curvatures [25].

3.2.2 Decomposition of *eigenstrain*

An interesting distinction can be made between two types of *eigenstrain* (Nyashin, Lokhov, and Ziegler 2005): *impotent eigenstrain* that doesn't produce stress and *nilpotent eigenstrain* that doesn't produce strain. In fact, any *eigenstrain* can be decomposed into a *impotent-*

24. The first term of this equation gives the stress corresponding to the total strain. In fact, only the elastic strain creates stress.

25. The natural curvatures are one-dimensional measures of the three-dimensional *eigenstrain*. There is no bijection between the natural curvatures and the *eigenstrain* due to the possibility of *nilpotent eigenstrain* which do not produce any strain (subsection 3.2.2).

and a *nilpotent* part. Let's consider an arbitrary *eigenstrain* $\boldsymbol{\epsilon}^*$. In order to fulfill the set of equations given in (eq. 3.23), this *eigenstrain* induces an elastic strain $\boldsymbol{\epsilon}^{el}$, which generates an auto-equilibrated stress field $\boldsymbol{\sigma}$ (that respects equilibrium as well as the free surface boundary condition). In addition, the object is deformed according to the total strain $\boldsymbol{\epsilon}$ [26]

Impotent eigenstrain Let $\boldsymbol{\epsilon}_I^* = \boldsymbol{\epsilon}$ be the *eigenstrain* which is equal to the total strain. This *eigenstrain* is *impotent* and does not produce any stress in the body [27]. Subtracting this *eigenstrain* on both sides of the additive decomposition of strain (eq. 3.16), one obtains:

$$0 = \boldsymbol{\epsilon}^{el} + \boldsymbol{\epsilon}^* - \boldsymbol{\epsilon}_I^*. \tag{3.26}$$

Nilpotent eigenstrain Let's define the *eigenstrain* $\boldsymbol{\epsilon}_N^* = \boldsymbol{\epsilon}^* - \boldsymbol{\epsilon}_I^*$. The previous equation becomes:

$$0 = \boldsymbol{\epsilon}^{el} + \boldsymbol{\epsilon}_N^*. \tag{3.27}$$

Thus, $\boldsymbol{\epsilon}_N^*$ is *nilpotent* as it does not create any strain. By construction, $\boldsymbol{\epsilon}^* = \boldsymbol{\epsilon}_I^* + \boldsymbol{\epsilon}_N^*$, which shows that an arbitrary *eigenstrain* can be decomposed into an *impotent* and a *nilpotent* part. In fact, it can be proven that this decomposition is unique (Nyashin, Lokhov, and Ziegler 2005). This decomposition of *eigenstrain* enables to fully separate the generation of strain and stress in actuated structures. *Impotent eigenstrain* enable to generate arbitrary shape changes and only depends on the chosen *initial* geometry and the desired *final* geometry [28].

One-dimensional example To understand how *eigenstrain* can create both displacements (strain) and forces (stress), let's look at a bar of length L and rigidity EA attached to a spring of stiffness K growing with an *eigenstrain* ε^* such that the bar is in compression when $\varepsilon^* > 0$ (fig. 3.3). Hooke's law in the presence of *eigenstrain* (eq. 3.19) $\sigma = E(\varepsilon - \varepsilon^*)$ states that the internal stress σ is proportional to the elastic strain, which is the difference between the geometric strain $\varepsilon = \delta u/\delta\varepsilon$ and the *eigenstrain* ε^*. Integrating over the cross-section and considering the boundary conditions $u(x = 0) = 0$ and $N = Ku(x = L)$ where N is the internal force, one obtains $N = \lambda EA\varepsilon^*/(1 - \lambda)$ and $u = \varepsilon^* x/(1 - \lambda)$, where $\lambda = KL/EA$ is the rigidity contrast. This example shows that there are no efforts in the bar when $\lambda \to 0$ and all eigenstrain gives rise to displacements. If $\lambda \to \infty$, there are no displacements and all eigenstrain is taken up in compression.

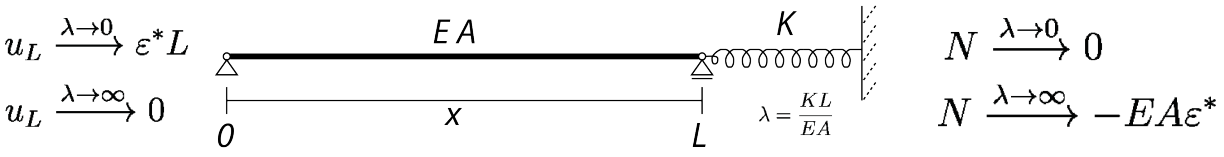

Figure 3.3 – One-dimensional bar of length L and stretching rigidity EA expanding against a spring of rigidity K. Depending on the rigidity contrast between the bar and the spring ($\lambda = KL/EA$), the *eigenstrain* is either converted into stress (*nilpotent*) or strain (*impotent*).

26. One should be careful to note that the total strain depends on the *eigenstrain* and so tuning the *eigenstrain* effectively changes the total strain.

27. This *eigenstrain* is obviously compatible as the total strain must be compatible.

28. The only limitation is given by topological consideration. In particular, *eigenstrain* only enable to trigger shape changes within the homotopic class of an object.

3.2.3 Diffusion-driven *morphing*

As we'll discuss in chapter 8, the *eigenstrain* can be applied progressively instead of instantaneously. This can be modeled using a diffusion equation similar to the heat equation:

$$\frac{\delta \boldsymbol{\epsilon}}{\delta t} = D\Delta_L \boldsymbol{\epsilon}, \tag{3.28}$$

where Δ_L is the Laplace operator [29] and D the diffusion constant. From eq. 3.28, the characteristic length of diffusion is given by:

$$L_c \approx \sqrt{D\tau_c}, \tag{3.29}$$

where τ_c is the characteristic time. Analytical solutions to eq. 3.28 are not trivial in 2D, which is why we used the fem as described in section 4.3.

29. The Laplace operator is defined by $\Delta_L = \nabla^2 = \frac{\delta^2}{\delta x} + \frac{\delta^2}{\delta y} + \frac{\delta^2}{\delta z}$.

Conclusions

This chapter describes the theoretical framework used to explore the design space of *morphers*. It consists of a combination of fundamental concepts of continuum mechanics (e.g. strain, stress, equilibrium, energy) with the concept of *eigenstrain* from micro-mechanics. Due to the fact that *morphing* patterns often imply large shape changes, the common small displacements assumption can not be made. This justifies using the non-linear theory of elasticity, which is presented in the case of elongated rod-like objects.

References

Audoly, Basile and Yves Pomeau (2010). *Elasticity and geometry*. Oxford Univ. Press.

Chopra, Inderjit (2002). « Review of state of art of smart structures and integrated systems ». In: *AIAA journal* 40.11, pp. 2145–2187.

Eshelby, John D. (1957). « The determination of the elastic field of an ellipsoidal inclusion, and related problems ». In: *Proceedings of the Royal Society of London. Series A. Mathematical and Physical Sciences* 241.1226, pp. 376–396.

Loewy, Robert G (1997). « Recent developments in smart structures with aeronautical applications ». In: *Smart Materials and Structures* 6.5, R11.

Mura, Toshio (1987). *Micromechanics of defects in solids*. Vol. 3. Springer.

Nyashin, Y, V Lokhov, and F Ziegler (2005). « Decomposition method in linear elastic problems with eigenstrain ». In: *ZAMM-Journal of Applied Mathematics and Mechanics/Zeitschrift für Angewandte Mathematik und Mechanik* 85.8, pp. 557–570.

Reissner, H (1931). « Eigenspannungen und Eigenspannungsquellen ». In: *ZAMM-Journal of Applied Mathematics and Mechanics/Zeitschrift für Angewandte Mathematik und Mechanik* 11.1, pp. 1–8.

Ueda, Yukio et al. (1975). « A new measuring method of residual stresses with the aid of finite element method and reliability of estimated values ». In: *Transactions of JWRI* 4.2, pp. 123–131.

Chapter 4

Numerical methods

Contents

Finding analytical solutions to the theoretical models presented in chapter 3 is not trivial in general and numerical methods are helpful. This chapter presents the numerical methods as well as the software environment used to calculate and represent some of the patterns of shape changes presented in chapter 6, chapter 7 and chapter 8. Three different and complementary approaches are used:

1. elongated (continuous) *morphers* can be represented by a discrete mass-spring particle system, where the differential *eigenstrain* is tuned by modifying the rest length of the springs. The equilibrium configuration of the structure is found by minimizing the forces inside the system using dynamic relaxation. This is done within the 3D modeling software Rhinoceros® with the help of the plug-in Kangaroo^{TM}, which is itself a module of the visual programming interface of Rhinoceros called Grasshopper® (section 4.1);
2. elongated *morphers* can also be represented as one-dimensional rods (section 3.1), where the differential *eigenstrain* is tuned directly through the natural curvatures. The equilibrium configuration of the structure is found by minimizing the energy of the system using a quasi-newton method. This is done with the help of python programming language within the working environment IPython using the Scipy package for computation and MayaVi for visualization (section 4.2);
3. *morphing* patterns can also be calculated using the finite-element method in order to solve for the static equilibrium of a thermo-mechanical problem, where the differential *eigenstrain* is imposed by means of a thermal field interacting with the thermal expansion coefficients of the material. This is done using the software Abaqus® with the help of parametric models written in python within the Python Developing Environment (PDE) (section 4.3).

4.1 Relaxation of springs

Instead of representing *morphers* as continuous media, they can be represented by three-dimensional squared lattice connected by springs. The stiffness of the springs (k) accounts for the elasticity of the material while their rest length (l_0) corresponds to their natural state. Modifying the rest lengths of the springs relatively to the initial geometrical distance between the nodes of the lattice amounts to impose a differential *eigenstrain* throughout the structure. This representation enables to grasp the somehow abstract concept of strain more intuitively and can be used to visualize the bending and twisting *morphing* patterns discussed in subsubsection 6.1.3.1 and subsubsection 7.1.4.1. Subsection 4.1.1 presents the software environment that used to implement the model, while subsection 4.1.2 describes the squared lattice model used to represent elongated *morphers*.

4.1.1 Rhinoceros®

Rhinoceros® (Rhino) is computer aided design (CAD) program based on non-rational uniform b-splines (NURBS) that enables to draw willingly complex shapes. Currently, its usage is widespread in the architectural community and it experienced an intense development in recent years (McNeel and Associates 2014b). Besides its capabilities in terms of drawing complex three-dimensional geometries, its key features are its relatively low learning curve as well as its interoperability making it a useful software in a workflow with other programs such as finite-element (subsection 4.3.1) and 3-D printing programs (subsection 5.3.2). Subsubsection 4.1.1.1 and subsubsection 4.1.1.2 present the visual programming plug-in for Rhino called Grasshopper [1] and the Kangaroo plug-in for grasshopper, which is used to draw and to calculate the squared lattice model representing a beam.

4.1.1.1 Grasshopper®

Grasshopper® is a plug-in for Rhino that enables to parametrize geometries [2] using visual programming [3] (McNeel and Associates 2014a). The advantage of parametric geometry over datum geometry, is that it enables to explore families of geometries instead of just one. Compared to standard scripting methods, visual programming offers a simpler toy-like interface, which allows for efficient interactive scripting as long as the size of the block diagram is reasonably small (fig. 4.1). Also, besides the standard objects already defined within Grasshopper, one is also able to write new blocks with their own code.

4.1.1.2 Kangaroo

Kangaroo is a live physics engine for Grasshopper written in visual basic for grasshopper by Daniel Piker (Piker 2014a). It enables to embed physical or pseudo-physical [4] behavior between the geometrical entities defined in grasshopper, such as gravity and springs. It is mainly used in the context of form-finding and is based on dynamic relaxation.

1. All the plug-ins for Rhino happen to have animal names.
2. A parametric geometry is defined through the formal relations between the parameters which define the geometry, where these parameters are subjected to change.
3. Visual programming uses block diagrams to connect the geometrical parameters and the objects which generate the geometry.
4. See Piker 2014b for an interesting discussion about pseudo-physical materials.

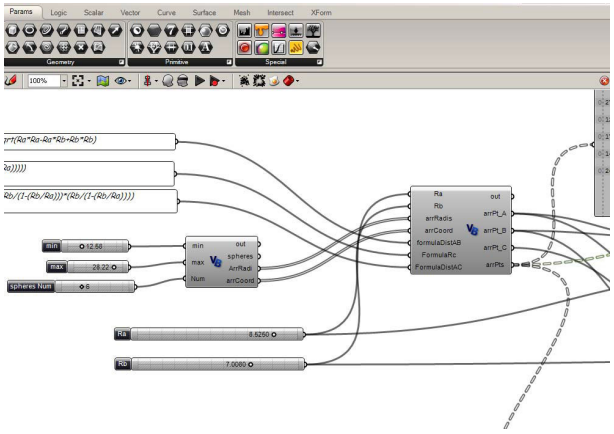

Figure 4.1 – Example of a block diagram in Grasshopper.

Dynamic relaxation Dynamic relaxation is a numerical method, which aims at finding the equilibrium geometry of a lattice model where all the forces are in equilibrium. For each iteration, the sum of the forces acting on each node are converted into accelerations using Newton's second law of motion. The acceleration is then doubly integrated numerically over a small time step in order to determine the positions of the nodes for the next iteration. This actualization of the geometry leads to different forces within the system and the process is repeated iteratively until all the forces in the system are zero [5]. In order to make the system converge faster, one can had a damping factor in the form of a drag force pointing in the opposite direction of the particle motion. In Kangaroo, this damping can be defined either globally throughout the lattice, or locally for each individual spring. If no damping factor is defined or if the damping factor is too low, the system might oscillate for a long time before reaching equilibrium. If the damping factor is too high, the nodes will move very slowly and convergence will be slow. Finding the accurate damping factor is a matter of trial and error and is hard to know beforehand.

Springs The force exerted by a spring on a node of the lattice is given by:

$$f = k(l - l_0), \tag{4.1}$$

where k is the stiffness, l the actual and l_0 the natural length of the spring. When the spring is at its natural length ($l = l_0$), the force exerted by the spring is zero. When the spring is stretched or compressed ($l > l_0$ or $l < l_0$), the equation above states that the force is proportional to the relative change in distance. This relation is the discrete equivalent of Hooke's law (appendix A.2.4) defined in the continuous case. In the case where the natural length of the spring is also a variable, this relation appears to be equivalent to Hooke's law in the presence of *eigenstrain* (eq. 3.19), where the difference between the natural length and the initial geometrical distance between the nodes of the lattice is equivalent to the *eigenstrain*.

4.1.2 Squared lattice model for elongated objects

In order to model a continuous *morpher* as particle system, one needs to discretize the continuum into a lattice. Subsubsection 4.1.2.1 presents the discretization chosen to represent elongated *morphers*, while subsubsection 4.1.2.2 discusses the connection between the lattice model and the continuous model.

5. In practice, the process is finished when the residual forces are smaller than a specified value.

4.1.2.1 Description of the model

In the case of elongated objects [6], the cross-section is modeled using four nodes connected by six springs [7], which are then repeated along the longitudinal direction and connected by longitudinal and diagonal springs [8] (fig. 4.2).

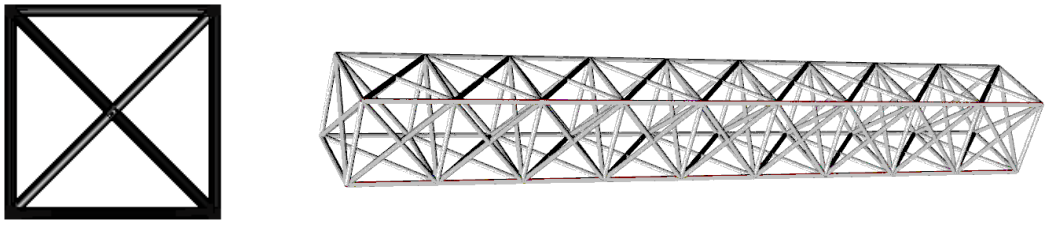

(a) (b)

Figure 4.2 – (Left) The cross-section of an elongated *morpher* is represented by four nodes connected by six springs. The horizontal and vertical springs correspond to extensional strains, while the diagonal springs correspond to shear strains within the plane of the cross-section. (Right) Extruded squared lattice structure representing an elongated *morpher*. The longitudinal springs account for extensional strains, while the diagonal springs between the transversal and the longitudinal direction account for shear strains perpendicular to the plane of the cross-section.

4.1.2.2 Connection between discrete and continuous model

As shown in subsubsection 6.1.3.1 and subsubsection 7.1.4.1, the longitudinal springs account for extensions or contractions normal to the plane of the cross-section (ϵ_{zz}) while the diagonal springs account for the longitudinal shears (ϵ_{xz} and ϵ_{yz}). Indeed, changing the side-length of a square leads to extension, while changing the length of the diagonals leads to a change in angle (fig. 4.3).

4.2 Energy minimization

In the case of elongated *morphers*, the *morphing* pattern at equilibrium corresponds to a minimum of the elastic energy as given in subsection 3.1.3 and eq. 3.25. This minimum is characterized by specific values for the actual curvatures ($\kappa_1^{eq}(s)$, $\kappa_2^{eq}(s)$, $\kappa_3^{eq}(s)$) along the rod amongst all possible candidates for the actual curvatures ($\kappa_1(s)$, $\kappa_2(s)$, $\kappa_3(s)$). Knowing the equilibrium curvatures, the material frame described in subsubsection 3.1.1.1 is obtained by integrating eq. 3.4 along the rod [9]. The configuration of the rod is then entirely characterized by the orientation of its material frame, such that it suffices to know the equilibrium curvatures to know the *morphing* pattern. Subsection 4.2.1 presents the software environment used to implement the energy minimization and summarizes the python code written in subsection 4.2.2.

6. This approach could also be used to model two- or three-dimensional *morphers*.

7. In order to be more accurate, the number of nodes could be increased to fit the specific shape of the cross-section. Also, a finer lattice would enable to impose more complex variations of *eigenstrain* within the *morpher* and to capture the resulting elastic strains in more details.

8. In the following, we call diagonal springs the springs between the longitudinal and the transversal direction. As distortions within the plane of the cross-section can be neglected in the case of sufficiently elongated objects, the length of transversal diagonal springs is fixed and their is no ambiguity.

9. One needs to impose a boundary conditions at a point of the rod, such as fixing the orientation of the material frame at one end of the rod for example.

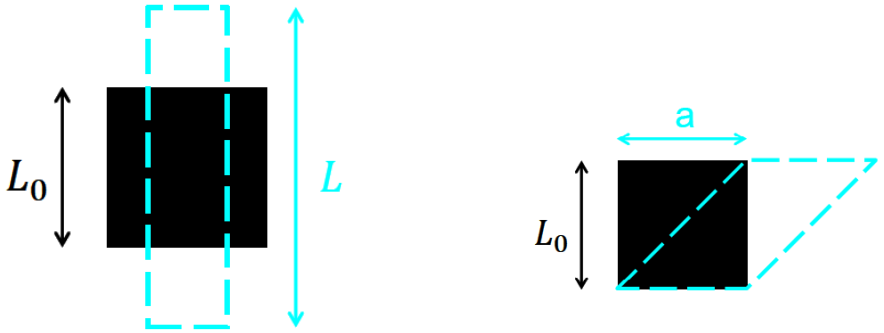

(a) (b)

Figure 4.3 – A square representing a side-view of the beam can be extended or sheared by changing the length of the longitudinal or diagonal springs respectively. (Left) Extension (Right) Shear.

4.2.1 Python

In order to solve for the minimum of the elastic energy of an elongated *morpher*, one can use the capabilities of the python programming language [10] taking advantage of its scientific library Pylab (Developers 2014). The Ipython shell (Pérez and Granger 2007) was used to compute the code and Mayavi (Ramachandran and Varoquaux 2011) to visualize the *morphing* patterns.

4.2.2 Code

The python code that computes and visualizes the *morphing* of rods in 2-D and 3-D is give in appendix B.1 and appendix B.2 [11]. Thanks to the characteristics of python, the code is almost readable straightforwardly. It can be summarized as follows [12]:

1. The initial configuration of the rod is defined by the coordinates of its middle line and the orientation of its material frame [13];
2. The rod is discretized by a finite number of points along its length;
3. For a given set of natural curvatures (κ_i^*), the elastic energy is minimized using the quasi-Newtonian minimization algorithm Broyden-Fletcher-Goldfarb-Shanno (Alben, Balakrisnan, and Smela 2011);
4. Without the presence of external constraints or other forces, the solution is trivial and the energy is minimum when ($\kappa_i = \kappa_i^*$). The configuration of the rod is reconstructed by integrating twice [14] over the material curvatures;
5. In the presence of an external field such as gravity, the energy does not only depend on the shape of the rod given by the components of its material Darboux vector (κ_i), but also on its position in space given by its absolute coordinates (x, y, z). This is why the minimization of energy becomes an iterative process where the absolute coordinates need to be calculated at each iteration of the energy minimization;

10. Python is a widely used general-purpose high-level programming language. Its main advantages over other commonly used programming languages such as C/C++ are its readability and the conciseness of its syntax.

11. I give credit to Felix Repp, who introduced me to python and helped me writing and debugging the first canvas of the code.

12. The 2-D and 3-D versions follow the same logic.

13. We choose a straight initial middle line ($\kappa_1 = \kappa_2 = 0$) with zero twist ($\kappa_3 = 0$).

14. The first integration of the material curvatures gives the material frame along the curve, while the second integration gives the coordinates of the middle line.

6. Finally, the final equilibrium configuration is plotted using Mayavi.

4.3 Finite-Element analysis

In the general case of an arbitrary distribution of eigenstrain, one can use a "brute-force" [15] finite-element approach. Subsection 4.3.1 presents the commercial software Abaqus® and its python development environment (PDE), which was used to parametrize and calculate *morphing* patterns. Subsection 4.3.2 summarizes the workflow of a finite-element calculation.

4.3.1 Abaqus®

Abaqus is a commercial [16] software, which can solve a variety of physical problems using fem. A thorough presentation of the fem would be beyond the scope of this thesis (Hibbett, Karlsson, and Sorensen 1998). The general idea behind fem, is to decompose a complex problem into a large number of simple problems. Instead of trying to solve the equations for mechanical equilibrium in the presence of *eigenstrain* as given in eq. 3.23 across the whole domain of the *morpher*, these equations are solved on a lot of small elements which pave the geometry of the *morpher*. This discretization follows a similar approach to the one proposed in section 4.1, where the continuum was represented by a lattice model. Instead of connecting the nodes of the domain with linear springs, the elements can display a more complex behavior depending on the modeled physical phenomenon. Similarly to what is described in section 4.2 where the unknown material curvatures along the rod where reduced to a finite number of unknowns, the unknown displacement field within the *morpher* is replaced by a finite number of displacement vectors at the nodes of the domain. The discretized solution can then be smoothen again, leading to an approximate continuous solution.

4.3.1.1 Python development environment

The python development environment (PDE) is a graphical interface of Abaqus, which enables to create and analyze Abaqus models using the python scripting language. Similarly to the Grasshopper plug-in for Rhino (subsubsection 4.1.1.1), this allows to do parametric studies of models by defining formal relations between the parameters rather than having fixed values. Also, scripting a model instead of defining it through the graphical user interface, has the benefit of being more easily editable and reproducible (appendix B.3).

4.3.2 Workflow

This subsection presents the workflow behind a finite-element calculation, which consists of three stages: pre-processing, processing and post-processing. These stages are captured in the script given in (appendix B.3).

4.3.2.1 Pre-processing

The pre-processing stage consists of defining the input file which contains all the information of the finite-element model: the geometry, the material architecture, the material properties,

15. The expression "brute-force" emphasizes the fact that the finite-element method (fem) is a powerful numerical method, but one can sometimes loose a simple understanding of the *morphing* process.

16. Commercial fem software have the disadvantage to be expensive, but the advantage of being more reliable than open source fem softwares.

the load, the boundary conditions and the mesh.

Geometry The geometrical objects are rectangular cuboids or right rectangular cylinders. The width, thickness and length of the object are respectively given by w, t, L (fig. 4.4).

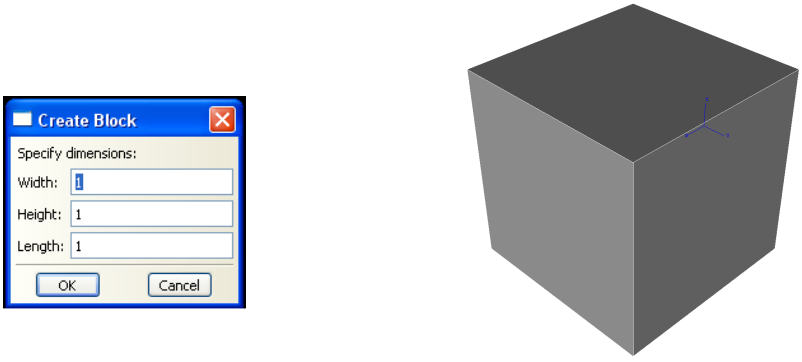

(a) (b)

Figure 4.4 – Using the script given in appendix B.3, (left) one can input different sizes of cuboids by specifying their width (w), thickness (t) and length (L). The resulting geometry is shown on the right.

Material architecture The geometry is partitioned through an orthogonal grid parametrized by h, v, l. The result is an assembly of $N_r = h * v * l$ rectangular cuboids of dimension $\frac{w}{h}, \frac{t}{v}, \frac{L}{l}$. The partition is needed in order to assign different material properties to different regions of the solid (fig. 4.5).

Material properties Two different materials are used. They both follow a linear isotropic elastic material behavior and a linear orthotropic thermal expansion behavior, which leads to four elastic constants E^1, E^2, ν^1, ν^2 and six coefficient of thermal expansion α_{T1}^1, α_{T2}^1, α_{T3}^1, α_{T1}^2, α_{T2}^2, α_{T3}^2 (fig. 4.6).

Load Two uniform constant temperature fields are defined over the solid, one in the initial state T_0 and one in the final state T. The initial state is considered to be stress-free ($T_0 = 0$), so that only the thermal gradient matters ΔT (fig. 4.7).

Boundary Condition Under the thermal load case only, the stress-state solution is auto-equilibrated and no boundary conditions are needed. However, we still need to fix rigid-body motions, otherwise the object "flies around". We do this by fixing a point (center or one corner).

Mesh The mesh is composed of linear 8-node brick elements (C3D8). Its degree of refinement is defined through the mesh density factor (fig. 4.8).

4.3.2.2 Processing

During the processing step, the static thermo-mechanical problem is solved considering geometric nonlinearity. The solver works like a black-box and the user only needs to tune size of the increments in order for the calculation to converge.

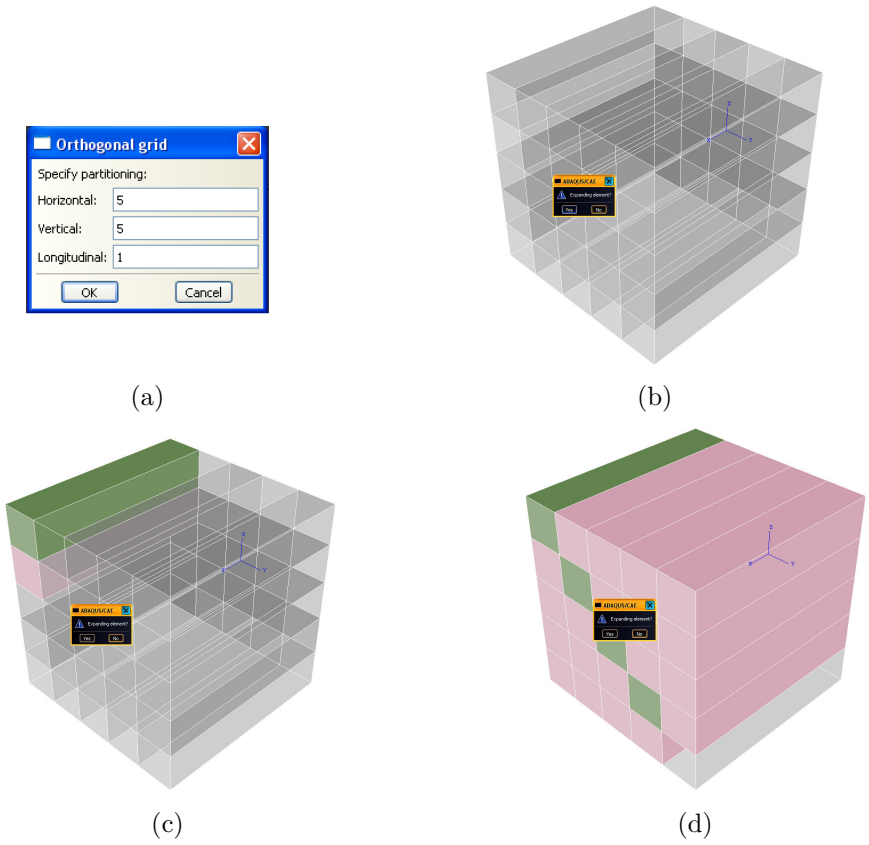

Figure 4.5 – Using the script given in appendix B.3, one can partition the geometry using an orthogonal grid parametrized by h, v, l (top left). The user is then prompted to associate either an *active* (green) or a *passive* (pink) element to the different regions of the grid (rest of the figures).

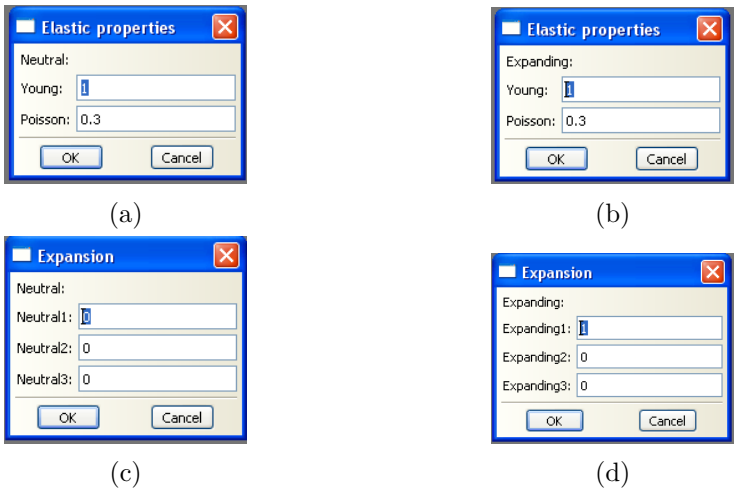

Figure 4.6 – Using the script given in appendix B.3, the user is prompted to input the material properties. (Top) Elastic constants of the *active* (left) and *passive* (right) phase. (Bottom) Expansion constants the *active* (left) and *passive* (right) phase.

4.3.2.3 Post-processing

Once the calculation converged, the output file containing the results can be analyzed by looking at the deformed configuration in terms of displacements, strain and stress (fig. 4.9).

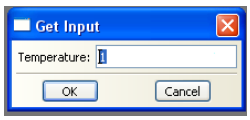

Figure 4.7 – Temperature in the initial (T_0) and final state (T).

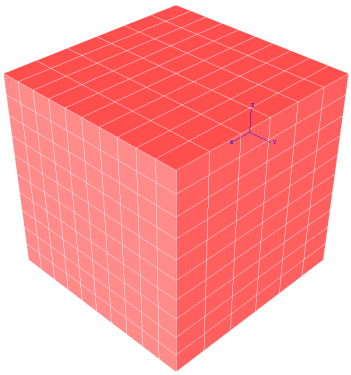

Figure 4.8 – The mesh is composed of linear 8-node brick elements (C3D8). The size of the mesh is adjusted by the mesh density factor.

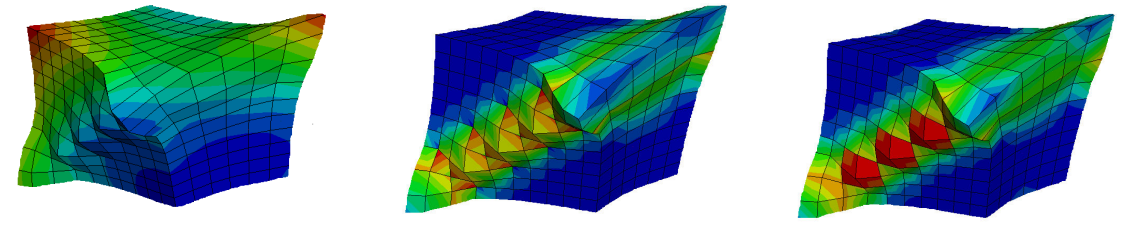

(a) (b) (c)

Figure 4.9 – Once the calculation converged, the deformed configuration can be analyzed in terms of displacements (left), strain (middle) and stress. (red) represents a high value and (blue) a zero value.

Conclusions

This chapter presents the numerical methods used to simulate *morphing* patterns. Elongated *morphers* can either be represented by an extruded square lattice connected springs—which relaxes into an equilibrium configuration upon changing the rest-length of the springs, or as a one-dimensional rod which equilibrium configuration corresponds to a minimum of its elastic energy. Finally, the finite-element method can also be used to solve for arbitrary *eigenstrain* distributions.

References

Alben, Silas, Bavani Balakrisnan, and Elisabeth Smela (2011). « Edge effects determine the direction of bilayer bending ». In: *Nano letters* 11.6, pp. 2280–2285.

Developers, Scipy (2014). *SciPy: Open source scientific tools for Python*. URL: `http://scipy.org/`.

Hibbett, Karlsson, and Sorensen (1998). *ABAQUS/standard: User's Manual*. Vol. 1. Hibbitt, Karlsson & Sorensen.

McNeel, Robert and Associates (2014a). *Grasshopper*. URL: `http://www.grasshopper3d.com/`.

— (2014b). *Rhinoceros*. URL: `http://www.rhino3d.com/`.

Pérez, Fernando and Brian E. Granger (2007). « IPython: a System for Interactive Scientific Computing ». In: *Computing in Science and Engineering* 9.3, pp. 21–29. ISSN: 1521-9615. DOI: `10.1109/MCSE.2007.53`. URL: `http://ipython.org`.

Piker, Daniel (2014a). *Kangaroo live physics engine*. URL: `http://www.grasshopper3d.com/group/kangaroo`.

— (2014b). *Pseudo-physical materials*. URL: `http://spacesymmetrystructure.wordpress.com/2011/05/18/pseudo-physical-materials/`.

Ramachandran, P. and G. Varoquaux (2011). « Mayavi: 3D Visualization of Scientific Data ». In: *Computing in Science and Engineering* 13.2, pp. 40–51. ISSN: 1521-9615.

Chapter 5

Experimental systems

Contents

This chapter presents experimental systems that can be used to explore *morphing* patterns controlled by *eigenstrain* distributions. Those systems provide a real world demonstration or "toy-model" that can be used to illustrate specific *morphing* patterns and to confirm or infirm theoretical calculations. Amongst the various existing means to produce *eigenstrain* distributions experimentally (from crocheting or knitting the hyperbolic plane (Henderson and Taimina 2001) to frying potato chips), we looked at three: prestrain (section 5.1), thermal expansion [1](section 5.2) and swelling (section 5.3). For each technique, one can find relatively cheap and easy to manufacture materials available in the commerce. The following describes the manufacturing and assembly process of these experimental systems [2].

5.1 Prestrain

Prestrain is arguably the most comfortable method of all three as it occurs in a dry environment and only requires stretching and gluing. The idea is to introduce a differential prestrain in a structure by stretching parts of it and glue them to unstretched parts. Upon release, the stretched parts tend to go back to their natural state, which is partially prohibited by their neighboring unstretched parts. This imposes an *eigenstrain* distribution in the structure of opposite sign to the prestrain distribution. However, an important drawback of this method is

1. This work was down by Fanny Chouteau, Madge Martin and Alan le Goallec, three students from my former engineering school (École des Ponts) in a six month student project which I set up and supervised.

2. Our goal was mainly the qualitative reproduction of *morphing* patterns. Nevertheless, mechanical and expansion properties were also measured in order to allow for subsequent quantitative comparison with theoretical calculations (see appendix C).

that the produced *morphing* patterns are irreversible. One could unglue them to see if the parts relax to their original state, but it is a rather cumbersome procedure. The order of magnitude of the imposable *eigenstrain* with this technique is only limited by the failure strain of the material ($\epsilon^* < \epsilon_f$). Upon release, the prestrain is accommodated by an elastic strain as the structure relaxes to its equilibrium. The total strain ($\epsilon = \epsilon^{el} + \epsilon^*$) is smaller than the failure strain (ϵ_f) as the elastic strain relaxes the prestrain ($\operatorname{sgn}(\epsilon^{el}) = -\operatorname{sgn}(\epsilon^*)$). In the literature (Liang and Mahadevan 2009), straining is also used directly without gluing by stretching the structure in such a way that only some parts of it are stretched above the yield point. The elastic regions relax to their original state, while the plastic regions go back to a state containing residual plastic strain. This mismatch in the natural state caused by plastic regions acts as an *eigenstrain* and leads to elastic relaxation as well. Subsection 5.1.1 describes the two types of elastomers considered and subsection 5.1.2 presents the setup used to prestrain and assembly them [3].

5.1.1 Choice of materials

To be able to generate large *eigenstrain* using preferably small force installations, one can look at soft materials with large elastic range such as elastomers. Amongst those, the one with a simple manufacturing process allows to test new *eigenstrain* distributions quickly. Due to its good availability, we opted for the widely used Polydimethylsiloxane (PDMS). We also tested a similar silicon compound called Elite-Double produced by Zhermack®, which is typically used for dental molds and requires an even quicker manufacturing than standard PDMS [4].

5.1.1.1 Polydimethylsiloxane

Description Polydimethylsiloxane (PDMS) belongs to a family of organo-silicon compound also known as silicones. It is optically clear, non-hazardous (inert, non-toxic and non-inflammable) and particularly known for its rheological properties. PDMS is elastic at room temperatures and becomes viscous at higher temperatures.

Manufacturing process Monomer and cross-linking agent are mixed in a beaker with a ratio of 10 : 1. Mixing is done manually with a wooden spatula. The mixture is put in a vacuum desiccator for ~ 30 min in order to remove potential bubbles that formed during mixing. Alternatively, remaining bubbles can be sucked out manually with a micro-pipette. When no more bubbles are visible the liquid polymer is poured on a glass plate with a resulting thickness of $t \sim 1$ mm. The solution is then cured in an oven at a controlled temperature of 80 °C for ~ 3 h. PDMS can then be easily pulled from the glass plate, before cutting it with a scalpel into desired shapes. All in all, the manufacturing process lasts ~ 5 h.

5.1.1.2 Elite-double

Description Elite double is a silicone produced by Zhermack® which is used for duplications by artists or dental technicians. It comes in different hardness of Shore A value 8, 16 and 22.

Manufacturing process Both components are mixed in a glass beaker with a ratio of 1 : 1. Mixing is done manually with a wooden spatula. The viscous liquid is then poured on a glass plate with a resulting thickness of $t \sim 1$ mm. Elite Double cures at room temperature in ~ 5 min

3. See appendix C.1 for the characterization of the mechanical properties of these elastomers.
4. We'd like to thank Etienne Reyssat for pointing out this convenient material.

and can be easily pulled from the glass plate, before cutting it with a scalpel into desired shapes. All in all, the manufacturing process last $\lesssim 1\,\mathrm{h}$.

5.1.2 Applying prestrains

Two setups were fabricated from the mechanical lab in order to apply uniaxial and biaxial prestrains. Uniaxial strain is applied by clamping an elastomer strip on its two ends and increasing the distance between the clamps (fig. 5.1a). A ruler enables to read the elongated length in order to deduce the applied strain. Biaxial strain is applied by applying uniaxial strain in two perpendicular directions (fig. 5.1b). Once the sample is prestrained, one can glue unstrained elastomer onto it.

(a) (b)

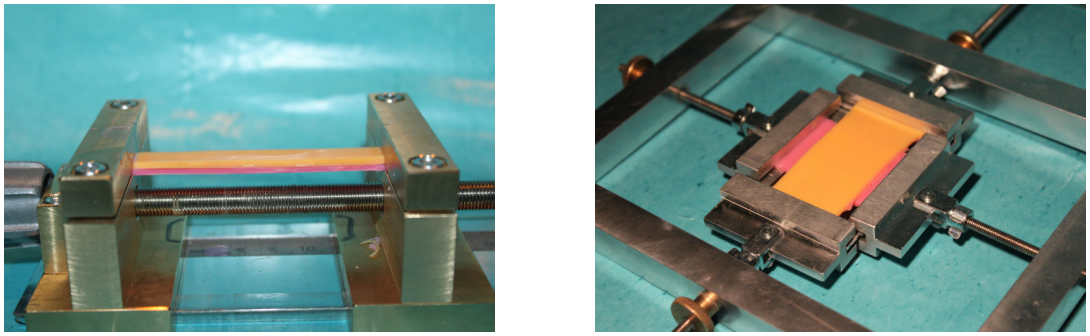

Figure 5.1 – Setups used to apply uniaxial (a) and biaxial (b) prestrain on elastomer strips. The prestrain is tuned by changing the distance between the clamps holding the elastomer strips.

5.1.2.1 Gluing

Composite structures are achieved by applying uncured solution (PDMS or Elite Double) at the interface between differentially stretched parts before undergoing a subsequent hardening step. The complete manufacturing process of prestrained composite shapes with PDMS takes $\sim 1\,\mathrm{d}$ and $\lesssim 3\,\mathrm{h}$ for Elite Double [5].

5.2 Thermal Expansion

Gradients in thermal expansion are probably the oldest mechanism used to trigger shape changes. Its main limitation is the relatively low coefficients of thermal expansion (CTE) of most materials. According to Ashby maps, the highest CTE of materials are quite small ($\alpha_T \lesssim 10^{-4}\,°\mathrm{C}^{-1}$). Even a temperature change of $\Delta T = 100\,°\mathrm{C}$—which is high compared to daily temperature changes—would result in a relatively small *eigenstrain* of the order of $\varepsilon^* = \alpha_T \Delta T \sim 1\,\%$ (assuming constant CTE as justified by the small temperature range). As geometry can counterbalance the effect of low *eigenstrain* to some extent, thermal expansion is still a reasonable candidate for *morphing*, but it requires sufficiently elongated structures. Subsection 5.2.1 describes the materials used and subsection 5.2.2 the assembly and activation of thermal *morphers* [6].

5. Gluing can become quite tricky in the biaxial case due to accessibility issues.

6. See appendix C.2 for the characterization of the mechanical and expansion properties of these thermal *morphers*.

5.2.1 Choice of materials

Thermal expansion based actuators—also known as thermostats—are classically used as passive sensors or switches and very common in industry. They are usually made from metallic alloys, which ensure good structural integrity. In this case, they typically consist of a low expansion alloy such as Invar, which is combined with a high expansion alloy usually iron-based and containing nickel and chromium (Harner 2013). The students [7] were asked to choose two materials with high CTE mismatch amongst the ones available to them. They chose silicone elastomer with a CTE of $\alpha_T \sim 10^{-4}\,°C^{-1}$ and simple balsa with a CTE of $\alpha_T \sim 10^{-6}\,°C^{-1}$. Also, their choose a temperature difference of $\Delta T \sim 20\,°C$, which is realistic for West European latitudes.

5.2.1.1 Silicone elastomer

Three types of Wacker Silicones produced by Elastosil® of increasing hardness were used: M4601, M4643 and M4670. They were cured in a square shaped mold of side length 4.5 cm ∗ 4.5 cm and with different heights: 2.34 mm for red, 3.15 mm for white and 3.76 mm for grey (fig. 5.2). In order to measure their elastic properties and their CTE (see appendix C.2), flat rectangular sheets as well as cylindrical samples were respectively cast.

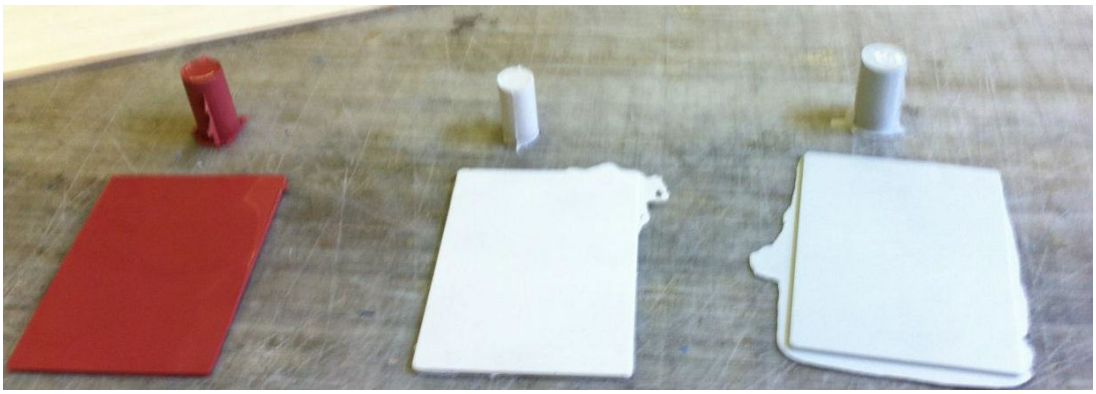

Figure 5.2 – Rectangular silicone sheets for tensile testing of dimensions ∼ 10 cm ∗ 5 cm ∗ 5 mm and cylinders for CTE measurements of dimensions ∼ 3 cm ∗ 5 mm. M4601 is red (left), M4643 is white (middle) and M4670 is gray (right).

5.2.1.2 Balsa

Thin balsa slices were cut perpendicular and parallel to their fibers with the same shape as the silicone parts of side length 4.5 cm ∗ 4.5 cm and three different heights: 1.0 mm, 1.5 mm and 2.0 mm (fig. 5.3). For tensile testing (see appendix C.2), flat rectangular sheets were prepared along and perpendicular to the fiber direction .

5.2.2 Assembly and activation

Nine samples were prepared by combining the three types of silicones with the three thicknesses of balsa (table 5.1).

A thorough choice for the glue is crucial as it should bound the two materials together for assembly, but it is also crucial that it does not unbound during heating and deformation of the

7. See footnote 1.

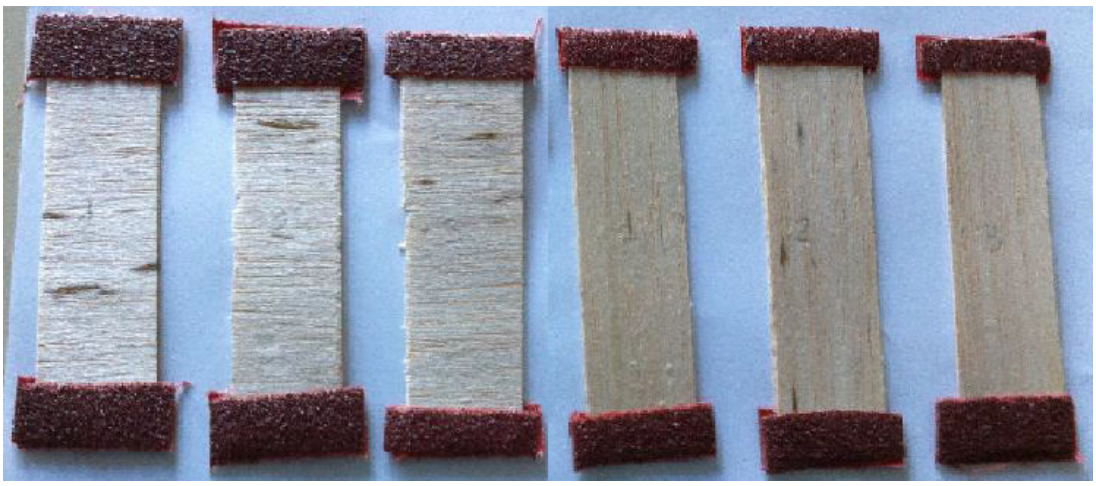

Figure 5.3 – Flat rectangular balsa sheets of dimensions $\sim 10\,\text{cm} * 4\,\text{cm} * 2\,\text{mm}$ samples for tensile testing. The three on the left are cut perpendicular to the fiber direction, whereas the three on the right are cut parallel to it.

sample	1	2	3	4	5	6	7	8	9
$t_{silicon}$[mm]	2.34	2.34	2.34	3.15	3.15	3.15	3.76	3.76	3.76
t_{balsa}[mm]	1.0	1.5	2.0	1.0	1.5	2.0	1.0	1.5	2.0

Table 5.1 – Silicone and balsa thicknesses for the samples shown in fig. 5.4.

system. Also, the glue layer's impact on the mechanical behavior of the structures should be minimal. In view of the chosen temperature difference of $\Delta T \sim 20\,°\text{C}$, a simple sealing mastic—which is typically used to prevent water leakages in bathroom—was used. After a night rest, the samples are now ready for heat treatment (fig. 5.4). Heating took place in an oven during 3 h at 40 °C to simulate the effect of a temperature increase of $\Delta T \sim 20\,°\text{C}$ for a room temperature of $T_0 \sim 20\,°\text{C}$.

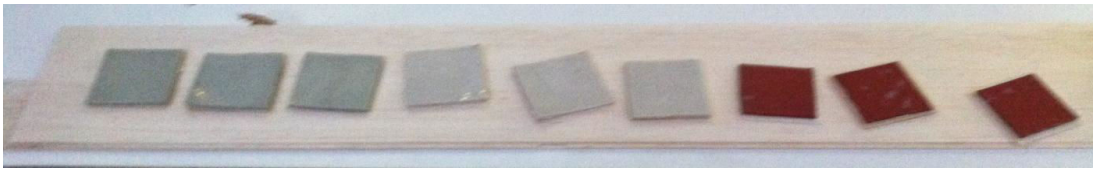

Figure 5.4 – Glued silicone-balsa bilayer samples before heat treatment. (Left, gray) M4670, (middle, white) M4643, (right, red) M4601 with different thicknesses of elastomer and three different thicknesses of balsa (table 5.1).

5.3 Swelling

Swelling is the actual physical phenomenon that leads to *morphing* in many natural systems (Dawson, Vincent, and Rocca 1997). Influx of solvent inside the material induces a volume change that acts as an *eigenstrain*. What makes swelling intricate is that the swelling content depends on the actual stress state (Treloar 1975, chapter 7). A compressed material swells less whereas an extended material swells more. This introduces a coupling between the *eigenstrain* and the elastic relaxation, which adds a theoretical difficulty. Also, the stiffness of the material changes as a function of swelling—materials becomes softer as swelling increases. Finally, re-

versibility can still be an issue as the structural integrity tends to deteriorate upon swelling cycles. Subsection 5.3.1 presents the wood-based materials, subsection 5.3.2 the printed multi-materials and subsection 5.3.3 the thermo-activated polymers used to produce swelling *morphers*.

5.3.1 Wood based materials

The simplest [8] "toy model" to mimic *morphing* of natural systems is to take the building blocks of those systems and to arrange them differently. This could be done by tuning the average micro-fibril angle inside the cell walls of a wooden structure. Until this is technically feasible, another possibility is to play with "higher order" building blocks such as macroscopic wood slices which swell considerably more perpendicular to the fiber direction than parallel to it: $\alpha_T^{perp} \gg \alpha_T^{paral}$ (section 6.3).

5.3.2 Printed multi-materials

We had access to multi-material structures made with the printer Object Connect 500 from Stratasys® [9]. The printer works similarly to an inkjet traditional printer, but instead of jetting drops of ink onto paper, it jets layers of liquid photo-polymer onto a build tray and instantly cures them with UV light. This process is repeated layer-by-layer with a very fine spatial resolution of $\sim 10\,\mu m$. By using different combinations of polymer precursors (monomer and cross-linkers), which are jetted simultaneously, the printer can produce up to 90 digital materials. The materials used where variants of thermoplastic polyurethanes (TPU) with different hardnesses as well as polyacrylates for the passive parts. As shown in appendix C.1, hardness correlates with stiffness, which inversely correlates with swelling. The ability to print three-dimensional composite structures of different hardnesses allows us thus to control the distribution of *eigenstrain* inside the active parts of the structure. TPUs swell slightly in aliphatic alcohols such as isopropanol and a lot in ketones such as acetone (Huntsman 2013). See appendix C.3 for the characterization of the mechanical and swelling properties of printed multi-materials.

5.3.3 Thermo-activated polymers

5.3.3.1 Material description

Two families of polymeric bilayers, made of an active and a passive layer, are studied. The complete manufacturing process can be found in (Zakharchenko et al. 2010).

Active component The active component is a thermoresponsive hydrogel formed either by photo-cross-linked poly-(N-isopropylacrylamide-co-acrylic acid-co-benzophenone acrylate) (P(NIPAM-AA-BA)) or by poly(N-isopropylacrylamide-co-benzophenone acrylate) (P(NIPAM-BA)). Thermo-responsive hydrogels swell and shrink at reduced and elevated temperature, respectively.

Passive component The passive component is either hydrophobic polycaprolactone (PCL) or random copolymer poly-(methylmethacrylate-co-benzophenone acrylate) (P(MMA-BA)). The passive hydrophobic layers restrict swelling of the active hydrogel.

8. An even simpler illustration of swelling inspired from (Reyssat and Mahadevan 2011) is to place a piece of tracing paper on water, which triggers differential swelling across its thickness (see fig. 6.10).

9. Thanks to the collaboration with James Weaver from the Wyss Institute at Harvard.

5.3.3.2 Manufacturing process

P(NIPAM-AA-BA)/P(MMA-BA) and P(NIPAM-BA)/PCL bilayers were prepared using photolithography. In a typical experiment, the active polymer was spin-coated from solution on a silica wafer substrate. The passive layer was then spin-coated on top of it. The bilayer film was then illuminated through specific masks by halogen lamp for 15 min to crosslink polymers. Finally, the illuminated film was rinsed in chloroform to remove non-irradiated polymer areas. The resulting bilayers have the desired shapes (rectangle, stars) and their characteristic length is $L \sim 500\,\mu m$.

5.3.3.3 Activation

When the temperature goes under a critical value T_c, which can be tuned by changing the composition of the solution, the active polymer starts to swell (fig. 5.5).

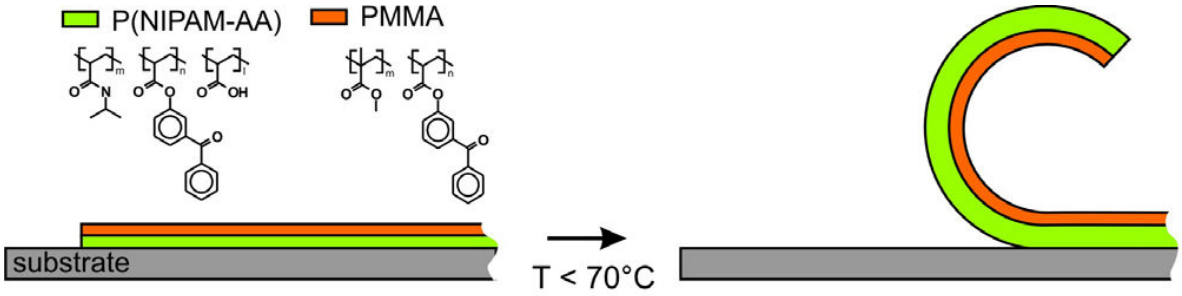

Figure 5.5 – Scheme of folding of a bilayer polymer film consisting of two polymers: hydrophobic P(MMA-BA) and thermoresponsive hydrogel P(NIPAM-AA-BA). Reprinted with permission from (Stoychev et al. 2012). Copyright (2012) American Chemical Society (see appendix F.2).

Conclusion

This chapter describes experimental "toy-models" which are used to illustrate *morphing* patterns. Amongst the various means that mimic plant *morphing*, we looked at three: pre-straining, swelling and thermal expansion. Pre-straining is mostly illustrative as it is irreversible by nature, but it has the advantage of working in a dry environment. On the other hand, swelling and thermal expansion are both good candidates for real world applications.

References

Dawson, Colin, Julian FV Vincent, and Anne-Marie Rocca (1997). « How pine cones open ». In: *Nature* 390.6661, pp. 668–668.

Harner, Leslie L. (2013). *Selecting Controlled Expansion Alloys*. URL: `http://www.cartech.com/techarticles.aspx?id=1674/`.

Henderson, David W and Daina Taimina (2001). « Crocheting the hyperbolic plane ». In: *The Mathematical Intelligencer* 23.2, pp. 17–28.

Huntsman (2013). *A guide to thermoplastic polyurethanes*. URL: `http://www.huntsman.com/portal/page/portal/polyurethanes/Media%20Library/global/files/guide_tpu.pdf`.

Liang, Haiyi and L Mahadevan (2009). « The shape of a long leaf ». In: *Proceedings of the National Academy of Sciences* 106.52, pp. 22049–22054.

Reyssat, E and L Mahadevan (2011). « How wet paper curls ». In: *EPL (Europhysics Letters)* 93.5, p. 54001.

Stoychev, Georgi et al. (2012). « Shape-programmed folding of stimuli-responsive polymer bilayers ». In: *ACS nano* 6.5, pp. 3925–3934.

Treloar, Leslie Ronald George (1975). *The physics of rubber elasticity*. Oxford University Press.

Zakharchenko, Svetlana et al. (2010). « Temperature controlled encapsulation and release using partially biodegradable thermo-magneto-sensitive self-rolling tubes ». In: *Soft Matter* 6.12, pp. 2633–2636.

Part III

Results and Discussions

Chapter 6

Benders

Contents

This chapter defines *benders* as a type of elongated *morphers* that bends when activated. As discussed in subsection 3.1.2, bending is one of the fundamental deformation modes of rod-like objects.

Section 6.1 starts by studying standard bilayers, which consist of an *active* layer expanding against a *passive* producing bending. According to Timoshenko's solution (Timoshenko et al. 1925), the curvature of a bilayer is proportional to the ratio of the differential longitudinal *eigenstrain* divided by the total thickness of the bilayer (subsection 6.1.1). The proportionality factor is a function of the thickness and stiffness contrasts as discussed in subsubsection 6.1.1.1. Subsubsection 6.1.1.2 derives the elastic strain inside a bilayer, which gives rise to the interfacial stress [1]. Knowing the strain state inside a bilayer, bending is confirmed to be more favorable than stretching from an energetical viewpoint (subsubsection 6.1.1.3). Subsection 6.1.2 considers the effect of adding intermediates layers and discuss the limiting case of a transversally graded *bender*. As the number of layers increases, the elastic strain inside the *bender* progressively decreases eventually leading to stress-free bending. Subsection 6.1.3 shows numerical and experimental illustrations of bilayers using the techniques described in section 4.1 and chapter 5.

Section 6.2 extends the bilayer principle by showing how to generate variations in curvature along the length of a *bender* and how to produce helical morphologies. On the one hand, variations in curvature are achieved by changing the differential *eigenstrain* along the length of a *bender* (subsection 6.2.1). On the other hand, helical morphologies are produced by either rotating the bending plane along the *bender* or by introducing an angle between the principal directions of *eigenstrain* and the principal directions of geometry (subsection 6.2.2).

1. When the interfacial stress exceeds the interfacial resistance delamination occurs, which is the main cause of failure in bilayers (and in composite structures in general).

Section 6.3 presents the concept of *geometric amplification*, which enables to transform a relatively small *eigenstrain* into a relatively large displacements. This is done by introducing one more level of hierarchy in the material looking at an assembly of bilayers forming a honeycomb like geometry [2].

6.1 Single *Benders*

One fundamental example of a distribution of *eigenstrain* inside a one-dimensional elongated object is the bilayer. The invention of the bi-metallic strip is usually accredited to 18^{th} century clockmaker John Harrison (Betts 1993) and these thermo-actuators are commonly used since then for example to compensate temperature-induced changes in clocks, as thermostats in heating and cooling systems, as switches in electrical systems or simply as thermometers. A bilayer is made out of two flat strips of materials displaying a different longitudinal *eigenstrain* [3], which are bonded on top of each other. If the differential longitudinal *eigenstrain* is small, the elastic strain will also be small and the material can be considered linear elastic. As soon as the differential longitudinal *eigenstrain* is nonzero, the straight configuration becomes less favorable than the bended configuration and the bilayer starts to bend.

6.1.1 Bilayers

According to appendix D.1, the curvature of a bilayer experiencing uniform heating is given by:

$$\kappa = \frac{6(\alpha_{T2} - \alpha_{T1})\Delta T(1+m)^2}{t[3(1+m)^2 + (1+mn)(m^2+1/mn)]}, \tag{6.1}$$

where $\alpha_{T\beta}$ is the coefficient of thermal expansion of each layer, ΔT the temperature difference, t the total thickness, $m = t_1/t_2$ the thickness contrast and $n = E_1/E_2$ the stiffness contrast. Equation 6.1 is known as Timoshenko's formula (Timoshenko et al. 1925). Subsubsection 6.1.1.1 studies the influence of the thickness and stiffness contrasts on the curvature of a bilayer, subsubsection 6.1.1.2 presents the elastic strain distribution in a bilayer of unitary thickness and stiffness contrasts and subsubsection 6.1.1.3 calculates the energy in the straight and curved configuration.

6.1.1.1 Influence of thickness and stiffness contrast

In a concise form, eq. 6.1 can be written as:

$$\kappa = f(m,n)\frac{\Delta\epsilon^*}{t}, \tag{6.2}$$

where m and n are the thickness and stiffness contrasts respectively. Equation 6.2 shows that the curvature of a bilayer is proportional to the differential longitudinal *eigenstrain* and inversely proportional to the total thickness of the bimetallic strip. The coefficient of proportionality is given by:

$$f(m,n) = \frac{6(1+m)^2}{3(1+m)^2 + (1+mn)(m^2+1/mn)}. \tag{6.3}$$

2. The concept as well as the experimental realization of honeycomb bilayers was made by Khashayar Razghandi (Razghandi 2014). His idea was inspired by the origami-like unfolding of ice-plant seed capsules (Harrington et al. 2011) (See also (Guiducci 2013) for an in-depth study of meso-structural lattice systems that enable to amplify and tune microscopic *eigenstrain*.)

3. As we consider elongated rod-like objects ($t, w \ll L$), we do not consider extension/contraction strains within the plane of the cross-section ($\boldsymbol{\epsilon}_x x = \boldsymbol{\epsilon}_y y = 0$. In the same way, we only consider the longitudinal component of the *eigenstrain* ($\boldsymbol{\epsilon}^* = \epsilon^*_{zz} = \epsilon^*$).

The proportionality factor $f(m, n)$ is plotted in fig. 6.1. It takes its maximal value for $m = n = 1$ and decreases smoothly to 0 when $m, n \to \infty$.

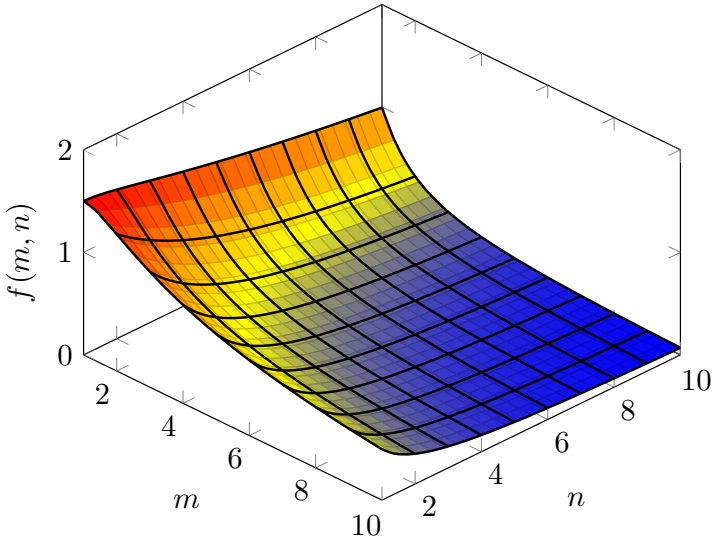

Figure 6.1 – The proportionality factor between the curvature κ and the ratio of the differential longitudinal *eigenstrain* $\Delta\epsilon^*$ with the total thickness t is a function of the thickness contrast $(1 < m < 10)$ and the stiffness contrast $(1 < n < 10)$.

Equal thickness If both layers have the same thicknesses $(m = 1)$, the coefficient of proportionality reduces to:

$$f(m = 1, n) = \frac{24}{14 + n + 1/n}. \tag{6.4}$$

In this expression, we see that n and $1/n$ play symmetric roles, which is consistent with the fact that the way we label the layers shouldn't affect the curvature. Also, when the stiffness of one layer becomes predominant compared to the other, the curvature goes to zero:

$$f(m = 1, n) \xrightarrow[n \to \infty]{n \to 0} 0.$$

This means that when one of the layers is sufficiently stiff compared to the other, it can be considered rigid and the bilayer does not curve [4]. The effect of the stiffness contrast (n) on the curvature (κ) of a strip with unitary thickness contrast $(m = 1)$ is plotted in fig. 6.2 for $1 \leq n \leq 10$.

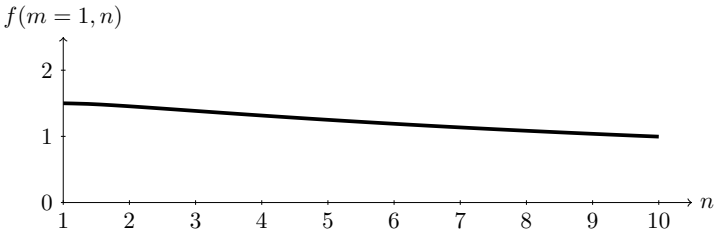

Figure 6.2 – The effect of the stiffness contrast (n) for a unitary thickness contrast $(m = 1)$ on curvature (κ) is given by $f(m = 1, n)$, which decreases slowly to zero. For $n = 1$ we have $f(m = 1, n) = 1.5$ while for $n = 10$ we have $f(m, n = 1) \approx 1$.

4. $f(m = 1, n) = 0.01 \implies n \approx 2400$

Equal stiffness On the contrary, if the stiffnesses of both layers are equal ($n = 1$), the coefficient of proportionality becomes:

$$f(m, n = 1) = \frac{6(1+m)^2}{3(1+m)^2 + (1+m)(m^2 + 1/m)} = \frac{6m}{(m+1)^2}. \tag{6.5}$$

Again, if we replace $1/m$ for m in this expression we obtain the same expression, which is consistent with the fact that the way we label the layers shouldn't affect the curvature. Also, when the thickness of one layer becomes predominant compared to the other, the curvature goes to zero:

$$f(m, n = 1) \xrightarrow[m\to\infty]{n\to 0} 0.$$

This means that when one layer is sufficiently thin relatively to the other, it becomes effectively negligible and the bilayer can be considered a mono-layer which has no reason to bend. The effect of the thickness contrast (m) on the curvature of the strip (κ) with unitary stiffness contrast (n=1) is plotted in fig. 6.3 for $1 \leq m \leq 10$.

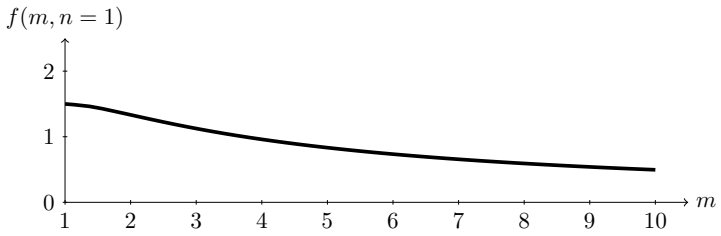

Figure 6.3 – The effect of the thickness contrast (m) for unitary stiffness contrast ($n = 1$) on the curvature (κ) as given by $f(m, n = 1)$ is also small. For $m = 1$ we have $f(m, n = 1) = 1.5$ while for $n = 10$ we have $f(m, n = 1) \approx 0.5$.

Equal thickness and stiffness If both contrast are equal to one (same thickness contrast $m = 1$ and same stiffness contrast $n = 1$), then $f(m = 1, n = 1) = 1.5$ and the curvature is given by:

$$\kappa = \frac{3}{2}\frac{\Delta\epsilon^*}{t}. \tag{6.6}$$

Remark (Influence of thickness and stiffness contrast on curvature.)**.** *The influence of the thickness contrast (m) and the stiffness contrast (n) on the curvature of the bender κ is relatively small. An increase of one order of magnitude in stiffness for unitary thickness contrast leads to a reduction of the curvature by 2/3, while an increase of one order of magnitude in thickness for unitary stiffness contrast leads to a reduction of curvature by 1/3. What mainly controls the curvature of bilayers is the magnitude of the differential eigenstrain ($\Delta\epsilon^*$) and the total thickness (t). If one wants to generate the maximum amount of curvature, one should aim for the maximum differential eigenstrain and the minimum total thickness, which makes intuitive sense. This curvature can then be slightly lowered compared to the equal thickness and stiffness scenario by tuning the stiffness and thickness contrasts.*

6.1.1.2 Interfacial stress

From subsection 3.2.1, the total strain is equal to the sum of the elastic strain and the eigenstrain. Thus, given the imposed eigenstrain distribution inside a bilayer, the elastic strain distribution can be deduced by subtracting the eigenstrain from the total strain. The corresponding stress distribution is related to the elastic strain distribution using the simplified

one-dimensional constitutive law of the material ($\sigma_{zz} = E\epsilon_{zz}$, see appendix A.2.4). In particular, the jump in elastic stress at the interface between the two layers, also called interfacial stress, can be calculated. At the center line ($x = 0$) the total strain is zero and the jump in interfacial elastic strain is equal to the jump in eigenstrain ($[\![\epsilon^{el}]\!]_{x=0} = \Delta\epsilon^*$). The expanding layer on bottom is mainly compressed ($\epsilon^{el} < 0$) and the contracting layer on top is mainly stretched ($\epsilon^{el} > 0$), which fits intuition. In the case of equal thickness and stiffness, the maximum total strain at the outer layers can be computed using eq. 6.6:

$$\epsilon_{\left(x=\pm\frac{t}{2}\right)} = \pm\kappa\frac{t}{2} = \pm 3\frac{\Delta\epsilon^*}{4}. \tag{6.7}$$

The value of the elastic strain is obtained by a simple subtraction, which can be done graphically in fig. 6.4 [5]:

$$\epsilon^{el}_{\left(x=\pm\frac{t}{2}\right)} = \epsilon_{\left(x=\pm\frac{t}{2}\right)} - \epsilon^*_{\left(x=\pm\frac{t}{2}\right)} = \pm\frac{\Delta\epsilon^*}{4}. \tag{6.8}$$

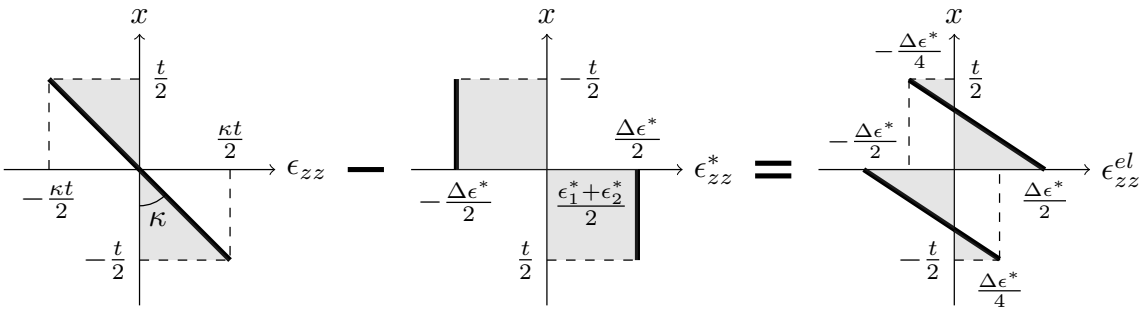

Figure 6.4 – (Left) Total longitudinal strain component ϵ_{zz}, which is proportional to the transversal coordinate x in the case of bending where the curvature κ is the coefficient of proportionality. (Middle) Eigenstrain longitudinal component in the case of a bilayer. One must be careful to plot the eigenstrain distribution around the average extension of the two layers which is equal to $(\epsilon_1^* + \epsilon_2^*)/2$. This "eigen-stretching" of the bilayer doesn't produce any stress and corresponds to a re-parametrization of the length of the rod (subsubsection 3.1.2.1). (Right) Elastic longitudinal strain component, which can be deduced by subtracting the eigenstrain from the total strain.

6.1.1.3 Energetic considerations

Another way to understand the bending of bilayers, is to look at it from an energetical viewpoint. Amongst the various possible configurations for the rod, two scenarios are considered: the rod remains straight and the rod bends. In each case, an increase in differential eigenstrain as given by (ΔT) leads to an increase in the elastic energy of the rod. Which of the stretching and bending energy is lower will determine if the rod stays straight or bends. In this sense, the bending of *benders* can be seen as a mechanical instability.

Straight If the rod remains straight, the only nonzero displacement component is along the z direction and is equal to $u_z = (L - L_0)z/L_0$. The total strain is thus constant and its only

5. Even if the longitudinal elastic strain component ϵ^{el}_{zz} is a function of the transversal coordinate x, we prefer to plot x as a function of ϵ^{el}_{zz} such that the cross-section of the bilayer is vertical and the longitudinal strain is horizontal.

nonzero components is:

$$\epsilon_{zz} = \frac{L - L_0}{L_0} + \frac{1}{2}\left(\frac{L - L_0}{L_0}\right)^2 = \frac{1}{2}\left(\left(\frac{L}{L_0}\right)^2 - 1\right). \tag{6.9}$$

The elastic longitudinal[6] strain in the top and bottom layers are constant as well and equal to:

$$\epsilon_\beta^{el} = \epsilon - \epsilon_\beta^* = \frac{1}{2}\left(\left(\frac{L}{L_0}\right)^2 - 1\right) - \alpha_{T\beta}\Delta T. \tag{6.10}$$

According to appendix A.4, the elastic energy with only the longitudinal stress and strain components reduces to:

$$\frac{\mathcal{E}_{straight}}{L_0} = \int_{CS} E(\epsilon_{zz}^{el})^2 \,\mathrm{d}x\,\mathrm{d}y. \tag{6.11}$$

Plugging the expression eq. 6.10 for the elastic longitudinal strain components, one obtains:

$$\frac{\mathcal{E}_{straight}}{L_0} = Ew\left[t_1\left[\frac{1}{2}\left(\left(\frac{L}{L_0}\right)^2 - 1\right) - \alpha_{T1}\Delta T\right]^2 + t_2\left[\frac{1}{2}\left(\left(\frac{L}{L_0}\right)^2 - 1\right) - \alpha_{T2}\Delta T\right]^2\right]. \tag{6.12}$$

At equilibrium, the elastic energy is minimum:

$$\frac{\delta\mathcal{E}_{straight}}{\delta L} = 0. \tag{6.13}$$

In the case of equal thickness, this implies that the total longitudinal strain is equal to the average of the *eigenstrains*[7]:

$$\epsilon_{zz} = \frac{(\alpha_{T1} + \alpha_{T2})\Delta T}{2}. \tag{6.14}$$

From eq. 6.10, the elastic strain components are:

$$\epsilon_{zz}^{el_1} = \frac{\Delta\epsilon^*}{2}, \qquad \epsilon_{zz}^{el_2} = -\frac{\Delta\epsilon^*}{2}, \tag{6.15}$$

and the energy per unit length becomes:

$$\frac{\mathcal{E}_{straight}}{L_0} = Ewt\frac{(\Delta\epsilon^*)^2}{4}. \tag{6.16}$$

Curved In the bended configuration, the longitudinal elastic strain component is stepwise linear instead of constant (see fig. 6.4 in the case of equal thickness):

$$\epsilon_{zz}^{el} = \begin{cases} -\frac{3\Delta\epsilon^*}{2t}x + \frac{\Delta\epsilon^*}{2} & 0 < x < \frac{t}{2}, \\ -\frac{3\Delta\epsilon^*}{2t}x - \frac{\Delta\epsilon^*}{2} & -\frac{t}{2} < x < 0. \end{cases} \tag{6.17}$$

Using eq. 6.11, the elastic energy per unit length is:

$$\frac{\mathcal{E}_{bended}}{L_0} = Ew\int_{t=0}^{\frac{t}{2}}\left(-\frac{3\Delta\epsilon^*}{2t}x + \frac{\Delta\epsilon^*}{2}\right)^2 \mathrm{d}x + Ew\int_{t=-\frac{t}{2}}^{0}\left(-\frac{3\Delta\epsilon^*}{2t}x - \frac{\Delta\epsilon^*}{2}\right)^2 \mathrm{d}x, \tag{6.18}$$

which after simplification leads to:

$$\frac{\mathcal{E}_{bended}}{L_0} = Ewt\frac{(\Delta\epsilon^*)^2}{16}. \tag{6.19}$$

6. The subscript $_{zz}$ is dropped for the sake of readability.
7. One obtains the same value for the total longitudinal strain considering only the linearized strain $L - L_0/L_0$.

Comparison between stretching and bending energy Let us compare the stretching energy of the bilayer in case it remains straight as given in eq. 6.16 and the bending energy in case it's curved as given in eq. 6.19. The bending energy in the curved scenario is four times lower than the stretching energy in the straight scenario. This means that bending is always energetically favored when $\epsilon_1^* \neq \epsilon_2^*$ [8]. In this sense, the bending instability is supercritical [9].

6.1.2 Multi-layer and graded *benders*

This section shows how adding intermediate layers between the bottom *active* and top *passive* layers affects the behavior of a *bender*: the interfacial is decreased for a finite amount of layers (subsubsection 6.1.2.1) and becomes zero for an infinite amount of layers possessing adequate CTEs (subsubsection 6.1.2.2).

6.1.2.1 Multi-layer *benders*

The previous analysis of bilayers was extended to the case of N-layers (Vasudevan and Johnson 1961). Using the same three steps as in appendix D.1 (balance of forces, balance of moments and compatibility of strain), a general expression for the curvature of an N-strip as a function of the thickness, stiffness and expansion coefficient of the different layers can be found. These expressions are rather cumbersome in the general case, but they reduce to simple expressions in the case where all thicknesses are the same ($t_i = t/N$) and all stiffnesses are the same ($E_i = E$). In the case of a tri-layer for example, the curvature takes a similar form to eq. 6.6:

$$\kappa^{tri} = \frac{4}{3}\frac{(\alpha_{T1} - \alpha_{T3})\Delta T}{t}. \tag{6.20}$$

The expansion coefficient of the intermediate layer (α_{T2}) does not affect the overall curvature [10]. Its effect is to decrease the distribution of normal stress at the intersurface. In this sense, adding intermediate layers smooths out the distribution of elastic strains in the normal direction (see subsubsection 6.1.2.3).

6.1.2.2 Graded *benders*

If the number of intermediate layers is very large ($N \to \infty$), the multi-layer becomes effectively a graded *bender* [11]. The coefficient of thermal expansion can now be seen as a scalar field that varies through the thickness of the *bender* ($\alpha_T = \alpha_T(x)$ [12]) producing a continuously varying eigenstrain ($\boldsymbol{\epsilon}^*(x) = \alpha_T(x)\Delta T$). For simple bending, the longitudinal elastic strain component [13] is given by (see fig. E.3b):

$$\epsilon_{zz}^{el} = \kappa x. \tag{6.21}$$

If the differential longitudinal *eigenstrain* is imposed to be equal to this elastic strain, one obtains the following definition for the scalar field representing the graded coefficient of thermal expansion:

$$\alpha_T(x) = \frac{\kappa x}{\Delta T}. \tag{6.22}$$

8. When $\epsilon_1^* = \epsilon_2^*$, both energies are zero.

9. Supercritical instability means that the bilayer is linearly stable when going from the straight into the curved configuration. On the contrary, a subcritical instability would mean that the bilayer jumps from the straight into the curved configuration (see subsubsection 7.1.3.3).

10. This is true as long as $\alpha_{T3} > \alpha_{T2} > \alpha_{T1}$.

11. So-called functionally graded materials are not new (Ichikawa 2001), but the idea of grading the *eigenstrain* instead of the stiffness appears to be original.

12. We regard a graded *bender* as a one-dimensional rod where the transversal coordinate is $-t/2 \leq x \leq t/2$

13. Disregarding the Poisson effect, bending only affects the longitudinal component of the strain tensor ϵ_{zz}.

6.1.2.3 Adding layers decreases interfacial stress

As discussed in subsubsection 6.1.1.2, the elastic strain (or stress) distribution is due to the difference between the total strain and the imposed eigenstrain. If the eigenstrain becomes closer to the total strain, the generated elastic strains and thus the interfacial jumps decrease. This means that when N additional layers are added between the *passive* and *active* layers with staggered expansion coefficients ($\alpha_{T1} < \alpha_{T2} < \ldots < \alpha_{TN}$) there will be more, but smaller jumps. In the limiting case of a graded *bender* ($N \to \infty$), the eigenstrain $\epsilon^*_{zz} = \alpha_T(x)\Delta T = \kappa x$ is *impotent*[14] and as such produces no stress (see subsection 3.2.2). In particular, there are no interfacial stress.

6.1.3 Experimental illustrations of bilayers

This section presents numerical and experimental illustrations of the bending of bilayers. Subsubsection 6.1.3.1 shows bending using the mass-spring model presented in section 4.1. Using three of the techniques presented in chapter 5, bending is then illustrated experimentally: pre-straining (subsubsection 6.1.3.2), thermal expansion (subsubsection 6.1.3.3) and swelling (subsubsection 6.1.3.4).

6.1.3.1 Mass-spring system undergoing bending

Using the mass-spring model presented in section 4.1, the differential longitudinal *eigenstrain* between the bottom *active* and top *passive* layer is represented by a different *rest length* of the longitudinal springs on each side of the extruded square lattice structure that represents the bilayer (see fig. 6.5).

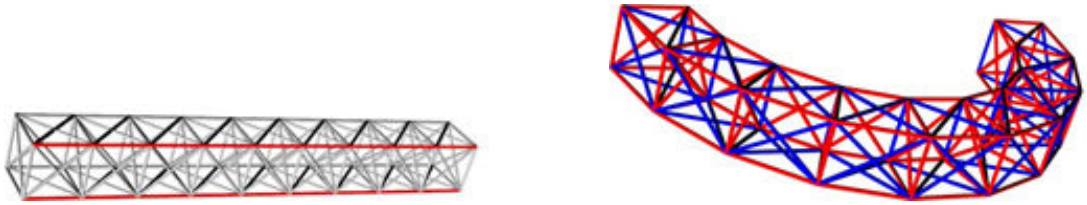

(a) (b)

Figure 6.5 – Bending corresponds to a different *rest length* of the longitudinal springs on each side of the extruded square lattice structure that represents a bilayer. (Left) Initial straight state. (Right) Final bended state. (Red) compression. (Blue) tension).

6.1.3.2 Bending using prestrained systems

The prestrained systems presented in section 5.1 enable to illustrate the concept of a bilayer. One layer is prestretched by a certain amount and then glued to an unstretched layer. Upon release, the unstretched layer tries to go back to its initial state. From the perspective of the stretched layer (pink on bottom), the unstretched layer (yellow on top) appears to have become bigger by the amount by which the stretched layer was stretched. This mismatch in natural strain implies a relatively important stretching energy, which is lowered through bending of the bilayer. In the longitudinal direction, bending is concave downwards (see fig. 6.6[15]). Observing the deformed configuration of the bilayer, we see that curvature is also generated along the

14. It is obviously compatible, because the elastic strain that results from bending is compatible by definition.
15. We'd like to thank Ailyn Bornmüller for helping us in doing the pre-strained experiments.

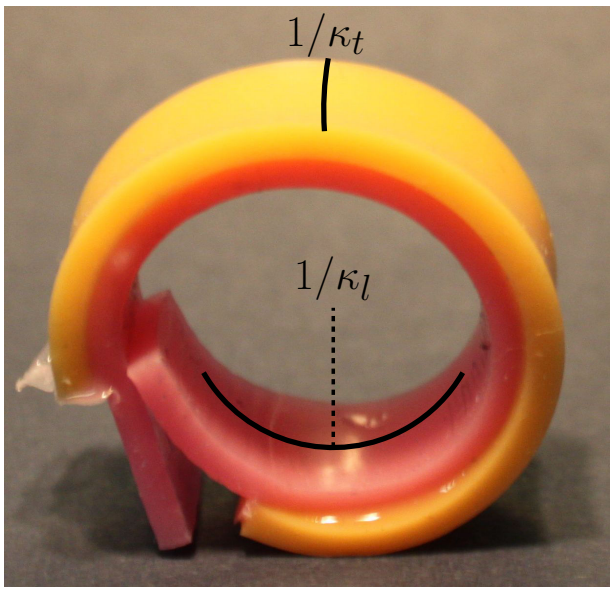

Figure 6.6 – A stretched layer of elastomer (pink on bottom) is glued to an unstretched layer of elastomer (yellow on top). Upon release, the stretched layer tries to go back to its unstreched state, which compresses the unstreched layer. Bending occurs in order to release the stretching energy of the bilayer.

transverse direction (the two black lines in fig. 6.6 live in perpendicular planes and are both curved). Indeed, when the pink layer is stretched in the longitudinal direction before gluing, the rubber band contracts in the transversal directions in accordance with Poisson effect (see appendix A.2.4). This leads to a differential longitudinal *eigenstrain* along the transversal direction (width) between the pre-stretched and the unstretched rubber. The differential transversal *eigenstrain* due to pre-stretching is $\Delta\epsilon_t^* \approx -0.5\Delta\epsilon_l^*$ [16].

6.1.3.3 Bending using thermal expansion

As being the original focus of Timoshenko's paper and as also presented in section 5.2, thermal expansion is a suitable way to impose *eigenstrain* distributions inside shapes. The relatively low CTE of elastomers leads to small curvature of the bilayer (fig. 6.7).

6.1.3.4 Bending using swelling

Bending can also be demonstrated using swelling systems (section 5.3). The simplest example of such a system is a piece of tracing paper gently laid on the surface of a water bath (subsection 5.3.1 and illustrated for helical *benders* in fig. 6.10). Due to the separation of time scales between the diffusion of water through the medium and the speed of mechanical waves (see subsection 3.2.3), the diffusion process triggers quasi-static actuation (see fig. 6.10).

16. The minus signs is due to the fact that the pink layer contracts in the transversal direction while stretched in the longitudinal direction. From the perspective of the pink layer, the yellow layer appears to be shorter and the bending is concave upwards. Also, rubber is usually considered incompressible, which explains the value $\nu \approx 0.5$.

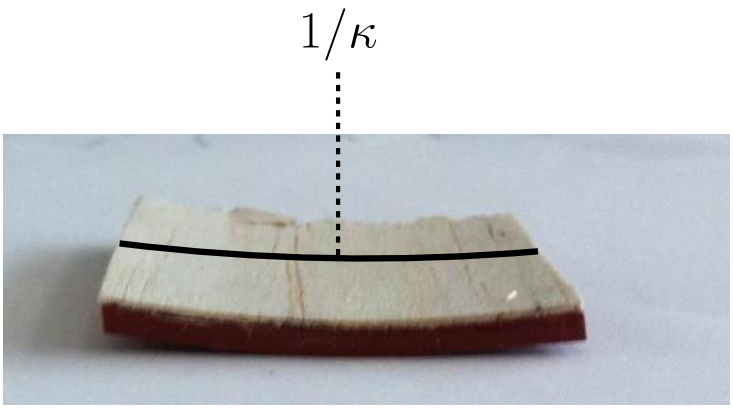

Figure 6.7 – Upon heating, the silicone expands isotropically, which leads to a slight bending perpendicular to the fiber direction.

6.2 Playing with *benders*

Section 6.1 described how a transversal differential longitudinal *eigenstrain* produces bending. This section shows how the curvature along the longitudinal direction of a *bender* can be tuned (subsection 6.2.1) and how to produce helical bending (subsection 6.2.2).

6.2.1 Longitudinally graded *benders*

Changing the curvature along the longitudinal direction can be achieved by changing the differential longitudinal *eigenstrain* along this direction. As long as the characteristic length of change of the differential longitudinal *eigenstrain* along the longitudinal direction is larger than the total thickness of the bilayer, the analysis given in appendix D.1 still applies. According to eq. 6.2, we have:

$$\kappa(z) = f(m,n)\frac{\Delta\epsilon^*(z)}{t}, \tag{6.23}$$

Figure 6.8 illustrates this using the mass-spring model [17] presented in section 4.1 and the energy minimization presented in section 4.2.

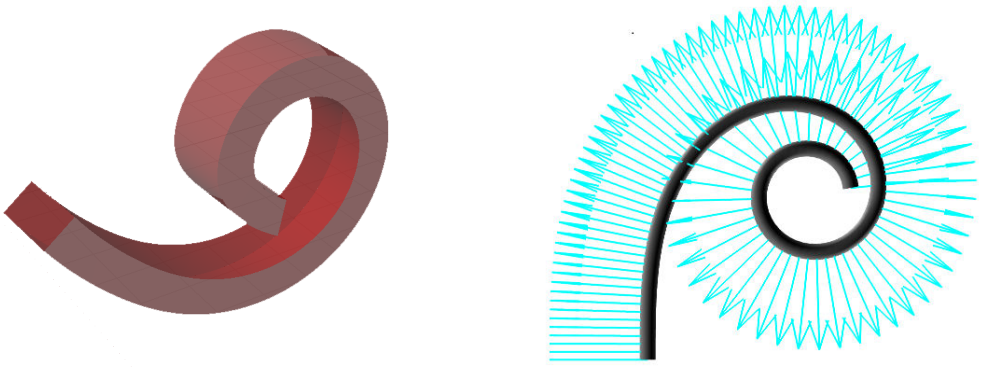

(a) (b)

Figure 6.8 – Illustration of longitudinally graded bending using a mass-spring model (left) or energy minimization (right).

17. Only the hull of the rod-like object is shown (not the springs).

6.2.2 Helical *benders*

It is also possible to produce helical geometries from bilayer eigenstrain distributions. This can be achieved by rotating the bending plane along the rod (fig. 6.9).

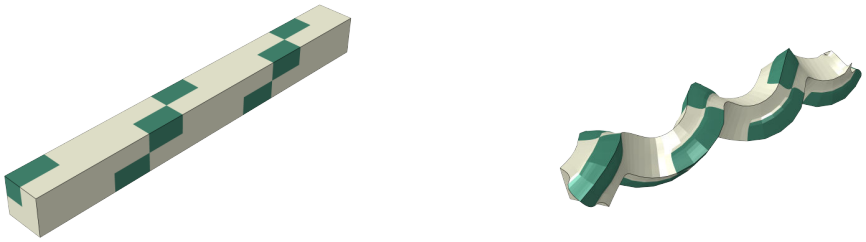

(a) (b)

Figure 6.9 – Helical bending is obtained by rotating the bending plane along the rod. Locally, the rod bends along the direction given by the *eigenstrain* gradient. (white) *passive*, (green) *active* regions.

Another option is to introduce an angle between the principal directions of eigenstrain and either the principal directions of the material stiffness or the principal directions of the geometry. This idea, which enriches the *morphing* potentiality of the bilayer principle, is illustrated in the following using two of the approaches presented in chapter 5 (swelling and pre-straining) [18].

Swelling helical *benders* The printing direction of paper is the direction of maximal stiffness. Upon swelling [19], the *eigenstrain* will be maximal in the plane perpendicular to the printing direction. When cutting strips at an angle θ with respect to the printing direction from a piece of tracing paper [20], the strips undergo helical bending where the pitch of the helix is a function of θ as shown in fig. 6.10.

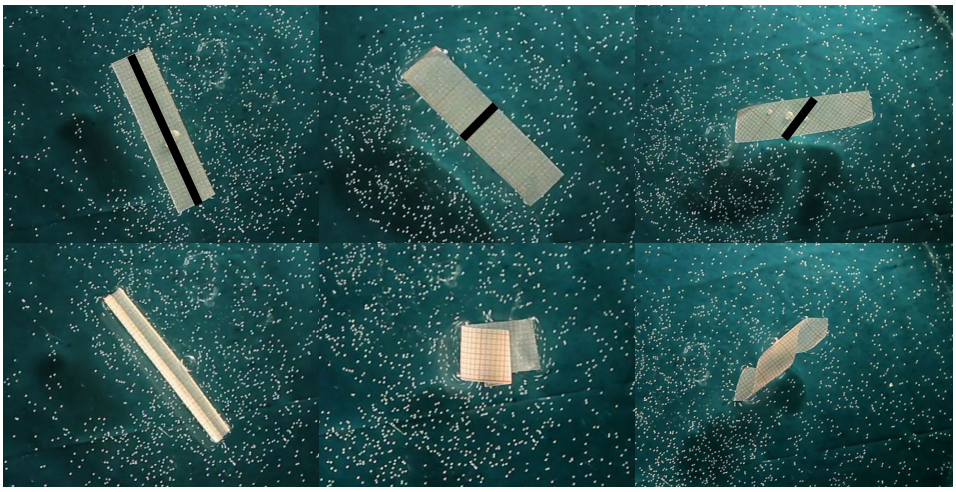

Figure 6.10 – Tracing paper is probably the simplest toy-model to illustrate *benders*. (Top) Geometry vs. direction of maximal stiffness (black line). (Bottom) Resulting rolling geometry. Depending on the angle between the geometry and the direction of maximal stiffness, the strips undergo: long-side rolling (left), short-side rolling (middle) or diagonal rolling (right).

18. See (Chen et al. 2011) for an extensive study of helical *benders*.
19. The swelling is controlled by the diffusion of water through the thickness of the strip (see chapter 8).
20. Common paper looses its structural integrity upon wetting.

Prestrained helical *benders* Helical bending through prestrain can be demonstrated by prestraining a rectangular PDMS square sheet in one direction, which is then glued to a rectangular PDMS square sheet that has been prestrained in the perpendicular direction. The release of the differential longitudinal *eigenstrain* in both directions leads to a saddle-shaped configuration (fig. 6.11a). Elongated strips cut in different directions will *morph* into different helical configurations depending on the cutting angle (fig. 6.11b).

(a)

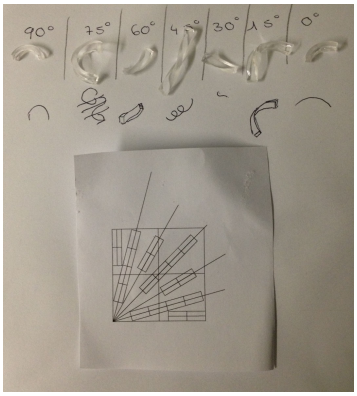

(b)

Figure 6.11 – (Left) Saddle-shaped configuration of a biaxially stretched elastomer. (Right top) Different helical configurations are obtained depending on the cutting angle of elongated strips. (Right bottom) Cutting pattern. This experiment reproduces the results of (Chen et al. 2011).

6.3 *Geometric amplification* using hierarchical architecture

This section present the concept of *geometric amplification* and compares theoretical predictions to the experimental results of (Razghandi 2014).

6.3.1 The concept of *geometric amplification*

The relatively small differential *eigenstrain* within a *bender* generates curvature through eq. 6.1. This curvature is converted into a relatively large mid-deflection depending on the length of the bilayer [21]. This mid-deflection can be further amplified by stacking *benders* on top of each other (fig. 6.15). This way, the relatively small *eigenstrain* is converted into a relatively large displacement by a factor that only depends on the length and the total amount of bilayers. This is the meaning of *geometric amplification*. Subsubsection 6.3.1.1 derives the mid-deflection of a *bender*, subsubsection 6.3.1.2 the opening of a *bender* cell and subsubsection 6.3.1.3 the opening of stacked cells.

6.3.1.1 Deflection of a single *bender*

A simply supported *bender* between two points separated by L will bend into an arc of circle of radius $1/\kappa$. The deflection δ is expressed using Pythagoras's theorem in the triangle ABC (see fig. 6.12):

$$\left(\frac{1}{\kappa}-\delta\right)^2+\left(\frac{L}{2}\right)^2=\left(\frac{1}{\kappa}\right)^2 \implies \delta\left(\frac{2}{\kappa}-\delta\right)=\left(\frac{L}{2}\right)^2. \tag{6.24}$$

21. The conversion factor is a quadratic function of the length of the bilayer (eq. 6.25).

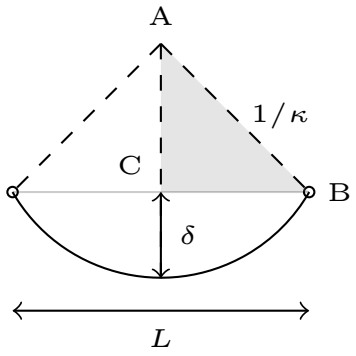

Figure 6.12 – Deflection of a simply supported *bender*.

Assuming that the deflection is small compared to the radius of curvature ($\delta \ll 1/\kappa$), eq. 6.24 becomes:

$$\delta \approx \kappa \frac{L^2}{8}. \tag{6.25}$$

6.3.1.2 Opening of a *bender* cell

Let's place two *benders* on top of each other and call it a cell (see fig. 6.13). If they are simply supported, the opening of the cell is just the double deflection ($2\delta \approx \kappa L^2/4$). According to eq. 6.2, the opening of the cell is:

$$2\delta \approx f(m,n)\frac{\Delta\epsilon^* L^2}{4t}, \tag{6.26}$$

where m and n are the thickness and stiffness contrasts respectively. For unitary stiffness and thickness contrasts, the double deflection according to eq. 6.6 becomes:

$$2\delta \approx \frac{3\Delta\epsilon^* L^2}{8t}. \tag{6.27}$$

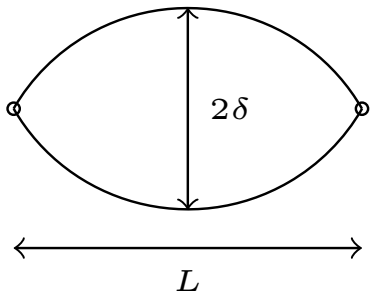

Figure 6.13 – Cell composed of two *benders* stacked on top of each other.

6.3.1.3 Opening of many *bender* cell

Let's stack *bender* cells on top of each other (see fig. 6.14). If they are simply supported[22], then the opening of each cell is equal to the double deflection ($2\delta \approx \kappa L^2/4$). For N cells stacked

22. A simple support has no rotational stiffness. In other words, it allows for free rotations.

upon each other, the total opening amounts to $O_N = 2\delta N$. According to eq. 6.26, the total opening is:

$$O_N \approx N f(m,n) \frac{\Delta\epsilon^* L^2}{4t}. \tag{6.28}$$

For unitary stiffness and thickness contrasts, the total opening is according to eq. 6.27:

$$O_N \approx N \frac{3\Delta\epsilon^* L^2}{8t}. \tag{6.29}$$

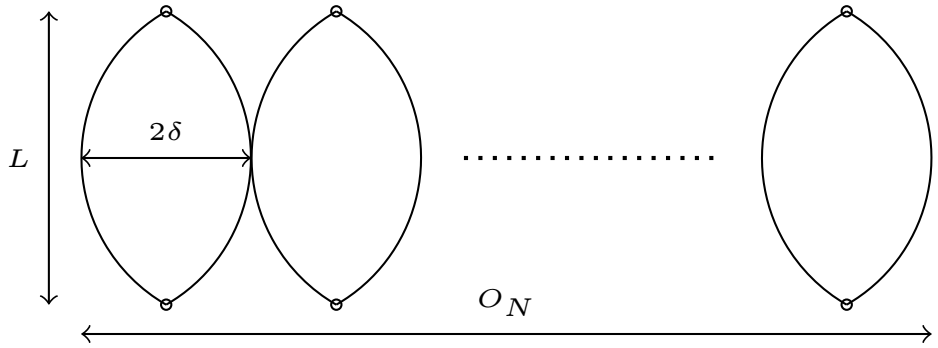

Figure 6.14 – Vertical stacking of multiple cells. The total opening of the stack is given by $D = 2\delta N$, where N is the amount of cells.

6.3.2 Comparison between theory and experimental prototype

As mentioned in footnote 2, an experimental prototype of a honey-comb bilayer was developed by Khashayar Razghandi in his PhD-thesis (Razghandi 2014). The bilayers are made up of spruce veneer (*active* layer), which is glued to thick paper (*passive* layer). Due to the anisotropic structure of wood, the spruce veneers swell mainly in their longitudinal direction, which is perpendicular to the orientation of the cellulose fibrils and placed along the long direction of the bilayer. This leads to a differential longitudinal *eigenstrain* along the longitudinal direction which generates curvature according to the *bender* principle highlighted previously in section 6.1. By connecting two *benders* together into a cell, the mid-deflection of such a *bender* is doubled as described in subsubsection 6.3.1.2. If the cells are stacked upon each other, the openings of each cell add up as described in subsubsection 6.3.1.3. As a result, the relatively small *eigenstrain* generated within the *benders* is amplified by the geometry of the stacking into a large displacement (fig. 6.15).

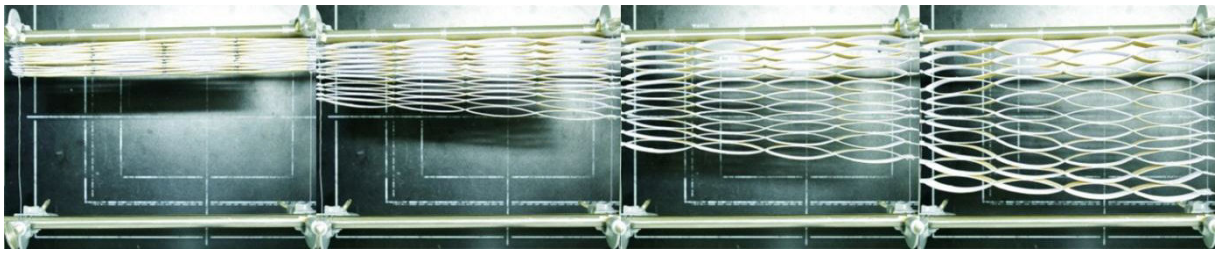

Figure 6.15 – Snapshots during the opening process of the bilayer-honeycomb at 0, 2, 4 and 16 hours in 95% relative humidity. This picture was taken from the PhD-Thesis of Khashayar Razghandi (Razghandi 2014).

6.3.2.1 Experimental parameters of honey-comb bilayers

The parameters describing the experimental prototype of a honey-comb bilayer are its thickness contrast ($m = t_1/t_2$), its stiffness contrast ($n = E_1/E_2$) as well as its differential longitudinal *eigenstrain* ($\Delta\epsilon^* = \epsilon_2 - \epsilon_1$). For the two layers, the thickness and stiffness were measured experimentally. The *eigenstrain* is evaluated for each layer separately as it undergoes free swelling [23]. According to table 6.1 we have $m = 3$, $n \approx 0.05$ and $\Delta\epsilon^* \approx 0.05$.

Layer	thickness (t[mm])	stiffness (E[MPa])	*eigenstrain* (ϵ^*)
active	$t_1 = 0.6$	$E_1 = 284$	$\epsilon_1^* = 0.05$
passive	$t_2 = 0.2$	$E_2 = 5147$	$\epsilon_2^* = 0.001$

Table 6.1 – Parameters describing the experimental prototype of a honey-comb bilayer.

6.3.2.2 Experimental- vs. theoretical curvature

Using the parameters given in subsubsection 6.3.2.1, the coefficient of proportionality is $f(m = 3, n \approx 0.05) \approx 1.5$ (6.3) and the theoretical curvature is $\kappa_{theory} \approx 1.5 * 0.05/0.8 \approx 0.094\,\mathrm{mm}^{-1}$ (eq. 6.2). The theoretical radius of curvature is thus $R_{theory} \approx 10\,\mathrm{mm}$. As measured from the experimental pictures using Rhino, the experimental radius of curvature is $R_{exp} \approx 60\,\mathrm{mm}$. The analytical radius of curvature is much smaller than the experimental radius curvature ($R_{exp} \approx 6 * R_{theory}$). Assuming that there was no error in our calculation nor in measuring the experimental parameters, this means that some of the assumption underlying the theoretical model must be revised. One assumption that is made throughout this thesis, is that the constitutive law is not affected by the *eigenstrain*. In reality, increasing the *eigenstrain* within a material usually decreases its stiffness (fig. C.7). However, as plotted in fig. 6.1, the influence of the stiffness contrast on the curvature is too small to explain this discrepancy [24]. Another assumption which was made in calculating the theoretical curvature, is that the bilayer is simply supported. Regarding the experimental system, this assumption can be questioned (subsubsection 6.3.2.3).

6.3.2.3 Rigidity of the connections

The assumption of simple supports leads to a theoretical curvature that is much larger than the experimental one ($\kappa_{theory} \approx 6 * \kappa_{exp}$) as discussed in subsubsection 6.3.2.2. If instead one assumes that the support has some rotational rigidity, then the curvature of each bilayer will be reduced. Indeed, the experimental geometry of the connection does not allow for free rotation. Using the finite-element method, one can draw the geometry of the connection, thereby given it some rotational rigidity (fig. 6.16).

23. By doing this, we assume that the *eigenstrain* of each layer taken separately is the same when they are together.

24. The proportionality factor is already close to its maximum value ($f(m = 3, n \approx 0.2) \approx 1.5$).

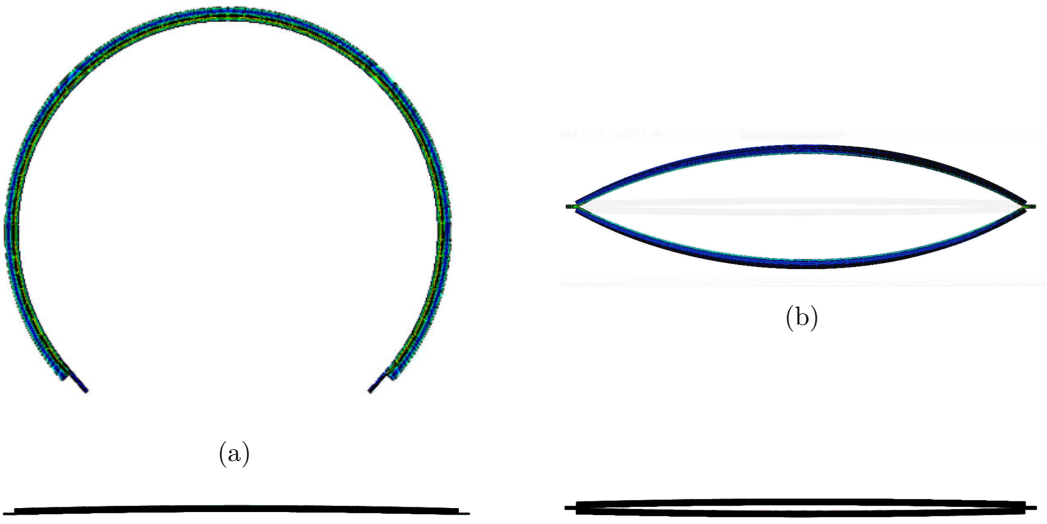

(a) (b) (c) (d)

Figure 6.16 – Dry (bottom) and wet (top) configuration of a single bilayer (left) or a bilayer cell (right). The radius of curvature of a simply supported bilayer found by fem is equal to its theoretical value $R_{theory} \approx 10\,\text{mm}$, while the radius of curvature of the bilayer cell is reduced by the rigidity of the supports, thus getting closer to its experimental value $R_{exp} \approx 60\,\text{mm}$.

Conclusions

Bilayers are known since more than 150 years. However, they remain a clever way to transform some external source of energy (like heat or water) into bending. The main cause of failure of bilayers (and composite structures in general) is delamination which is due to high interfacial stress. This interfacial stress can be lowered by adding intermediate layers between the most *passive* and the most *active* layer. In the limiting case of a graded *bender*, the actuation is stress-free. Variations of curvature along the longitudinal direction can be achieved by grading the *benders* along its length. Also, introducing an angle between the principal directions of eigenstrain and the principal directions of the geometry (either directly or by using the principal directions of stiffness), one obtains different helical morphologies. Finally, bilayers can also be used to transform a relatively small differential *eigenstrain* into a relatively large displacement by adding higher levels of hierarchy in the geometry of the material (*geometric amplification*).

References

Betts, Jonathan (1993). « John Harrison: inventor of the precision timekeeper ». In: *Endeavour* 17.4, pp. 160–167.

Chen, Zi et al. (2011). « Tunable helical ribbons ». In: *Applied Physics Letters* 98.1, p. 011906.

Guiducci, Lorenzo (2013). « Passive biomimetic actuators: the role of material architecture ». PhD thesis. Universität Potsdam.

Harrington, Matthew J et al. (2011). « Origami-like unfolding of hydro-actuated ice plant seed capsules ». In: *Nature communications* 2, p. 337.

Ichikawa, Kiyoshi (2001). *Functionally graded materials in the 21st century: a workshop on trends and forecasts*. Springer.

Razghandi, Khashayar (2014). « Passive hydro-actuated unfolding of ice plant seed capsules as a concept generator for autonomously deforming devices ». PhD thesis. Technische Universität Berlin.

Timoshenko, S et al. (1925). « Analysis of bi-metal thermostats ». In: *J. Opt. Soc. Am* 11.3, pp. 233–255.

Vasudevan, M and W Johnson (1961). « On multi-metal thermostats ». In: *Applied Scientific Research, Section B* 9.6, pp. 420–430.

Chapter 7

Twisters

Contents

Intrigued by twisting motions of some natural *morphers* like the twist-like opening of seed pods (Armon et al. 2011) and the coiling actuation of the stork's bill awn (Abraham et al. 2012), one can ask the question if there exist an analogous solution for twisting as *benders* are for bending. This chapter concerns itself with finding *eigenstrain* architectures that produces twisting inside elongated rod-like shapes.

Section 7.1 explores the design space of elongated translationally invariant [1] binary [2] *morphers* with the goal of finding analogous solutions for twisting as *benders* are for bending. Based on Curie's principle, the design space is restricted to rotationally symmetric *morphers* in terms of shape and *eigenstrain* (subsection 7.1.1). Using the finite-element method (section 4.3), this reveals a new class of twisting *morphers* which we call *twisters* (subsection 7.1.2). The *morphing* of these *twisters* consists of a stretched configuration followed by a twisted configuration. Subsection 7.1.3 identifies the critical transition point using an analytical approach. Subsection 7.1.4 illustrates *twisters* using the mass-spring model presented in section 4.1 as well as the swelling of 3d printed materials presented in subsection 5.3.2.

As described in subsection 3.1.2, the fundamental *morphing* modes of rods are stretching, bending and twisting [3]. Section 7.2 shows how an arbitrary configuration (with some restrictions) of a rod-like object can be achieved by combining *benders* and *twisters*. In this sense, *twisters* appear as a complementary solution to the *benders* presented in chapter 6.

1. Translationally invariant structures have the advantage of being extrudable, which makes them easy to process. This can be done by co- or multi-extrusion in the case of bi- or multi-nary structures.

2. Here binary means that the longitudinal components of the *eigenstrain* take two constant values in two complementary regions of the object, whereas all the other components of *eigenstrain* are zero everywhere ($\boldsymbol{\epsilon}^*(\boldsymbol{r}) = \epsilon^*_{zz} \in \{\epsilon^*_1, \epsilon^*_2\}$ where $\Omega_1 \cup \Omega_2 = \Omega$).

3. We use to world coiling to refer to a combination of bending and twisting.

7.1 Analog of a *bender* for twisting?

This section presents the *twisters*, which were partially published in (Turcaud et al. 2011). As in the case of bilayers, we first look at binary *eigenstrain* inside elongated rod-like shapes. For production purposes, translationally invariant arrangement of the *active* and *passive*[4] regions is preferred[5].

Subsection 7.1.1 explores the design space of such binary *morphers* looking for *eigenstrain* architectures that leads to twisting. Subsubsection 7.1.1.1 recalls the symmetry operations in two dimensions and subsubsection 7.1.1.2 discusses the symmetry of a *morpher* in terms of the symmetry of its cross-section section and of its *eigenstrain* architecture. Based on these symmetry considerations and Curie's principle, the design space is restricted to rotationally symmetric *eigenstrain* architectures inside rotationally symmetric cross-sectional shapes (subsubsection 7.1.1.3). Subsection 7.1.2 presents the deformed configuration of these *morphers* based on the finite-element method. Some of the designs display twisting, while others don't. We call *twisters* the ones that twists and identify two configurations during their *morphing*: stretching and twisting (subsubsection 7.1.2.2). In subsection 7.1.3, we parametrize the stretched and twisted state using a simple geometrical model (subsubsection 7.1.3.1), from which we can calculate the corresponding energies and discuss the transition between the two configurations (subsubsection 7.1.3.2). Finally, *twisters* are illustrated in subsection 7.1.4 using the mass-spring model (subsubsection 7.1.4.1) as well as the swelling of 3d printed materials (subsubsection 7.1.4.2).

7.1.1 Restricting the design space of *morphers*

Not knowing beforehand if an analogous solution as *benders* for bending exists for twisting, the design space of extrudable binary *morphers* is restricted through *symmetry* considerations. Using Curie's principle[6], which states that the symmetry of some effects cannot be smaller than the symmetry of their causes, this unravels a class of binary *morphers* that might display a twisting behavior. Subsubsection 7.1.1.1 discusses the symmetry operations in two-dimensions and subsubsection 7.1.1.2 uses them to classify *morphers* according to the symmetry of their cross-section and *eigenstrain* architecture. Subsubsection 7.1.1.3 then restricts the design space of potentially twisting *morphers* based on Curie's principle.

7.1.1.1 Symmetry operations

The characteristic symmetry of a *morpher* is the symmetry of its geometry and of its *eigenstrain* architecture. In the case of extrudable shapes with uniform cross-sections, both the geometry of the cross-section and the *eigenstrain* are a function of the two transversal coordinates spanning the cross-section. In the two-dimensional plane of the cross-section the symmetry operations thus reduce to two: mirror symmetry and rotational symmetry.

Mirror symmetry Mirror symmetry is defined by the presence of mirror planes. In the case of objects which are translationally invariant in one direction, all mirror planes are parallel to the center line[7]. The projection of such a mirror plane in the plane of the cross-section is a line

4. We use the terminology *active* and *passive* to denote the regions with the highest ($\epsilon_a^* = \epsilon_2^*$) and lowest *eigenstrain* ($\epsilon_p^* = \epsilon_1^*$) respectively ($\alpha_2 > \alpha_1$).

5. See footnote 1.

6. See (Ismael 1997) for a general discussion about the relevance of Curie's principle in science.

7. There is one other trivial mirror plane which lies perpendicular to the center line at half-length ($z = L/2$).

that corresponds to a mirror axis of the cross-section. We note mirror planes [8] as (M_i) with $(1 \leq i \leq n)$, where n is the total number of mirror planes (see fig. 7.1).

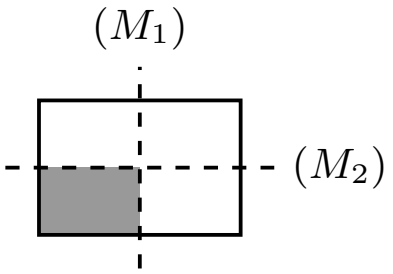

Figure 7.1 – Mirror symmetry is characterized by a mirror plane. In the case of translationally invariant shapes, only mirror planes parallel to the center line of the object matter (see footnote 7). The projection of those planes in the plane of the cross-section is a line that corresponds to a mirror axis of the cross-section. This figure shows the two mirror axis in the case of a rectangular cross-section ($n = 2$). The area in gray represents the smallest portion of the cross-section, which if reflected along the mirror axes generates the entire cross-section (see Repetitive unit cell).

Rotational symmetry Rotational symmetry is defined by the presence of a rotational axis. In the case of objects which are translationally invariant in one direction, the only possible rotational axis is along the center line [9]. Its projection onto the plane of the cross-section is the centroid of the cross-section. We note this rotational axis R_n, where n is the order of the rotational symmetry [10]. The angle of a n-fold rotation is given by $\alpha_n = 360/n^\circ$, where $n \geq 2$ [11] (see figure 7.2).

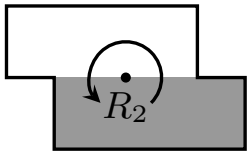

Figure 7.2 – Rotational symmetry is characterized by a rotational axis. In the case of translationally invariant shapes, only the center line is a potential rotational axis (see footnote 9), which projection onto the plane of the cross-section is its centroid. This figure shows a two-fold rotationally symmetric shape made out of two shifted rectangles. The angle of rotation is 180°. The small gray area represents the smallest portion of the cross-section, which if reflected along the mirror axis generates the entire cross-section (see Repetitive unit cell).

8. As we only consider translationally invariant shapes, there is no need to have separate notations for the mirror planes and the mirror axis.

9. Contrary to mirror planes, there cannot be multiple rotational axis perpendicular to the plane of the cross-section. The axes along the two transversal direction contained in the trivial mirror plane (see footnote 7) are also trivial rotational axis of order 2.

10. In two-dimensions the order of the rotational symmetry of the cross-section is either equal to its number of mirror planes or its number of mirror planes is zero. That's why we can choose the same symbol n to denote both the number of mirror planes and the order of the rotational symmetry.

11. If an object displays n-fold rotational symmetry then it also displays p-fold rotational symmetry, where p is the product of a subset of the primary numbers present in the decomposition of n ($n = p_1 \cdot p_2 \cdot \ldots \cdot p_m$ and $p = p_{i_1} \cdot p_{i_2} \cdot \ldots \cdot p_{i_k}$, where $\{i_1, \ldots, i_k\}$ is a subset of $\{1, \ldots, m\}$).

Repetitive unit cell We name repetitive unit cell (RUC) the smallest portion of the cross-section, which if reflected and rotated along the symmetry elements (M_n) and (R_n) generates the entire cross-section (see gray regions in fig. 7.1, fig. 7.2 and fig. 7.3). In this sense, the RUC is the smallest building block required to reconstruct the cross-section.

7.1.1.2 Symmetry of shape and symmetry of *eigenstrain*

The symmetry elements of the *morpher* correspond to the intersection between the symmetry elements of its shape and the symmetry elements of its *eigenstrain*. Because the *eigenstrain* is defined within the geometry of the shape, the symmetry elements of the *eigenstrain* are a subset of the symmetry elements of the shape. The symmetry of the *morpher* is thus equal to the symmetry of the *eigenstrain*. The following presents examples of cross-sectional shapes along with their symmetry elements and discuss how the choice of *eigenstrain* diminishes the symmetry of the *morpher*.

Symmetry of shape Cross-sections can be anything from asymmetric to multiply symmetric. Examples of the latter are regular n-sided polygons, which posses (M_n) mirror axis and (R_n) rotational symmetry [12]. Figure 7.3 shows regular n-sided polygons along with their symmetry elements and their RUC for $n = 3$, 4, 5, 6, 7 and 36.

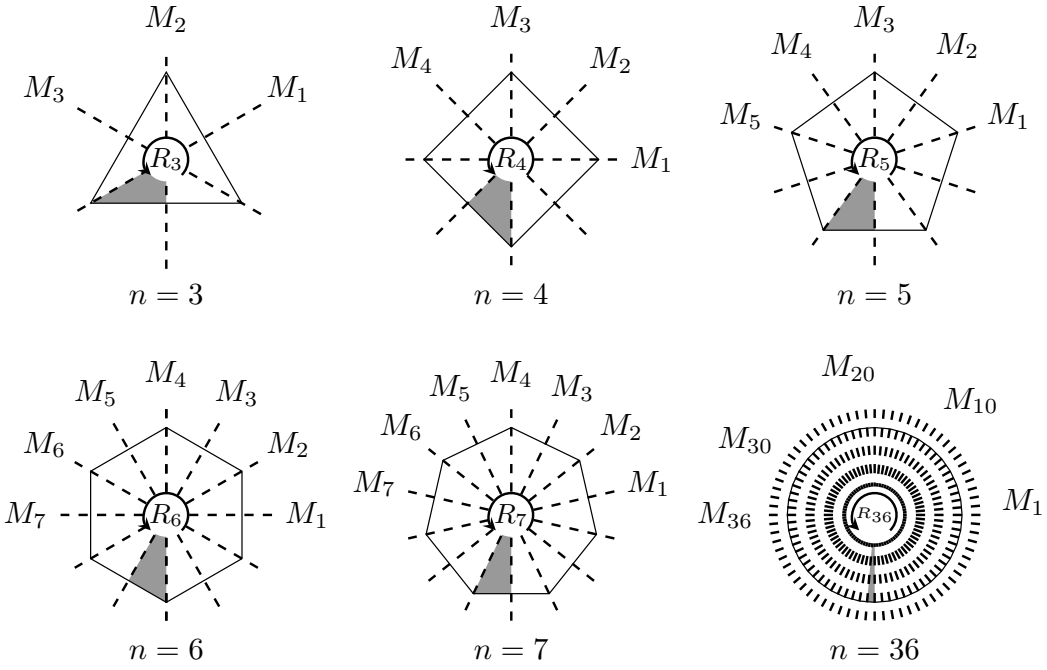

Figure 7.3 – Regular n-sided polygons possess (M_n) mirror axis and (R_n) rotational symmetry. (From left to right) triangle ($n = 3$), square ($n = 4$), pentagon ($n = 5$), hexagon ($n = 6$), heptagone ($n = 7$). For $n \to \infty$, the number of symmetry elements increases as n and the n-sided polygon converges to its circumscribed circle (see the 36-gone on the bottom right).

Symmetry of *eigenstrain* As mentioned above, the symmetry elements of the *eigenstrain* form a subset of the symmetry elements of the shape. For a given shape, the *eigenstrain* can only

12. This is why there is no ambiguity in using the same symbol n for the number of sides of a regular polygon, the number of mirror planes and the order of rotational symmetry (see footnote 10).

maintain or decrease its symmetry elements. In this sense, the *eigenstrain* breaks the symmetry of the shape [13] (see fig. 7.4).

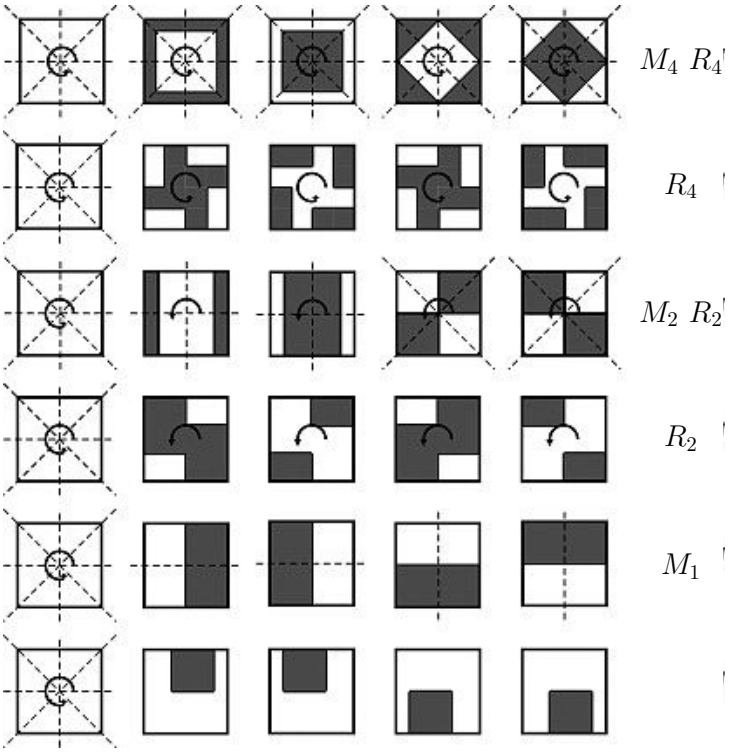

Figure 7.4 – The *eigenstrain* reduces the symmetry given by the shape. In case of a square cross-section, we have 4 mirror planes and a 4-fold rotational axis. (First column) Square cross-section with its symmetry elements. (Other columns) Non-exhaustive examples of *eigenstrain* that reduces the symmetry of the *morpher* (Last column) symmetry of the *morpher* (M_n, R_n, where n is the number of mirror planes and the order of rotational symmetry). (Black) *active* region. (White) *passive* region. Figure reprinted with permission from (Bruno et al. 2010). Copyright (2010) Carl Hanser Verlag, Muenchen.

7.1.1.3 Restricting the design space using Curie's principle

The following recalls the definition of Curie's principle and uses to restrict the design space of potentially twisting *morphers*.

Curie's principle

> When certain causes produce certain effects, the element of symmetry of the causes must be found in the effects [14]. (Curie 1894, p. 9)

In short, Curie's principle can be rephrased as "effects have at least the symmetry of their causes" [15]. Here, the effect we consider is twisting, which corresponds to a differential rotation

13. Actually the word breaking is misleading. Adding *eigenstrain* simply reduces the symmetry of the *morpher* relatively to the symmetry of its geometry.

14. The original statement in french is "Lorsque certaines causes produisent certains effets, les éléments de symétrie des causes doivent se retrouver dans les effets produits."

15. It is important that all the effects be considered. In the case of Euler buckling of a circular rod for example, there is no privileged plane for the buckling to happen. The problem is entirely symmetric along the longitudinal direction and one needs to introduce an imperfection in order to trigger buckling. In an experiment, the ensemble of solutions will be symmetric along the longitudinal direction in accordance with Curie's principle, even if each individual solution breaks the longitudinal symmetry.

of the cross-sections around the longitudinal direction [16]. Due to this differential rotation of the cross-sections, all existing mirror planes parallel to the center line in the initial configuration are no longer mirror planes in the twisted configuration. However, if a *morpher* displays rotational symmetry in its initial configuration, then the rotationally symmetry is maintained in its final twisted configuration.

Rotationally symmetric *morphers* According to Curie's principle, the design space of potentially twisting *morphers* is restricted to the ones possessing a rotationally symmetric initial configuration (both in terms of their shape as in terms of their *eigenstrain*). It is important that they do not possess any mirror plane in their initial configuration, because no mirror plane is present in the final twisted configuration [17].

The rotational order of the cross-section, restricts the potential rotational symmetry of the *eigenstrain* candidates [18]. For example, a triangular cross-section($n = 3$) only allows for a 3-fold rotational symmetric *eigenstrain*, while a square cross-section ($n = 4$) allows for both 2- and 4-fold rotational symmetric *eigenstrain*. In the case of a circular cross-section, as the circle possesses an infinite order or rotation ($n = \infty$), all orders $2 \leq n \leq \infty$ are possible for the rotational symmetry of the *eigenstrain* (see fig. 7.5).

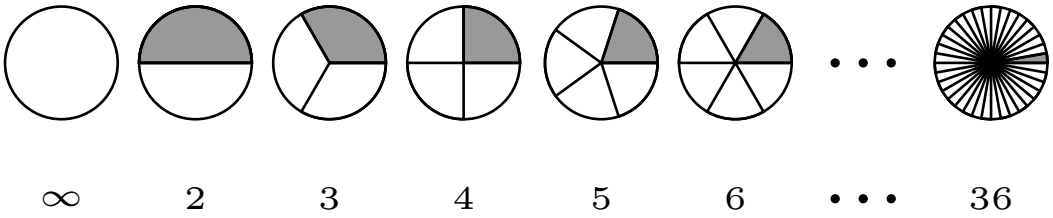

Figure 7.5 – The rotational order of the cross-section restricts the possible rotational orders of the *eigenstrain*. In the case of a circular cross-section, which has as an infinite order of rotation($n = \infty$), all orders $2 \leq n \leq \infty$ are possible for the rotational symmetry of the *eigenstrain*. (From left to right) $n = 2$, 3, 4, 5, 6, ..., 36. The RUCs are represented in gray (see Repetitive unit cell).

The choice of *eigenstrain* within the cross-section reduces to the choice of *eigenstrain* within the RUC for a given rotation order. Inside the RUC, any choice for the *passive* and *active* regions will preserve the rotation order of the *eigenstrain*, but some choices will display unwanted mirror symmetry (see fig. 7.6 top-left, center and bottom-right), which should be avoided [19].

Convex vs. concave cross-sections Another global way to restrict the design space, is to classify the shapes of the cross-sections into *convex* and *concave*. An informal definition of a *convex* shape is that any line drawn between two arbitrary points of the shape is entirely contained in the shape. On the contrary, for *concave* shapes it is always possible to find a line connecting two points of the shape, that is not entirely contained in the shape (see fig. 7.7). Subsubsection 7.1.2.1 shows that the concavity of the cross-sections of a *morpher* has an impact on whether it twist or stays straight.

16. This is a approximation as the cross-sections don't remain planar in general and warp out of plane during twisting (see subsubsection 3.1.2.3).

17. *Morphers* displaying both rotational and mirror symmetry are locked according to Curie's principle in the sense that they cannot bend nor twist as both *morphing* would break one of these symmetries (see fig. 7.4 first and third row).

18. See footnote 11.

19. See footnote 17.

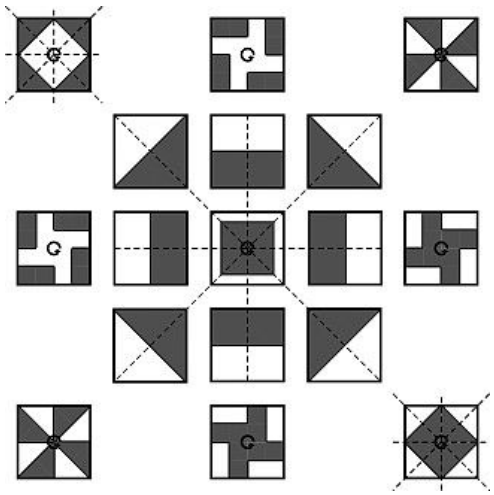

Figure 7.6 – Filling the RUC of a rotationally symmetric shape can result in unwanted mirror symmetries. In the case of a square (M_4, R_4) (middle), choosing mirror symmetric *eigenstrain* for the RUCs (first crown) can result in unwanted mirror planes (top-left, center and bottom-right) that leads to lock the *morpher*. (Black) *active* region. (White) *passive* region. Figure reprinted with permission from (Bruno et al. 2010). Copyright (2010) Carl Hanser Verlag, Muenchen.

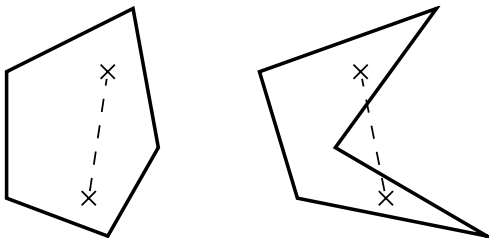

Figure 7.7 – Convex (left) and concave (right) shape.

7.1.2 A new type of *morpher*: the *twister*

According to subsection 7.1.1, binary elongated extrudable *morphers* are considered where both the cross-section (which can be convex or concave) as well as the *eigenstrain* displays rotational symmetry without mirror symmetry. We look at their final configuration using the finite-element method (section 4.3) and discuss their *morphing* patterns obtained (subsubsection 7.1.2.1). This reveals a special family of concave *morphers* that display twisting, which we call *twisters*. The *morphing* of these *twisters* consists of a stretched configuration followed by a twisted configuration, which we'll describe in (subsubsection 7.1.2.2).

7.1.2.1 Finite-element results

This section presents the deformed configuration of elongated translationally invariant binary *morphers* displaying rotationally symmetric *eigenstrain* using the finite-element method as described in section 4.3 inside Abaqus®. The following observations are made from fig. 7.8 [20]:

— Rotational symmetric *eigenstrain* (even in the absence of mirror symmetry) is not a sufficient condition for twisting. In the case of a convex cross-section such as a square, the *morpher* remains straight no matter how much the differential *eigenstrain* is increased (fig. 7.8(b));

20. The bilayer shown on the left of fig. 7.8 is for confirmation of the finite-element model only.

— In the case of a concave cross-section, twisting is obtained for a sufficiently high value of the differential *eigenstrain* (fig. 7.8 (c));
— The twisting rate appears to be inversely correlated to the inertia of the cross section (see (fig. 7.8(c)) and (fig. 7.8(d)));
— The concavity of the cross-section is not a sufficient conditions for twisting (fig. 7.8 (e));
— The *morphers* in fig. 7.8(b) and fig. 7.8(e) appear to be locked in the sense that they remain straight regardless of how much the differential *eigenstrain* is increased.

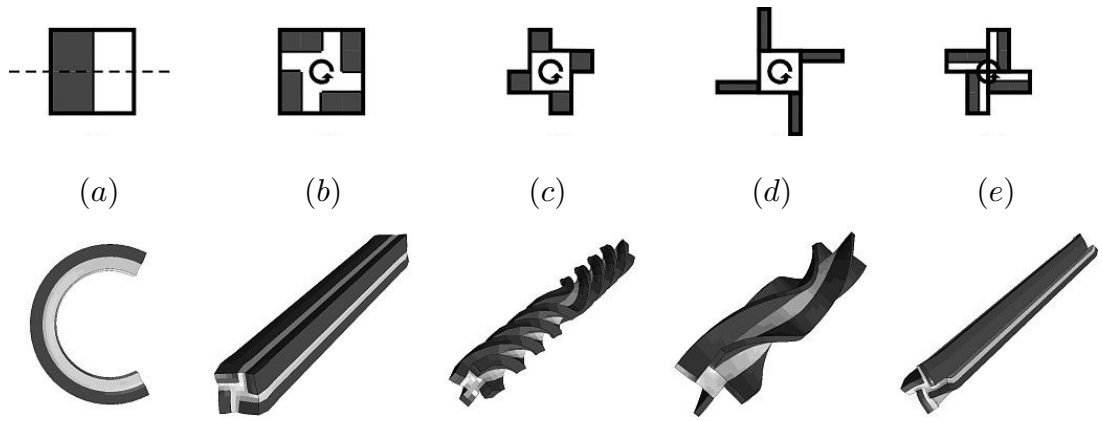

Figure 7.8 – Final configuration of *morphers* with different cross-sectional shapes and *eigenstrain* distributions using the finite-element method in Abaqus®. (Top row) Cross-section with *active* (black) and *passive* (white) regions. (Bottom row) Deformed configuration (a) Convex (square) cross-section with one mirror plane *eigenstrain* displays bending (for reference). (b) Convex (square (M_4, R_4)) cross-section with 4-fold rotationally symmetric *eigenstrain* remains straight. (c) Concave (R_4) cross-section with 4-fold rotationally symmetric *eigenstrain* display twisting. (d) Same as (c) with more elongated *wings* leads to less twisting. (d) Same as (c) with different *eigenstrain* inside the RUC remains straight. Figure reprinted with permission from (Bruno et al. 2010). Copyright (2010) Carl Hanser Verlag, Muenchen.

As discussed in subsubsection 7.1.4.1, when a rod-like object undergoes twisting, its center line remains approximately unchanged, while its external lines [21] deform helically and wind around the center line. The *morpher* shown in fig. 7.8(c) display a similar behavior. We refer to it as a *twister* and describe its *morphing* in subsubsection 7.1.2.2.

7.1.2.2 Stretching and twisting configuration of *twisters*

The *morphing* of a *twister* consists of two configurations: a stretched configuration where the *twister* extends while remaining straight followed by a twisted configuration in which the *twister* twists without extending. From the finite-element simulation, the critical differential temperature [22] depicted in fig. 7.9, which correspond to the *twister* shown in fig. 7.8(c), is $\Delta T_c \approx 0.75$°C for $a = 0.5$ (see fig. 7.11), $\alpha_{T2} = 1$ and $\alpha_{T1} = 0$. Subsection 7.1.3 studies these two configurations theoretically and identifies the critical differential *eigenstrain* at which the transition occurs.

7.1.3 Theoretical description of *twisters*

Subsection 7.1.1 explored the design space of elongated binary extrudable *morphers*. Based on symmetry considerations, the design space was restricted to rotationally symmetric *morphers*

21. The external lines are parallel to the center line and constitute the boundary of the rod.
22. We call differential temperature the temperature difference between the initial and the final state.

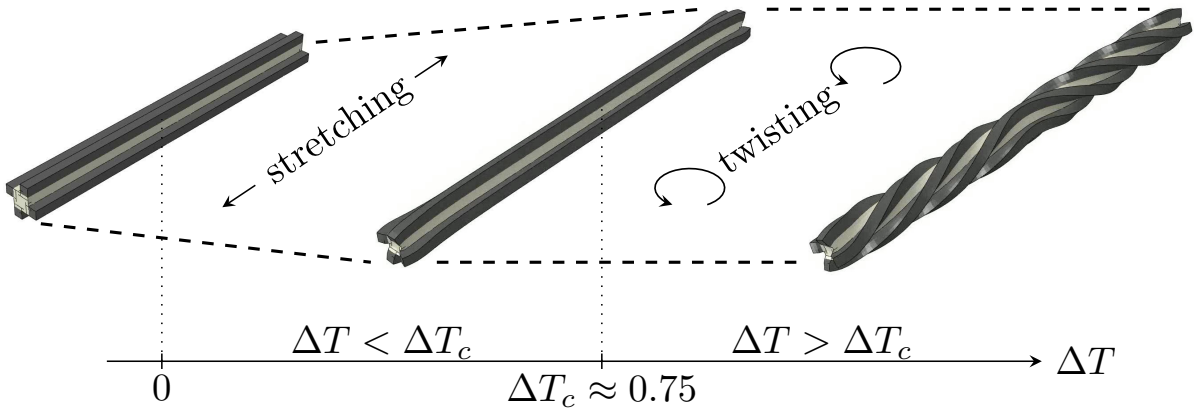

Figure 7.9 – (Left) Initial straight configuration. (Middle) Transition point (Right) Twisting configuration. The critical differential temperature is $\Delta T_c \approx 0.75$°C for $a = 0.5$, $\alpha_{T2} = 1$ and $\alpha_{T1} = 0$. The pictures are at scale and were obtained using the finite-element method in Abaqus®

that allow for twisting to occur according to Curie's principle. Subsubsection 7.1.2.1 presented the deformed configuration of these *morphers* according to the finite-element method. This revealed a particular family of *morphers* that we call *twisters*[23], which possess a concave cross-section and are such that the *active* regions (*wings*) are positioned around the *passive* (*core*) region in an eccentric manner[24]. Figure 7.9 shows that the *morphing* of such a *twister* consist of two configurations: a stretched configuration followed by a twisted configuration. This subsection aims at studying these two configurations theoretically and identifies the critical differential *eigenstrain* at which the transition occurs using the one-dimensional rod model presented in section 3.1. As the *eigenstrain* depends on the transversal coordinates of the rod and doesn't correspond to a simple deformation mode such as bending or twisting, the *natural* curvatures[25] of a *twister* are functions of the final configuration of the rod. This is why the *twister* is considered to be made of five distinct rods linked through geometry (the *core* and the four *wings*), each possessing their own elastic energy.

Subsubsection 7.1.3.1 parametrizes the two configurations of the *morphing* of *twisters* using a simple geometrical model: the winding of the *wings* around the *core* during the twisting configuration is assumed to be a perfect helix. This helps us in relating the *morphing* of the *wings* to the *morphing* of the *core*. Subsubsection 7.1.3.2 calculates the elastic energy in the straight and in the twisted configurations and identifies the equilibrium stretch (ϵ_{eq}) and the equilibrium torsion (τ_{eq}) in the stretched and in the twisted configuration respectively as well as identify the critical temperature difference between the final and the initial state (ΔT_c) at which the transition between the two regimes occurs.

7.1.3.1 Geometrical description of the *morphing* of *twisters*

Figure 7.9 shows that—as the temperature difference between the final and the initial state (ΔT) increases—the *twister* adopts two different configurations. For $0 < \Delta T < \Delta T_c$, the *twister*

23. We coined the word *twister* in analogy to the word *bender* that we used for bending.
24. We call *wings* the *active* regions and *core* the *passive* region and so we write equivalently $\epsilon_2^* = \epsilon_a^* = \epsilon_{wing}^*$ and $\epsilon_1^* = \epsilon_p^* = \epsilon_{core}^*$.
25. Sometimes in the text, we make no explicit distinction between the natural curvatures (κ_1^* and κ_2^*) and the natural torsion (κ_3^*), but call them all natural curvatures.

follows a stretched configuration and both *wings* and *core* are stretched [26]. For $\Delta T > \Delta T_c$, the *twister* follows a twisted configuration where the *wings* wind around the *core* in a helical manner thereby twisting the *core* whose extension remains constant. The transition between the two configurations (stretched and twisted [27]) happens for a critical temperature difference between the final and the initial state (ΔT_c) [28].

In order to find the equilibrium stretch (ϵ_{eq}) and the equilibrium torsion (τ_{eq}) in the stretched and twisted configuration as a function of the differential temperature (ΔT), the strain state of the *twister* in the two configurations needs to be described. In general, the total strain inside a rod depends on its extension and material curvatures [29] (see subsection 3.1.1). As the *twister* is described as five distinct rods (one *core* and four *wings*), the total strain inside the *twister* is expressed by the extension and material curvatures of both the *core* and the *wings*. By symmetry, the extension and material curvatures are equal in each *wing*. This means that there are a priori 8 parameters that characterize the total strain inside the *twister* (ϵ^β and κ_i^β, where $\beta \in \{core, wing\}$). The following shows how the number of parameters that describe the total strain inside the *twister* reduces to one in each configuration: the total extension (ϵ) in the first stretched configuration and the material torsion of the *core* (κ_3^{core}) in the second twisted configuration.

Straight configuration In the first configuration where the *twister* remains straight (fig. 7.10 left), all material curvatures are zero ($\kappa_i^\beta = 0$) and both *core* and *wings* have the same total extension:

$$\epsilon = \frac{(L/L_0)^2 - 1}{2}, \tag{7.1}$$

where L_0 and L are the initial and final length of the *twister* respectively [30]. The strain in the stretched configuration is thus entirely parametrized by the extension of the *twister* (ϵ).

Twisted configuration Let us express the extensions (ϵ^β) and material curvatures (κ_i^β) of the *wings* and *core* in the second configuration where the *twister* twists (fig. 7.10 right). The total extension of the *core* remains constant and equal to its value at the end of the first configuration ($\epsilon^{core} = \epsilon_c$, where ϵ_c is the critical total extension of the *twister*). Assuming that the *wings* wind around the *core* in a perfect helical manner, their center line follows a helix between the two end-points of the *core* spanned by $\boldsymbol{r}(\theta) = \boldsymbol{r}(x(\theta), y(\theta), z(\theta))$ parametrized by the azimuthal angle along the longitudinal direction (θ). The coordinates $x(\theta), y(\theta), z(\theta)$ of this helix are given

26. Both *core* and *wings* are stretched in terms of the total strain. In terms of the elastic strain, the *wings* are contracted while the *core* is stretched (eq. 7.16).

27. We refer to the configuration of the *twister* in the two configurations by describing the configuration of its *core* which is stretched in the first configuration and twisted in the second. However, one should keep in mind that the configuration of the *wings* is contracted in the first configuration and helical in the second, which implies a combination of contraction, bending and twisting.

28. The temperature difference between the final and the initial state (ΔT) corresponds to a differential *eigenstrain* ($\Delta\epsilon^* = \Delta\alpha_T \Delta T = (\alpha_{T2} - \alpha_{T1})(T - T_0)$) between the *active* and *passive* regions. Also, the critical temperature difference between the final and the initial state (ΔT_c) corresponds to a critical differential *eigenstrain* ($\Delta\epsilon_c^*$). As we consider constant expansion coefficients ($\alpha_{T\beta}$), we can use both temperature and *eigenstrain* equivalently.

29. Sometimes in the text, we make no explicit distinction between the two material curvatures (κ_1, κ_2) and the material torsion κ_3, but call them all material curvatures (see footnote 25).

30. The initial length of the *core* is equal to initial length of the *wings* ($L^{core} = L_0^{wing} = L_0$).

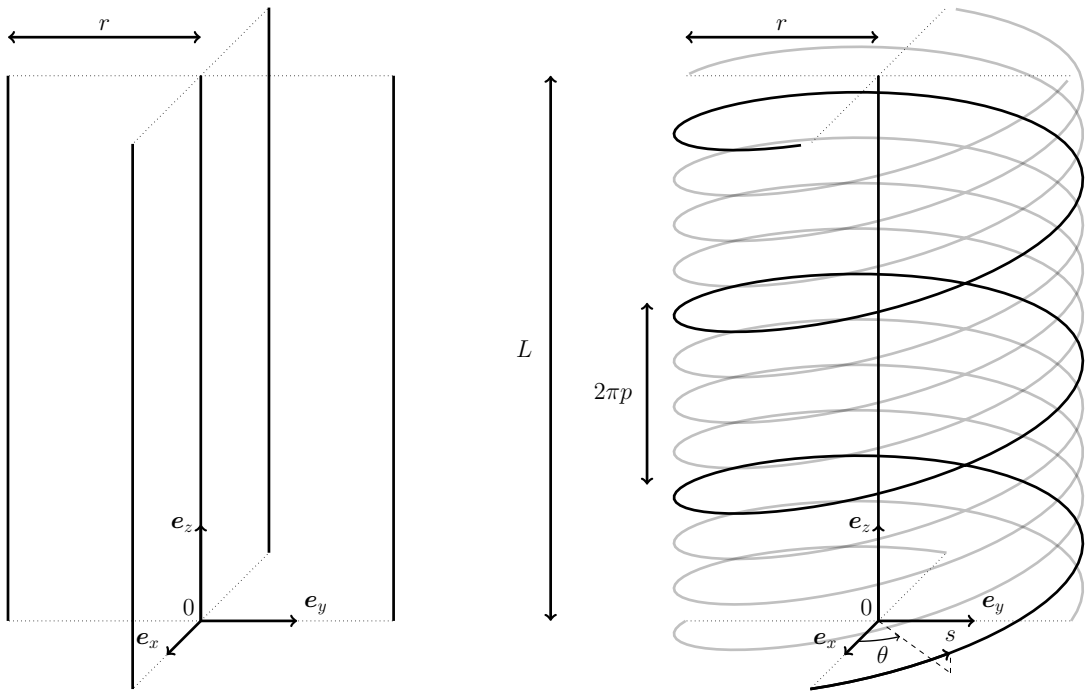

Figure 7.10 – Center lines of the *core* and *wings* from a *twister* in its first stretched configuration (left) and in its second twisted configuration (right). (Left) All center lines are straight and the total strain inside the *twister* is parametrized by the total extension of the *twister* (ϵ). (Right) The center line of the *core* is straight and the center lines of the *wings* wind around the center line of the *core* in a perfect helical manner (only one *wing* center line is drawn fully opaque for the sake of visual readability). The total strain is parametrized by the torsion of the *core* (τ^{core}).

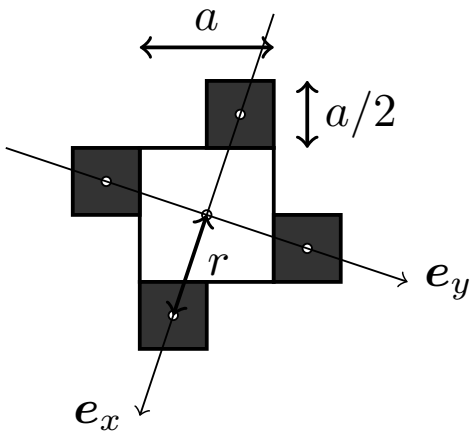

Figure 7.11 – Rotationally symmetric concave cross-section of twister. In the case of unitary volume contrast between the *active* and *passive* regions, the side-length of the *wings* are half the side-length of the *core*. The coordinate axes whose orientation is given by $\boldsymbol{e}_x$ and $\boldsymbol{e}_y$ intersect the centroids of the *core* and *wings*. (Black) *active wings*. (White) *passive core*.

by [31]:

$$\begin{cases} x(\theta) = r\,cos(\theta), \\ y(\theta) = r\,sin(\theta), \\ z(\theta) = p\,\theta, \end{cases} \qquad 0 < \theta < \frac{L^{core}}{p}, \tag{7.2}$$

31. This set of parametric equations gives the coordinates of the fully opaque center line drawn in fig. 7.10 right. The coordinates of the other *wings* are obtained by adding $k\pi/2$ ($k = 1, 2, 3$) to θ.

where r is the radius of the cylinder onto which the helix is drawn and $2\pi p$ is the pitch of the helix. The radius of the helix is known and equal to the distance between the center lines of the *wings* and the center line of the *core* as given by the geometry of the cross-section (fig. 7.11). Using Pythagoras's theorem one has $r = \sqrt{5}a/(2\sqrt{2})$ where a is the side-length of the *core*[32]. The curvilinear abscissa of a *wing* ($0 < s < L^{wing}$) is related to the azimuthal angle (θ) by:

$$\begin{aligned} \mathrm{d}s &= \|\mathrm{d}\boldsymbol{r}(\theta)\|, \\ &= \sqrt{(\mathrm{d}x(\theta))^2 + (\mathrm{d}y(\theta))^2 + (\mathrm{d}z(\theta))^2}, \\ &= \sqrt{(-r\,sin(\theta)\,\mathrm{d}\theta)^2 + (r\,cos(\theta)\,\mathrm{d}\theta)^2 + (p\,\mathrm{d}\theta)^2}, \\ &= \sqrt{r^2 + p^2}\,\mathrm{d}\theta. \end{aligned} \tag{7.3}$$

Also, the curvilinear abscissa of the *core* ($0 < z < L^{core}$)[33] is related to the azimuthal angle (θ) by:

$$\mathrm{d}z = p\,\mathrm{d}\theta. \tag{7.4}$$

In particular, the length of a *wing* and of the *core* are related by:

$$L^{core} = \int_0^{L^{core}} \mathrm{d}z = p\int_0^{\frac{L^{core}}{p}} \mathrm{d}\theta = \frac{p}{\sqrt{r^2+p^2}}\int_0^{L^{wing}} \mathrm{d}s = \frac{L^{wing}}{\sqrt{1+\dfrac{r^2}{p^2}}} \tag{7.5}$$

Using eq. 7.5 and the nonlinear definition of the extensional strain (eq. A.40 with $\lambda = \dfrac{L}{L_0}$), the extension of the *wings* (ϵ^{wing}) is linked to the extension of the *core* (ϵ^{core}) by:

$$\begin{aligned} \epsilon^{wing} &= \frac{\left(\dfrac{L^{wing}}{L_0}\right)^2 - 1}{2}, \\ &= \frac{\left(1+\dfrac{r^2}{p^2}\right)\left(\dfrac{L^{core}}{L_0}\right)^2 - 1}{2}, \\ &= (0.5+\epsilon^{core})\,\frac{r^2}{p^2} + \epsilon^{core}. \end{aligned} \tag{7.6}$$

Let us identify the material vectors ($\boldsymbol{d}_i^{wing}(s)$) of one *wing* in order to compute its material curvatures ($\kappa_i^{wing}(s)$). We first compute the geometric curvature and geometric torsion of a helix by looking at its local geometrical frame ($\boldsymbol{t}(s)$, $\boldsymbol{n}(s)$, $\boldsymbol{b}(s)$). By applying eq. 3.1 to eq. 7.2 one

32. In the case of a unitary volume contrast ($V^{core} = V^{wings} = a^2L$), the side-length of the *wings* is half the side-length of the *core*.

33. We directly denote the curvilinear abscissa of the *core* by its longitudinal coordinate z in order to avoid ambiguity with the curvilinear abscissa of the *wing* denoted by s.

obtains [34]:

$$\begin{cases} \boldsymbol{t}(s) = \boldsymbol{r}'(s) = \begin{pmatrix} -r\,sin(\theta) \\ r\,cos(\theta) \\ p \end{pmatrix} \dfrac{1}{\sqrt{r^2+p^2}}, \\ \boldsymbol{n}(s) = \dfrac{\boldsymbol{t}'(s)}{\|\boldsymbol{t}'(s)\|} = \begin{pmatrix} -r\,cos(\theta) \\ -r\,sin(\theta) \\ 0 \end{pmatrix} \dfrac{1}{r^2+p^2} \Big/ \dfrac{r}{r^2+p^2} = \begin{pmatrix} -cos(\theta) \\ -sin(\theta) \\ 0 \end{pmatrix}, \\ \boldsymbol{b}(s) = \boldsymbol{t}(s) \times \boldsymbol{n}(s) = \begin{pmatrix} p\,sin(\theta) \\ -p\,cos(\theta) \\ r \end{pmatrix} \dfrac{1}{\sqrt{r^2+p^2}}, \end{cases} \tag{7.7}$$

where $\boldsymbol{t}(s)$, $\boldsymbol{n}(s)$, $\boldsymbol{b}(s)$ are the tangent-, normal- and binormal-vectors. By definition $\kappa(s) = \|\boldsymbol{t}'(s)\|$ and $\tau(s) = \boldsymbol{n}'(s) \cdot \boldsymbol{b}(s)$, so the geometric curvature and geometric torsion of a helix are constant and given by:

$$\kappa^{wing} = \frac{r}{r^2+p^2}, \qquad \tau^{wing} = \frac{p}{r^2+p^2}. \tag{7.8}$$

Assuming perfect attachment between the *wing* and the *core* (which is required by the compatibility of strain before delamination), the orientation between the material frame and the geometrical frame of the *wings* is constant. This means that the material torsion of the *wing* is equal to its geometric torsion ($\kappa_3^{wing} = \tau^{wing}$). Also, because the squared cross-section of the *wing* is isotropic, one can set one of its transversal material vector equal to its binormal vector ($\boldsymbol{d}_1^{wing}(s) = \boldsymbol{b}(s)$). The geometrical and the material frame of the *wing* can thus be identified:

$$\begin{pmatrix} \boldsymbol{d}_1^{wing}(s) \\ \boldsymbol{d}_2^{wing}(s) \\ \boldsymbol{d}_3^{wing}(s) \end{pmatrix} = \begin{pmatrix} \boldsymbol{t}(s) \\ \boldsymbol{n}(s) \\ \boldsymbol{b}(s) \end{pmatrix}.$$

The material curvatures of the *wing* are thus equal to its geometric curvatures [35] and constant along the center line of the *wings*:

$$\kappa_1^{wing} = \frac{r}{r^2+p^2}, \qquad \kappa_2^{wing} = 0, \qquad \kappa_3^{wing} = \frac{p}{r^2+p^2}. \tag{7.9}$$

Let us identify the material vectors ($\boldsymbol{d}_i^{core}(z)$) of the *core* in order to compute its material curvatures ($\kappa_i^{core}(z)$) where $0 < z = p\,\theta < L^{core}$ is the curvilinear abscissa of the center line of the *core*. Its center line remains straight and so its tangent vector is along the longitudinal direction ($\boldsymbol{d}_3^{core}(z) = \boldsymbol{e}_z$). Because the tangent vector is constant, the geometric curvature and the geometric torsion of the *core* are zero ($\kappa(z) = \tau(z) = 0$). As the *wing* is perfectly attached to the *core*, the transversal material vector of the *core* $\boldsymbol{d}_1^{core}(z)$ can be identified with the projection of the position vector of the helix $\boldsymbol{r}(\theta)$ onto the xy-plane:

$$\boldsymbol{d}_1^{core}(z) = \frac{\boldsymbol{r}(\theta) - \boldsymbol{r}(\theta)\cdot\boldsymbol{e}_z}{\|\boldsymbol{r}(\theta) - \boldsymbol{r}(\theta)\cdot\boldsymbol{e}_z\|} = \begin{pmatrix} r\,cos(\theta) \\ r\,sin(\theta) \\ 0 \end{pmatrix} \frac{1}{r} = \begin{pmatrix} cos\left(\dfrac{z}{p}\right) \\ sin\left(\dfrac{z}{p}\right) \\ 0 \end{pmatrix}, \qquad \boldsymbol{d}_2^{core}(z) = \begin{pmatrix} -sin\left(\dfrac{z}{p}\right) \\ cos\left(\dfrac{z}{p}\right) \\ 0 \end{pmatrix},$$

34. We parametrize the helix by its azimuthal angle (θ), but derive the geometrical and material vectors with respect to the arc-length (s). Applying the chain rule, derivation amounts to multiply by a factor $1/\sqrt{r^2+p^2}$ (eq. 7.3).

35. Sometimes in the text, we make no explicit distinction between the geometric curvature (κ) and the geometric torsion (τ), but call them both geometric curvatures (see footnote 25 and 29).

where the fact that the material frame is orthonormal is used to write $\boldsymbol{d}_2^{core}(z)$. The material curvatures of the *core* are thus:

$$\kappa_1^{core}(z) = 0, \qquad \kappa_2^{core}(z) = 0, \qquad \kappa_3^{core}(z) = (\boldsymbol{d}_1^{core}(z))' \cdot \boldsymbol{d}_2^{core}(z) = \frac{1}{p}. \tag{7.10}$$

This means that the material torsion of the *core* and the pitch of the helix representing the center line of the *wing* are inverse quantities ($\kappa_3^{core} = 1/p$). Indeed, the material torsion of the *core* is defined by the rotation of its transversal material vectors ($\boldsymbol{d}_1^{core}(z)$, ($\boldsymbol{d}_2^{core}(z)$) along its center line, which is expressed by their change in orientation in the xy-plane given by the azimuthal angle ($\kappa_3^{core} = \mathrm{d}\theta/\mathrm{d}z$). From eq. 7.4 the change in azimuthal angle along the longitudinal direction and the pitch p of the helix are inverse quantities ($\mathrm{d}\theta/\mathrm{d}z = 1/p$). For simplicity of notation, we note $\tau = \kappa_3^{core}$ to denote the material torsion of the *core*[36] and so $p\,\tau = 1$.

The strain in the twisted configuration is parametrized by the extensions (ϵ^β) and material curvatures (κ_i^β) of the *wings* and *core*, which are all functions of the pitch (p) of the helix representing the center line of the *wings*. The pitch and the material torsion of the *core* are inverse quantities and so the strain in the twisted configuration is entirely characterized by the material torsion of its *core* ($\tau = \kappa_3^{core}$) through eq. 7.6, eq. 7.9 and eq. 7.10.

7.1.3.2 Energetic considerations

Subsubsection 7.1.3.1 showed that the strain inside a *twister* is entirely parametrized by its stretching in its stretched configuration (ϵ as given by eq. 7.1) and by the torsion[37] of its core in its twisted configuration (τ through eq. 7.9 and eq. 7.10). The following calculates the elastic energy of a *twister* in its straight and twisted configuration and find the equilibrium stretch (ϵ_{eq}) and equilibrium twist (τ_{eq}), which correspond to a minimum of the elastic energy.

The elastic energy of a *twister* is the sum of the elastic energy of its *core* and of the elastic energy of its *wings* ($\mathcal{E}^{twister} = \mathcal{E}^{core} + 4 * \mathcal{E}^{wing}$). According to eq. 3.25, the elastic energy of a rod with natural extension (ϵ^*) and natural curvatures (κ_i^*) is given by:

$$\mathcal{E}_{rod} = 0.5 \int \Big(EA\,(\epsilon - \epsilon^*)^2 + EI^{(1)}(\kappa_1 - \kappa_1^*)^2 + EI^{(2)}(\kappa_2 - \kappa_2^*)^2 + \mu J(\kappa_3 - \kappa_3^*)^2 \Big)\,\mathrm{d}s, \tag{7.11}$$

where E and μ are the Young and the shear modulus and A, I^α, J the area, bending inertias and twisting inertia of the cross-section of the rod. In the case of translationally invariant *morphers*, the integration along the longitudinal coordinate (s for the *wings* and z for the *core*) amounts to a simple multiplication by the length of the *core* or of the *wings*[38] (L^{core} or L^{wing}). Also, as only a differential longitudinal *eigenstrain* is imposed, the natural curvatures of the *core* and of the *wings* are equal to zero ($\kappa_i^{*\beta} = 0$) and only the natural extensions are nonzero ($\epsilon_1^* = \alpha_{T1}\Delta T$ and $\epsilon_2^* = \alpha_{T2}\Delta T$ where $\alpha_{T2} > \alpha_{T1}$). According to eq. 7.8, the *wings* undergo simple bending and only one of the transversal material curvatures is nonzero as the first material vector ($\boldsymbol{d}_1$) is defined along the bending direction[39] ($\kappa_1 = \kappa$ and $\kappa_2 = 0$ according to eq. 7.9). The elastic energy of a rod with natural extension undergoing a combination of stretching, single bending and torsion is thus given by:

$$\mathcal{E}_{rod}(\epsilon, \kappa, \tau) = \frac{L}{2}\left(EA(\epsilon - \epsilon^*)^2 + EI\kappa^2 + \mu J\tau^2 \right), \tag{7.12}$$

36. There is no ambiguity with the geometric torsion of the *core*, which is zero as its center line remains straight, and the geometric torsion of the *wings* as we'll only consider material curvatures during the energy considerations.

37. Equivalently, the twisted configuration can be entirely characterized by the pitch of the helix representing the center line of the *wings* winding around the *core* ($p\,\tau = 1$).

38. In the straight configuration, the length of the *core* and of the *wings* is equal ($L^{core} = L^{wing} = L$). In the twisted configuration, the length of the *wing* is related to the length of the *core* through eq. 7.5.

39. The *wings* have an isotropic cross-section (square) in terms of their bending inertia ($EI^{(1)} = EI^{(2)}$) and so their bending energy is unchanged if we define the first material vector ($\boldsymbol{d}_1$) not along the bending direction ($Ea^2\kappa^2/12 = Ea^2(\kappa_1^2 + \kappa_2^2)/12$ because $\kappa = \kappa_1^2 + \kappa_2^2$).

where L is the length of the rod. As the *core* has a square cross-section of side-length a, we have $A^{core} = a^2$, $I^{core} = a^4/12$ and $J^{core} \approx a^4/7$. In the case of a unitary volume contrast, the *wings* have a square cross-section of side-length $a/2$ and so we have $A^{wing} = a^2/4$, $I^{wing} = a^4/192$ and $J^{wing} \approx a^4/112$.

Elastic energy in the straight configuration In the straight configuration, the *core* and the *wings* undergo simple stretching, which is characterized by the stretch ϵ. Also, the *core* and *wings* have the same length ($L^{core} = L^{wing} = L$). According to eq. 7.12, the elastic energy of the *twister* is:

$$\mathcal{E}^{twister}_{straight}(\epsilon) = \mathcal{E}^{core}_{straight}(\epsilon) + 4 * \mathcal{E}^{wing}_{straight}(\epsilon) = \frac{Ea^2L}{2}\left[(\epsilon - \epsilon_1^*)^2 + (\epsilon - \epsilon_2^*)^2\right]. \tag{7.13}$$

At equilibrium, the elastic energy of the *twister* is minimum. In the straight configuration, we have:

$$\frac{\mathrm{d}\mathcal{E}^{twister}_{straight}(\epsilon)}{\mathrm{d}\epsilon} = 0 \implies 4\epsilon - 2(\epsilon_1^* + \epsilon_2^*) = 0. \tag{7.14}$$

The equilibrium stretch is thus simply the average of the two *eigenstrains*:

$$\epsilon_{eq} = \frac{\epsilon_1^* + \epsilon_2^*}{2} = \frac{\alpha_{T1} + \alpha_{T2}}{2}\Delta T. \tag{7.15}$$

Knowing the equilibrium stretch (ϵ_{eq}), we can deduce the elastic strain in the *core* and *wings* using eq. 3.16:

$$\epsilon^{el}_{core} = \epsilon_{eq} - \epsilon_1^* = \frac{\Delta\epsilon^*}{2}, \qquad \epsilon^{el}_{wing} = \epsilon_{eq} - \epsilon_2^* = -\frac{\Delta\epsilon^*}{2}, \tag{7.16}$$

which shows that in the straight configuration the *core* is stretched and the *wings* are compressed ($\Delta\epsilon^* > 0$ for $\alpha_{T1} > \alpha_{T2}$). In the straight configuration, the elastic energy of a *twister* is then simply a quadratic function of the differential *eigenstrain*:

$$\mathcal{E}^{twister}_{straight} = \frac{Ea^2L}{4}(\Delta\epsilon^*)^2. \tag{7.17}$$

Elastic energy in the twisted configuration In the twisted configuration, the elastic energy of a *twister* is parametrized by the stretch (ϵ) and the material torsion of its *core* (τ). However, as its expression is more complicated than in the straight configuration, we look at the elastic energy of the *core* and of the *wings* in two separate steps.

In the twisted configuration, the *core* is twisted as given by eq. 7.10. According to eq. 7.12, its elastic energy is given by:

$$\mathcal{E}^{core}_{twisted}(\tau, \epsilon) = \frac{Ea^2L}{2}(\epsilon - \epsilon_1^*)^2 + \frac{\mu a^4 L}{14}\tau^2, \tag{7.18}$$

where $L = L^{core}$ is the length of the *core*.

In the twisted configuration, the *wings* are stretched as given by eq. 7.6, and bended and twisted as given by eq. 7.9. Also, their final length is related to the length of the *core* through eq. 7.5. According to eq. 7.12, the elastic energy of one *wing* is given by:

$$\begin{aligned}\mathcal{E}^{wing}_{twisted}(\tau, \epsilon) = {} & \frac{Ea^2L}{8}(\epsilon - \epsilon_2^*)^2\sqrt{1 + r^2\tau^2}\left(1 + \frac{0.5 + \epsilon}{\epsilon - \epsilon_2^*}r^2\tau^2\right)^2 \\ & + \frac{Ea^4L}{384}\sqrt{1 + r^2\tau^2}\left(\frac{r\tau^2}{1 + r^2\tau^2}\right)^2 + \frac{\mu a^4 L}{224}\sqrt{1 + r^2\tau^2}\left(\frac{\tau}{1 + r^2\tau^2}\right)^2.\end{aligned} \tag{7.19}$$

Simplifying and combining eq. 7.18 and eq. 7.19, we obtain the elastic energy of the *twister* in the twisted configuration in term of the stretch (ϵ) and the torsion of its *core* (τ):

$$\begin{aligned}\mathcal{E}^{twister}_{twisted}(\tau,\epsilon) &= \mathcal{E}^{core}(\tau,\epsilon) + 4 * \mathcal{E}^{wing}(\tau,\epsilon),\\ &= \frac{Ea^2L}{2}\left[(\epsilon-\epsilon_1^*)^2 + (\epsilon-\epsilon_2^*)^2\sqrt{1+r^2\tau^2}\left(1+\frac{0.5+\epsilon}{\epsilon-\epsilon_2^*}r^2\tau^2\right)^2\right]\\ &+ \frac{Ea^4L}{96}\left[\frac{r^2\tau^4}{(1+r^2\tau^2)^{3/2}}\right] + \frac{\mu a^4 L}{14}\left[\tau^2\left(1+\frac{1}{4(1+r^2\tau^2)^{3/2}}\right)\right].\end{aligned} \tag{7.20}$$

For $\tau = 0$ the elastic energy of the *twister* in the twisted configuration is equal to the elastic energy of the *twister* in the straight configuration ($\mathcal{E}^{twister}_{twisted}(\tau=0,\epsilon) = \mathcal{E}^{twister}_{twisted}(\epsilon)$ according to eq. 7.17). This means that we can use eq. 7.20 to describe the elastic energy of the *twister* in both the straight ($\tau = 0$) and in the twisted configuration ($\tau \neq 0$). In this equation, the prefactors appear as the product of the effective stretching, bending and twisting inertias of the *twister* (Ea^2, $Ea^4/48$ and $\mu a^4/7$) with the half-length of the *core* ($L/2$), while the parts in brackets represent the corresponding stretching, bending [40] and twisting contributions of the *core* and the *wings* to the elastic energy of the *twister*.

Solving for the cancellation of the derivatives of the elastic energy of the *twister* with respect to the stretch (ϵ) and the torsion (τ) of its *core* is difficult as it requires finding the roots of a 9-order fractional polynomial. Instead, let us look at the scaled elastic energy of a *twister* ($\hat{\mathcal{E}}^{twister} = 2\,\mathcal{E}^{twister}/(Ea^2L)$) as a function of the stretching (ϵ) and of the torsion (τ) of its *core* for different values of the *eigenstrains* (ϵ_1^* and ϵ_2^*) in more details:

$$\begin{aligned}\hat{\mathcal{E}}^{twister}(\tau,\epsilon) &= \frac{2\,\mathcal{E}^{twister}(\tau,\epsilon)}{Ea^2L}\\ &= \left[(\epsilon-\epsilon_1^*)^2 + (\epsilon-\epsilon_2^*)^2\sqrt{1+r^2\tau^2}\left(1+\frac{0.5+\epsilon}{\epsilon-\epsilon_2^*}r^2\tau^2\right)^2\right]\\ &+ \frac{a^2}{48}\left[\frac{r^2\tau^4}{(1+r^2\tau^2)^{3/2}}\right] + \frac{\mu a^2}{7E}\left[\tau^2\left(1+\frac{1}{4(1+r^2\tau^2)^{3/2}}\right)\right].\end{aligned} \tag{7.21}$$

In accordance with the finite-element simulations, the side-length of the squared cross-section of the *core* is $a = 0.5$, which implies that the radius of the cylinder onto which the helix is drawn is fixed ($r^2 = 0.25 * 5/8 = 0.39$) where $a^2 = 0.25$. Also, we have $\alpha_{T1} = 0°\mathrm{C}^{-1}$ and $\alpha_{T2} = 1°\mathrm{C}^{-1}$, so that the *eigenstrain* in the *passive* region is zero ($\epsilon_1^* = 0$) and the *eigenstrain* in the *active* region equal to differential *eigenstrain* ($\epsilon_2^* = \Delta\epsilon^*$) and to the differential temperature ($\epsilon_2^* = \Delta T$). As we consider elongated objects, we neglect shape changes within the plane of the cross-section ($\nu = 0$) and so the contrast between the shear modulus and the Young modulus of the material is given by: $\mu/E = 1/2(1+\nu) = 1/2$. The scaled elastic energy of the *twister* is then only a function the differential temperature (ΔT):

$$\begin{aligned}\hat{\mathcal{E}}^{twister}(\tau,\epsilon) &= \left[\epsilon^2 + (\epsilon-\Delta T)^2\sqrt{1+0.39\tau^2}\left(1+\frac{0.5+\epsilon}{\epsilon-\Delta T}0.39\tau^2\right)^2\right]\\ &+ \frac{0.25}{48}\left[\frac{0.39\tau^4}{(1+0.39\tau^2)^{3/2}}\right] + \frac{0.25}{14}\left[\tau^2\left(1+\frac{1}{4(1+0.39\tau^2)^{3/2}}\right)\right].\end{aligned} \tag{7.22}$$

40. The bending contribution is entirely due to the *wings* as the *core* remains straight in the twisted configuration.

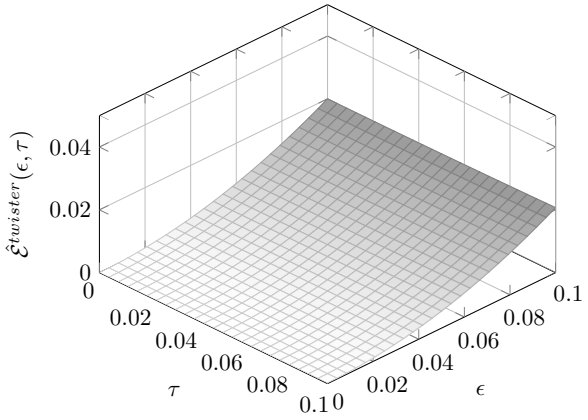

(a) $\Delta T = 0°\text{C}$.

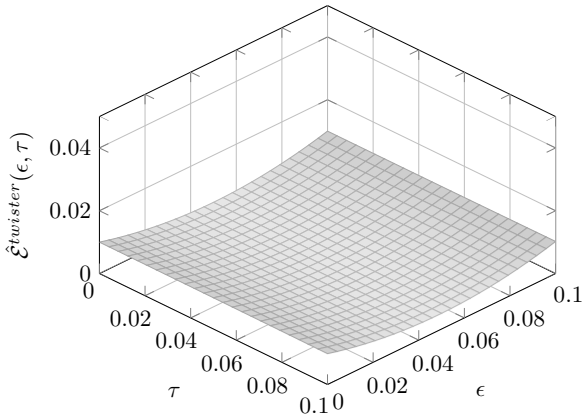

(b) $\Delta T = 0.1°\text{C}$.

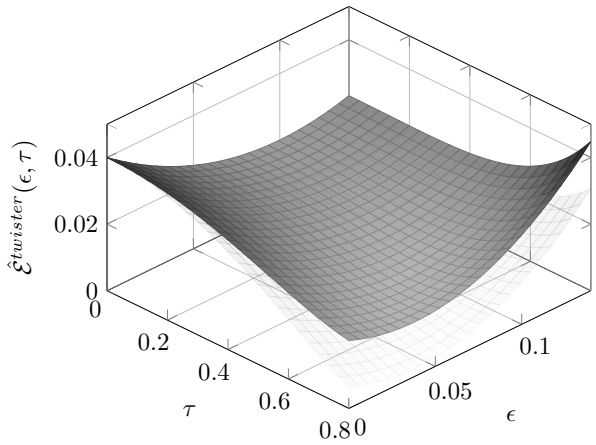

(c) $\Delta T = 0.2°\text{C}$.

Figure 7.12 – Elastic energy of a *twister* as a function of the stretching (ϵ) and of the torsion (τ) of its *core* for different values of the differential temperature: (a) $\Delta T = 0°\text{C}$, (b) $\Delta T = 0.1°\text{C}$ and (c) $\Delta T = 0.2°\text{C}$ (opaque surface with the same gray-scale for the three differential temperatures). The transparent surface represents the stretching contribution. For $\Delta T = 0°\text{C}$ and $\Delta T = 0.1°\text{C}$, the bending and twisting contributions are negligible. For $\Delta T = 0.2°\text{C}$, the bending contribution is still negligible (half-transparent surface indistinguishable from the total elastic energy), but the twisting contribution becomes more and more relevant as the twist (τ) increases.

In fig. 7.12, we plot the scaled elastic energy (eq. 7.22) as a function of the stretching (ϵ) and of the torsion (τ) of its *core* for different values of the differential differential temperature ($\Delta T = 0$, 0.1, 0.2 °C) [41]. We make the following observations:

1. For the trivial case $\Delta T = 0$°C, the scaled energy of the *twister* is monotonically increasing in ϵ and τ and its minimum is reached at the origin $\epsilon_{eq} = \tau_{eq} = 0$ (fig. 7.12a).
2. For the case $\Delta T = 0.1$°C, the scaled energy of the *twister* is monotonically increasing in τ and is concave upward in ϵ. Its minimum is reached at $\tau_{eq} = 0$ and $\epsilon_{eq} = 0.5 = \Delta T/2$ (fig. 7.12b).
3. For the case $\Delta T = 0.2$°C, the scaled energy of the *twister* possesses a complex double-curved shape and its minimum appears to be reached around $\epsilon_{eq} \approx 0.05 \neq \Delta T/2$ and $\tau_{eq} \approx 0.6$ (fig. 7.12c).

As the differential temperature increases, the energetic landscape changes and its minimum switches from stretching with zero torsion ($\epsilon_{eq} \neq 0$ and $\tau_{eq} = 0$) to a combination of stretching with some torsion ($\epsilon_c \neq 0$ and $\tau_{eq} \neq 0$) for $0.1°C < \Delta T < 0.2°C$. Using Mathematica®, we can compute this minimum for a given differential temperature. According to fig. 7.13, the critical differential temperature is equal to $\Delta T_c \approx 0.10$°C.

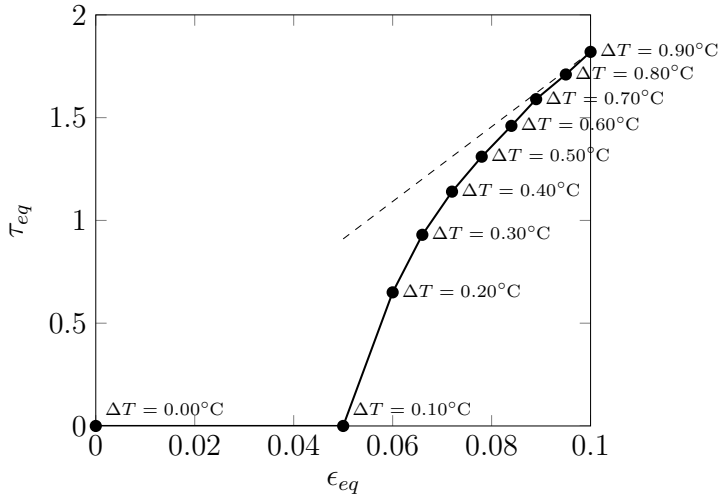

Figure 7.13 – Equilibrium stretching and torsion of the *core* (ϵ_{eq} and τ_{eq}) that minimize the elastic energy of the *twister* at different differential temperature (ΔT). The dotted line is the tangent to the curve at ($T = 0.1$°C), which gives the trend of the torsion-stretching curve.

7.1.3.3 Comparison between numerical and theoretical model

Contrary to what we observed in the finite-element simulation (subsubsection 7.1.2.2), the stretch of the *core* is not constant as its torsion increases. Also, the theoretical critical differential temperature is much smaller than the numerical differential temperature ($\Delta T_c^{numeric} \approx 7\Delta T_c^{theory}$). A potential reason for this discrepancy, is that the straight configuration is an unstable equilibrium for the *twister*, which jumps into the twisted configuration after the critical differential temperature is reached. Indeed, making the finite-element calculation converge is rather difficult, which would corroborate the instability argument (section 4.3). However, even for high differential temperatures, the theoretical model does not converge to a constant stretch

41. The differential temperature are rather small, because we choose an thermal expansion coefficients of $\alpha_{T1} = 1°C^{-1}$ for the *active* region. In fact, only the *eigenstrain* is meaningful $\epsilon_1^* = \alpha_{T1}\Delta T \approx 0.1$, which is reasonably large.

corresponding to a vertical asymptote in fig. 7.13, but rather tends to a diagonal asymptote (dashed line in fig. 7.13).

7.1.4 Experimental illustrations of *twisters*

Here, we present simple table-top experiments which illustrate the twisting of *twisters*. First, we present a simple numerical experiment based on the mass-spring model presented in section 4.1 that illustrates twisting and relate it to the behavior of *twisters* (subsubsection 7.1.4.1). Then, we use differential swelling as presented in chapter 5 to illustrate twisting experimentally (subsubsection 6.1.3.4). These illustrations help our intuition regarding the understanding of the twisting of *twisters*.

7.1.4.1 Mass-spring system undergoing twisting

Using our mass-spring model presented in section 4.1 to represent a rod-like elongated object, twisting is obtained by activating [42] one of the families [43] of the diagonal [44] springs spanning the sides of the extruded square lattice structure (compressed springs (red) in the initial state fig. 7.14a). Upon relaxation, the straight lattice morphs into a twisted configuration, where the stress state redistributes across the structure (tensed (blue) and compressed (red) springs in fig. 7.14b). Indeed, the longitudinal springs account for extensions or contractions normal to the plane of the cross-section while the diagonal springs are related to longitudinal shears, which correspond to twisting (subsubsection 3.1.2.3).

(a) (b)

Figure 7.14 – Twisting corresponds to a different *rest length* of the diagonal springs spanning the sides of the extruded square lattice structure that represents a *twister*. (Left) Initial straight state with one set of diagonals activated. (Right) Final twisted state where the stress state redistributes across the springs. (Red) compression. (Blue) tension.

In the deformed configuration, both the diagonal and the longitudinal springs wind around the center line of the lattice in a helical way (fig. 7.14b). In fact, any straight line in the initial configuration, becomes helical upon twisting (fig. A.2). In this sense, our mass-spring model helps us to understand the *morphing* of *twisters*.

7.1.4.2 Proof of principle of twisting using swelling

Using multi-material 3D printing as presented in (section 5.3), we can inquire *twisters* experimentally. In fig. 7.15, we observe the *morphing* of a 3D printed multi-material *twister* triggered by differential swelling. Here the *active* and *passive* regions are reversed and the *core* is softer

42. We use the word activate to describe the process of applying nonzero *eigenstrain* to some regions of an object. In our mass-spring model, *eigenstrain* corresponds to the rest length of the springs.

43. Depending on the choice of the diagonal spring family which we activate, twisted configurations with opposite chiralities are obtained (left-handed or right-handed).

44. We call diagonal the diagonal springs between the longitudinal and the transversal direction. See footnote subsubsection 4.1.2.1.

than the *wings*[45]. Interestingly, this leads to an interesting *morphing* pattern, where the expanding *core* seems to follow a helical configuration while the *wings* simply follow its geometry[46].

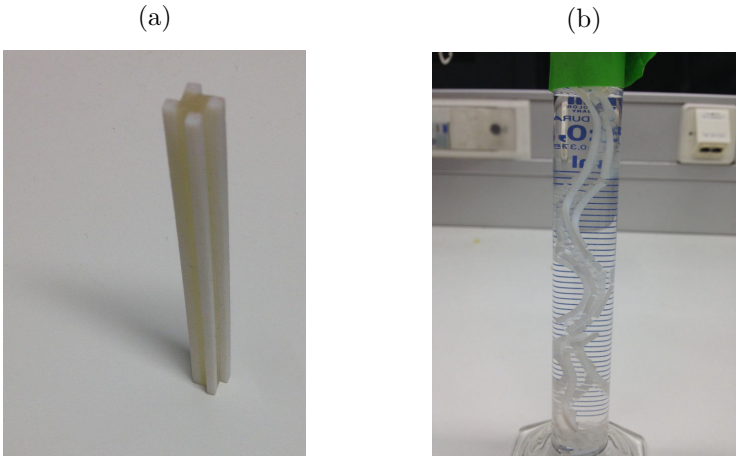

Figure 7.15 – Biphasic soft-stiff structure in its dry state (a) displaying a curling behavior (b) when plunged into an acetone bath due to differential swelling between the soft core and the stiff wings.

7.2 Generating arbitrary configurations of spatial rods

The fundamental modes of deformation of a rod-like object are stretching, bending and twisting (subsection 3.1.2). Generating stretching inside a *morpher* is trivial[47], bending was discussed in chapter 6 and twisting in section 7.1. Similarly to subsection 6.2.1, the twisting rate can be varied along the length of a *morpher* by relaxing the assumption of translational invariance (see appendix E.2). Subsection 7.2.1 shows how coiling is obtained by adding the *eigenstrains* architectures that lead to bending and twisting. This enables to generate an arbitrary configuration of a rod-like object starting with the desired material curvatures (subsection 7.2.2).

7.2.1 Coiling is a combination of bending and twisting

Using the mass-spring model presented in section 4.1, bending and twisting can be combined by activating the according spring families. Bending corresponds to a differential activation of the longitudinal springs, while twisting is produced by a differential activation of the diagonal springs. This leads to a helical configuration, coiling (fig. 7.16).

Coiling can also be demonstrated using fem as presented in section 4.3. Figure 7.17a, fig. 7.17b and fig. 7.17c shows the elastic strain distributions associated with the three-fundamental *morphing* modes of rods (extension, bending and twisting):

— Extension is produced by a uniform stretching strain over the cross-section (see fig. 7.17a);

— Bending is produced by a transversal gradient in stretching strain over the cross-section (see fig. 7.17b);

45. This inversion is explained by the fact that we first wanted to use hydrostatic pressure to impose differential *eigenstrain* inside the *twister*, so the *core* needed to be softer than the *wings* in order to shrink less. It would be interesting to try out a real *twister*.

46. This particular geometry could be due to the confinement of the tube.

47. To generate stretching, it suffices to build a rod out of a uniformly expanding material.

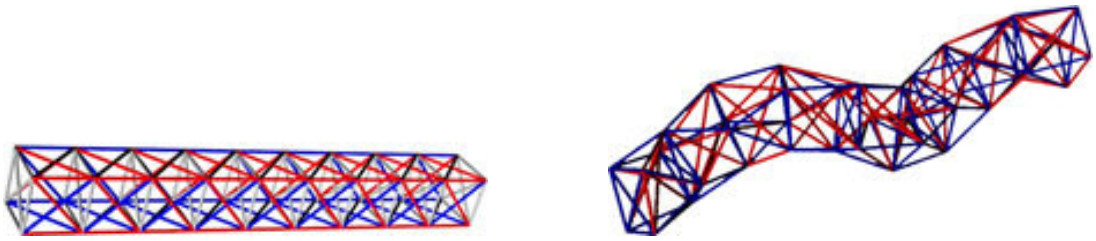

(a) (b)

Figure 7.16 – Initial (left) and final (right) configuration of a straight rod-like object. A differential activation of the longitudinal springs leads to bending, while a differential activation of the diagonal springs produces twisting. When combined, coiling is obtained.

— Twisting is produced by a radial gradient in shearing strain over the cross-section (see fig. 7.17c);

Subsection 7.2.1 shows how an arbitrary combination of these three fundamental *morphing* modes of rods produces a locally helical configuration[48]. Using the concept of impotent *eigenstrain*, these elastic strain distributions can be imposed as *eigenstrain*, which will lead to the same final configuration. The only difficulty consists in imposing a shear strain distribution through an *eigenstrain*, which is why we designed *twisters* in section 7.1.

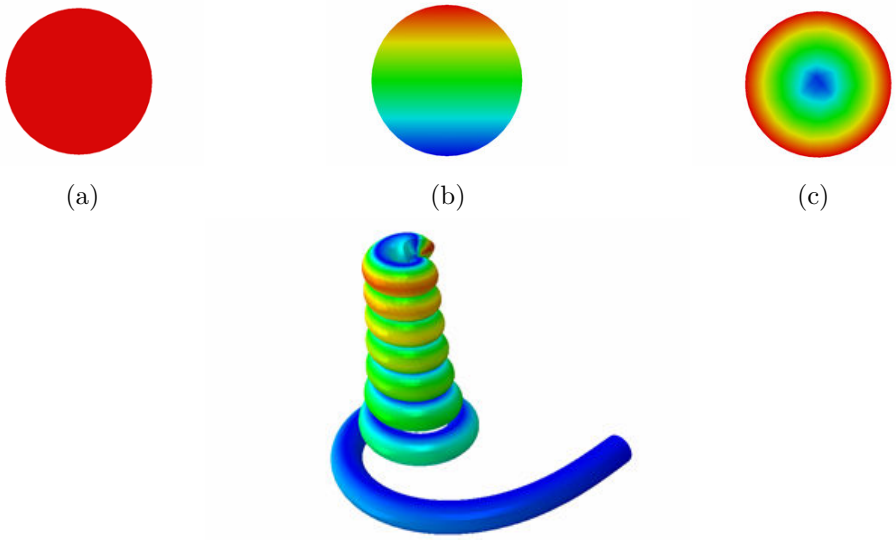

(a) (b) (c)

(d)

Figure 7.17 – (Top) Strain distributions corresponding to the fundamental *morphing* modes of a rod-like object: extension (left), bending (middle) and twisting (right). (Bottom) An arbitrary combination of these modes produces a locally helical configuration.

7.2.2 The inverse problem

Take an arbitrary configuration of a rod, what is the *eigenstrain* distribution one has to apply to a straight rod in order to obtain this configuration? This question can now be answered using what we learned in chapter 6 and in the current chapter. An arbitrary configuration of a rod is characterized by its material curvatures $\kappa^{(i)}(s)$ along the rod (fig. 7.18). Locally,

48. We don't give the specific values of the strain fields as we only want to make a qualitative statement here.

the two material curvatures κ^1 and κ^2 of a rod can be obtained by tuning the transversal gradients of longitudinal strain in the two material directions $\boldsymbol{d}_1$ and $\boldsymbol{d}_2$. The third material curvature (or rather material torsion) κ^3 can be obtained by tuning the radial shear gradient. Alternatively, using the *twister* design, material torsion can be obtained using differentially longitudinally expanding *wings* around a *core*[49]. In the case where shear is used to produce twisting, the gradients of longitudinal strain can simply be added to the radial gradient of shear as discussed in subsection 7.2.1. In the case where *twisters* are used to produce twisting, one could introduce local twisting hinges between bending domain similarly to what we discussed in subsection 6.2.2[50].

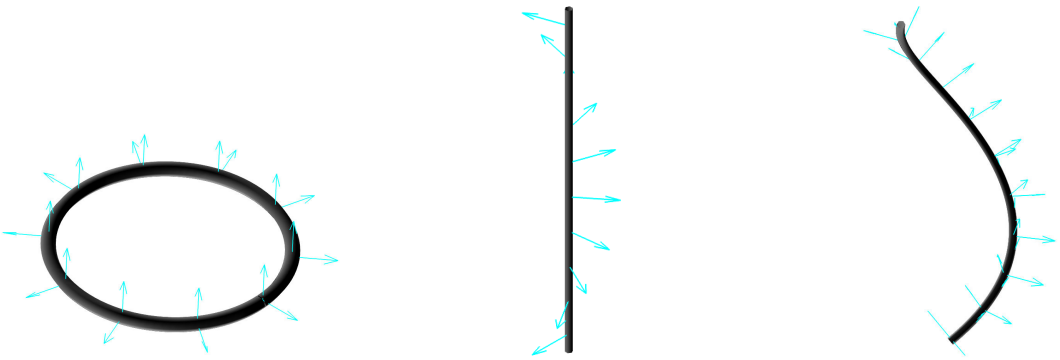

(a) (b) (c)

Figure 7.18 – An arbitrary configuration of a rod is locally characterized by its material curvatures κ^i. (left) single bending ($\kappa^1 \neq 0$), (middle) torsion ($\kappa^3 \neq 0$), (right) coiling ($\kappa^1 \neq 0 \wedge \kappa^3 \neq 0$).

49. As we discussed in subsubsection 7.1.2.2, the twisting of a *twister* is preceded by a stretching regime. Instead of having *active* (expanding) *wings* around a passive (not expanding) *core*, making a *twister* with a *core* that contracts at the same rate as the *wings* are extending could potentially lower the critical transition point at which twisting occurs.

50. Another option would be to make a *twister* with a bending *core*.

Conclusions

This chapter explored the design space of extrudable biphasic *morphers* and found a specific design, which exhibits a stretching-twisting instability according to finite-element simulations. We described its behavior using an energetical approach and found that the twisted configuration becomes favorable for a sufficient differential *eigenstrain*. Using a mass-spring model and a simple experiment, we can understand why the *twisters* twist qualitatively. Similarly to the *benders* described in chapter 6, these *twisters* can be graded along their longitudinal direction in order to exhibit tunable twisting. The combination of *benders* and *twisters* enables to generate arbitrary configurations of a rod in space, and as such appear as fundamental units for the *morphing* of one-dimensional objects.

References

Abraham, Yael et al. (2012). « Tilted cellulose arrangement as a novel mechanism for hygroscopic coiling in the stork's bill awn ». In: *Journal of The Royal Society Interface* 9.69, pp. 640–647.

Armon, Shahaf et al. (2011). « Geometry and mechanics in the opening of chiral seed pods ». In: *Science* 333.6050, pp. 1726–1730.

Bruno, Andrea et al. (2010). *Featuring Steel*.

Curie, Pierre (1894). « Sur la symétrie dans les phénomènes physiques, symétrie d'un champ électrique et d'un champ magnétique ». In: *J. Phys. Theor. Appl.* 3.1, pp. 393–415.

Ismael, Jenann (1997). « Curie's principle ». In: *Synthese* 110.2, pp. 167–190.

Turcaud, Sébastien et al. (2011). « An excursion into the design space of biomimetic architectured biphasic actuators ». In: *International Journal of Materials Research* 102.6, pp. 607–612.

Chapter 8

Diffusion-driven *morphing* in 2D

Contents

Chapter 6 and chapter 7 proposed specific design of *morphers*, *benders* and *twisters*, which demonstrate the fundamental deformation modes of elongated rod-like objects (bending and twisting respectively). This chapter considers objects where only one dimension is smaller than the other two ($t \ll L$, W)—sheets [1]. Another difference with the previous chapters, is that here the *eigenstrain* is applied progressively [2] instead of instantaneously as motivated by experiments [3]. This demonstrates path-dependent *morphing* patterns in the case of two-dimensional objects [4] in the sense that, even if the final activation state is equal as the one reached instantaneously, the resulting *morphing* pattern is different depending on the history of activation.

Section 8.1 discusses the *morphing* pattern of rectangular bilayers, where the *active* layer is progressively activated from the sides of the bilayer. As opposed to the short-side rolling of instantaneously activated bilayers (chapter 6), this progressive activation leads to long-side rolling as shown by experiments (subsection 8.1.1). Subsection 8.1.2 models this *morphing* pattern theoretically using energetical considerations and finite-element simulations. We show that, even if instantaneous activation of rectangular bilayers leads to short-side rolling as recently proven in the literature (Alben, Balakrisnan, and Smela 2011) [5], progressive activation leads to

1. In structural engineering, the distinction between flat (plates) and curved (shells) two-dimensional objects is often made. We consider flat objects in their initial configuration, which become curved in their final configuration and refer to them as sheets.

2. By progressive, we mean that the value of the *eigenstrain* at a given location inside the body is a function of some time ($\boldsymbol{\epsilon}^* = \boldsymbol{\epsilon}^*(\boldsymbol{x}, t)$), whereas an instantaneous *eigenstrain* (as considered in chapter 6 and chapter 7) only depends on location ($\boldsymbol{\epsilon}^* = \boldsymbol{\epsilon}^*(\boldsymbol{x})$).

3. The experiments where performed by Leonid Ionov's team at the IPFDD and we contributed to the theoretical modeling and understanding of the experimental results.

4. In the case of one-dimensional objects, bending and twisting are path-independent as the corresponding strain states can simply be added (subsection 7.2.1). In the presence of non-conservative forces, some *morphing* patterns of rods still display path-dependency (such as knots for example).

5. In appendix D.1, the analysis of the bending of bilayers was performed by neglecting the transversal direction and by setting ($w = 1$). If what happens in the transversal direction is not neglected, the reason why the bilayer rolls along the long direction is not trivial as discussed in subsubsection 8.1.2.1.

long-side rolling as published in (Stoychev, Zakharchenko, et al. 2012) (see appendix F.1).

Section 8.2 discusses the multi-step *morphing* pattern of star-shaped bilayers as published in (Stoychev, Turcaud, et al. 2013) (see appendix F.2). Due to the progressive activation from the sides of the bilayer, the *morphing* process goes through two different intermediate configurations (subsection 8.2.1): a combination of bending and wrinkling, which we call tubular-wrinkling (subsubsection 8.2.2.1) followed by a folding step (subsubsection 8.2.2.2). For specific geometrical parameters, the flat star-shaped pyramids remarkably morph into perfect three-dimensional pyramids (see appendix F.3). Subsection 8.2.2 describes the *morphing* process theoretically using the knowledge of patterns of shape change (chapter 2) and backed up with energetical considerations and finite-element calculations.

8.1 Long-side rolling of rectangular bilayers

This section discusses the long-side rolling of rectangular bilayers which were partially published in (Stoychev, Zakharchenko, et al. 2012) (see appendix F.1). Subsection 8.1.1 presents the experimental results of thermo-responsive rectangular bilayers, which show that long-side rolling is preferred for a sufficient aspect ratio of the bilayers. Subsection 8.1.2 discusses the short- and long-side rolling scenarios in energetical terms for instantaneous (subsubsection 8.1.2.1) and progressive activation (subsubsection 8.1.2.2).

8.1.1 Experimental observations

This subsection recalls the experimental preparations (subsubsection 8.1.1.1) and summarizes the experimental results published in (Stoychev, Zakharchenko, et al. 2012) [6].

8.1.1.1 Experimental preparation

Rectangular bilayers where prepared according to the method presented in subsection 5.3.3. Two sets of experiments were made, each consisting of many rectangular bilayers with different lengths (L = 100, 200, 500 and 1000 µm) and different aspect ratios (L/W = 1, 2, 4 and 5), where the only difference between the two sets is the thickness of the *passive* layer ($t_p^1 = 500\,\text{nm}$ and $t_p^2 = 1200\,\text{nm}$) for the same thickness of the *active* layer ($t_a^1 = t_a^2 = 1200\,\text{nm}$) (see fig. 8.1).

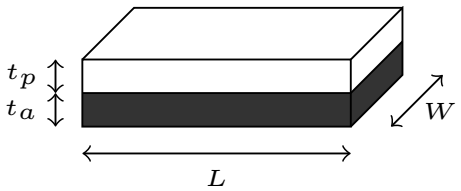

Figure 8.1 – Geometrical parameters of rectangular bilayers: length (L), width (W) and thickness of the *active* (t_a) and *passive* layer (t_p).

8.1.1.2 Experimental results

The bilayer is undeformed while exposed to a phosphate buffered saline (PBS) solution (0.1M and $pH = 7.4$) at $T > 70\,°\text{C}$ and when the temperature drops below $T < 70\,°\text{C}$, the *active*

6. The interested reader is strongly advised to look into (Stoychev, Zakharchenko, et al. 2012) given in appendix F.1 for a complete presentation of the experimental results.

layer starts to swell and the bilayers *morph* into tubes. Using optical microscopy, the *morphing* pattern and the rolling radius as well as the activation mechanism is determined for the different rectangular bilayers.

Activation mechanism In order to assess the activation mechanism of the rectangular bilayers, one can look at a bilayer possessing a relatively thin *active* layer ($t_a = 35\,\text{nm}$) and a sufficiently thick *passive* layer ($t_p = 400\,\text{nm}$), such that bending is prevented. This enables to investigate the evolution of swelling using a optical microscope. Indeed, the swollen regions have a longer optical path length (OPL) than the unswollen ones (the OPL varies as a function of the film thickness and refractive index, which in turn depends on the swelling degree). This reveals that swelling starts from the edges of the active layer (see figure 6 of appendix F.1).

Morphing patterns and rolling radius In accordance with Timoshenko's formula (eq. 6.1), the rolling curvature [7] of the bilayers was confirmed to be independent of the size the bilayer (L, W) and constant for each set (see table 8.1). Indeed, as discussed in subsection 6.1.1, the curvature of a bilayer is only a function of the thickness and stiffness contrast for a given differential *eigenstrain*. The fact that the rolling radius is smaller (or equivalently that the curvature is larger) for the first experimental set makes intuitive sense as the thickness of the *passive* resisting layer is smaller for the same thickness of the *active* layer [8]. This is also confirmed by our study of the influence of the thickness contrast on the curvature of a bilayer for equal stiffness (subsubsection 6.1.1.1) [9].

Experimental set	Thickness of the *passive* layer t_p [nm]	Rolling radius r [µm]	Curvature κ [1/µm]
1	500	20	0.05
2	1200	80	0.0125

Table 8.1 – According to optical microscopy, the rolling radius (r) or equivalently the curvature (κ) upon *morphing* of the rectangular bilayers is approximately constant for each set of experiment.

Interestingly, contrary to the *benders* described in chapter 6, sufficiently elongated rectangular bilayers display long-side (transversal) rolling instead of short-side (longitudinal) rolling (see figure 2, 3, 4 and 5 of appendix F.1).

8.1.2 Theoretical considerations

This subsection aims at understanding the observed experimental results from subsubsection 8.1.1.2 theoretically, namely that rectangular bilayers display long-side (transversal) rolling. Subsubsection 8.1.2.1 starts by recalling the reason why instantaneously activated rectangular bilayers display short-side rolling (Alben, Balakrisnan, and Smela 2011). This step is necessary, as it will reveal the conceptual arguments, which we use afterwards. Subsubsection 8.1.2.2 considers the case of progressive activation and shows that long-side rolling is always preferred as long as the *active* layer is not entirely activated [10] using simple energetic arguments.

7. The curvature is the inverse of the radius $r\kappa = 1$.

8. In a subsequent work, one could assess the mechanical and swelling characterization of the experimental system to verify Timoshenko's formula quantitatively.

9. We don't know the exact values of the stiffness contrast for our experimental system. Nevertheless, the trend is is the same for unequal stiffnesses.

10. Actually, short-side rolling becomes preferable slightly before the *active* layer is fully activated.

8.1.2.1 Instantaneous activation

The fact that rectangular bilayers display short-side rolling is less trivial than it may seem. As the *active* layer expands isotropically, curvature can a priori be generated along any direction. Generation of curvature along more than one direction is unfavored [11] as a double curved bilayer would imply a significant stretching energy [12] due to Gauss *theorema egregium* [13]. The bilayer thus assumes a single-curved configuration (longitudinal, transversal or diagonal). As the curvature is solely dictated by the thickness and stiffness contrasts for a given differential *eigenstrain* (eq. 6.1), the energy is the same in any rolling direction [14]. Based on symmetry arguments, we don't consider the diagonal scenario, but only the longitudinal- and transversal-scenarios.

The detailed demonstration why short-side rolling is preferred can be found in (Alben, Balakrisnan, and Smela 2011). There, the authors minimize the energy of a bilayer, which they express in the framework of the Föppl-von-Karman theory of sheets [15]. This results in energy density maps of the two scenarios, which show that short-side rolling has a lower energy than long-side rolling. The reason for this energy difference is due to an edge-effect, which lowers the elastic energy by different amounts depending on the rolling direction. Indeed, as observed by the authors:

> "The bilayer does not bend into a perfect tube, but has narrow regions of double-curvature at the curved edges that lower the energy density at those locations. The total length of curled edge is greater for bending in the long direction, so during the transition from a spherical to a singly curved shape, it is more favorable for the rectangle to adopt the spiral geometry." [16]
>
> (Alben, Balakrisnan, and Smela 2011)

This means that the bilayer is single curved in its bulk, but double curved along its edges. If we denote by (b) the depth of this boundary layer [17](fig. 8.2), then the energy in the short- and long-side rolling scenarios is given by:

$$\begin{aligned} \mathcal{E}_{short} &= (W - 2\,b)\,L\,\mathcal{E}_{single} + 2\,b\,L\,\mathcal{E}_{double}, \\ \mathcal{E}_{long} &= (L - 2\,b)\,W\,\mathcal{E}_{single} + 2\,b\,W\,\mathcal{E}_{double}, \end{aligned} \tag{8.1}$$

where the energy along the free edge is smaller [18] than the energy in the bulk ($\mathcal{E}_{double} \ll \mathcal{E}_{single}$). The difference between these two energies is given by:

$$\mathcal{E}_{short} - \mathcal{E}_{long} = -2\,b\,(L - W)(\mathcal{E}_{single} + \mathcal{E}_{double}) < 0. \tag{8.2}$$

11. In fact, for a relatively small *eigenstrain* compared to the total thickness of the bilayer, a double-curved (spherical) configuration is obtained, but becomes unstable as the *eigenstrain* increases further.

12. The stretching energy of a plate scales linearly with its thickness, while the bending energy scales to the power three of its thickness ($\mathcal{E}_{el} = t\,\hat{\mathcal{E}}_{stretch} + t^3\,\hat{\mathcal{E}}_{bend}$), so when the thickness is sufficiently small ($t \ll 1$), bending transformations are favored in front of stretching transformations.

13. Gauss *theorema egregium* implies the conservation of the Gaussian curvature ($K = \kappa_1 * \kappa_2$, where κ_1 and κ_2 are the two principal curvatures of the surface) under local isometries (isometries are distance preserving transformation). As the initial configuration of the bilayer is flat, its initial Gaussian curvature is zero ($\kappa_1 * \kappa_2 = 0$) and so any double-curved configuration would imply stretching of the surface. This is illustrated by the fact that it is impossible to draw a flat map of the earth without introducing distortions.

14. The energy density is given by the curvature in the rolling direction and the frustrated stretching in the orthogonal direction. When multiplied by the area of the bilayer, this leads to the same elastic energy independently of the rolling direction.

15. This theoretical framework is the two-dimensional counterpart of the one-dimensional rod theory presented in section 3.1

16. Here, "long direction" and "spiral" are synonymous to our notion of short-side rolling.

17. The depth of this boundary layer is estimated to scale as $\sqrt{t}$ where t is the thickness of the bilayer (Efrati, Sharon, and Kupferman 2009).

18. The fact that the double curved edge has less energy than the single curved bulk seems to be contradicting the argument we gave previously for dismissing double-curved configurations of the bilayer. It would be interesting to look into this in more details.

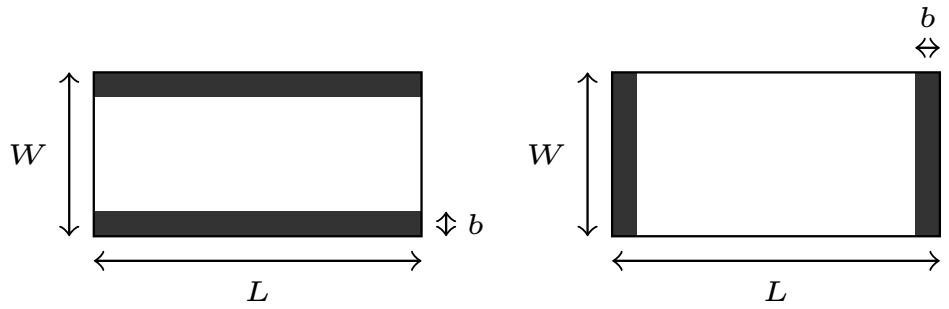

Figure 8.2 – Double-curved boundary layer along the edge of the single curved bilayer. For clarity, we show the regions in the flat configuration. (left) short-side rolling, (right) long-side rolling, (black) double-curved region, (white) single curved region.

This shows that the energy in the short-side rolling scenario is smaller than the energy in the long-side rolling scenario because $L > W$ for rectangular bilayers. This explains why instantaneous activation of rectangular bilayers results in short-side rolling.

8.1.2.2 Progressive activation

Diffusion of *eigenstrain* In the first moments after the beginning of activation, only the edges of the *active* layer are activated as observed experimentally (subsubsection 8.1.1.2). The reason for this is purely geometrical, the *active* layer being confined between the substrate below and the *passive* layer above. The activation front then slowly diffuses through the active layer following a diffusion law as described in (subsection 3.2.3). This diffusion process is modeled using fem as shown in figure 6a of appendix F.1. In general, the activation profile depends on the shape, boundary conditions and diffusive properties of the active layer (fig. 8.3). This introduces a history in the activation of the bilayer, which biases the configuration of the bilayer.

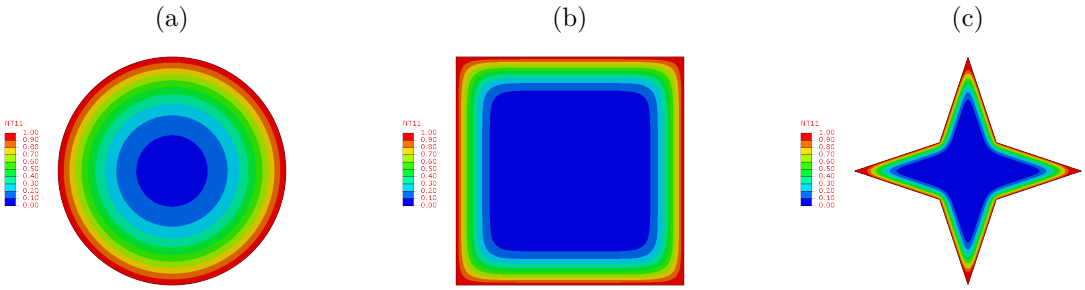

Figure 8.3 – The activation profile depends on the shape, boundary conditions and diffusive properties of the active layer. (red) maximum normalized temperature ($T = 1\,°\mathrm{C}$), (blue) minimum temperature ($T = 0\,°\mathrm{C}$).

Separation of timescales The characteristic timescale of the diffusion of the activation front inside the *active* layer is much larger ($\tau_d \sim$ s) than the characteristic timescale of *morphing* ($\tau_m \sim$ ms) [19]. This is convenient as it enable to decouple the two phenomena and to consider *morphing* to be quasi-static.

Quasi-static *morphing* Due to the separation of time scales, the modeling of the *morphing* process can be done in two subsequent steps:

19. A similar separation of timescales is observed in natural actuatorsSkotheim and Mahadevan 2005.

1. Calculate the activation profile at a given time point;
2. Calculate the corresponding shape change.

It is sufficient to consider what happens immediately after the beginning of activation in order to explain why long-side rolling is preferred over short-side rolling in the case of progressive activation [20]. Once the bilayer starts to *morph* according to the short- or long-side rolling scenario, it will continue to do so when activated further even if the other configuration becomes energetically more favored.

Comparaison of energies between short- and long-side rolling Let us apply a similar reasoning as in subsubsection 8.1.2.1 with the difference that only the edge of the *active* layer is activated. We denote by d the depth of the activated edge (fig. 8.4).

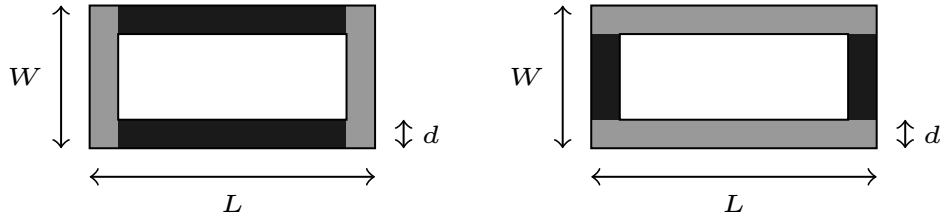

Figure 8.4 – Single curved (gray) and flat (black) regions of the activated crown in the short-side (left) and long-side (right) rolling scenario.

Neglecting the boundary layers, the energy in the short-side and long-side rolling scenarios are given by [21]:

$$\begin{aligned} \mathcal{E}_{short} &= 2\,d\,W\,\mathcal{E}_{bend} + 2\,d\,(L-d)\,\mathcal{E}_{stretch}, \\ \mathcal{E}_{long} &= 2\,d\,L\,\mathcal{E}_{bend} + 2\,d\,(W-d)\,\mathcal{E}_{stretch}, \end{aligned} \tag{8.3}$$

Calculating the difference between these two energies, we obtain:

$$\mathcal{E}_{short} - \mathcal{E}_{long} = 2\,d\,(L-W)\,[\mathcal{E}_{stretch} - \mathcal{E}_{bend}] > 0. \tag{8.4}$$

This shows that long-side rolling is preferred because the bending energy of a plate is smaller than its stretching energy ($\mathcal{E}_{stretch} \gg \mathcal{E}_{bend}$).

Finite-element confirmation Figure 7 of appendix F.1 shows that long-side rolling is preferred according to fem calculations,at least for a sufficiently elongated rectangular bilayer (aspect ratio larger than 4) [22]. According to the previous energetic considerations, long-side rolling is always preferred as long as $L > W$.

8.2 Multi-step folding of star-shaped bilayers

This section discusses the multi-step folding of star-shaped bilayers, which were partially published in (Stoychev, Turcaud, et al. 2013) (see appendix F.2). Subsection 8.2.1 presents the

20. If one wanted to exactly reproduce the *morphing* process, the two steps mentioned above should be reiterated as time increases. One complexity which arises is that the boundary conditions of the diffusive process change as *morphing* goes on. Indeed, as soon as the bilayer starts to bend, the *active* layer detaches from the substrate and so is no longer confined. This means that the diffusion profile would have to be recalculated for each change of configuration.

21. Single curved bending releases the *eigenstrain* perpendicular to the edge of the bilayer, while the *eigenstrain* parallel to the edge of the bilayer is frustrated and leads to stretching. In the expression of the energy, we didn't write the frustrated stretching *eigenstrains*, which cancel out in the difference anyway.

22. The short-side rolling like *morphing* pattern found for an aspect ratio smaller than 4 is not possible experimentally as the long edges are slightly curved downwards, which is prevented by the presence of the substrate.

experimental results of thermo-responsive star-shaped bilayers. This reveals two *morphing* steps (tubular-wrinkling and folding), which can be codified according to phenomenological rules. Subsection 8.2.2 discusses these steps using the knowledge of patterns of shape changes (chapter 2) combined with energetical considerations and finite-element calculations (subsection 8.2.2).

8.2.1 Experimental observations

Similarly to subsection 8.1.1, this subsection recalls the experimental preparations (subsubsection 8.2.1.1) and summarizes [23] the experimental results published in (Stoychev, Turcaud, et al. 2013) (subsubsection 8.2.1.2).

8.2.1.1 Experimental preparation

Similarly to subsubsection 8.1.1.1, bilayers were prepared according to the method presented in subsection 5.3.3, the only difference being the shape of these bilayers. Instead of rectangles, the bilayers now have rounded shapes, either convex like ellipses or concave like stars (with four or six arms) (see figure 2 in appendix F.2).

8.2.1.2 Experimental results

Similarly to subsubsection 8.1.1.2, the bilayer is undeformed while exposed to a phosphate buffered saline (PBS) solution (0.1M and $pH = 7.4$) at $T > 70\,°C$ and when the temperature drops below $T < 70\,°C$, the *active* layer starts to swell and the bilayers undergo a complex multi-step *morphing*. Using optical microscopy, the activation mechanism is resolved and the different steps of the *morphing* process are analyzed.

Activation mechanism Identically to the case of rectangular bilayers, looking at bilayers possessing a relatively thin *active* layer ($t_a = 35\,nm$) and a sufficiently thick *passive* layer ($t_p = 400\,nm$ or $t_p = 500\,nm$), such that bending is prevented. This enables to investigate the evolution of swelling using a optical microscope. Indeed, the swollen regions have a longer optical path length (OPL) than the unswollen ones (the OPL varies as a function of the film thickness and refractive index, which in turn depends on the swelling degree). This reveals that swelling starts from the edges of the active layer (see figure 2a-f of appendix F.2). Also, one can distinguish the evolution of the swelling front from the evolution of the detachment front (fig. 8.5).

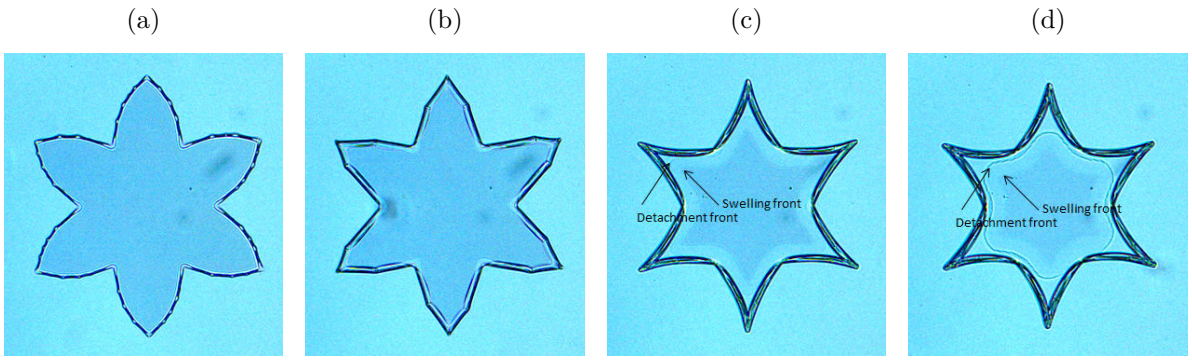

Figure 8.5 – Evolution of the swelling and detachment front in a 6-arm star-shaped bilayer. (Experimental figure send to us by Leonid Ionov.)

23. See footnote 6.

Multi-step *morphing* process The *morphing* process of star-shaped bilayers is more complex than the *morphing* of rectangular bilayers. Contrary to the straight edges of the rectangular bilayer which simply roll up, the curved edges of the star-shaped bilayers also display wrinkling as they roll up [24] (see figure 2i-l of appendix F.2). As the swelling front progresses, the number of wrinkles decreases until it finally stops when the edges are composed of straight tubes. Then, the *morphing* process stops for a while until the *arms* suddenly flap (see figure 3 of appendix F.2). By playing with the number and shape of the *arms*, one achieves a variety of *morphing* patterns (see figure 4 of appendix F.2). Interestingly, this enables to create three-dimensional structures from two-dimensional bilayers such as pyramids (see figure 4 of appendix F.2 and appendix F.3).

8.2.2 Theoretical considerations

This subsection aims at understanding the two stages of the *morphing* of star-shaped bilayers presented in subsubsection 8.2.1.2 using the knowledge of patterns of shape change presented in chapter 2 as well as finite-element calculations: tubular wrinkling in subsubsection 8.2.2.1 and folding in subsubsection 8.2.2.2.

8.2.2.1 Tubular wrinkling

As discussed in chapter 2, a radial gradient (edge-activation) in swelling leads to the formation of wrinkles. The number of wrinkles is inversely proportional to the activation depth d [25]. In the presence of a transversal gradient (bilayer), wrinkling and bending add up according to finite-element calculations(fig. 8.6). This is what we call tubular-wrinkling.

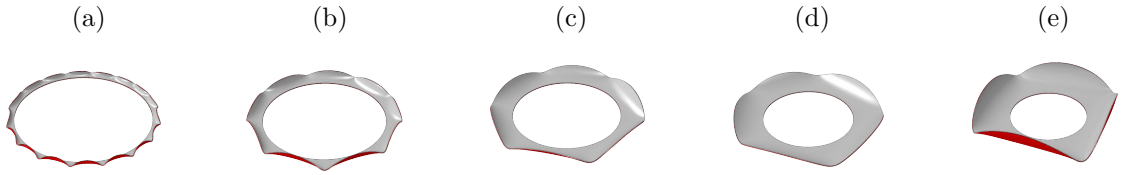

Figure 8.6 – Number of wrinkles inversely proportional to the activation depth.

Finite-element calculations also predict tubular-wrinkling in the case of a straight edge, which means that rectangular bilayers should display them in the first moment of *morphing* (fig. 8.7).

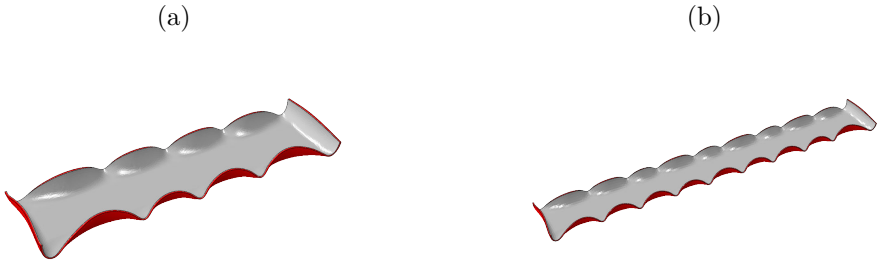

Figure 8.7 – Finite-element calculation also predicts tubular-wrinkling in the case of rectangular bilayers.

24. For the anecdote, the experimentalists confirmed the presence of wrinkles after I predicted them.
25. We call activation depth the distance over which the differential edge-growth occurs.

8.2.2.2 Folding

Once the tubular-wrinkling *morphing* stage is over, the *arms* suddenly fold. This happens when the swelling front crosses a hinge line connecting two weak points (see figure 3 of appendix F.2).

Conclusions

This chapter discussed the diffusion-driven *morphing* of bilayer sheets. If the *eigenstrain* architecture follows the simple bilayer as discussed in chapter 6, the obtained patterns are quite rich due to two factors: two-dimensional sheets are considered instead of one-dimensional rods and the *eigenstrain* is applied progressively instead of instantaneously. This enables to obtain different *morphing* patterns than if the sheets were activated instantaneously (as highlighted in the case of the long-side rolling of rectangular sheets). Also, this allows to control the formation of three-dimensional structures (such as pyramids) from two-dimensional sheets.

References

Alben, Silas, Bavani Balakrisnan, and Elisabeth Smela (2011). « Edge effects determine the direction of bilayer bending ». In: *Nano letters* 11.6, pp. 2280–2285.

Efrati, Efi, Eran Sharon, and Raz Kupferman (2009). « Buckling transition and boundary layer in non-Euclidean plates ». In: *Physical Review E* 80.1, p. 016602.

Razghandi, Khashayar et al. (2012). *Automobile objects*. URL: `https://www.hu-berlin.de/pr/medien/publikationen/pdf/hu_wissen4.pdf`.

Reyssat, E and L Mahadevan (2009). « Hygromorphs: from pine cones to biomimetic bilayers ». In: *Journal of The Royal Society Interface* 6.39, pp. 951–957.

Skotheim, Jan M and L Mahadevan (2005). « Physical limits and design principles for plant and fungal movements ». In: *Science* 308.5726, pp. 1308–1310.

Stoychev, Georgi, Sébastien Turcaud, et al. (2013). « Hierarchical Multi-Step Folding of Polymer Bilayers ». In: *Advanced Functional Materials* 23.18, pp. 2295–2300.

Stoychev, Georgi, Svetlana Zakharchenko, et al. (2012). « Shape-programmed folding of stimuli-responsive polymer bilayers ». In: *ACS nano* 6.5, pp. 3925–3934.

Conclusion and Outlook

This thesis explored some patterns of shape change inspired by natural actuators. We suggest to build *morphing* structures, which change shape in response of fluctuating external stimuli (such as humidity or temperature). This could serve to make already existing moving elements in Architecture sustainable and challenges designers to think about new applications of movement in Architecture.

Conclusions

The theoretical framework needed to explore *morphing* patterns consists of a combination of fundamental concepts of continuum mechanics (e.g. strain, stress, equilibrium, energy) with the concept of *eigenstrain* from micro-mechanics. Due to the fact that *morphing* patterns are usually associated with large shape changes in the case of elongated objects (rods and sheets), the common small displacements assumption can not be made. This justifies using the so-called non-linear theory of elasticity, which we presented in the case of elongated rod-like objects.

The numerical methods used to simulate patterns of shape change are diverse. We used a simple lattice representation of rod-like objects using springs, which relax into an equilibrium configuration upon changing the rest-length of the springs, a script written in Python which minimizes the elastic energy of a one-dimensional rod, and the "brute force" finite-element method to analyze arbitrary *eigenstrain* distributions (e.g. *twisters* and sheets). The experimental systems we used to illustrate the *morphing* patterns rely on three driving forces: prestraining, swelling and thermal expansion. These methods were used in a systematic investigation of rods (*benders* and *twisters*) and for an exploration of sheets.

We discussed the bending of elongated *morphers*, which we call *benders*. Bilayers are known for more than 150 years and represent the simplest example of an *eigenstrain* architecture. The intersurfacial stress within a *bender* can be lowered by smoothening the transversal gradient of *eigenstrain* leading to stress-free bending in the case where the *eigenstrain* architecture is equal to the elastic strain distribution associated to bending. Variations of curvature along the longitudinal direction can be achieved by grading the *benders* along its length. Also, bilayers are a way to transform relatively small strains into a relatively large displacement—through the concept of *geometric amplification*—by adding higher levels of hierarchy in the geometry of the material. Introducing an angle between the principal directions of eigenstrain and the principal directions of the geometry (either directly or by using the principal directions of stiffness), helical morphologies can also be obtained.

In analogy to *benders*, we propose a new design of *morphers* with a rotationally symmetric *eigenstrain* architecture that twists, which we call *twisters*. Such *twisters* exhibit a stretching-twisting instability according to finite-element simulations. The behavior of *twisters* is described using an energetical approach, which enables to find the critical *eigenstrain* at which the instability occurs. This twisting instability can be understood qualitatively using the mass-spring model. Similarly to *benders*, *twisters* can be graded along their longitudinal direction in order to

exhibit tunable twisting. The combination of *benders* and *twisters* enables to generate arbitrary configurations of a rod in space, and as such appear as fundamental units for the *morphing* of one-dimensional objects.

Finally, we discussed the diffusion-driven *morphing* of bilayer sheets as motivated by experiments. Due to the fact that the *eigenstrain* is applied progressively instead of instantaneously, the two-dimensional bilayers *morph* into different patterns than if they were activated instantaneously. This leads to long-side rolling of rectangular bilayers (instead of short-side rolling) and enables the formation of three-dimensional structures (such as pyramids) from two-dimensional star-shaped bilayers through a complex multi-step *morphing* process (tubular-wrinkling of the edges, locking, and folding).

Outlook

Analyzing, modeling and mimicking patterns of shape change is growing new field, where a lot can still be done. Concerning one-dimensional objects, generation of curvature and torsion suffice to generate arbitrary configurations. In the case of two-dimensional objects, there are still many open questions regarding the generation of specific patterns, which we only started to inquire in this thesis. The fact that different *morphing* patterns are obtained depending on the history of activation drastically increases the number of potential patterns. A systematization of diffusion-driven two-dimensional *morphing* patterns would require a thorough investigation.

As a long term goal, we would like to design macroscopic *morphers* for Architecture based on the ideas presented in this thesis. Figure 9.8 shows a wood-plastic prototype for an umbrella, which *morphs* upon wetting thus providing a shelter for rainy days [26]. In order to scale up such *morphers*, one would need to find sufficiently strong driving forces that balance gravity. Also, in the case of load-bearing elements, the rigidity of *morphers* during the *morphing* process becomes essential. Intuitively, we believe that the rigidity of a *morpher* could be tuned as a function of its internal stress state, which would be interesting to look into in more details.

26. This prototype—inspired by (Reyssat and Mahadevan 2009)—was developed in collaboration with Khashayar Razghandi (researcher), Alexander Warth (designer) and Ulises Iturbe (architect) during the Kosmos Summer University 2012 (Razghandi et al. 2012).

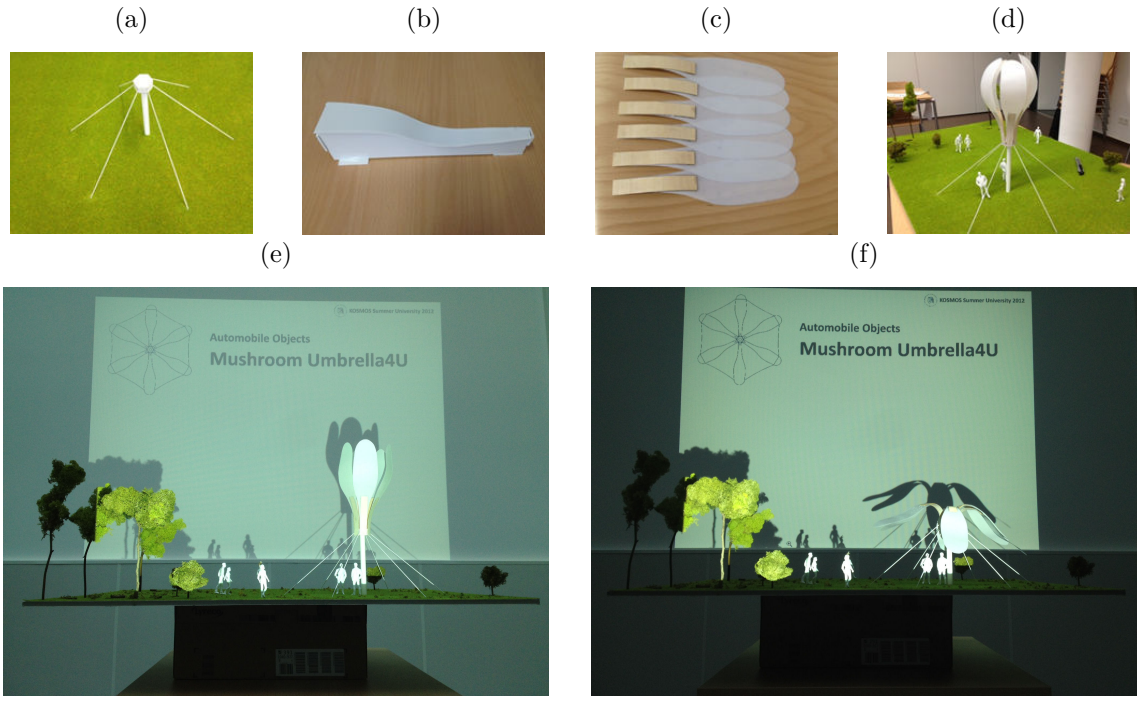

Figure 9.8 – (a) Simply supported mast held by cables, (b) mold for shaping the plastic elements, (c) individual wood-plastic leafs (d) complete structure, (e) closed and (f) open configuration of the wood-plastic prototype triggered by humidity change.

Appendices

Appendix A

Three-dimensional elasticity

This appendix is meant to be both a refresher for the reader already familiar with standard continuum mechanics and a broad introduction for the layman. The concepts of strain (appendix A.1), stress (appendix A.2), constitutive law (appendix A.2.4), mechanical equilibrium (appendix A.3) as well as elastic energy (appendix A.4) are presented and emphasis is drawn upon the notion of *geometric nonlinearity*. Some definitions are very close (or even identical) to the ones given in (Audoly and Pomeau 2010, chapter 2). In particular, the same notations are used which leads to the same formal definitions of the concepts of three-dimensional elasticity. For the sake of brevity, some jumps in the derivations of concepts were made and the interested reader is strongly advise to look therein for the complete derivations.

A.1 The concept of strain

> "Given the positions of the points of the body in its initial state (i.e. before deformation) and in its terminal state (i.e. after deformation), determine the change in the distance between two arbitrary infinitely near points of the body caused by its transition from the first state to the second. This question is purely geometrical, and neither the causes which give rise to the deformation nor the law according to which the body resists are of any importance in its study." (Novozhilov 1999)

As highlighted by Novozhilov in 1947, strain is a pure geometric concept that measures the change of the shape of an object independently of the underlying causes and the generation of stress. This change of shape is expressed in terms of differences in infinitesimal distances between the *initial* and *final*[1] configuration[2] of the object. The important part is to remove rigid-body motions that do not affect the size nor the shape of the object, but only its position in space. In a three-dimensional setting, this is best done through a rank-two tensor field, which contains all the information concerning local changes in distances and changes in angles in all directions[3].

1. To avoid a potentially confusing reference to time, the words *initial* and *final* are sometimes replaced by *reference* and *actual*.

2. The words state and configuration are used synonymously. They correspond to a snapshot of the geometry of the object, the *initial* one before the cause of shape change and the *final* one after the shape reached static equilibrium.

3. The concept of tensor can be intimidating and are introduce here it merely as a convenient notation to represent the matrix containing the components of strain in the reference frame. Also, as only orthonormal frames are used, there is no need to distinguish covariant and contravariant indices.

A.1.1 Transformation

In the continuum approach, a solid object is represented by a closed region in Euclidean space delimited by an envelope representing its external boundary. The material points of the body are reached by a position vector field expressed in some reference frame. We define two configurations that correspond to two states of the object: the *initial* configuration before deformation and the *final* configuration after deformation.

Initial configuration Let Ω be the *initial* state of the object with Γ its boundary. Let $\boldsymbol{r} = (x, y, z)$ be the *initial* position vector field where its coordinates (x, y, z) correspond to the projections of the material points on the axis of some fixed orthonormal frame ($\boldsymbol{e_x}$, $\boldsymbol{e_y}$, $\boldsymbol{e_z}$) (see fig. A.1).

Final configuration Let Ω' be the *final* state of the object with Γ' its boundary. Let $\boldsymbol{r}' = (x', y', z')$ be the *final* position vector field where its coordinates [4](x', y', z') are expressed in the same fixed orthonormal frame ($\boldsymbol{e_x}$, $\boldsymbol{e_y}$, $\boldsymbol{e_z}$) (see fig. A.1).

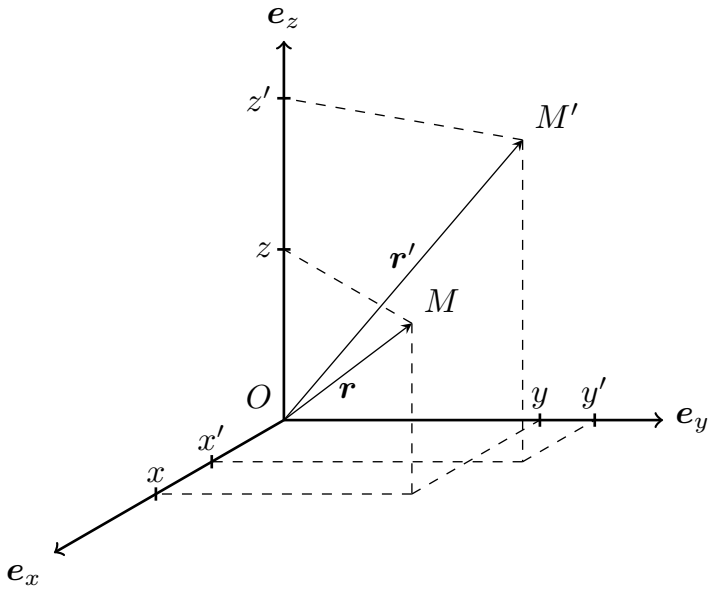

Figure A.1 – Position vectors $\boldsymbol{r}(x, y, z)$ and $\boldsymbol{r}'(x', y', z')$ expressed in the fixed orthonormal frame $(\boldsymbol{e_x}, \boldsymbol{e_y}, \boldsymbol{e_z})$ spanning the solid body in its *initial* state Ω and *final* state Ω' respectively.

The transformation between the *initial* and the *final* configuration is simply defined by the mapping between Ω spanned by $\boldsymbol{r}$ and Ω' spanned by $\boldsymbol{r}'$ (see fig. A.1). This mapping requires expressing the *final* state as a function of the *initial* state [5] ($\boldsymbol{r}'(\boldsymbol{r})$). The *final* configuration is thus characterized by the three scalar functions ($x'(x, y, z)$, $y'(x, y, z)$, $z'(x, y, z)$) giving the *final* coordinates (x', y', z') as functions of the *initial* coordinates (x, y, z). In vector form, this is expressed by:

$$\boldsymbol{r}'(x', y', z') = \begin{pmatrix} x'(x, y, z) \\ y'(x, y, z) \\ z'(x, y, z) \end{pmatrix}. \tag{A.1}$$

4. In the three-dimensional setting, we use the prime symbol ' to refer to the *final* (deformed) configuration. We use another notation in the context of rods (see footnote subsubsection 3.1.1.1).

5. This is the so-called Lagrangian description of the system. The other approach consisting in describing the system by referring to its current state is known as Eulerian description.

A.1.2 Displacement

Let $\boldsymbol{u} = (u, v, w)$ be the displacement vector field defined by $\boldsymbol{u}(\boldsymbol{r}) = \boldsymbol{r'}(\boldsymbol{r}) - \boldsymbol{r}$, where its coordinates (u, v, w) in the same fixed orthonormal frame ($\boldsymbol{e_x}$, $\boldsymbol{e_y}$, $\boldsymbol{e_z}$) all potentially depend on position [6]. In vector form we have:

$$\boldsymbol{u}(x,y,z) = \begin{pmatrix} u(x,y,z) \\ v(x,y,z) \\ w(x,y,z) \end{pmatrix} = \begin{pmatrix} x'(x,y,z) - x \\ y'(x,y,z) - y \\ z'(x,y,z) - z \end{pmatrix}. \tag{A.2}$$

We can then write the *final* configuration spanned by $\boldsymbol{r'}$ in terms of the displacement field $\boldsymbol{u}$:

$$\boldsymbol{r'}(x,y,z) = (x + u(x,y,z))\,\boldsymbol{e_x} + (y + v(x,y,z))\,\boldsymbol{e_y} + (z + w(x,y,z))\,\boldsymbol{e_z}. \tag{A.3}$$

In order to use Einstein's notation [7], we write equivalently:

$$\boldsymbol{r'}(x,y,z) = \boldsymbol{r'}(x_1,x_2,x_3) = (x_i), \qquad \boldsymbol{u} = (u,v,w) = (u_x,u_y,u_z) = (u_1,u_2,u_3) = (u_j).$$

This enable us to write eq. A.3 in a more compact form:

$$\boldsymbol{r'}(x_j) = \sum_{i=1}^{3} [x_i + u_i(x_j)]\,\boldsymbol{e_i} = [x_i + u_i(x_j)]\,\boldsymbol{e_i}. \tag{A.4}$$

An interesting observation (pointed out in Novozhilov 1999) is that the Cartesian coordinates of the *initial* state (x, y, z) become curvilinear coordinates in the *final* state (see appendix A.1.3). The important point is that the *final* configuration spanned by $\boldsymbol{r'}$ is entirely characterized by the knowledge of the *initial* configuration spanned by $\boldsymbol{r'}$ and of the displacement field $\boldsymbol{u}$ expressed in the fixed orthonormal frame $(\boldsymbol{e_x}, \boldsymbol{e_y}, \boldsymbol{e_z})$.

A.1.3 Cartesian and curvilinear coordinates

As pointed out in Novozhilov 1999, the cartesian coordinates of the *initial* state (x, y, z) become curvilinear coordinates in the *final* state. Let's illustrate this by looking at the deformation of a line initially parallel to the z-axis. In the *initial* state, it is parametrized by $\boldsymbol{r} = (x_0, y_0, z)$, where x_0 and y_0 are constants. From eq. A.4, we obtain its coordinates in the *final* state:

$$\boldsymbol{r'}(x_0,y_0,z) = \begin{pmatrix} x_0 + u(x_0,y_0,z) \\ y_0 + v(x_0,y_0,z) \\ z + w(x_0,y_0,z) \end{pmatrix}. \tag{A.5}$$

The deformed line is curved along the z direction if $u \vee v \neq 0$. In general, this means that straight lines in the initial state become curved lines in the *final* state (see fig. A.2). Equivalently, the Cartesian coordinates of the *final* state x', y', z' correspond to curvilinear coordinates of the *initial* state, which means that straight lines in the *final* state were in general curved lines in the *initial* state.

6. For the sake of notation, we sometimes drop the dependency on position of the displacement vector field $\boldsymbol{u}(\boldsymbol{r}) = \boldsymbol{u}$.

7. Einstein's notation implies implicit summation over repeated indices such as $\sum_i x_i \boldsymbol{e_i} = x_i \boldsymbol{e_i} = x\,\boldsymbol{e_x} + y\,\boldsymbol{e_y} + z\,\boldsymbol{e_z} = x_1\,\boldsymbol{e_1} + x_2\,\boldsymbol{e_2} + x_3\,\boldsymbol{e_3}$. Also, indices are generic, which means that an equality is true for all values of an index when it is present only once on one side of an equation.

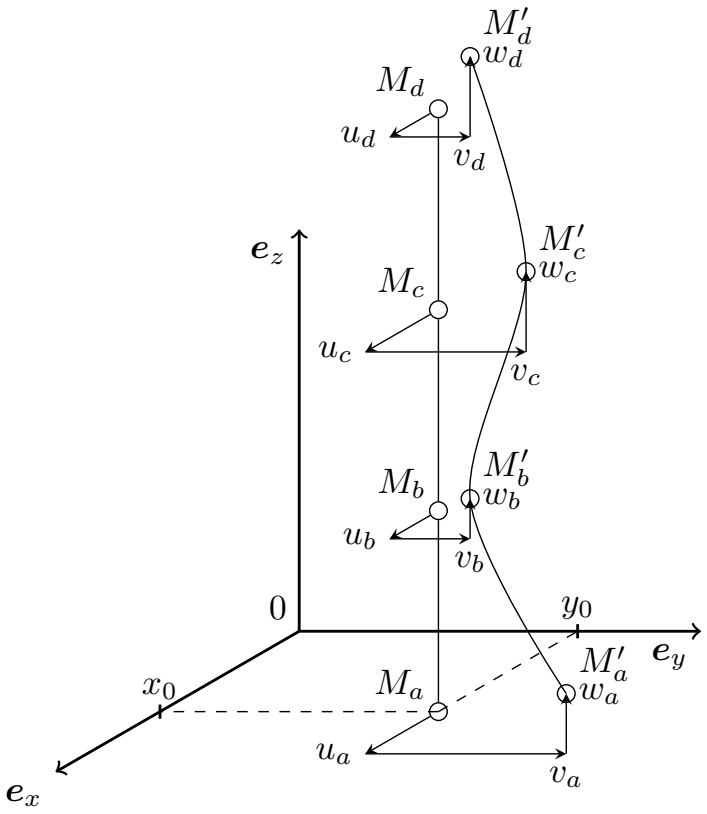

Figure A.2 – Straight line in the *initial* state become curved lines in the *final* state and vice-versa. Here we see the displacements components (u, v, w) at different points (a, b, c, d) along an initial straight line.

A.1.4 Derivation of the strain tensor

The concept of strain aims at measuring the change of an object's shape between its *initial* and *final* state. The important point is to define strain such that it is invariant under rigid-body motions. Indeed, rigid-body motions don't affect the shape of the object, but only its position and orientation in space. In order to express the strain tensor, let's look at the change in length of an infinitesimal vector $\mathrm{d}\boldsymbol{r}$ between the *initial* and *final* state. The variation of the squared [8] length of this infinitesimal vector is given by:

$$\begin{aligned}(\mathrm{d}\boldsymbol{r}')^2 - (\mathrm{d}\boldsymbol{r})^2 &= (\mathrm{d}[x_i + u_i(x_j)]\,\boldsymbol{e_i})^2 - (\mathrm{d}x_i\,\boldsymbol{e_i})^2, \\ &= \left(\left[\mathrm{d}x_i + \frac{\delta u_i}{\delta x_j}\,\mathrm{d}x_j\right]\,\boldsymbol{e_i}\right)^2 - (\mathrm{d}x_i\,\boldsymbol{e_i})^2. \end{aligned} \tag{A.6}$$

8. If we only look at the variation of length, the displacement gradients $\delta u_i/\delta x_j$ appear as a *natural* measure of deformation. However, this is not a good candidate for strain as it is not invariant under rigid-body motions. Actually, it is invariant under translations, but not under rotations (see appendix A.1.9).

Expanding the first square in the right-hand side of eq. A.6 as $\boldsymbol{a}^2 = a_i \boldsymbol{e_i} \cdot a_k \boldsymbol{e_k}$, one obtains:

$$\begin{aligned}
\left[\left(\mathrm{d}x_i + \frac{\delta u_i}{\delta x_j}\,\mathrm{d}x_j\right)\,\boldsymbol{e_i}\right]^2 &= \left(\mathrm{d}x_i + \frac{\delta u_i}{\delta x_j}\,\mathrm{d}x_j\right)\boldsymbol{e_i} \cdot \left(\mathrm{d}x_k + \frac{\delta u_k}{\delta x_l}\mathrm{d}x_l\right)\boldsymbol{e_k}, \\
&= \left(\mathrm{d}x_i\,\mathrm{d}x_k + \frac{\delta u_i}{\delta x_j}\,\mathrm{d}x_j\,\mathrm{d}x_k + \mathrm{d}x_i\,\frac{\delta u_k}{\delta x_l}\,\mathrm{d}x_l + \frac{\delta u_i}{\delta x_j}\,\mathrm{d}x_j\,\frac{\delta u_k}{\delta x_l}\,\mathrm{d}x_l\right)\delta_{ik}, \\
&= \left(\mathrm{d}x_i\,\mathrm{d}x_i + \frac{\delta u_i}{\delta x_j}\,\mathrm{d}x_j\,\mathrm{d}x_i + \mathrm{d}x_i\,\frac{\delta u_i}{\delta x_l}\,\mathrm{d}x_l + \frac{\delta u_i}{\delta x_j}\,\mathrm{d}x_j\,\frac{\delta u_i}{\delta x_l}\,\mathrm{d}x_l\right), \\
&= \left(\delta_{ij} + \frac{\delta u_i}{\delta x_j} + \frac{\delta u_j}{\delta x_i} + \frac{\delta u_k}{\delta x_i}\,\frac{\delta u_k}{\delta x_j}\right)\mathrm{d}x_i\,\mathrm{d}x_j.
\end{aligned} \tag{A.7}$$

The fact that the frame $(\boldsymbol{e_x}, \boldsymbol{e_y}, \boldsymbol{e_z})$ is orthonormal is used to derive the second line of the above equation ($\boldsymbol{e_i} \cdot \boldsymbol{e_j} = \delta_{ij}$). The zero contributions are suppressed by setting $k = i$ to derive the third line. Finally, the indices are renamed in order to collect the coefficients in front of $\mathrm{d}x^2$, $\mathrm{d}x\mathrm{d}y$, etc. in the last line. The second square in the right-hand side of eq. A.6 is written in tensorial form:

$$\mathrm{d}\boldsymbol{r}^2 = \mathrm{d}x_i\,\mathrm{d}x_i = \delta_{ij}\,\mathrm{d}x_i\,\mathrm{d}x_j. \tag{A.8}$$

Combining eq. A.7 and eq. A.8leads to:

$$(\mathrm{d}\boldsymbol{r'})^2 - (\mathrm{d}\boldsymbol{r})^2 = \left(\frac{\delta u_i}{\delta x_j} + \frac{\delta u_j}{\delta x_i} + \frac{\delta u_k}{\delta x_i}\,\frac{\delta u_k}{\delta x_j}\right)\mathrm{d}x_i\,\mathrm{d}x_j. \tag{A.9}$$

This equation shows that the variation of the squared length of an infinitesimal vector $(\mathrm{d}\boldsymbol{r'})^2 - (\mathrm{d}\boldsymbol{r})^2$ is a quadratic form [9] of this vector $\mathrm{d}\boldsymbol{r}$ [10]. The coefficients of this quadratic form are combinations (sums and products) of the derivatives of the components of displacement (u_x, u_y, u_z) with respect to the components of position (x_1, x_2, x_3). These displacement gradients are functions of position through the implicit dependence of the displacement vector field on position [11]. Equation A.9 can be written concisely as [12]:

$$(\mathrm{d}\boldsymbol{r'})^2 - (\mathrm{d}\boldsymbol{r})^2 = 2\,\epsilon_{ij}(\boldsymbol{r})\,\mathrm{d}x_i\,\mathrm{d}x_j. \tag{A.10}$$

The tensor field $\boldsymbol{\epsilon}(\boldsymbol{r})$ is the so-called *Green-St. Venant strain tensor* [13]. According to eq. A.9, its coordinates in the orthonormal frame $(\boldsymbol{e_x}, \boldsymbol{e_y}, \boldsymbol{e_z})$ are given by:

$$\epsilon_{ij}(\boldsymbol{r}) = \frac{1}{2}\left(\frac{\delta u_i(\boldsymbol{r})}{\delta x_j} + \frac{\delta u_j(\boldsymbol{r})}{\delta x_i}\right) + \frac{1}{2}\frac{\delta u_k(\boldsymbol{r})}{\delta x_i}\frac{\delta u_k(\boldsymbol{r})}{\delta x_j}. \tag{A.11}$$

By construction and looking at eq. A.11, the indices i and j play a symmetric role, which means that the strain tensor $\boldsymbol{\epsilon}(\boldsymbol{r})$ is symmetric:

$$\epsilon_{ij}(\boldsymbol{r}) = \epsilon_{ji}(\boldsymbol{r}). \tag{A.12}$$

The strain tensor $\boldsymbol{\epsilon}(\boldsymbol{r})$ thus has six a priori independent components [14] [$\epsilon_{xx}(\boldsymbol{r})$, $\epsilon_{yy}(\boldsymbol{r})$, $\epsilon_{zz}(\boldsymbol{r})$, $\epsilon_{xy}(\boldsymbol{r})$, $\epsilon_{xz}(\boldsymbol{r})$, $\epsilon_{yz}(\boldsymbol{r})$] that all potentially depend on $\boldsymbol{r}$. It can thus be represented by a 3 by 3

9. A quadratic form is an homogeneous polynomial of degree two as is for example the distance in Euclidean space ($\boldsymbol{r}^2 = x^2 + y^2 + z^2$). In the case of strain, the cross-terms (xy, xz, yz) are nonzero and its components are s ($\delta u_i / \delta x_j$).

10. $\mathrm{d}\boldsymbol{r} = (\mathrm{d}x, \mathrm{d}y, \mathrm{d}z) = (\mathrm{d}x_1, \mathrm{d}x_2, \mathrm{d}x_3)$.

11. See footnote 6.

12. See footnote 25 for the reason why a factor 2 is introduced here.

13. The *Green-St.Venant strain tensor* $\boldsymbol{\epsilon}$ is also sometimes called the *Green-Lagrange strain tensor*.

14. Due to the necessary compatibility of strain which is an implicit consequence of the continuum assumption (there is no appearance of holes or overlaps in the body as it deforms into its *final* configuration), the six components of strain are in fact subjected to three compatibility equations (appendix A.1.11). This is in accordance with the fact that the displacement field only has three components.

symmetric matrix [15]:

$$\boldsymbol{\epsilon}(\boldsymbol{r}) = \begin{pmatrix} \epsilon_{xx}(\boldsymbol{r}) & \epsilon_{xy}(\boldsymbol{r}) & \epsilon_{xz}(\boldsymbol{r}) \\ & \epsilon_{yy}(\boldsymbol{r}) & \epsilon_{yz}(\boldsymbol{r}) \\ & & \epsilon_{zz}(\boldsymbol{r}) \end{pmatrix}. \tag{A.13}$$

Let's write a diagonal and a non-diagonal component of strain in explicit terms using eq. A.11. Along the x-axis for example, the diagonal component of strain ($\epsilon_{xx}(\boldsymbol{r})$) is given by:

$$\epsilon_{xx}(\boldsymbol{r}) = \frac{\delta u_x}{\delta x} + \left[\frac{1}{2}\left(\left(\frac{\delta u_x}{\delta x}\right)^2 + \left(\frac{\delta u_y}{\delta x}\right)^2 + \left(\frac{\delta u_z}{\delta x}\right)^2\right)\right]. \tag{A.14}$$

Between the x- and y-axis for example, the non-diagonal component of strain ($\epsilon_{xy}(\boldsymbol{r})$) is given by:

$$\epsilon_{xy}(\boldsymbol{r}) = \frac{1}{2}\left(\frac{\delta u_x}{\delta y} + \frac{\delta u_y}{\delta x}\right) + \left[\frac{1}{2}\left(\frac{\delta u_x}{\delta x}\frac{\delta u_x}{\delta y} + \frac{\delta u_y}{\delta x}\frac{\delta u_y}{\delta y} + \frac{\delta u_z}{\delta x}\frac{\delta u_z}{\delta y}\right)\right]. \tag{A.15}$$

In these two expressions, the parts in brackets is quadratic with respect to the gradients of displacement. This nonlinearity appears naturally in the definition of strain (see appendix A.1.9).

The strain tensor characterizes local changes in distance in the neighborhood of a point and varies with position. As shown in appendix A.1.5, it fully characterizes the deformed state of the body in terms of change of lengths (appendix A.1.6) and change of angles (appendix A.1.7). By construction, the strain tensor vanishes for rigid-body motions (rigid-body rotations and rigid-body translations), which do not modify distances between material points (see appendix A.1.10).

A.1.5 Change of lengths and angles

The strain tensor fully characterizes the deformed state of the body in terms of change of lengths (appendix A.1.6) and angles (appendix A.1.7).

A.1.6 Change of length

The strain tensor ($\boldsymbol{\epsilon}$) contains all the information about the change in lengths between the two (*initial* and *final*) state of the object. Let's calculate the deformed length of an arbitrary curve given by $\boldsymbol{r}(s) = (x_i(s))$ $(0 \leq s \leq 1)$ in the *initial* state. Using eq. A.10 we have:

$$|\mathrm{d}\boldsymbol{r}'| = \sqrt{(\mathrm{d}\boldsymbol{r}')^2} = \sqrt{(\mathrm{d}\boldsymbol{r})^2 + 2\,\epsilon_{ij}\,\mathrm{d}x_i\,\mathrm{d}x_j}. \tag{A.16}$$

Writing $\mathrm{d}\boldsymbol{r} = \delta_{ij}\mathrm{d}x_i\,\mathrm{d}x_j$, the length of the curve in the deformed configuration is:

$$l' = \int_0^1 \mathrm{d}s \sqrt{(\delta_{ij} + 2\,\epsilon_{ij})\,\frac{\mathrm{d}x_i}{\mathrm{d}s}\,\frac{\mathrm{d}x_j}{\mathrm{d}s}}. \tag{A.17}$$

This equation shows that the strain tensor can be used to compute the actual length of an arbitrary material curve drawn into the solid. In this sense, the strain tensor fully characterizes the change of lengths that occurs during deformation.

15. Alternatively, the strain tensor can be represented through its principal strains expressed in the principal directions of strain (see appendix A.1.8).

A.1.7 Change of angles

The strain tensor ($\boldsymbol{\epsilon}$) also contains full information about the change of angles between the two two (*initial* and *final*) state of the object. Let $\boldsymbol{r}$, $\boldsymbol{r}+\mathrm{d}\boldsymbol{r}_1$ and $\boldsymbol{r}+\mathrm{d}\boldsymbol{r}_2$ be three position vectors pointing to three neighboring points M, M_1 and M_2 in the *initial* state and $\boldsymbol{r}'$, $\boldsymbol{r}'+\mathrm{d}\boldsymbol{r}'_1$ and $\boldsymbol{r}'+\mathrm{d}\boldsymbol{r}'_2$ the three position vectors pointing to their location M', M'_1 and M'_2 in the *final* state. To calculate the change of the angle $\widehat{MM_1M_2}$ we use the definition of the scalar product:

$$\cos\theta' = \frac{\mathrm{d}\boldsymbol{r}'_{\boldsymbol{1}}\cdot\mathrm{d}\boldsymbol{r}'_{\boldsymbol{2}}}{|\mathrm{d}\boldsymbol{r}'_{\boldsymbol{1}}|\,|\mathrm{d}\boldsymbol{r}'_{\boldsymbol{2}}|} = \frac{(\mathrm{d}\boldsymbol{r}_{\boldsymbol{1}}\cdot\mathrm{d}\boldsymbol{r}_{\boldsymbol{2}})+(\mathrm{d}\boldsymbol{r}'_{\boldsymbol{1}}\cdot\mathrm{d}\boldsymbol{r}'_{\boldsymbol{2}}-\mathrm{d}\boldsymbol{r}_{\boldsymbol{1}}\cdot\mathrm{d}\boldsymbol{r}_{\boldsymbol{2}})}{|\mathrm{d}\boldsymbol{r}'_{\boldsymbol{1}}|\,|\mathrm{d}\boldsymbol{r}'_{\boldsymbol{2}}|} \tag{A.18}$$

On the right-side of this equation, the first term of the numerator concerns the *initial* configuration and so is known and the denominator can be calculated using eq. A.16. There is only the need to calculate the variation of the scalar product:

$$\begin{aligned}\mathrm{d}\boldsymbol{r}'_1\cdot\mathrm{d}\boldsymbol{r}'_2-\mathrm{d}\boldsymbol{r}_1\cdot\mathrm{d}\boldsymbol{r}_2 &= \frac{1}{4}\left([\mathrm{d}\boldsymbol{r}'_1+\mathrm{d}\boldsymbol{r}'_2]^2-[\mathrm{d}\boldsymbol{r}'_1-\mathrm{d}\boldsymbol{r}'_2]^2\right)-\frac{1}{4}\left([\mathrm{d}\boldsymbol{r}_1+\mathrm{d}\boldsymbol{r}_2]^2-[\mathrm{d}\boldsymbol{r}_1-\mathrm{d}\boldsymbol{r}_2]^2\right),\\ &= \frac{1}{4}\left([\mathrm{d}\boldsymbol{r}'_1+\mathrm{d}\boldsymbol{r}'_2]^2-[\mathrm{d}\boldsymbol{r}_1+\mathrm{d}\boldsymbol{r}_2]^2\right)-\frac{1}{4}\left([\mathrm{d}\boldsymbol{r}'_1-\mathrm{d}\boldsymbol{r}'_2]^2-[\mathrm{d}\boldsymbol{r}_1-\mathrm{d}\boldsymbol{r}_2]^2\right).\end{aligned}$$

Here a geometric identity is used to deduce the first equality above and the terms are simply reordered in the second. The two terms in parentheses in the second line of the above equation can be expressed in terms of the strain tensor using eq. A.10:

$$\mathrm{d}\boldsymbol{r}'_1\cdot\mathrm{d}\boldsymbol{r}'_2-\mathrm{d}\boldsymbol{r}_1\cdot\mathrm{d}\boldsymbol{r}_2 = \frac{2\,\epsilon_{ij}\,\mathrm{d}(\boldsymbol{r}_1+\boldsymbol{r}_2)_i\,\mathrm{d}(\boldsymbol{r}_1+\boldsymbol{r}_2)_j}{4}-\frac{2\,\epsilon_{ij}\,\mathrm{d}(\boldsymbol{r}_1-\boldsymbol{r}_2)_i\,\mathrm{d}(\boldsymbol{r}_1-\boldsymbol{r}_2)_j}{4}.$$

By writing the components of $\mathrm{d}\boldsymbol{r}_1$ and $\mathrm{d}\boldsymbol{r}_2$ as $\mathrm{d}x_i^{(1)}$ and $\mathrm{d}x_i^{(2)}$ respectively and by using the symmetry of the strain tensor, the above expression can be expanded into:

$$\mathrm{d}\boldsymbol{r}'_1\cdot\mathrm{d}\boldsymbol{r}'_2-\mathrm{d}\boldsymbol{r}_1\cdot\mathrm{d}\boldsymbol{r}_2 = 2\,\epsilon_{ij}\,\mathrm{d}x_i^{(1)}\,\mathrm{d}x_j^{(2)}. \tag{A.19}$$

This equation generalizes eq. A.10 and shows that strain characterizes not only the change in length of material vectors, but also the change of scalar products between two material vectors. Combined with eq. A.16, this equation can be used to calculate an angle θ' in the deformed configuration between two arbitrary material directions using eq. A.18:

$$\cos\theta' = \frac{(\delta_{ij}+2\epsilon_{ij})\mathrm{d}x_i^1\,\mathrm{d}x_j^2}{\sqrt{(\mathrm{d}\boldsymbol{r}_1)^2+2\,\epsilon_{ij}\,\mathrm{d}x_i^1\,\mathrm{d}x_j^1}\sqrt{(\mathrm{d}\boldsymbol{r}_2)^2+2\,\epsilon_{ij}\,\mathrm{d}x_i^2\,\mathrm{d}x_j^2}}. \tag{A.20}$$

It is in that sense that the strain tensor fully characterizes the changes in relative positions between material points in terms of distances and angles.

A.1.8 Diagonalization

As can be proven mathematically, any real symmetric matrix has real eigenvalues and so can be diagonalized by a suitable rotation of the reference frame. Let $(\hat{\boldsymbol{e}}_{\boldsymbol{x}},\hat{\boldsymbol{e}}_{\boldsymbol{y}},\hat{\boldsymbol{e}}_{\boldsymbol{z}})$ be the orthonormal basis that diagonalizes the strain tensor $\boldsymbol{\epsilon}$ at a given position $\boldsymbol{r}$ and let $\hat{\boldsymbol{\epsilon}}_{xx},\hat{\boldsymbol{\epsilon}}_{yy},\hat{\boldsymbol{\epsilon}}_{zz}$ be the associated eigenvalues. In this frame, the strain matrix at a given point $\boldsymbol{r}$ is given by:

$$\hat{\boldsymbol{\epsilon}} = \begin{pmatrix}\hat{\boldsymbol{\epsilon}}_{xx} & 0 & 0\\ 0 & \hat{\boldsymbol{\epsilon}}_{yy} & 0\\ 0 & 0 & \hat{\boldsymbol{\epsilon}}_{zz}\end{pmatrix} = diag\left(\hat{\boldsymbol{\epsilon}}_{xx},\hat{\boldsymbol{\epsilon}}_{yy},\hat{\boldsymbol{\epsilon}}_{zz}\right). \tag{A.21}$$

This means that for any points in the solid, there exist a frame in which the deformation can be expressed by a combination of pure stretching and contraction. The directions defined by this

frame are called the principal directions of strain, while the eigenvalues $(\hat{\boldsymbol{\epsilon}}_{xx}, \hat{\boldsymbol{\epsilon}}_{yy}, \hat{\boldsymbol{\epsilon}}_{zz})$ are called the principal strains [16] The frame of principal directions is obtained by a 3D rotation of the reference frame that can be expressed by three parameters (i.e. Euler angles). This is consistent with the fact that the strain tensor possesses six independent components.

A.1.9 The difference between the approximation of small strain and the approximation of small displacements

Until now the notion of strain has been derived in all generality. In our work, we focus our interest on a special class of transformation where the values of the components of strain are everywhere small, but we still allow for large displacement gradients (large transformations). In the following, we highlight the nonlinearity which appears naturally in the definition of strain. Then, we discuss two approximations which are both common in continuum mechanics, but often confused: the approximation of small strains and the approximation of small displacements. We make the point that we only use the first one.

Geometric nonlinearity As we see in eq. A.11 the components of the strain tensor $\boldsymbol{\epsilon}$ depend non-linearly on the displacement gradients $(\delta u_i/\delta x_j)$. As Audoly puts it: "Geometry, through the squares in the definition of the Euclidean distance, brings nonlinearity at the heart of the theory of elasticity" (Audoly and Pomeau 2010, p. 23). To be more precise, we can split eq. A.11 into a linear and a non-linear part:

$$\epsilon_{ij}(\boldsymbol{r}) = \epsilon_{ij}^{lin}(\boldsymbol{r}) + \epsilon_{ij}^{nl}(\boldsymbol{r}), \tag{A.22}$$

where

$$\epsilon_{ij}^{lin}(\boldsymbol{r}) = \frac{1}{2}\left(\frac{\delta u_i(\boldsymbol{r})}{\delta x_j} + \frac{\delta u_j(\boldsymbol{r})}{\delta x_i}\right), \tag{A.23a}$$

$$\epsilon_{ij}^{nl}(\boldsymbol{r}) = \frac{1}{2}\frac{\delta u_k(\boldsymbol{r})}{\delta x_i}\frac{\delta u_k(\boldsymbol{r})}{\delta x_j}. \tag{A.23b}$$

In table A.1, we summarize the linear or nonlinear strain dependency on the displacement gradients depending on their magnitude. As we discuss in the following, we only look at cases where the components of strain are small, but it is possible that the linear and nonlinear parts of strain are both large if a cancellation takes place between them.

	Displacement gradients $\left\lvert\frac{\delta u_i}{\delta x_j}\right\rvert$	
	small ($\ll 1$)	large ($\gg 1$)
Strain	eq. A.23a	eq. A.11
Dependency	linear	nonlinear

Table A.1 – Linear or nonlinear definition of strain depending on the magnitude of the displacement gradients.

The approximation of small strain The components of strain are dimensionless numbers (also called *pure* numbers) as they are obtained by taking spatial derivatives of the components of displacement, which have the dimension of a length. This means that the values of strain

16. It should be noted that both the principal directions of strain and the principal values of strain are fields, which means that they vary in general within the solid.

have an absolute meaning (they can be small or large absolutely without comparison to another physical quantity) and that the following approximation makes sense:

$$|\epsilon_{ij}| \ll 1. \tag{A.24}$$

In the general, this geometric approximation enables to make a physical approximation which applies to most materials, namely that they respond elastically and linearly for small strains. This enable us to consider the simplest material behavior law there is (Hooke's law, see appendix A.2.4).

The approximation of small displacements The approximation of small displacements is broader than the approximation of small strains [17]. Let's assume that the components of the displacement field are everywhere small compared to the linear dimensions of the body. Then we have the following condition:

$$\left|\frac{\delta u_i}{\delta x_j}\right| \ll 1. \tag{A.25}$$

Let's also assume that the gradients of displacements all have approximately the same typical value ($x \in \mathbb{R}_+$) throughout the solid body:

$$\left|\frac{\delta u_i}{\delta x_j}\right| \approx x. \tag{A.26}$$

According to eq. A.23a and eq. A.23b, the linear and nonlinear part of the strain tensor can then be estimated as:

$$\left|\epsilon_{ij}^{lin}\right| \approx x, \qquad \left|\epsilon_{ij}^{nl}\right| \approx \frac{3x^2}{2}. \tag{A.27}$$

As $x \ll 1$, the nonlinear term appears to be negligible compared to the linear term in the definition of strain:

$$|\epsilon_{ij}| = \left|\epsilon_{ij}^{lin} + \epsilon_{ij}^{nl}\right| \approx x\left(1 + \frac{3x}{2}\right) \underset{x \ll 1}{\approx} x. \tag{A.28}$$

In general, this means that the nonlinear part of strain is smaller than its linear part for small displacement gradients:

$$\left|\epsilon_{ij}^{nl}\right| \ll \left|\epsilon_{ij}^{lin}\right|. \tag{A.29}$$

Thus, in the small displacement approximation, the quadratic term can be neglected in the definition of strain and the strain expression is linearized into:

$$\epsilon_{ij}(\boldsymbol{r}) \approx \epsilon_{ij}^{lin}(\boldsymbol{r}) = \frac{1}{2}\left(\frac{\delta u_i(\boldsymbol{r})}{\delta x_j} + \frac{\delta u_j(\boldsymbol{r})}{\delta x_i}\right). \tag{A.30}$$

This tensor is the so-called linearized strain tensor and is commonly used [18] as a definition of strain [19].

17. Broader means that small displacement gradients imply small strains, but the converse implication is false (see footnote 19).

18. Using the linearized strain tensor is absolutely fine as long the approximation of small displacements holds.

19. The distinction between the approximation of small strain and the approximation of small displacements is subtle and often confused in the literature (as already pointed out in Novozhilov 1999). We can guess three reasons why it is the case: The approximation of small displacements implies the approximation of small strains, but the converse is false ($A \implies B$, but $B \not\Rightarrow A$). This implication can be wrongly taken for an equivalence (*logical fallacy*). Also, as highlighted in the citation at the beginning of the chapter, considering nonlinear term adds complexity to the subject. According to Ockham's razor principle, unnecessary terms are rightfully ignored, but wrongfully if those terms are necessary (*oversimplification*). The displacements and rotations characterize the deformation of a body as a whole (deflection of a beam, twisting of a shaft), whereas the extensions and shears (strain) characterize the deformation of an infinitesimal element of volume of the body. The same word "deformation" used to describe either the microscopic or macroscopic change of shape is a potential source of confusion (*imprecise vocabulary*).

A.1.10 Examples of transformation

Let us consider a few simple examples of transformations in order to illustrate the concepts of displacement and strain defined previously. First, we'll make sure that strain as defined by eq. A.11 is invariant under rigid-body motions (translations and rotations). In particular, we'll see that the linearized strain (eq. A.23a) is not invariant under rigid-body rotations. This highlights the importance of considering the nonlinear part of strain (eq. A.23b) when dealing with large rotations. Then, we'll consider two simple types of transformations: stretching or contraction and shearing. These transformations will help us to identify the physical meaning of the components of strain.

Rigid-body translation A rigid-body translation of the entire object by a constant vector $\boldsymbol{a} = a_i \boldsymbol{e}_i$ ($a_i \in \mathbb{R}$) is defined by the transformation:

$$\boldsymbol{r}'(x', y', z') = \begin{pmatrix} x'(x,y,z) \\ y'(x,y,z) \\ z'(x,y,z) \end{pmatrix} = \begin{pmatrix} x + a_x \\ y + a_y \\ z + a_z \end{pmatrix}. \tag{A.31}$$

The corresponding displacement field is then simply the translation vector $\boldsymbol{a}$:

$$\boldsymbol{u}(r) = \boldsymbol{r}'(\boldsymbol{r}) - \boldsymbol{r} = \begin{pmatrix} a_x \\ a_y \\ a_z \end{pmatrix} = a_i \boldsymbol{e}_i = \boldsymbol{a}. \tag{A.32}$$

As the displacement field is a constant vector, all the displacement gradients are equal to zero. From eq. A.11, the strain is zero everywhere:

$$\boldsymbol{\epsilon}(\boldsymbol{r}) = \mathbf{0}. \tag{A.33}$$

This shows that strain does not measure changes in absolute position [20].

Rigid-body rotation A rigid-body rotation of the entire object by an angle ($\theta \in [0; \pi]$) about the z direction is defined by the transformation [21]:

$$\boldsymbol{r}'(x', y', z') = \begin{pmatrix} x'(x,y,z) \\ y'(x,y,z) \\ z'(x,y,z) \end{pmatrix} = \begin{pmatrix} x\cos\theta - y\sin\theta \\ x\sin\theta + y\cos\theta \\ z \end{pmatrix}. \tag{A.34}$$

The displacement field is then given by:

$$\boldsymbol{u}(r) = \boldsymbol{r}'(\boldsymbol{r}) - \boldsymbol{r} = \begin{pmatrix} x(\cos\theta - 1) - y\sin\theta \\ x\sin\theta + y(\cos\theta - 1) \\ 0 \end{pmatrix}. \tag{A.35}$$

Here, only the displacement gradients of the z displacement components or with respect to z are equal to zero, whereas the ones with respect to x or y are not:

$$\begin{aligned} &\frac{\delta u_x}{\delta x} = \cos\theta - 1, && \frac{\delta u_x}{\delta y} = -\sin\theta, && \frac{\delta u_x}{\delta z} = 0, \\ &\frac{\delta u_y}{\delta x} = \sin\theta, && \frac{\delta u_y}{\delta y} = \cos\theta - 1, && \frac{\delta u_y}{\delta z} = 0, \\ &\frac{\delta u_z}{\delta x} = 0, && \frac{\delta u_z}{\delta y} = 0, && \frac{\delta u_z}{\delta z} = 0. \end{aligned} \tag{A.36}$$

20. Both the linearized and the nonlinear strain tensor are invariant under rigid-body translations.

21. In all generality, we should consider a rotation about an arbitrary direction. However, the expressions become rather long, so we only consider specific rotations about one of the main directions of the orthonormal frame (the z direction could easily be replaced by the x or y direction).

However, from eq. A.11 we find that all the strain components are all equal to zero as the nonzero terms cancel out:

$$\begin{aligned}
\boldsymbol{\epsilon}_{xx} &= (\cos\theta - 1) + \frac{1}{2}\left((\cos\theta - 1)^2 + (\sin\theta)^2\right) = 0, \\
\boldsymbol{\epsilon}_{xy} &= \frac{1}{2}(-\sin\theta + \sin\theta) + \frac{1}{2}\left((\cos\theta - 1)(-\sin\theta) + \sin\theta(\cos\theta - 1)\right) = 0, \\
\boldsymbol{\epsilon}_{yy} &= (\cos\theta - 1) + \frac{1}{2}\left((\cos\theta - 1)^2 + (-\sin\theta)^2\right) = 0, \\
\boldsymbol{\epsilon}_{iz} &= 0.
\end{aligned} \tag{A.37}$$

This shows that strain does not measure changes in absolute orientation [22].

Remark (Importance of the nonlinear terms in the definition of strain)**.** *Per definition, rigid-body motions don't affect the distances between material points of a solid object and thus create no strain (nor stresses). In calculating the strain associated with a rigid-body rotation, we see that a cancellation occurs between the linear and the nonlinear part of strain ($\epsilon_{ij}^{nl} = -\epsilon_{ij}^{lin}$). If we had omitted the nonlinear term, the strain would not have been zero. This illustrates the fact that the linearized strain tensor is not invariant under rotations.*

Uniaxial stretching/contraction Uniaxial stretching or contraction of an object along the x direction is defined by the transformation:

$$\boldsymbol{r}'(x', y', z') = \begin{pmatrix} x'(x,y,z) \\ y'(x,y,z) \\ z'(x,y,z) \end{pmatrix} = \begin{pmatrix} \lambda_x x \\ y \\ z \end{pmatrix}, \qquad \lambda_x \in \mathbb{R}_+^*. \tag{A.38}$$

Lines parallel to the x-axis are stretched when $\lambda_x > 1$ or contracted when $0 < \lambda_x < 1$. For $\lambda_x = 1$ there is no deformation [23]. Also, negative values of λ_x are not possible [24]. The displacement field is then:

$$\boldsymbol{u}(\boldsymbol{r}) = \boldsymbol{r}'(\boldsymbol{r}) - \boldsymbol{r} = \begin{pmatrix} (\lambda_x - 1)\, x \\ 0 \\ 0 \end{pmatrix} = (\lambda_x - 1)\, x\, \boldsymbol{e}_x. \tag{A.39}$$

The only nonzero component of the displacement vector field is $u_x = (\lambda_x - 1)\, x$, which is equal to zero in the absence of deformation ($\lambda_x = 1$). The only non-zero displacement gradient is thus $\delta u_x / \delta x = \lambda_x - 1$ and from eq. A.11 we have:

$$\boldsymbol{\epsilon}(\boldsymbol{r}) = \left[(\lambda_x - 1) + \frac{(\lambda_x - 1)^2}{2}\right] \boldsymbol{e}_x \otimes \boldsymbol{e}_x = \frac{\lambda_x^2 - 1}{2}\, \boldsymbol{e}_x \otimes \boldsymbol{e}_x. \tag{A.40}$$

We see that $\epsilon_{ij} = 0$ except for $\epsilon_{xx} = (\lambda_x^2 - 1)/2$. In the first bracket, we distinguish the linear and nonlinear contributions to the strain component ϵ_{xx}. The difference between the non-linearized strain and the linearized strain in the case of uniaxial stretching is plotted in fig. A.3 for $0 < \lambda_x < 2$.

Remark (Physical interpretation of the diagonal components of strain)**.** *The interpretation of the strain component ϵ_{xx} becomes straightforward if we consider an elementary material vector*

22. Only the nonlinear strain tensor (not the linearized strain tensor) is invariant under rigid-body translations.
23. For $\lambda_x = 1$, the *final* configuration is identical to the *initial* configuration and the transformation is the identity mapping.
24. Negative values of λ_x would imply an inversion of the orientation of space.

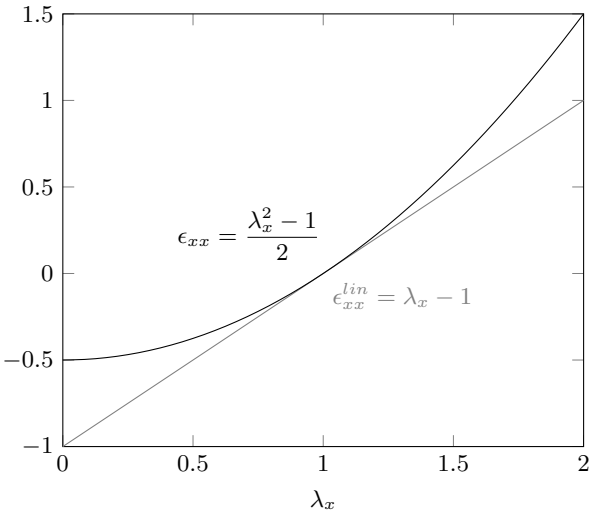

Figure A.3 – Non-linearized ($\epsilon_{xx} = (\lambda_x^2 - 1)/2$) and linearized ($\epsilon_{xx}^{lin} = \lambda_x - 1$) strain in the case of uniaxial stretching for ($0 < \lambda_x < 2$). The linearized strain is a good approximation of the non-linearized strain when the transformation is close to identity ($\lambda_x \approx 1$).

aligned with the x direction in the reference configuration $\mathrm{d}\boldsymbol{r} = \mathrm{d}x\,\boldsymbol{e}_x$*. Upon transformation, the length of this vector is scaled by a factor:*

$$\lambda = \frac{|\mathrm{d}\boldsymbol{r}'|}{|\mathrm{d}\boldsymbol{r}|} = \sqrt{\frac{\mathrm{d}\boldsymbol{r}'^2}{\mathrm{d}\boldsymbol{r}^2}} = \sqrt{\frac{\mathrm{d}x^2 + 2\epsilon_{xx}\mathrm{d}x^2}{\mathrm{d}x^2}} = \sqrt{1 + 2\epsilon_{xx}}. \tag{A.41}$$

When there is no stretching ($\lambda_x = 1$, $\epsilon_{xx} = 0$)*, this number is* $\lambda = 1$*. The stretching rate of* $\mathrm{d}\boldsymbol{r}$ *is then defined as:*

$$\lambda - 1 = \sqrt{1 + 2\epsilon_{xx}} - 1, \tag{A.42}$$

which is positive for actual stretching, negative for contraction and zero when the length is not modified. Combining eq. A.42 with eq. A.40 we find $\lambda = \lambda_x$*, which means that the rate of stretching imposed when building the transformation is recovered for elementary vectors. Another remark is that the strain of this particular transformation is uniform, that is independent of position. This is by no means general and defines what is called a homogeneous transformation. Under the approximation of small strain (eq. A.24), we can do a finite expansion of eq. A.42 around* $|\epsilon_{xx}| \approx 0$ *and obtain:*

$$\lambda - 1 \approx \epsilon_{xx}. \tag{A.43}$$

Under this approximation, the strain component ϵ_{xx} *can be directly interpreted as the rate of stretching or contraction along the x direction*[25]*. In the frame of principal directions*[26]*, the components of the diagonalized strain tensor (the principal strains* $\hat{\epsilon}_{ii}$*) correspond to simple extensions/contractions.*

Simple shear Simple shear between the x and y directions of an object is a priori defined by the transformation:

$$\boldsymbol{r}'(x', y', z') = \begin{pmatrix} x'(x,y,z) \\ y'(x,y,z) \\ z'(x,y,z) \end{pmatrix} = \begin{pmatrix} x + 2\gamma_{xy}y \\ y \\ z \end{pmatrix}, \qquad \gamma_{xy} \in \mathbb{R}_+^*. \tag{A.44}$$

25. This simple interpretation of ϵ_{xx} explains why a factor two was introduced in the definition of the strain tensor in eq. A.10.

26. See appendix A.1.8.

The displacement field is then given by:

$$\boldsymbol{u}(r) = \boldsymbol{r}'(\boldsymbol{r}) - \boldsymbol{r} = \begin{pmatrix} 2\gamma_{xy} y \\ 0 \\ 0 \end{pmatrix} = \gamma_{xy} y \, \boldsymbol{e}_x. \tag{A.45}$$

The only non-zero displacement gradient is:

$$\frac{\delta u_x}{\delta y} = 2\gamma_{xy}. \tag{A.46}$$

From eq. A.11, the components of strain are:

$$\begin{aligned} &\epsilon_{xy} = \frac{1}{2}(2\gamma_{xy}) = \gamma_{xy}, && \epsilon_{yy} = \frac{1}{2}(2\gamma_{xy})^2 = 2\gamma_{xy}^2, \\ &\epsilon_{xx} = 0, && \epsilon_{iz} = 0. \end{aligned} \tag{A.47}$$

The ϵ_{yy} strain component [27] can be nullified by adding a displacement gradient in the y direction:

$$\frac{\delta u_y}{\delta y} = \alpha, \qquad \alpha \in \mathbb{R}. \tag{A.48}$$

When plugged back in eq. A.14, ϵ_{yy} becomes:

$$\epsilon_{yy} = \alpha + \frac{1}{2}(\alpha^2 + 4\gamma_{xy}^2). \tag{A.49}$$

Requiring $\epsilon_{yy} = 0$, the adequate value [28] for α is:

$$\alpha = -1 + \sqrt{1 - 4\gamma_{xy}^2}. \tag{A.50}$$

The correct transformation for simple shear is thus:

$$\boldsymbol{r}'(x', y', z') = \begin{pmatrix} x'(x, y, z) \\ y'(x, y, z) \\ z'(x, y, z) \end{pmatrix} = \begin{pmatrix} x + 2\gamma_{xy} y \\ \sqrt{1 - 4\gamma_{xy}^2}\, y \\ z \end{pmatrix}, \qquad \gamma_{xy} \in \mathbb{R}_+^*. \tag{A.51}$$

$$\boldsymbol{r}'(x', y', z') = \begin{pmatrix} x'(x, y, z) \\ y'(x, y, z) \\ z'(x, y, z) \end{pmatrix} = \begin{pmatrix} x + 2\gamma_{xy} y \\ \sqrt{1 - 4\gamma_{xy}^2}\, y \\ z \end{pmatrix}, \qquad \gamma_{xy} \in \mathbb{R}_+^*. \tag{A.52}$$

The displacement field is then given by:

$$\boldsymbol{u}(r) = \boldsymbol{r}'(\boldsymbol{r}) - \boldsymbol{r} = \begin{pmatrix} 2\gamma_{xy} y \\ (-1 + \sqrt{1 - 4\gamma_{xy}^2})y \\ 0 \end{pmatrix}. \tag{A.53}$$

The only non-zero displacement gradient are:

$$\frac{\delta u_x}{\delta y} = 2\gamma_{xy}, \qquad \frac{\delta u_y}{\delta y} = (-1 + \sqrt{1 - 4\gamma_{xy}^2}). \tag{A.54}$$

27. In the small strain approximation, $\epsilon_{xy} = \gamma_{xy} \ll 1$ and so the ϵ_{yy} strain component is of second order, thus negligible in front of the ϵ_{xy} strain component.

28. According to eq. A.49, there are two displacements gradients in the y direction (α) which lead to the cancellation of the ϵ_{yy} strain component: $\alpha = -1 \pm \sqrt{1 - 4\gamma_{xy}^2}$. As we have $y' = (1 + \alpha)y = \pm\sqrt{1 - 4\gamma_{xy}^2}$ and $y' > 0$, we find $\alpha = -1 + \sqrt{1 - 4\gamma_{xy}^2}$.

From eq. A.11, we find the components of strain:

$$\begin{aligned}\epsilon_{xy} &= \frac{1}{2}(2\gamma_{xy}) = \gamma_{xy}, \qquad \epsilon_{xx} = 0, \qquad \epsilon_{iz} = 0, \\ \epsilon_{yy} &= (-1 + \sqrt{1 - 4\gamma_{xy}^2}) + \frac{1}{2}\left[(-1 + \sqrt{1 - 4\gamma_{xy}^2})^2 + (2\gamma_{xy})^2\right] = 0.\end{aligned} \tag{A.55}$$

In simple shear between the x- and y-axis, only the non-diagonal component ϵ_{xy} is nonzero.

Remark (Physical interpretation of non-diagonal strain components)**.** *Using eq. A.19, the scalar product of two perpendicular material vectors* $\mathrm{d}\boldsymbol{r}^{(x)} = \mathrm{d}x\,\boldsymbol{e}_x$ *and* $\mathrm{d}\boldsymbol{r}^{(y)} = \mathrm{d}y\,\boldsymbol{e}_y$ *which are perpendicular in the initial configuration becomes in the final configuration:*

$$(\mathrm{d}\boldsymbol{r}^{(x)})' \cdot (\mathrm{d}\boldsymbol{r}^{(y)})' = 2\,\epsilon_{xy}\,\mathrm{d}x\,\mathrm{d}y. \tag{A.56}$$

The cosine of the new angle between $(\mathrm{d}\boldsymbol{r}^{(x)})'$ *and* $(\mathrm{d}\boldsymbol{r}^{(y)})'$ *is thus:*

$$\cos\theta' = \frac{2\epsilon_{xy}}{\sqrt{1 + 2\epsilon_{xx}}\sqrt{1 + 2\epsilon_{yy}}}. \tag{A.57}$$

Under the approximation of small strain (eq. A.24), we obtain:

$$\cos\theta' \approx 2\epsilon_{xy}. \tag{A.58}$$

The strain component ϵ_{xy} *can thus be directly linked to the change of angle between the* x *and* y *directions. In general, the strain component* ϵ_{ij} $(i \neq j)$ *can thus be directly linked to the change of angle between the* i *and* j *directions.*

In the small strain approximation, the components of the strain tensor thus possess a straightforward meaning. The diagonal components represent extensions or contractions along the directions of the frame, while the non-diagonal components are associated with shears (change of angles) between these directions [29].

A.1.11 Compatibility of strain

The strain tensor has six independent components while the displacement vector only has three independent components. This means that the task of taking an arbitrary strain field and then trying to find a displacement field from which this strain field derives may be impossible (a solution does not always exist). Therefore the components of strain are subjected to compatibility conditions. These equations of compatibility have to do with the fact that the deformed object lives in Euclidean space and cannot display holes or overlaps upon deformation. If they can be written rather concisely in the small displacement approximation, these compatibility equations become rather cumbersome when keeping the nonlinear dependencies of strain. We do not write them here, because we don't attempt to solve them. However, the compatibility of strain plays a crucial role in *morphing* as we wish to control the *morphing* pattern by imposing an a priori arbitrary *eigenstrain* field. The compatible part of *eigenstrain* simply triggers shape change, while it is their incompatible part that generates internal stresses within the body (see subsection 3.2.2).

A.2 The concept of stress

In this subsection, we introduce the concept of stress. In appendix A.2.1, we start be distinguishing between two types of forces: remote forces, which act over the entire volume of the

29. The components of strain do not possess such a straightforward meaning outside this approximation.

object, and interior forces, which are transmitted across the boundary. In appendix A.2.2, we derive the concept of stress using the balance of linear momentum applied to a small tetrahedron. Similarly to strain, stress inside a body can be represented by a rank-two tensor field, which is symmetric due to the balance of angular momentum. Finally, in appendix A.2.3, we write the equation of static equilibrium in terms of stress.

A.2.1 Remote forces and interior forces

Forces are a foundational concept of physics. A force is defined as what causes mass to accelerate or a body to deform. At the fundamental level, four interactions are conventionally recognized (gravitational, electromagnetic, strong and weak nuclear) and there is an ongoing effort to try to unify them. In the continuum mechanics idealization, however, forces are defined from a classical viewpoint as simply what causes strain without necessarily linking them to elementary interactions. This descriptive gap between fundamental and non-fundamental forces is justified in practice by the utility of this approach [30]. Nevertheless, one should keep in mind that the continuum description is an idealization, which is only valid at orders of magnitude larger than any characteristic microscopic length scale where the material can no longer be considered homogeneous [31]. In order to introduce the concept of stress and to write down the conditions of mechanical equilibrium, let us isolate a small arbitrary volume V of the body and analyze the forces applied to it. We can distinguish between two types of forces [32]: volumic forces which act over the entire volume V and surface forces which are transmitted across its boundary $S = \mathrm{d}V$ [33].

Remote forces Remote forces are long-ranged forces (such as gravity, electric or magnetic forces) also known as volumic forces that affect all points inside V. Let ρ be the volumic mass of the body and $\boldsymbol{g}(\boldsymbol{r})$ the mass density of volumic forces. The total volumic force acting on V is:

$$\mathbf{G} = \iiint_V \rho(\boldsymbol{r})\, \boldsymbol{g}(\boldsymbol{r})\, \mathrm{d}x\, \mathrm{d}y\, \mathrm{d}z. \tag{A.59}$$

Interior forces Interior forces are short-ranged forces (such as interatomic, intermolecular or intergrain forces) between the elementary components of the body. Let $\boldsymbol{f}(\boldsymbol{r}, \boldsymbol{n})$ be the surface density of the interior forces transmitted through the boundary, where $\boldsymbol{r}$ is the position vector spanning the boundary and $\boldsymbol{n}(\boldsymbol{r})$ the local normal to the boundary pointing outwards [34]. The net interior force across the boundary S is:

$$\mathbf{F} = \iint_S \boldsymbol{f}(\boldsymbol{r}, \boldsymbol{n})\, \mathrm{d}S. \tag{A.60}$$

A.2.2 Derivation of the stress tensor

Stress aims at measuring the area density of internal forces throughout a solid body. It corresponds to a force divided by an area and has the dimension of a pressure (Pa or $\mathrm{N\,m^{-2}}$). It can be seen as an extension of the notion of hydrostatic pressure. Unlike most fluids, solids are not only capable to transmit normal forces, but also shear forces. Also, the magnitude of these

30. "We will not get very far in helping the engineer if we keep thinking a bridge as a pile of atoms" Z.Suo

31. In particular, it remains a challenge to successfully describe *natural* materials through a (potentially multi-scaled) continuum approach, as one their main features is to display hierarchical structure and thus possess many intermediate characteristic length scales.

32. We do not consider external forces such as pressure or contact forces.

33. These forces represent the effect of the surrounding medium on this arbitrary volume.

34. The fact that $\boldsymbol{f}$ only depends on the normal $\boldsymbol{n}$ for a given position $\boldsymbol{r}$ is referred to as Cauchy's postulate.

normal forces may also depend on the direction of space. The notion of hydrostatic pressure therefore needs to be extended to account both for shear stresses and for the possible anisotropy of stress.

Balance of linear momentum Let's apply Newton's fundamental law of dynamics to the volume V, with m its mass and $\boldsymbol{a}$ its acceleration:

$$\mathbf{G} + \mathbf{F} = m\boldsymbol{a}. \tag{A.61}$$

If we note $d \sim V^{1/3}$ the typical dimension of the volume, we observe that $\mathbf{G}$ and $m\boldsymbol{a}$ both scale like the volume ($\sim d^3$), whereas $\mathbf{F}$ scales like the area ($\sim d^2$). When d goes to zero area effects dominate volume effects ($d^2/d^3 = 1/d$) and so the net interior force $\mathbf{F}$ (proportional to area) dominates over the total volumic force $\mathbf{G}$ and the change in linear momentum $m\boldsymbol{a}$ (both proportional to volume). At this leading order, the net force $\mathbf{F}$ has to cancel:

$$\lim_{d\to 0} \frac{\mathbf{F}}{d^2} = 0. \tag{A.62}$$

Equilibrium of a tetrahedron Let us consider a tri-rectangular tetrahedron as shown in fig. A.4 positioned such that the normal $\boldsymbol{n}$ to its base displays an arbitrary orientation, while its three other faces are normal to the x, y and z axis of the reference frame. The net force per typical area d^2 of this tetrahedron is obtained by adding the contributions from each face:

$$\frac{\mathbf{F}}{d^2} = \boldsymbol{f}(\boldsymbol{r},\boldsymbol{n})\frac{\mathrm{d}S}{d^2} + \boldsymbol{f}(\boldsymbol{r},-\boldsymbol{e}_x)\frac{\mathrm{d}S^{(x)}}{d^2} + \boldsymbol{f}(\boldsymbol{r},-\boldsymbol{e}_y)\frac{\mathrm{d}S^{(y)}}{d^2} + \boldsymbol{f}(\boldsymbol{r},-\boldsymbol{e}_z)\frac{\mathrm{d}S^{(z)}}{d^2}. \tag{A.63}$$

Using eq. A.62 by letting $d \to 0$ and writing $\mathrm{d}S^{(i)}$ as projections of $\mathrm{d}S$ along the axes of the Cartesian frame ($\mathrm{d}S^{(i)} = \mathrm{d}S\,\boldsymbol{n}\cdot\boldsymbol{e}_i$), we can write:

$$\boldsymbol{f}(\boldsymbol{r},\boldsymbol{n}) = \sigma_{ij}(\boldsymbol{r})\,n_j\,\boldsymbol{e}_i, \tag{A.64}$$

where the quantity $\sigma_{ij}(\boldsymbol{r}) = \boldsymbol{e}_i \cdot \boldsymbol{f}(\boldsymbol{r},\boldsymbol{e}_j)$ [35] has been introduced. Plugging this in eq. A.60, we find:

$$\mathbf{F} = \iint_S \sigma_{ij}(\boldsymbol{r})\,n_j\,\boldsymbol{e}_i\,\mathrm{d}S. \tag{A.65}$$

The components $\sigma_{ij}(\boldsymbol{r})$ are the amount by which the j component of the vector $\boldsymbol{n}\,\mathrm{d}S$ gets multiplied when computing the i component of the interior force. The stress tensor $\boldsymbol{\sigma}(\boldsymbol{r})$ hereby defined entirely characterizes the local state of stress inside the body.

Balance of angular momentum Using a similar reasoning as previously, a balance of angular momentum over a small volume of typical size d shows that the torque due to internal forces is predominant (of order d^3) compared to the torque du to volumic forces (of order d^4) and to the acceleration of rotation (of order d^5). When $d \to 0$, the torque must cancel, which implies the symmetry of the stress tensor [36]:

$$\sigma_{ij} = \sigma_{ji}. \tag{A.66}$$

The stress tensor $\boldsymbol{\sigma}(\boldsymbol{r})$ thus has six a priori independent components [$\sigma_{xx}(\boldsymbol{r})$, $\sigma_{yy}(\boldsymbol{r})$, $\sigma_{zz}(\boldsymbol{r})$, $\sigma_{xy}(\boldsymbol{r})$, $\sigma_{xz}(\boldsymbol{r})$, $\sigma_{yz}(\boldsymbol{r})$] that all potentially depend on $\boldsymbol{r}$. It can be represented by a 3 by 3 symmetric matrix:

$$\boldsymbol{\sigma}(\boldsymbol{r}) = \begin{pmatrix} \sigma_{xx}(\boldsymbol{r}) & \sigma_{xy}(\boldsymbol{r}) & \sigma_{xz}(\boldsymbol{r}) \\ & \sigma_{yy}(\boldsymbol{r}) & \sigma_{yz}(\boldsymbol{r}) \\ & & \sigma_{zz}(\boldsymbol{r}) \end{pmatrix}. \tag{A.67}$$

35. $\boldsymbol{f}(\boldsymbol{r},\boldsymbol{e}_j) = -\boldsymbol{f}(\boldsymbol{r},-\boldsymbol{e}_j)$ according to Newton's third law (action-reaction).
36. See (Audoly and Pomeau 2010, chapter 2) for the complete derivation of the symmetry of the stress tensor.

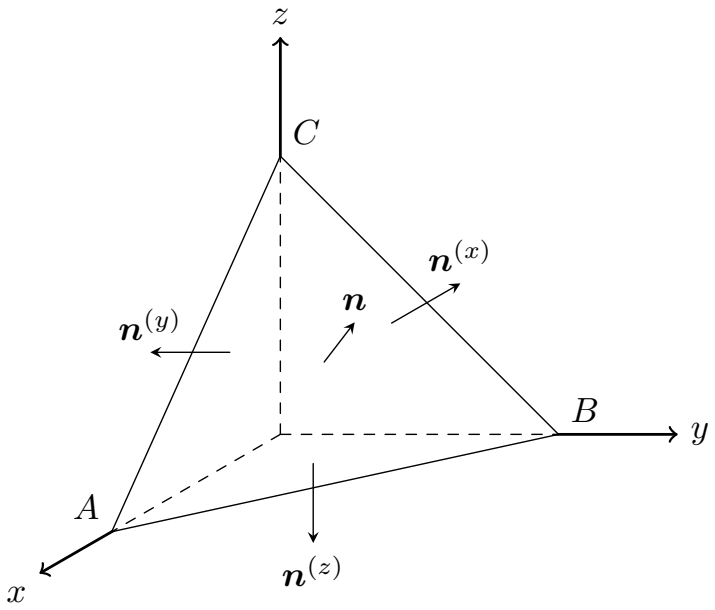

Figure A.4 – Tri-rectangular tetrahedron used to define the stress tensor.

Remark (Physical interpretation of stress components)**.** *The components of the stress tensor have a similar interpretation to the components of the strain tensor. The diagonal components correspond to normal stresses (the interior force $\boldsymbol{f}(\boldsymbol{r}, \boldsymbol{n})$ is aligned with the normal $\boldsymbol{n}$), while the non-diagonal components correspond to shear stresses (the internal force $\boldsymbol{f}(\boldsymbol{r}, \boldsymbol{n})$ is parallel to the boundary of the volume)*[37]*.*

A.2.3 Static equilibrium

The body is in static equilibrium when its linear momentum is equal to zero. Using eq. A.65 and eq. A.59, the balance of force on the isolated volume of the body is equal to:

$$\mathbf{F} + \mathbf{G} = \iint_S \sigma_{ij}(\boldsymbol{r})\, n_j\, \boldsymbol{e}_i \,\mathrm{d}S + \iiint_V \rho\, \boldsymbol{g}(\boldsymbol{r}) \,\mathrm{d}x\,\mathrm{d}y\,\mathrm{d}z. \tag{A.68}$$

Using the divergence theorem[38], the net internal force can be written as a volume integral:

$$\mathbf{F} + \mathbf{G} = \iiint_V \left(\frac{\delta \sigma_{ij}(\boldsymbol{r})}{\delta x_j} + \rho(\boldsymbol{r})\, g_i(\boldsymbol{r}) \right) \boldsymbol{e}_i \,\mathrm{d}V. \tag{A.69}$$

As this true for an arbitrary volume V, the condition of equilibrium for a continuous media is[39]:

$$\frac{\delta \sigma_{ij}(\boldsymbol{r})}{\delta x_j} + \rho(\boldsymbol{r})\, g_i(\boldsymbol{r}) = 0. \tag{A.70}$$

37. Being represented by a real symmetric matrix, the stress tensor can be diagonalized similarly to the strain tensor (see footnote 26). This defines the principal stress directions and the principal stresses. However, the principal stress directions do not correspond to the principal strain directions in general.

38. The divergence theorem is a multi-dimensional generalization of the fundamental formula of calculus $\int_p^q f(x)\mathrm{d}x = f(q) - f(p)$. It relates the divergence of a vector field in a volume to its flux across the boundary of this volume.

39. This is known as the Cauchy-Poisson condition of equilibrium.

In the absence of volumic forces, the equilibrium condition simply becomes [40]:

$$\sigma_{ij,j}(\boldsymbol{r}) = 0. \tag{A.71}$$

A.2.4 Hookean elasticity

In order to close the equations of elasticity, one needs to define a relationship between the strain tensor and the stress tensor. This is the so-called *constitutive* law of the material. As we restrict ourselves to small material strains, we consider the simplest constitutive law there is: Hooke's law of linear elasticity. Published two years before as an anagram *cediinnoopsssttuu* [41], Robert Hooke revealed the subject of the anagram *ut tensio sic vis* that translates to "as the extension, so the force" in Hooke 1678. In the continuum mechanics formalism, this is expressed by a relation of proportionality between the stress tensor and the strain tensor. In the absence of material symmetries, such a relationship possesses thirty-six parameters (the stress and strain tensors are symmetric order-two tensors with six parameters each). The amount of parameters if drastically decreased in the isotropic case as this proportionality relation should be invariant for all changes of the coordinate frame. In fact, it can be shown that any linear relation between two symmetric rank-two tensors that remains invariant under coordinate change takes the following form:

$$\sigma_{ij} = 2\mu\,\epsilon_{ij} + \lambda\,\epsilon_{kk}\,\delta_{ij}. \tag{A.72}$$

The coefficients μ and λ are called the Lamé coefficients and characterize the elasticity of the material and $\epsilon_{kk} = \epsilon_{xx} + \epsilon_{yy} + \epsilon_{zz}$ is the trace of the strain tensor. The previous equation can be rewritten as:

$$\sigma_{ij} = \frac{E}{1+\nu}\left(\epsilon_{ij} + \frac{\nu}{1-2\nu}\,\epsilon_{kk}\,\delta_{ij}\right). \tag{A.73}$$

Comparing the two previous equations shows the relation between the Lamé coefficients and the more known Young modulus E [42] and Poisson ratio ν as:

$$\mu = \frac{E}{2(1+\nu)} \qquad \lambda = \frac{E\nu}{(1+\nu)(1-2\nu)}. \tag{A.74}$$

The constitutive equation can be inverted to rather express the strain as a function of stress:

$$\epsilon_{ij} = \frac{1+\nu}{E}\sigma_{ij} - \frac{\nu}{E}\,\sigma_{kk}\,\delta_{ij}. \tag{A.75}$$

In compact form, we'll simply write:

$$\sigma_{ij} = \mathcal{C}_{ijkl} : \epsilon_{kl}, \qquad \epsilon_{ij} = \mathcal{S}_{ijkl} : \sigma_{kl}, \tag{A.76}$$

where $\mathcal{C}$ and $\mathcal{S} = \mathcal{C}^{-1}$ are the stiffness and compliance rank-four tensors respectively.

Remark (Interpretation of the elastic constants)**.** *The Young modulus E is a positive number, which has the same dimension as stress (*Pa*). A typical strain ϵ induces a typical strain $E\,\epsilon$. To illustrate the meaning of E and ν, let's take an elongated bar of length L and cross-sectional area A under simple traction by a force F. In this case, both stress and strain are homogeneous* [43] *within the bar and the only nonzero component of stress is the longitudinal one $\sigma_{zz} = F/A$. Using the inverse constitutive relation (eq. A.75), we find the diagonal strain components $\epsilon_{zz} = F/EA$ and $\epsilon_{xx} = \epsilon_{yy} = -\nu\epsilon_{zz}$ (the non-diagonal components of strain are zero by symmetry). This*

40. See footnote 23.
41. Anagrams were a common practice at that time to ensure intellectual property
42. The letter E is used in honour of Euler.
43. Actually, stress and strain are only homogeneous far from the ends of the bar, as they may be afffected by the boundary condiditons (this is known as St-Venant's principle).

reveals the meaning of the Poisson's ratio ν, which gives the ratio of the rate of contraction in the cross-section to the rate of elongation along the axis (with a minus sign). The admissible values of Poisson's ratio are in the range $-1 \leq \nu \leq 1/2$ [44].

A.3 Standard mechanical problem

We can now summarize all the equations describing the static equilibrium of a continuous elastic medium in a compact form [45]:

$$\textbf{(SF)} \begin{cases} \nabla \cdot \boldsymbol{\sigma} + \rho\, \boldsymbol{g} = \boldsymbol{0} & \text{in } \Omega, \\ \boldsymbol{\sigma} = \mathcal{C} : \boldsymbol{\epsilon} & \text{in } \Omega, \\ \boldsymbol{\epsilon} = \frac{1}{2}(\nabla \boldsymbol{u} + \nabla^t \boldsymbol{u}) + \frac{1}{2}(\nabla \boldsymbol{u} \cdot \nabla^t \boldsymbol{u}) & \text{in } \Omega, \\ \boldsymbol{\sigma} \cdot \boldsymbol{n} = \boldsymbol{T}_e & \text{on } \delta\Omega_\sigma, \\ \boldsymbol{u} = \boldsymbol{u}_e & \text{on } \delta\Omega_u, \end{cases} \tag{A.77}$$

where Ω is a solid object of boundary $\mathrm{d}\Omega$, $\boldsymbol{u}(\boldsymbol{r})$ is the displacement vector field between the *initial* and the *final* configuration, $\boldsymbol{\sigma}(\boldsymbol{r})$ and $\boldsymbol{\epsilon}(\boldsymbol{r})$ are the elastic stress and strain tensor fields, and $\mathcal{C}$ is the stiffness tensor. The first equation in eq. A.77 expresses static equilibrium [46], the second equation relates stress to strain (Hooke's law of linear elasticity) and the third equation is the definition of strain in terms of displacement gradients. The two last equations express the boundary conditions. $\delta\Omega_\sigma$ and $\delta\Omega_u$ are subsets of $\mathrm{d}\Omega$ where forces $\boldsymbol{T}_e$ and displacements $\boldsymbol{u}_e$ are applied respectively. We have $\delta\Omega = \delta\Omega_\sigma + \delta\Omega_u$, which means that those two boundary conditions are complementary (components by components). In the absence of external fields (such as gravity) or imposed external forces or displacements eq. A.77 becomes:

$$\textbf{(SF)}_0 \begin{cases} \nabla \cdot \boldsymbol{\sigma} = \boldsymbol{0} & \text{in } \Omega, \\ \boldsymbol{\sigma} = \mathcal{C} : \boldsymbol{\epsilon} & \text{in } \Omega, \\ \boldsymbol{\epsilon} = \frac{1}{2}(\nabla \boldsymbol{u} + \nabla^t \boldsymbol{u}) + \frac{1}{2}(\nabla \boldsymbol{u} \cdot \nabla^t \boldsymbol{u}) & \text{in } \Omega, \\ \boldsymbol{\sigma} \cdot \boldsymbol{n} = \boldsymbol{0} & \text{on } \delta\Omega, \end{cases} \tag{A.78}$$

where the boundary condition is now only relative to force as the boundary $\mathrm{d}\Omega$ is free to move. One trivial solution for $\textbf{(SF)}_\textbf{0}$ is that both stress and strain tensor are identically equal to zero within the whole body Ω. This is what is commonly assumed for the reference configuration: a stress-free state. In particular, the stresses due to inter-atomic forces (ionic, metallic and van der Waals forces) are supposed to cancel out and the stresses generated during the manufacturing process of the body are neglected. However, as we'll discuss in subsection 3.2.1, another way to trigger shape changes (generation of stress and strain) is to impose an internal strain distribution (*eigenstrain*) directly in the *initial* state.

A.4 Elastic energy

A different approach to describe the static equilibrium of a body, is to look at his mechanical energy. The equilibrium state of the body corresponds to the strain for which the mechanical

44. This can shown by considering particular classes of normal and shear deformations. The 1/2 bound corresponds to incompressible materials, while negative values for ν correspond to auxetic that have the unintuitive property to expand transversely when stretched.

45. The dependence on position $\boldsymbol{r}$ is implicit (see footnote 6).

46. The condition for static equilibrium can be replaced by the condition that the elastic energy is minimum (see appendix A.4).

energy is minimum [47]. The elastic energy of a continuous elastic medium is defined indirectly by its variation:

$$\delta\mathcal{E}_{el} = \iiint_V \sigma_{ij}\,\delta\epsilon_{ij}\mathrm{d}V. \tag{A.79}$$

By integration, the general expression for the elastic energy is:

$$\mathcal{E}_{el} = \frac{1}{2}\iiint_V \sigma_{ij}[\epsilon_{ij}(\boldsymbol{r}))]\,\epsilon_{ij}(\boldsymbol{r}))\mathrm{d}V. \tag{A.80}$$

where σ_{ij} is linked to ϵ_{ij} through the constitutive relation (see eq. A.72). The condition of equilibrium becomes:

$$\frac{\delta\mathcal{E}_{el}}{\delta\epsilon_{ij}} = 0. \tag{A.81}$$

47. The strain has to be kinematically admissible, which means that it has to be compatible (see appendix A.1.11) and satisfy the displacement boundary conditions (see appendix A.3).

Appendix B

Numerics

B.1 2-D Beam

```
# -*- coding: utf-8 -*-
"""
Created on Tue Feb 14 14:00:28 2012
@author: Felix Repp and Sebastien Turcaud
q
"""
import pdb
import time
import scipy.optimize as op
from enable.component_editor import ComponentEditor
from traits.api import HasTraits,Int,Float,Str,Property,Range,Array,
    cached_property,Color,Instance,on_trait_change
from traitsui.api import View,Item,Label,ApplyButton
from chaco.chaco_plot_editor import ChacoPlotItem
from chaco.api import Plot,ArrayPlotData
from pylab import *

class Beam_2D(HasTraits):
        x0=0.
        z0=0.
        theta0=Range(-pi,pi,pi/2)
        N=Range(10,1000,20)
        L=Float(1.)
        alpha=Range(-5.,5.,0.)
        beta=Range(0.,1000.,0.)
        x=Array()
        z=Array()
        theta=Array()
        kappa=Array()
        kappaopt=Array()
        e_elastic=Float()
        e_potential=Float()
        e_total=Float()
        plotinstance=None
        color=Color('blue')
```

```
    traits_view = View(
            ChacoPlotItem("x","z", x_bounds=(-1.,1.),y_bounds
                =(-1.,1.),
            x_auto=False,y_auto=False,resizable=True,show_label=
                False,x_label="x",y_label="z",title=""),
            Item(name='N'),Item(name='L'),Item(name='beta'),Item(
                name='alpha'),Item(name='theta0'),
            Item(name='e_elastic'),Item(name='e_potential'),Item(
                name='e_total'),
            #buttons=[ApplyButton],
            resizable=True,width=600,height=500,title="2D Beam")

    def __init__(self):
            self.kappa0=self.getKappa0()
            self.minimizeEnergy()

    def getKappa0(self):
            return -2*pi*self.L*self.alpha*ones(self.N-2)

    def intTheta(self,theta):
            ds=self.L/(self.N-1)
            x=zeros(theta.shape[0]+1)
            z=zeros(theta.shape[0]+1)
            x[0]=self.x0
            z[0]=self.z0
            for i in range(0,theta.shape[0]):
                    x[i+1]=x[i]+ds*cos(theta[i])
                    z[i+1]=z[i]+ds*sin(theta[i])
            return x,z

    # def derTheta(self,theta):
            # ds=self.L/(self.N-1)
            # kappa=(theta[1:]-theta[:-1])/ds
            # return kappa

    def intKappa(self,kappa):
            ds=self.L/(self.N-1)
            theta=zeros(kappa.shape[0]+1)
            theta[0]=self.theta0
            for i in range(0,kappa.shape[0]):
                    # theta[i+1]=theta[i]+math.atan(kappa[i]/2)
                    theta[i+1]=theta[i]+ds*kappa[i]
            return theta

    def Energy(self,kappa):
            # if  kappa.__class__==(1,0).__class__:
                    # kappa=kappaopt[0]
            ds=self.L/(self.N-1)
            theta=self.intKappa(kappa)
            x,z=self.intTheta(theta)
```

```
            self.e_elastic=ds/2*sum((kappa-self.kappa0)**2)
            self.e_potential=ds*self.beta*sum(z)
            self.e_total=self.e_elastic+self.e_potential
            return self.e_total

    def minimizeEnergy(self):
            # pdb.set_trace()
            kappa0=self.kappa0
            #
            self.kappaopt=op.fmin_bfgs(self.Energy,kappa0)
            #
            # if  kappaopt.__class__==(1,0).__class__:
                            # kappaopt=kappaopt[0]
            # self.thetafin=append([self.theta0],thetaopt,axis=0)
            self.theta=self.intKappa(self.kappaopt)
            self.x,self.z=self.intTheta(self.theta)
            return

    # def plotbeam(self):
            # self.plotinstance=plot(self.x,self.z,color=self.
                color)
            # print thetafin
            # print derTheta(thetaopt)

    def apply(self,info):
            self.apply_()
            self.kappa0=self.getKappa0()
            mimumizeEnergy()
            self.replot()
            return

    def _L_changed(self,info):
            self.kappa0=self.getKappa0()
            self.minimizeEnergy()
            return

    def _N_changed(self,info):
            self.kappa0=self.getKappa0()
            self.minimizeEnergy()
            return

    def _alpha_changed(self,info):
            self.kappa0=self.getKappa0()
            self.minimizeEnergy()
            return

    def _beta_changed(self,info):
            self.minimizeEnergy()
            return

    def _theta0_changed(self,info):
```

```
                self.minimizeEnergy()
                return

beam_2D=Beam_2D()

beam_2D.configure_traits()
```

B.2 3-D Beam

```
# -*- coding: utf-8 -*-
"""
Created on Tue Feb 14 14:00:28 2012
@author: Felix Repp and Sebastien Turcaud
q
"""
import pdb
import time
import scipy.optimize as op
from enable.component_editor import ComponentEditor
from traits.api import HasTraits,Int,Float,Str,Property,Range,Array,
    cached_property,Color,Instance,on_trait_change
from traitsui.api import View,Item,Label,ApplyButton
from chaco.chaco_plot_editor import ChacoPlotItem
from chaco.api import Plot,ArrayPlotData
from pylab import *
from mayavi.core.api import PipelineBase
from mayavi.core.ui.api import MayaviScene,SceneEditor,MlabSceneModel

class Beam_3D(HasTraits):
        #Number of Points
        N=Range(3,1000,10)
        #Length
        L=Float(1.)
        #Coordinates
        x=Array()
        y=Array()
        z=Array()
        #Origin
        x0=0.
        y0=0.
        z0=0.
        #Position Vector
        r=Array()
        r0=x0,y0,z0
        #Material Frames
        d1=Array()
        d2=Array()
        d3=Array()
        #Initial Material Frames (POSSIBILITY TO ROTATE INITIAL FRAME
            )
```

```
        d10=array([1.,0.,0.])
        d20=array([0.,1.,0.])
        d30=array([0.,0.,1.])
        #Scalar Products
        s12=Array()
        s13=Array()
        s23=Array()
        #Curvatures and Twist
        kappa1=Array()
        kappa2=Array()
        kappa3=Array()
        #Darboux Vector
        omega0=Array()
        omega=Array()
        #Natural Curvatures and Twist
        kappa10=Range(-20.,20.,0.)
        kappa20=Range(-20.,20.,0.)
        kappa30=Range(-20.,20.,0.)
        #Magnitude of Potential Energy
        g=Range(-10000.,10000.,0.)
        #Energy
        e_elastic1=Float()
        e_elastic2=Float()
        e_elastic3=Float()
        e_elastic=Float()
        e_potential=Float()
        e_total=Float()

        plotinstance=None
        color=Color('blue')
        scene=Instance(MlabSceneModel,())
        plot=Instance(PipelineBase)
        linesource=None
        vectorsource=None

        traits_view = View(
                Item('scene',editor=SceneEditor(scene_class=
                    MayaviScene),height=250,width=300,show_label=False
                    ),
                Item(name='N'),Item(name='L'),Item(name='kappa10'),
                    Item(name='kappa20'),Item(name='kappa30'),Item(
                    name='g'),
                Item(name='e_elastic1'),Item(name='e_elastic2'),Item(
                    name='e_elastic3'),Item(name='e_elastic'),Item(
                    name='e_potential'),Item(name='e_total'),
                #buttons=[ApplyButton],
                resizable=True,width=600,height=500,title="Beam_3D")

        def update_plot(self):
                if self.plot is None:
```

```
                self.plot=self.scene.mlab.plot3d(self
                    .x,self.y,self.z,tube_radius=0.01,
                    colormap='Spectral')
                self.linesource=self.plot.mlab_source
                self.plot=self.scene.mlab.quiver3d((
                    self.x[:-1]+self.x[1:])/2,(self.y
                    [:-1]+self.y[1:])/2,(self.z[:-1]+
                    self.z[1:])/2,self.d1[:,0],self.d1
                    [:,1],self.d1[:,2])
                self.vectorsource1=self.plot.
                    mlab_source
                self.plot=self.scene.mlab.quiver3d((
                    self.x[:-1]+self.x[1:])/2,(self.y
                    [:-1]+self.y[1:])/2,(self.z[:-1]+
                    self.z[1:])/2,self.d2[:,0],self.d2
                    [:,1],self.d2[:,2])
                self.vectorsource2=self.plot.
                    mlab_source
                self.plot=self.scene.mlab.quiver3d((
                    self.x[:-1]+self.x[1:])/2,(self.y
                    [:-1]+self.y[1:])/2,(self.z[:-1]+
                    self.z[1:])/2,self.d3[:,0],self.d3
                    [:,1],self.d3[:,2])
                self.vectorsource3=self.plot.
                    mlab_source
                self.plot=self.scene.mlab.quiver3d(
                    self.x[1:-1],self.y[1:-1],self.z
                    [1:-1],self.omega[:,0],self.omega
                    [:,1],self.omega[:,2])
                self.vectorsourceD=self.plot.
                    mlab_source
            else:
                self.linesource.reset(x=self.x,y=self
                    .y,z=self.z)
                self.vectorsource1.reset(x=(self.x
                    [:-1]+self.x[1:])/2,y=(self.y
                    [:-1]+self.y[1:])/2,z=(self.z
                    [:-1]+self.z[1:])/2,u=self.d1
                    [:,0],v=self.d1[:,1],w=self.d1
                    [:,2])
                self.vectorsource2.reset(x=(self.x
                    [:-1]+self.x[1:])/2,y=(self.y
                    [:-1]+self.y[1:])/2,z=(self.z
                    [:-1]+self.z[1:])/2,u=self.d2
                    [:,0],v=self.d2[:,1],w=self.d2
                    [:,2])
                self.vectorsource3.reset(x=(self.x
                    [:-1]+self.x[1:])/2,y=(self.y
                    [:-1]+self.y[1:])/2,z=(self.z
                    [:-1]+self.z[1:])/2,u=self.d3
                    [:,0],v=self.d3[:,1],w=self.d3
```

```
                                    [:,2])
                                self.vectorsourceD.reset(x=self.x
                                    [1:-1],y=self.y[1:-1],z=self.z
                                    [1:-1],u=self.omega[:,0],v=self.
                                    omega[:,1],w=self.omega[:,2])

    def __init__(self):
            self.omega0=self.getOmega0()
            self.minimizeEnergy()

    def getKappa10(self):
            return array(2*pi*self.L*self.kappa10*ones(self.N-1))
            # return array(self.kappa10*ones(self.N-1))

    def getKappa20(self):
            return array(2*pi*self.L*self.kappa20*ones(self.N-1))
            # return array(self.kappa20*ones(self.N-1))

    def getkappa30(self):
            return array(2*pi*self.L*self.kappa30*ones(self.N-1))
            # return array(self.kappa30*ones(self.N-1))

    def getOmega0(self):
            return array([self.getKappa10(),self.getKappa20(),
                self.getkappa30()])

    def inttOmega(self,omega):
            ds=self.L/(self.N-1)
            r=[self.r0]
            x=[self.x0]
            y=[self.y0]
            z=[self.z0]
            d1=[self.d10]
            d2=[self.d20]
            d3=[self.d30]
            s12=[]
            s13=[]
            s23=[]
            # pdb.set_trace()
            omega=omega.reshape(3,-1).transpose()
            for i in range(self.N-1):
                    d1.append((d1[i]+ds*cross(omega[i],d1[i]))/
                        norm(d1[i]+ds*cross(omega[i],d1[i])))
                    d2.append((d2[i]+ds*cross(omega[i],d2[i]))/
                        norm(d2[i]+ds*cross(omega[i],d2[i])))
                    d3.append((d3[i]+ds*cross(omega[i],d3[i]))/
                        norm(d3[i]+ds*cross(omega[i],d3[i])))
                    s12.append(d1[i][0]*d2[i][0]+d1[i][1]*d2[i
                        ][1]+d1[i][2]*d2[i][2])
                    s13.append(d1[i][0]*d3[i][0]+d1[i][1]*d3[i
                        ][1]+d1[i][2]*d3[i][2])
```

```
                s23.append(d2[i][0]*d3[i][0]+d2[i][1]*d3[i
                    ][1]+d2[i][2]*d3[i][2])
                print s12[i],s13[i],s23[i],omega[i],norm(ds*
                    omega[i])
        self.d1=array(d1)
        self.d2=array(d2)
        self.d3=array(d3)
        self.s12=array(s12)
        self.s13=array(s13)
        self.s23=array(s23)
        for i in range(self.N):
                r.append(r[i]+ds*self.d3[i])
        r=array(r)
        for i in range(1,self.N+1):
                x.append(r[i][0])
                y.append(r[i][1])
                z.append(r[i][2])
        x=array(x)
        y=array(y)
        z=array(z)
        return r,x,y,z

    def Energy(self,omega):
        ds=self.L/(self.N-1)
        r,x,y,z=self.inttOmega(omega)
        kappa1=[]
        kappa2=[]
        kappa3=[]
        omega=omega.reshape(3,-1)
        kappa1.append(omega[0])
        kappa2.append(omega[1])
        kappa3.append(omega[2])
        kappa1=array(kappa1)
        kappa2=array(kappa2)
        kappa3=array(kappa3)
        kappa10=self.getKappa10()
        kappa20=self.getKappa20()
        kappa30=self.getkappa30()
        self.e_elastic1=ds/2*sum((kappa1-kappa10)**2)
        self.e_elastic2=ds/2*sum((kappa2-kappa20)**2)
        self.e_elastic3=ds/2*sum((kappa3-kappa30)**2)
        self.e_elastic=self.e_elastic1+self.e_elastic2+self.
            e_elastic3
        self.e_potential=ds*self.g*sum(z)
        self.e_total=self.e_elastic+self.e_potential
        return self.e_total

    def minimizeEnergy(self):
        omega0=self.omega0
        self.omega=op.fmin_bfgs(self.Energy,omega0)
```

```
                self.r,self.x,self.y,self.z=self.inttOmega(self.omega
                    )
                self.omega=self.omega.reshape(3,-1)
                self.kappa1=self.omega[0]/(2*pi*self.L)
                # self.kappa1=self.omega[0]
                self.kappa2=self.omega[1]/(2*pi*self.L)
                # self.kappa2=self.omega[1]
                self.kappa3=self.omega[2]/(2*pi*self.L)
                # self.kappa3=self.omega[2]
                self.omega=self.omega.transpose()
                self.update_plot()
                return

        def apply(self,info):
                self.apply_()
                self.omega0=self.getOmega0()
                mimumizeEnergy()
                self.replot()
                return

        def _L_changed(self,info):
                self.omega0=self.getOmega0()
                self.minimizeEnergy()
                return

        def _N_changed(self,info):
                self.omega0=self.getOmega0()
                self.minimizeEnergy()
                return

        def _kappa10_changed(self,info):
                self.omega0=self.getOmega0()
                self.minimizeEnergy()
                return

        def _kappa20_changed(self,info):
                self.omega0=self.getOmega0()
                self.minimizeEnergy()
                return

        def _kappa30_changed(self,info):
                self.omega0=self.getOmega0()
                self.minimizeEnergy()
                return

        def _g_changed(self,info):
                self.minimizeEnergy()
                return
                return

beam_3D=Beam_3D()
```

```
# plot(beam_3D.x,beam_3D.z)

## 3D Plot
# import matplotlib.pyplot as plt
# from mpl_toolkits.mplot3d import Axes3D
# fig = plt.figure()
# ax = fig.add_subplot(111,projection='3d')
# ax.plot(beam.x,beam.y,zs=beam.z)
beam_3D.configure_traits()

# from mayavi import mlab
# h=1
# mlab.quiver3d((beam_3D.x[:-1:h]+beam_3D.x[1::h])/2,(beam_3D.y[:-1:h
    ]+beam_3D.y[1::h])/2,(beam_3D.z[:-1:h]+beam_3D.z[1::h])/2,beam_3D.
    d1[:,0][::h],beam_3D.d1[:,1][::h],beam_3D.d1[:,2][::h])
# mlab.quiver3d((beam_3D.x[:-1:h]+beam_3D.x[1::h])/2,(beam_3D.y[:-1:h
    ]+beam_3D.y[1::h])/2,(beam_3D.z[:-1:h]+beam_3D.z[1::h])/2,beam_3D.
    d2[:,0][::h],beam_3D.d2[:,1][::h],beam_3D.d2[:,2][::h])
# mlab.quiver3d((beam_3D.x[:-1:h]+beam_3D.x[1::h])/2,(beam_3D.y[:-1:h
    ]+beam_3D.y[1::h])/2,(beam_3D.z[:-1:h]+beam_3D.z[1::h])/2,beam_3D.
    d3[:,0][::h],beam_3D.d3[:,1][::h],beam_3D.d3[:,2][::h])

# Material Frames
# beam_3D.scene.mlab.quiver3d(beam_3D.x[:-1],beam_3D.y[:-1],beam_3D.z
    [:-1],beam_3D.d1[:,0],beam_3D.d1[:,1],beam_3D.d1[:,2])
# beam_3D.scene.mlab.quiver3d(beam_3D.x[:-1],beam_3D.y[:-1],beam_3D.z
    [:-1],beam_3D.d2[:,0],beam_3D.d2[:,1],beam_3D.d2[:,2])
# beam_3D.scene.mlab.quiver3d(beam_3D.x[:-1],beam_3D.y[:-1],beam_3D.z
    [:-1],beam_3D.d3[:,0],beam_3D.d3[:,1],beam_3D.d3[:,2])
```

B.3 Cuboid

```
"This Python script works with Abaqus 6.6"
"Author: Sebastien Turcaud"
"Date: June 2010"

from abaqus import *
from abaqusConstants import *

from abaqus import getInputs
from abaqus import getWarningReply,YES,NO
import random

os.chdir(r'C:/Documents and Settings/Sebastien Turcaud/My Documents/
    Seb/Abaqus')

# Create a model

Mdb()
myModel = mdb.Model(name='Beam')
```

```
del mdb.models['Model-1']

# Viewport

myViewport = session.viewports['Viewport: 1']

##########################
#GEOMETRY and PARTITION#
##########################

import part

## User input window

fields = (('a:','1'),('b:','1'),('L:','1'))
a,b,L = getInputs(fields=fields,label='Specify dimensions:',
    dialogTitle='Create Block',)
a = float(a)
b = float(b)
L = float(L)

# Create a sketch for the base feature

mySketch = myModel.Sketch(name='beamProfile',sheetSize=max(a,b))

# Create the rectangle

mySketch.rectangle(point1=(-a/2,b/2),point2=(a/2,-b/2))

# Create a three-dimensional, deformable part

myBeam = myModel.Part(name='Beam',dimensionality=THREE_D,type=
    DEFORMABLE_BODY)

# Coordinate system

myBeam.DatumCsysByThreePoints(origin=(0,0,0),point1=(0,0,L),point2=(a
    /2,0,0),name='CSYS',coordSysType=CARTESIAN)

# Create the part's base feature by extruding the sketch through a
    distance of L

myPart = myBeam.BaseSolidExtrude(sketch=mySketch,depth=L)

myViewport.view.fitView()
myViewport.view.setValues(session.views['Iso'])
myViewport.view.setProjection(projection=PARALLEL)
myViewport.setValues(displayedObject=myBeam)

# Partitions
```

```
## User input window

fields = (('Horizontal:','2'),('Vertical:','2'),('Longitudinal:','2')
    )
h,v,l = getInputs(fields=fields,label='Specify partitioning:',
    dialogTitle='Orthogonal grid',)
h = int(h)
v = int(v)
l = int(l)

horizontal,vertical,longitudinal = (),(),()

for i in range(1,h):
    horizontal = horizontal + ((-a/2+i*a/h,-b/2,0),)

for j in range(1,v):
    vertical = vertical + ((-a/2,-b/2+j*b/v,0),)

for k in range(1,l):
    longitudinal = longitudinal + ((-a/2,-b/2,k*L/l),)

for i in range(len(horizontal)):
    myBeam.PartitionCellByPlaneNormalToEdge(edge=myBeam.edges.findAt(
        horizontal[i]),point=horizontal[i],cells=myBeam.cells)

for j in range(len(vertical)):
    myBeam.PartitionCellByPlaneNormalToEdge(edge=myBeam.edges.findAt(
        vertical[j]),point=vertical[j],cells=myBeam.cells)

for k in range(len(longitudinal)):
    myBeam.PartitionCellByPlaneNormalToEdge(edge=myBeam.edges.findAt(
        longitudinal[k]),point=longitudinal[k],cells=myBeam.cells)

myViewport.setColor(colorMapping=myViewport.colorMappings['Section'])
myViewport.disableMultipleColors()
myViewport.enableMultipleColors()
myViewport.setColor(initialColor='#3DB3FF',translucency=0.3)

# Define regions

region = [[[0 for i in range(h)] for j in range(v)] for k in range(l)
    ]

for k in range(l):
    for j in range(v):
        for i in range(h):
            region[k][j][i] = (myBeam.cells.findAt(((-a/2+a/(2*h)+i*a
                /h,-b/2+b/(2*v)+j*b/v,L/(2*l)+k*L/l),),),)
            myBeam.DatumPointByCoordinate(coords=(-a/2+a/(2*h)+i*a/h
                ,-b/2+b/(2*v)+j*b/v,L/(2*l)+k*L/l))
```

```
            myBeam.assignMaterialOrientation(region=region[k][j][i],
                localCsys=myBeam.datums[1])

##########
#MATERIAL#
##########

import material

# Create materials

myNeutral = myModel.Material(name='Neutral')
myExpanding = myModel.Material(name='Expanding')

## User input window

fields1 = (('Young:','1'),('Poisson:','0.3'))
fields2 = (('Young:','1'),('Poisson:','0.3'))
youngn,poissonn = getInputs(fields=fields1,label='Neutral:',
    dialogTitle='Elastic properties',)
younge,poissone = getInputs(fields=fields2,label='Expanding:',
    dialogTitle='Elastic properties',)
youngn = float(youngn)
poissonn = float(poissonn)
younge = float(younge)
poissone = float(poissone)

## User input window

fields1 = (('Neutral1:','0'),('Neutral2:','0'),('Neutral3:','0'))
fields2 = (('Expanding1:','1'),('Expanding2:','0'),('Expanding3:','0'
    ))
alphan1,alphan2,alphan3 = getInputs(fields=fields1,label='Neutral:',
    dialogTitle='Expansion',)
alphae1,alphae2,alphae3 = getInputs(fields=fields2,label='Expanding:'
    ,dialogTitle='Expansion',)
T = float(getInput('Temperature:','1'))
alphan1 = float(alphan1)
alphan2 = float(alphan2)
alphan3 = float(alphan3)
alphae1 = float(alphae1)
alphae2 = float(alphae2)
alphae3 = float(alphae3)

# Create the material properties

expansionPropertiesNeutral=(alphan1,alphan2,alphan3)
myNeutral.Elastic(table=((youngn,poissonn),))
myNeutral.Expansion(type=ORTHOTROPIC,table=((
    expansionPropertiesNeutral),))
```

```
expansionPropertiesExpanding=(alphae1,alphae2,alphae3)
myExpanding.Elastic(table=((younge,poissone),))
myExpanding.Expansion(type=ORTHOTROPIC,table=((
    expansionPropertiesExpanding),))

##########################
#SECTION and ASSIGNEMENT#
##########################

import section

# Create sections

myNeutralSection = myModel.HomogeneousSolidSection(name='
    beamNeutralSection',material='Neutral',thickness=1.0)
myExpandingSection = myModel.HomogeneousSolidSection(name='
    beamExpandingSection',material='Expanding',thickness=1.0)

### Display the materials
##
##myViewport.setColor(initialColor='#BDBDBD',translucency=0.5)
##myViewport.setColor(colorMapping=myViewport.colorMappings['Material
    '])

# Assign algorithms #

##            # Pick
##for k in range(l):
##    for j in range(v):
##        for i in range(h):
##            highlight(region[k][j][i][0][0])
##            section = getWarningReply(message='Expanding element?',
    buttons=(YES,NO))
##            if section == YES:
##                myBeam.SectionAssignment(region=region[k][j][i],
    sectionName='beamExpandingSection')
##            elif section == NO:
##                myBeam.SectionAssignment(region=region[k][j][i],
    sectionName='beamNeutralSection')
##            unhighlight(region[k][j][i][0][0])
##            #
##            # Random
##P = float(getInput('Percent:','50'))
##for k in range(l):
##    for j in range(v):
##        for i in range(h):
##            R = random.random()
##            print R
##            if R <= P/100:
##                myBeam.SectionAssignment(region=region[k][j][i],
    sectionName='beamExpandingSection')
```

```
##                elif R > P/100:
##                    myBeam.SectionAssignment(region=region[k][j][i],
    sectionName='beamNeutralSection')
##                #
            # Helix (general)
for k in range(l):
    for j in range(v):
        for i in range(h):
            c_hp = int(ceil(h/2))
            c_vp = int(ceil(v/2))
            c_hm = int(floor(h/2))
            c_vm = int(floor(v/2))
            if k%4==0:
                if i==0 and j==0:
                    for x in range(c_hp):
                        for y in range(c_vp):
                            myBeam.SectionAssignment(region=region[k
                                ][j+y][i+x],sectionName='
                                beamExpandingSection')
                elif i>=c_hp or j>=c_vp:
                    myBeam.SectionAssignment(region=region[k][j][i],
                        sectionName='beamNeutralSection')
            elif k%4==1:
                if i==0 and j==c_vm:
                    for x in range(c_hp):
                        for y in range(c_vp):
                            myBeam.SectionAssignment(region=region[k
                                ][j+y][i+x],sectionName='
                                beamExpandingSection')
                elif i>=c_hp or j<c_vm:
                    myBeam.SectionAssignment(region=region[k][j][i],
                        sectionName='beamNeutralSection')
            elif k%4==2:
                if i==c_hm and j==c_vm:
                    for x in range(c_hp):
                        for y in range(c_vp):
                            myBeam.SectionAssignment(region=region[k
                                ][j+y][i+x],sectionName='
                                beamExpandingSection')
                elif i<c_hm or j<c_vm:
                    myBeam.SectionAssignment(region=region[k][j][i],
                        sectionName='beamNeutralSection')
            elif k%4==3:
                if i==c_hm and j==0:
                    for x in range(c_hp):
                        for y in range(c_vp):
                            myBeam.SectionAssignment(region=region[k
                                ][j+y][i+x],sectionName='
                                beamExpandingSection')
                elif i<c_hm or j>=c_vp:
```

```
                        myBeam.SectionAssignment(region=region[k][j][i],
                            sectionName='beamNeutralSection')
                #
##                  myViewport.forceRefresh()
##                  myViewport.setColor(initialColor='#BDBDBD',translucency
    =0.5)
##                  myViewport.setColor(colorMapping=myViewport.
    colorMappings['Material'])

##########
#ASSEMBLY#
##########

import assembly

# Create a part instance

myAssembly = myModel.rootAssembly
myInstance = myAssembly.Instance(name='beamInstance',part=myBeam,
    dependent=OFF)

######
#STEP#
######

import step

# Create a step

myModel.StaticStep(name='beamLoad',previous='Initial',timePeriod=1.0,
    initialInc=0.01,maxNumInc=1000,timeIncrementationMethod=AUTOMATIC,
    description='Thermal loading of the beam',nlgeom=ON)

######
#LOAD#
######

import load

# Create a boundary condition that fixes four point of the beam

##Point1 = myInstance.vertices.findAt(((-a/2,-b/2,0),))
##Point2 = myInstance.vertices.findAt((( a/2,-b/2,0),))
##Point3 = myInstance.vertices.findAt((( a/2, b/2,0),))
##Point4 = myInstance.vertices.findAt(((-a/2, b/2,0),))
##
##myModel.DisplacementBC(name='Fixed1',createStepName='Initial',
    region=(Point1,),u1=0,u2=0,u3=0)
##myModel.DisplacementBC(name='Fixed2',createStepName='Initial',
    region=(Point2,),u1=0,u2=0,u3=0)
```

```
##myModel.DisplacementBC(name='Fixed3', createStepName='Initial',
    region=(Point3,), u1=0, u2=0, u3=0)
##myModel.DisplacementBC(name='Fixed4', createStepName='Initial',
    region=(Point4,), u1=0, u2=0, u3=0)

# Create a thermal load

myModel.Temperature(name='Final', createStepName='beamLoad', region=(
    myInstance.cells,), distributionType=UNIFORM,
    crossSectionDistribution=CONSTANT_THROUGH_THICKNESS, magnitudes=(T
    ,))

######
#MESH#
######

import mesh

# Assign an element type to the part instance

elemType = mesh.ElemType(elemCode=C3D8, elemLibrary=STANDARD)
myAssembly.setElementType(regions=(myInstance.cells,), elemTypes=(
    elemType,))

## User input window

density = eval(getInput('Enter mesh density:', '2'))

# Seed the Edges

Edgesh1, Edgesh2 = (), ()
for i in range(h):
    for k in range(l+1):
        Edgesh1 = Edgesh1 + (myInstance.edges.findAt(((-a/2+a/(2*h)+i
            *a/h, b/2, L-k*L/l),)),)
        Edgesh2 = Edgesh2 + (myInstance.edges.findAt(((-a/2+a/(2*h)+i
            *a/h, -b/2, L-k*L/l),)),)

for i in range(h*(l+1)):
    myAssembly.seedEdgeByNumber(edges=Edgesh1[i], number=density)
    myAssembly.seedEdgeByNumber(edges=Edgesh2[i], number=density)

Edgesv1, Edgesv2 = (), ()
for j in range(v):
    for k in range(l+1):
        Edgesv1 = Edgesv1 + (myInstance.edges.findAt(((-a/2, b/2-b/(2*
            v)-j*b/v, L-k*L/l),)),)
        Edgesv2 = Edgesv2 + (myInstance.edges.findAt(((  a/2, b/2-b/(2*
            v)-j*b/v, L-k*L/l),)),)

for j in range(v*(l+1)):
```

```
    myAssembly.seedEdgeByNumber(edges=Edgesv1[j],number=density)
    myAssembly.seedEdgeByNumber(edges=Edgesv2[j],number=density)

Edgesl1,Edgesl2,Edgesl3,Edgesl4 = (),(),(),()
for k in range(l):
    Edgesl1 = Edgesl1 + (myInstance.edges.findAt(((-a/2, b/2,L-L/(2*l
        )-k*L/l),)),)
    Edgesl2 = Edgesl2 + (myInstance.edges.findAt(((  a/2, b/2,L-L/(2*l
        )-k*L/l),)),)
    Edgesl3 = Edgesl3 + (myInstance.edges.findAt(((-a/2,-b/2,L-L/(2*l
        )-k*L/l),)),)
    Edgesl4 = Edgesl4 + (myInstance.edges.findAt(((  a/2,-b/2,L-L/(2*l
        )-k*L/l),)),)
    myAssembly.seedEdgeByNumber(edges=Edgesl1[k],number=density)
    myAssembly.seedEdgeByNumber(edges=Edgesl2[k],number=density)
    myAssembly.seedEdgeByNumber(edges=Edgesl3[k],number=density)
    myAssembly.seedEdgeByNumber(edges=Edgesl4[k],number=density)

# Mesh the part instance

myAssembly.generateMesh(regions=(myInstance,))

# Display the meshed beam

myViewport.partDisplay.setValues(mesh=ON)
myViewport.setValues(displayedObject=myAssembly)

#####
#JOB#
#####

import job

# Create an analysis job for the model and submit it

jobName = 'beam_thermal'
myJob = mdb.Job(name=jobName,model='Beam',description='Beam thermal
    deformation')
myJob.setValues(preMemory=10000,standardMemory=1000000,
    standardMemoryPolicy=MAXIMUM)

# Output

myModel.FieldOutputRequest(name='Output',createStepName='beamLoad',
    variables=('S','E','EE','THE','U','RBANG','RBROT','TEMP','EVOL','
    COORD'))

# Wait for the job to complete

myJob.submit()
myJob.waitForCompletion()
```

```
###############
#VISUALIZATION#
###############

import visualization

# Open the output database and display a displacement contour plot

myOdb = session.openOdb(name=jobName + '.odb')
myViewport.setValues(displayedObject=myOdb)
myViewport.odbDisplay.setFrame(step='beamLoad',frame=100)
##myViewport.odbDisplay.setPrimaryVariable(variableLabel='U',
    outputPosition=NODAL, refinement=(INVARIANT, 'Magnitude'))
myViewport.odbDisplay.setPrimaryVariable(variableLabel='EE',
    outputPosition=INTEGRATION_POINT, refinement=(INVARIANT, 'Max.
    Principal'))
myViewport.odbDisplay.commonOptions.setValues(uniformScaleFactor=1,
    deformationScaling=UNIFORM)
myViewport.odbDisplay.display.setValues(plotState=(DEFORMED,))
myViewport.view.fitView()

# Movie

myViewport.forceRefresh()
myViewport.setColor(initialColor='#BDBDBD',translucency=0.5)
myViewport.setColor(colorMapping=myViewport.colorMappings['Material'
    ])
session.animationController.animationOptions.setValues(frameRate=40,
    mode=SWING)
session.animationController.setValues(animationType=TIME_HISTORY,
    viewports=('Viewport: 1', ))
session.animationController.play(duration=UNLIMITED)
```

Appendix C

Experiments

This appendix gives the characterization of the mechanical and expansion properties of the materials presented in chapter 5.

C.1 Characterization of mechanical properties of elastomers

Tensile testing was done using a classical tensile machine from Zwick®.

PDMS Dogbone samples were cast in a mold made of photo-polymer produced by 3D prototyping. The dimensions are $L = 2.5\,\text{cm}$, $B = 1.0\,\text{cm}$ and $T = 0.5\,\text{cm}$, where L, B and T are the length, center width and thickness respectively (fig. C.1a). At room temperature, PDMS

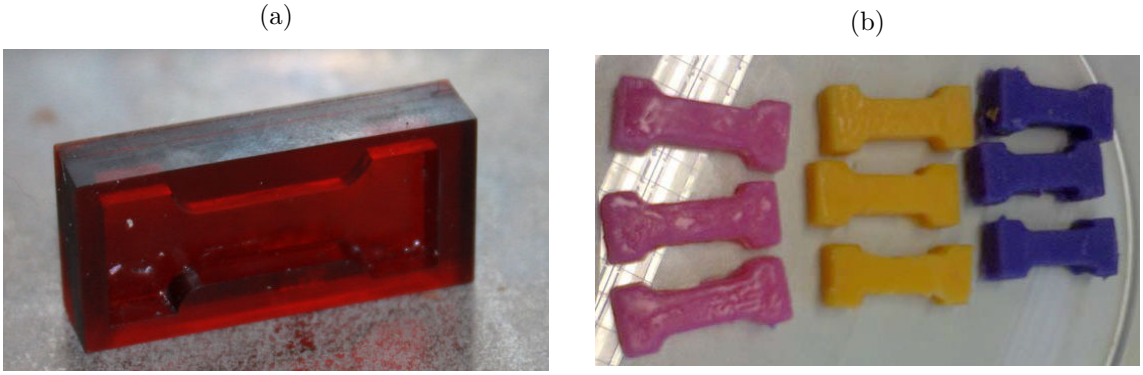

Figure C.1 – (a) Mold made of photopolymer by 3D prototyping for casting dogbone samples. (b) Elite Double dogbone samples of different Shore A hardness.

has a failure strain of $\varepsilon_{max} \sim 1$ and a Young modulus[1] of $E \sim 1 - 2\,\text{MPa}$. A decrease in cross-linking monomer concentration leads to a slight increase in failure strain and decrease in stiffness (fig. C.2).

Elite Double Dogbone samples were casted in the same molds used for PDMS (fig. C.1b). At the time, we only measured the failure strain with our homemade elongation machine (fig. 5.1a). We can assess the respective stiffness for the different hardnesses using Gent's relation between

1. Elastomers typically display a non-linear S-shaped stress-strain behavior, which is different from Hook's linear law of elasticity. The Young modulus here is a crude approximation that corresponds to the stress required to reach failure strain.

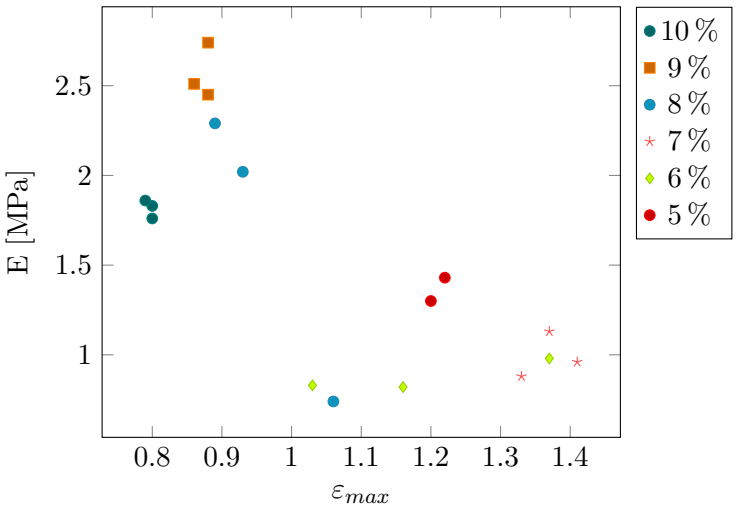

Figure C.2 – Stiffness versus failure strain of PDMS samples with different cross-linking agent concentrations. Increasing the cross-linking monomer concentration leads to an increase in stiffness (E) and to a decrease in failure strain (ϵ_{max}).

shore A hardness (H_A) and Young Modulus (E) derived from classical elasticity theory (Gent 1958):

$$E = \frac{0.0981(56 + 7.62336 * H)}{0.137505(254 - 2.54 * H)} \tag{C.1}$$

At room temperature, Elite Double has a failure strain of $\varepsilon_{max} \sim 1$ and a Young modulus of $E \sim 1\,\text{MPa}$. A decrease in hardness corresponds to a slight increase in failure strain and a decrease in stiffness (fig. C.3).

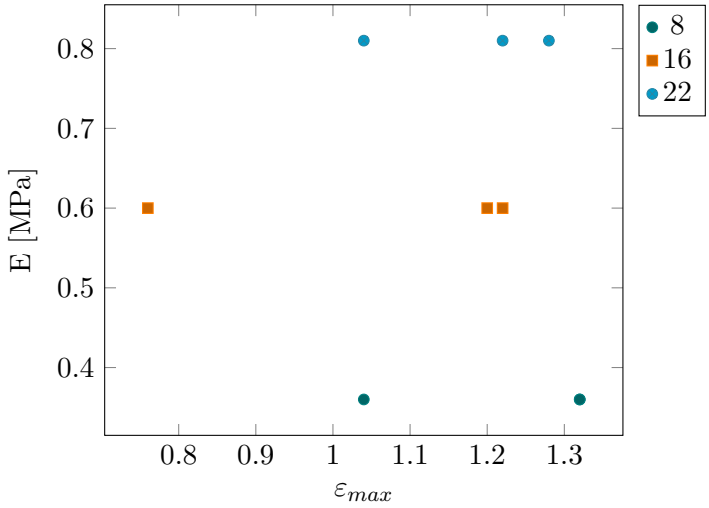

Figure C.3 – Stiffness versus failure strain of Elite Double samples of different shore A hardness. Increasing the hardness leads to an increase in stiffness (E) and to a slight decrease in failure strain (ϵ_{max}).

C.2 Characterization of mechanical and expansion properties of thermal *morphers*

C.2.0.1 Elastic properties

Tensile testing Uniaxial tensile testing was performed to assess the elastic modulus of the silicone and balsa samples using a typical tensile testing machine of the type (fig. C.4).

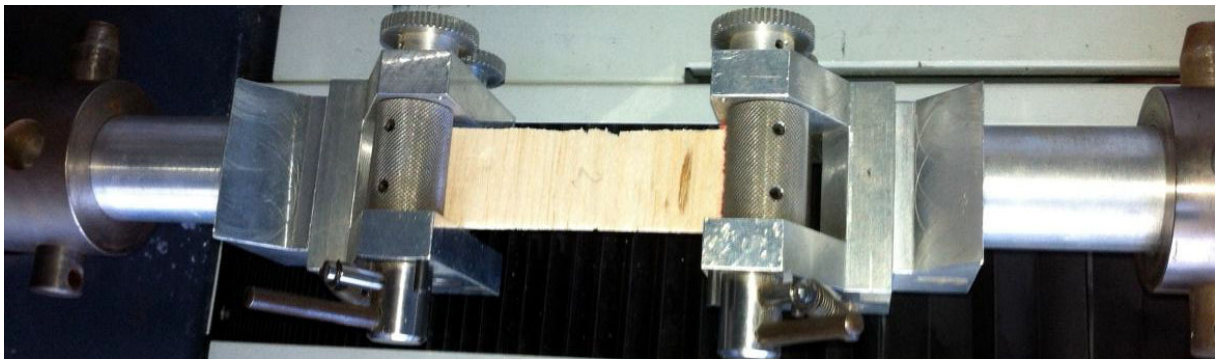

Figure C.4 – Uniaxial tensile machine where the clamped balsa sample is being tested perpendicular to its fiber direction.

Silicone The averaged Young modulus of the silicone samples is $E \approx 0.5\,\text{MPa}$.

Balsa The averaged measured Young moduli of the balsa samples are $E_\perp \approx 12.8\,\text{MPa}$ and $E_\parallel \approx 43.8\,\text{MPa}$. The longitudinal Young modulus is thus ~ 4 times higher than the transversal.

C.2.0.2 Coefficients of thermal expansion

Silicone The measure CTEs of the different silicone types are summarized in table C.1

sample	red	white	gray
$\alpha_T[^\circ\text{C}^{-1}]$	5×10^{-4}	3×10^{-4}	1×10^{-4}

Table C.1 – Measured CTE (α_T) of the different silicone types.

Balsa The balsa has a CTE of $\alpha_T \approx 0^\circ\text{C}^{-1}$.

C.3 Characterization of mechanical and swelling properties of printed multi-materials

Swelling In order to measure the swelling of the different varieties of materials, we printed homogeneous blocks of each material. One must choose a solvent in which makes the material swell, but that does not degrade it too much. TPUs swell slightly in aliphatic alcohols such as isopropanol and a lot in ketones such as acetone (Huntsman 2013). Acetone leads to important swelling (table C.2). However, after drying the structure is heavily degraded and visibly cracked

(fig. C.5). Isopropanol leads to less important swelling, but the structure is less deteriorated and *morphing* is thus "more" reversible.

Material	VW	95	85	70	60	50	40	T_+
Eigenstrain [%]	3	25	28	31	39	45	57	63

Table C.2 – Free swelling strain (*eigenstrain*) of different printed materials after ≈ 1 d.

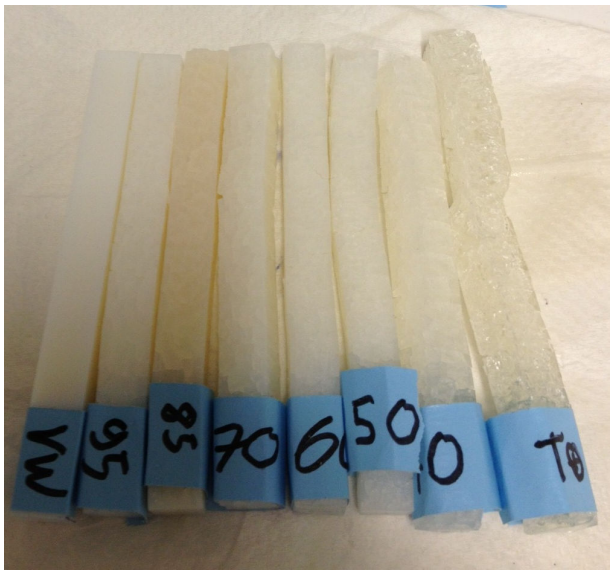

Figure C.5 – Homogeneous bars of different material varieties after one swelling cycle in acetone. The cracks are particularly visible for the softest material (T_+ on the right).

Stiffness We performed compression tests on small cylindrical samples while swelling was occurring (fig. C.6). As swelling occurs, the material becomes softer (fig. C.7).

(a)

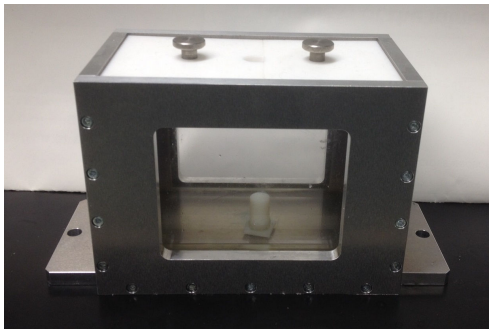

(b)

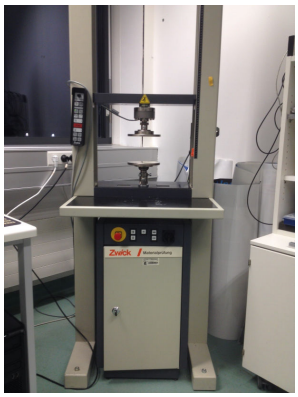

Figure C.6 – (a) Sealed setup with only a small opening on top used for measuring stiffness during swelling. (b) Tensile testing machine.

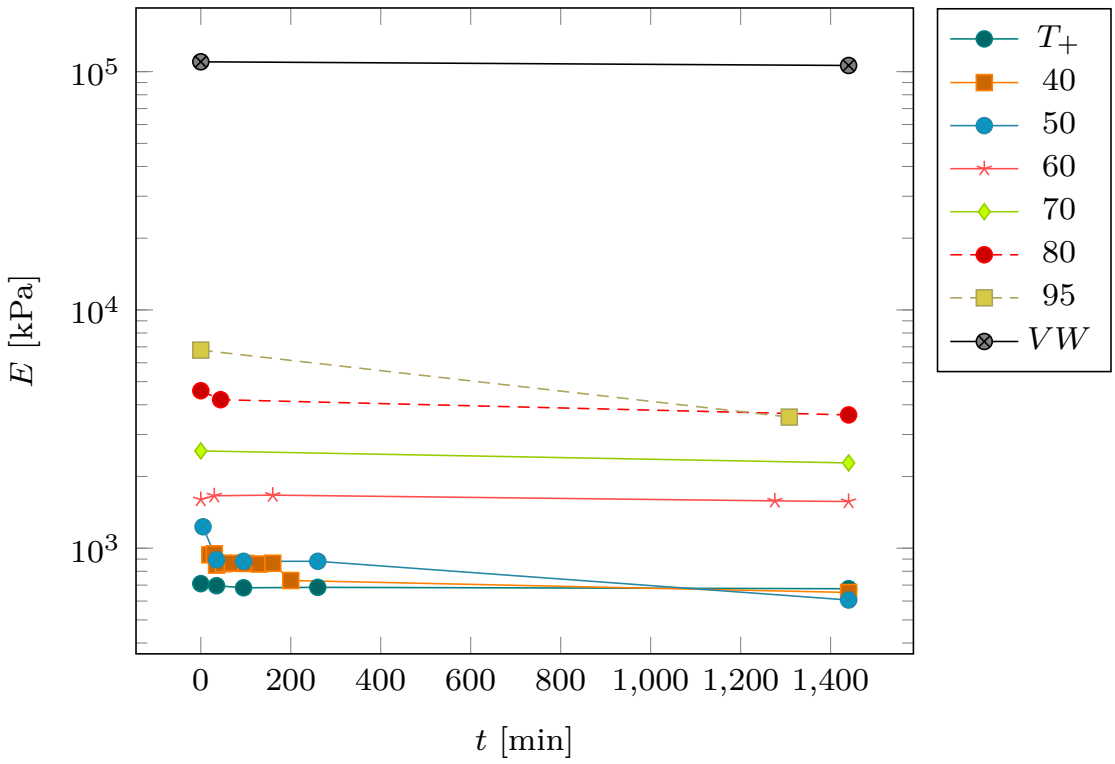

Figure C.7 – Stiffness variation during swelling of the different 3d printed materials in isopropanol. The stiffness is inversely correlated to the swelling, which is increasing in time.

Appendix D

Benders

D.1 Timoshenko's solution for bilayers

This section recalls Timoshenko's solution describing the bending of bilayers (Timoshenko et al. 1925). Consider two strips of equal length L and width w with thicknesses t_1 and t_2 respectively [1]. The following analysis applies for an elongated rod-like object (w, t_1, $t_2 \ll L$). The stiffness contrast between the two layers is given by $n = E_1/E_2$. In the case where *morphing* is triggered by thermal expansion, the *eigenstrain* in each layer is given by $\epsilon^*_\beta = \alpha_{T\beta}(T - T_0)$, where $\alpha_{T\beta}$ is the thermal expansion coefficient and T_0 the initial temperature of the bilayer [2]. When the temperature T increases, the differential longitudinal *eigenstrain* between the two layers is given by [3]:

$$\Delta\epsilon^* = \epsilon^*_2 - \epsilon^*_1 = (\alpha_{T2} - \alpha_{T1})(T - T_0) = \Delta\alpha_T \Delta T. \tag{D.1}$$

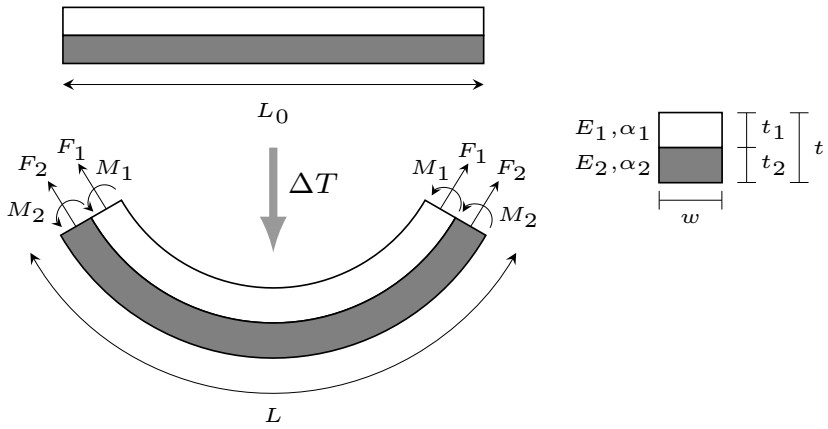

Figure D.1 – (Top) Side-view of the initial flat configuration of the bilayer. (Right) Cross-section of the bilayer. (Below) Side-view of the deformed configuration of the bilayer. We call the layer which expands the more *active* and the layer which expands the less *passive* ($\alpha_{T2} > \alpha_{T1}$). Figure adapted from (Timoshenko et al. 1925).

The curvature of a bilayer is a function of the geometrical parameters (the total thickness $t = t_1 + t_2$ and the thickness contrast $m = t_1/t_2$), the stiffness contrast $n = E_1/E_2$) and the

1. For a quantity x, the subscript x_1 and x_2 refer to the top and bottom layer respectively.
2. For $T = T_0$, $\epsilon^* = 0$ and we assume that the bilayer is stress-free.
3. The notation Δx just means a change in the quantity x. One should be careful that $\Delta\alpha_T$ denotes a spatial change while ΔT corresponds to a temporal change.

differential longitudinal *eigenstrain* ($\Delta\epsilon^* = \Delta\alpha_T \Delta T$). At equilibrium, both forces and moments balance out and the total strain is compatible.

Forces and moments inside a bilayer As shown in fig. D.1, a bilayer is translationally invariant in the longitudinal direction and possesses one mirror plane along the transversal direction. By symmetry considerations, the forces acting over the cross-section of each layer while activated by a differential longitudinal *eigenstrain* can be represented by an axial force N_β and a bending moment M_β.

Balance of forces As there is no applied external forces, the internal forces acting over any cross-section must balance out:

$$N_1 + N_2 = 0 \implies N_1 = -N_2 = F, \tag{D.2}$$

where N_β is the force in the layer $\beta \in \{1, 2\}$. Applying Hooke's law (see appendix A.2.4), the force N_β induces some longitudinal elastic strains $\epsilon_\beta^{el,s}$:

$$\frac{N_1}{wt_1} = E_1 \epsilon_1^{el}, \qquad \frac{N_2}{wt_2} = E_2 \epsilon_2^{el}. \tag{D.3}$$

Balance of moments As there is no applied external moment, the internal moments acting over any cross-section must balance out. The balance of moment at the intersurface between the two layers is [4]:

$$M_1 - \frac{N_1 t_1}{2} + M_2 + \frac{N_2 t_2}{2} = 0. \tag{D.4}$$

The moments inside the two layers M_1 and M_2 are related to the curvature [5] κ through the constitutive law (see appendix A.2.4):

$$M_1 = \kappa E_1 I_1, \qquad M_2 = \kappa E_2 I_2, \tag{D.5}$$

where $I_\beta = wt_\beta^3/12$ are the second moment of inertia of the two layers and $E_\beta I_\beta$ are the bending moduli of the two layers. Also, these bending moments induce a linear variation of longitudinal strain within each layer ($\epsilon_{zz}^{el,b} = \kappa x$ [6] see subsubsection 3.1.1.2). Using these relations and the previous balance of forces, the balance of moments becomes:

$$N\frac{t}{2} = \kappa(E_1 I_1 + E_2 I_2). \tag{D.6}$$

Compatibility of strain At the interface between the two strips, the total longitudinal strains must be equal in the two layers, so that:

$$\epsilon_1^* + \epsilon_1^{el,s} + \epsilon_1^{el,b} = \epsilon_2^* + \epsilon_2^{el,s} + \epsilon_2^{el,b}. \tag{D.7}$$

4. The minus sign in front of the second term comes from the fact that N_1 and N_2 are both defined as pointing outward the cross-section, but N_1 is above the intersurface.

5. In the case a single bending, only one material curvature in each layer is nonzero. Assuming sufficient elongation ($w, t \ll L$,) they are both equal and correspond to the geometric curvature ($\kappa = \kappa_1$) (see eq. 3.5.

6. In analyzing bilayers, we regard each layer as one-dimensional rods that are attached together through compatibility conditions. Because the thickness of both layers is small compared to their length ($t_\beta \ll L$), we assume that the curvature of their center line is equal (κ). The transversal coordinate in each layer is given by $-t_\beta/2 \leq x \leq t_\beta/2$.

Introducing $\epsilon^*_\beta = \alpha_{T\beta}\Delta T$, $\epsilon^{el}_\beta = N_\beta/(E_\beta w t_\beta)$ and $\epsilon^{el,b}_\beta = \kappa t_\beta/2$ in this equation [7], we have:

$$\alpha_{T1}\Delta T + \frac{N_1}{E_1 w t_1} - \kappa\frac{t_1}{2} = \alpha_{T2}\Delta T + \frac{N_2}{E_2 w t_2} + \kappa\frac{t_2}{2}. \tag{D.8}$$

Using eq. D.2 and eq. D.6, we can substitute the force N for the curvature κ in terms of the bending moduli $E_\beta I_\beta$ and the total thickness t. Using the definitions of the second moment of inertia ($I_\beta = w t_\beta^3/12$), we find the following expression for κ:

$$\kappa = \frac{6(\alpha_{T2} - \alpha_{T1})\Delta T(1+m)^2}{t[3(1+m)^2 + (1+mn)(m^2 + 1/mn)]}, \tag{D.9}$$

where $m = t_1/t_2$ is the thickness contrast and $n = E_1/E_2$ is the stiffness contrast. This is Timoshenko's formula that describes the curvature of a bilayer experiencing uniform heating.

7. Here again, the minus sign in front of the bending strain on the left-side of eq. D.7 is due to the fact that the first layer is above the interface.

Appendix E

Twisters

,

E.1 An excursion into the design space of biomimetic architectured biphasic actuators [1]

International Journal of
MATERIALS RESEARCH

Zeitschrift für METALLKUNDE

Original Contributions

Sébastien Turcaud[a], Lorenzo Guiducci[a], Peter Fratzl[a], Yves J. M. Bréchet[b], John W. C. Dunlop[a]
[a] Max Planck Institute of Colloids and Interfaces, Department of Biomaterials, Potsdam, Germany
[b] SIMaP-Grenoble Institute of Technology, Saint Martin d'Hères, France

An excursion into the design space of biomimetic architectured biphasic actuators

Dedicated to Prof. F. D. Fischer on the occasion of his 70th birthday

Natural hygromorph actuators, such as those found in the pine cone or in the awns of wheat and the storksbill, achieve a large variety of motions by controlling the distribution of swellable tissues inside their geometries. Such natural systems provide inspiration for the design of artificial actuators where swelling is triggered by any external expansion field. One way to achieve differential swelling inside a structure is to consider two elastic phases with different expansion properties and to apply a uniform expansion field. The resultant motion depends on the geometric distribution of the two phases and the cross-section of the structure. This paper uses the finite element method to explore how the geometry and symmetry of the initial structure controls the range of motion available.

Keywords: Actuators; Biomimetic; Architectured materials; Bilayer; Symmetry

1. Introduction

The recent increase in investigations of structure–function relationships in biological systems by materials scientists [1, 2] opens a large range of potentially interesting design principles that can be translated from Nature to the engineering world [3]. Passive actuated plant systems are particularly well-suited for a biomimetic approach to the development of artificial actuators, as they do not require hydrolysis of ATP (Adenosine triphosphate) to supply chemical energy to cells. Actuation in these systems is rather controlled by the architectural arrangement of dead tissues, which swell to differing degrees upon hydration [4–6], where water is transported via diffusion through the pores in the dead tissues. An additional advantage for bioinspired robotics shared by many simple natural actuating systems is their properties of decentralization and embodiment [7]. By this it is meant their ability to integrate sensing and actuating functions at the material level so as to avoid central control of the system, which typically needs a complex information pathway (sensors to central control unit to actuator). Hygrophilic swelling of dead plant tissues although somewhat simple in concept, still leads to complex macroscopic movements such as bending, twisting and helical actuation dependent on the underlying tissue architecture. This article is based on a top-down approach, where hygrophilic plant tissues are modelled as thermo-mechanical continua in order to explore the relation between the architectural distribution of expanding properties inside a given geometry and the resulting movement for a given stimulus.

Nature provides several examples of nastic actuated systems, in which plant organs move or generate stresses due to differential swelling of their constituent tissues. This is nicely illustrated by seed dispersal units like wheat awns and the pine cone. Wheat is propelled on and into the ground by daily humidity cycles that give rise to reversible planar bending of the awns [8, 9] while ratchets account

1. Reprinted with permission from (Bruno et al. 2010). Copyright (2010) Carl Hanser Verlag, Muenchen.

for unidirectional movement [10] and closed wet pines cones open while drying, thus releasing the seeds [11]. In both cases, the orientation of stiff cellulose microfibrils embedded in the hygroscopic hemicellulose matrix of the secondary cell walls is responsible for the differential swelling properties of the seed dispersal units, as the shrinkage upon drying will primarily occur transversally to the fibres. Such a multi-cellular bilayer with one region's fibres oriented parallel to the cell axis and the other region's fibres with random or perpendicular orientations will give rise to planar bending and can inspire simple biomimetic systems [12]. More generally, swelling can also generate either compressive or tensile growth stresses in so-called "reaction wood", depending on the average angle of the cellulose microfibrils to the main cell axis [13]. General mechanisms of multi-cellular stiff cellulose architecture inside a soft swellable matrix have been reviewed for plant actuation systems in [14] and mechanosensing [5]. In poplar tension wood for example [15], an additional G-layer of parallel cellulose microfibrils, also found in the tissue of contractile roots [16], is responsible for the generation of high tensile stresses. Design limits between fast movements in which active driving forces or instabilities are at play, as in the buckling of the Venus flytrap [17] or the explosive fracture of seed expulsions [18], and slow movements where passive dead tissue is at work, on which we focus here, can be made based on mechanical and hydraulic considerations [19]. Symmetry considerations (Curie's principle) of the geometry and material distribution can predict the planar bending of the aforementioned plant systems (wheat awn, pine cone). A large number of reversible motions or stresses can be powered by choosing a clever couple of the distribution of material properties inside the geometry and an appropriate expansion/contraction field.

Although nature is able to "design" its materials at each hierarchical length-scale, this is difficult to achieve for artificial materials, due to limitations in common manufacturing techniques. As in the pine cones, many artificial devices have been produced based on the bending of a bilayer made up of two materials, each showing a different volume change in response to a changing external field. Well established manufacturing techniques such as μ-stereolithography can be used to produce bilayers of photocurable polymers that bend upon changing humidity [20]. Other examples include Cu/Cr bilayers that change curvature reversibly upon oxidation/reduction cycles [21]. Shape-memory materials have also awakened a great interest in the design of artificial actuators. Actively foldable origami-like structures have been designed in which simple bending motion of shape-memory joints is coupled with a crease pattern of a planar sheet in order to obtain several programmable shapes [22]. Shape-memory polymers can in particular be tuned to respond not only to temperature changes but also to electrical fields, light intensity, humidity fields [23] or a combination of these [24]. Magnetic shape-memory foams are also becoming intriguing for tomorrow's applications since significant induced strains have been shown and some manufacturing drawbacks have been overcome [25]. Even if such systems show the feasibility of bioinspired actuation, many of them are based on bilayers bending in a single plane, with different materials distributed only along one transverse direction. More complex behaviour has been demonstrated in composite systems of epoxy [26] or silicon nanopillars [27] embedded in a swellable hydrogel matrix in which self-organised shape transitions occur during swelling.

Both the natural and artificial systems presented above are actuated through the generation of a volume change giving rise to differences in deformation or a stress in different regions of the material. Controlling the spatial distribution of deformation/stress is therefore fundamental to produce a given actuation behaviour. Ideally, this can be achieved by using different materials, which respond differently to a given stimulus. The goal of this paper is to explore the complexity of movements of one body shape (straight slender element) made of two elastic phases with different expansion coefficients distributed along the two transverse directions. The role of symmetry in sampling the space of allowable movements is addressed firstly in the next section. Examples of two different families of biphasic actuators are then simulated in the sections following using the finite element method in order to determine their actuation patterns.

2. Symmetry considerations

2.1. Curie's principle

As we consider invariant architectures along the length of the body (uniform cross-sections), symmetry elements reduce to mirror symmetries ($n \cdot M$) and rotation symmetries (R_n), where n is respectively the number of mirror planes and the multiplicity of the rotation (the angle of rotation is $360/n$). In the plane, the inversion centre is equivalent to R_2. Multiple mirror symmetries imply rotation symmetries, but the inverse statement doesn't hold in general ($n \cdot M \Rightarrow R_n$). If symmetry exists in the base configuration it is kept in the deformed configuration as stated by Curie's principle: "Effects have at least the symmetries of their causes" [28]. In general, this means that mirror symmetries only allow planar bending to occur in the mirror plane, whereas rotation symmetries only allow the structure to twist around its rotation axis. If multiple symmetries exist in the initial configuration, they all remain in the deformed configuration. As a result, overlapping symmetries result in no deformation (symmetrical locking). For example, the presence of both a mirror plane and a rotation axis implies no bending and no twisting as both movements would break one of the symmetries. Such preliminary consideration enables predictions to be made on the allowable actuation patterns based on the symmetry of the undeformed actuator.

2.2. Material distribution restricts symmetries of geometrical shape

Profiles can be anything from asymmetric to multiply symmetric. Examples of the latter are regular n-sided polygons, possessing n symmetry planes (mirrors) which imply n-fold rotational symmetries. Moreover n-sided polygons will also possess all p-fold rotational symmetries, where p is a product of a subset of primary numbers present in the decomposition of n ($n = p_1 \cdot p_2 \cdot \ldots \cdot p_m$ and $p = p_{i_1} \cdot p_{i_2} \cdot \ldots \cdot p_{i_k}$ where $(i_1 \ldots i_k)$ is a subset of $(1 \ldots m)$). Distribution of two material phases inside the profile can only maintain or decrease the number of the symmetry elements of the geometrical shape. The final symmetry elements of the body are thus equal to the symmetry elements of the geometry reduced by the choice of the material distribution (see Fig. 1).

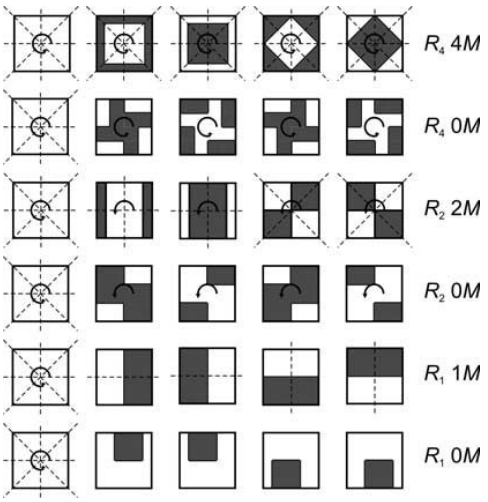

Fig. 1. Non-exhaustive examples of material-distributions reducing the number of symmetries of a square profile, where R_n stands for a n-fold rotational axis and $n \cdot M$ for n mirror planes. Breaking mirror symmetries while preserving rotational ones allows twisting to occur (rows 2 and 4). When only one mirror plane remains bending can occur (row 5). When two many symmetries remains, symmetry locking takes place (rows 1 and 3). When no symmetry elements is present,, actuation is apparently unpredictable (row 6).

2.3. Repetitive unit cell

A systematic way of designing complex material distribution inside a given geometrical shape is to look at the smallest portion of the profile, which if mirrored/rotated along a defined number of symmetry elements of the profile builds up the whole cross-section. The design of this portion, or repetitive unit cell (RUC) will produce different patterns. The symmetry of the patterns can be larger than the symmetry elements used for its generation (see Fig. 2).

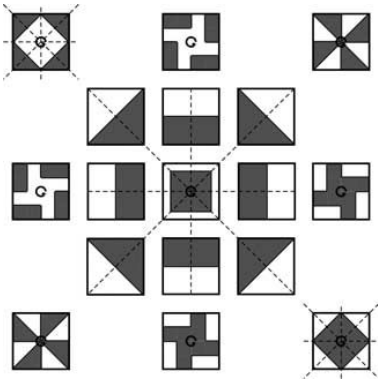

Fig. 2. The square profile possesses 4 mirror planes and a 4-fold rotational axis ($4 \cdot M$, R_4). For a constant passive/active area ratio of 50 : 50, those symmetry elements can either be maintained by the material distribution (centre, upper left and downer right corner), decreased to a single mirror plane (inner contour) or to one 4-fold rotational axis (outer contour). The inner contour is used as RUC for the outer contour showing that the 4-fold patterned cross-section can still possess 4 mirror planes if the RUC possess a mirror plane passing through the centre of rotation.

3. Setting of the FE model

In the context of continuum thermo–mechanics, the spatial distribution of the material properties (elastic Young modulus, Poisson ratio and thermal expansion coefficient) within a given geometry determines the deformation of the object subjected to a uniform expansion field and thus its overall movement. In principle a wide range of different fields could be applied that give rise to local volume changes. Examples include changes in humidity, pH, ionic content, and temperature, or by modifying magnetic or electrical fields. In the last two examples the orientation of the field with respect to the structure would also need to be taken into account. To keep the analysis simple, in the following the stimulus (temperature changes) is taken be uniform everywhere.

In this study, all the architectures are based on a straight slender beam with a square profile which can be mapped to any geometrical form in the plane [29].

3.1. Implementation

Analytical solutions are known for the special case of thermal bilayers, where thermal expansion coefficients vary in one direction of the cross-section leading to a planar bending of the structure in its longitudinal mirror plane [30]. However, the general case of an arbitrary distribution of materials is difficult to address analytically. This motivates a solution using the finite element method implemented parametrically in Abaqus 6.9 (www.simulia.com) through an appropriate script written in Python. All the architectures are based on a cubic lattice defined by adjustable length and partitioning parameters. The lattice is filled with two different material phases, active and passive, having the same elastic properties (elastic modulus and Poisson's ratio) and different expansion properties (longitudinal coefficient of thermal expansion). Additionally, a void phase made of a very soft extensible material enables the making of mechanical holes in the system. A uniform constant expansion field is applied to the structure and the static equilibrium configuration is computed taking non-linear geometrical effects into account. An adaptive meshing technique (ALE) is used in order to reduce distortion effects of the elements which are simple 8-node linear brick elements (C3D8). No boundary condition is needed as the thermal load only induces an eigenstrain and no external loads are applied. The aim of the calculation is to qualitatively predict actuation patterns and to explore the space of allowable movements.

3.2. Simplifying assumptions

The reversibility of natural actuation processes translates into elasticity in the context of continuum mechanics and the differential swelling expansion of the actuating material is analogous to thermal expansion with spatially varying thermal expansion coefficients. In the calculation the assumption of linear thermo-elasticity is made, and, thus, does not consider potential changes in elastic and swelling properties with the intensity of the expansion field. In order to compare this simulation with classical beam theory in the future, only expansion perpendicular to the cross-section is considered. Looking at qualitative effects, the Young's modulus, Poisson ratio and expansion coefficient are respectively taken equal to 1, 0.3 and 1 %. The uniform tem-

perature field is also taken equal to 1. Also, the focus on biphasic materials and constant cross-section does not enable modelling continuously varying properties as in functionally graded materials (FGM). Nevertheless, the context of linear elasticity seems well suited to reproducing slowly actuated movements and to reflect, at least qualitatively, the symmetry effects.

4. Results and discussion

In the context of elastic materials, actuation is reversible, as observed in many natural actuators. Thus, it is possible to go from a straight element to a curved or twisted one, and to reverse the transformation. In the absence of buckling phenomena, this transformation will be continuous, fully reversible, and with no hysteresis. Complex movements can be achieved by combining basic patterns. This combination, however, is not linear, as there is a coupling between bending and twisting. Indeed, if stresses are additive, the strain energy is quadratic, and the cross terms will give the coupling between the different deformation modes. It appears to be more difficult to bend a twisted shape and vice-versa. Depending on whether the aim is to generate displacement or force, the stiffness must be respectively small or large. Slender elements will enable large displacements with small deformations and stresses through geometrical amplification. A classification of actuators could further emphasise the ambivalence between displacement and force generation [31].

4.1. Actuation patterns

All the symmetry elements of the initial object are preserved in the deformed state, which delimits the space of allowable movements. In the absence of symmetry locking, one mirror plane or rotational axis allows for planar bending and twisting respectively. The actual actuation pattern inside the space of allowable movements for a given object appears to depend on several geometrical properties of the cross-section.

4.2. Bending

Bending is straightforward as the presence of a mirror plane implies planar bending (Fig. 3a). Analytical formulas for curvature are known for simple bilayers [30] and can be generalised to other geometries. It is also possible to control the local curvature of the straight element by rotating the mirror plane of the cross-section along the length of the object. Helical actuation can be achieved this way. The second moment of inertia of the cross-section is inversely proportional to the radius of curvature leading to large displacements in the case of small inertia. Geometrical effects such as opened cross-sections can amplify the global displacements.

4.3. Twisting

Twisting seems more sensitive to other geometrical factors. In the case of a compact cross-section (Fig. 3b), no actual twisting is observed despite the 4-fold rotational symmetry axis. However, the augmentation of free-borders with the volume ratio of the two phases staying equal seems to trigger twisting (Fig. 3c). The moment of inertia of the cross-section seems to relate inversely to the amount of twisting (Figs. 3d). The eccentricity of the expanding region relative to the geometric centre of the cross-section is proportional to the degree of twisting.

4.4. Geometrical parameters

Empirical definitions of geometrical parameters that control actual actuation can be proposed. These empirical definitions arise from the observed actuation patterns. The next step (not attempted here) would be to try correlating quantitative measures of movements (radius of curvature, twisting angle) to these geometrical parameters.

A general parameter is the phase fraction, corresponding to the ratio between the volume of the active and passive domains. For a constant cross-section, the area ratio is equal to the volume ratio. Topological considerations such as the

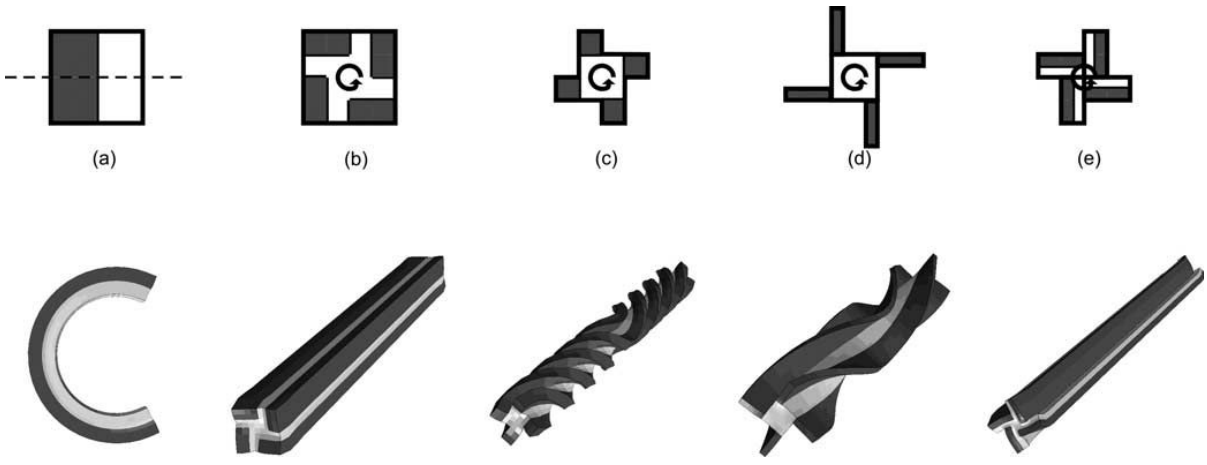

Fig. 3. Simulated actuation patterns for several cross-sections with passive/active area ratio of 50 : 50: (from left to right) (a) Classical bilayer bending in its mirror plane; (b) Closed 4-fold cross-section with bilayer RUC remains straight; (c) Opened 4-fold cross-section with bilayer RUC shows huge twisting; (d) Opened 4-fold cross-section with bigger moment of inertia shows less twisting than (c). (e) Opened 4-fold cross-section with differently oriented bilayer RUC remains straight.

connectivity of the phase regions also play a role in the control of the actuation patterns.

In the case of twisting, other geometrical parameters are necessary to distinguish between the observed actuation patterns. One of them is compactness, defined as the ratio between the area of the cross-section and the area of the n-sided regular polygon (with the smallest possible n value) containing the cross-section. All other parameters being equal, a compact cross-section will not twist, whereas an open cross-section will. Concavity defined as the ratio between the perimeter of the shape and the perimeter of the smallest convex contour containing the shape also plays a role similar to geometrical amplification. Compactness and concavity are truly disjoined concepts as there are cross-sections with equal compactness but different concavity and vice-versa. Eccentricity defined as the distance between the centres of the active regions to the geometrical centre of the shape controls the twisting rate of the section. These are only qualitative considerations based on the results of the finite element calculations, without the attempt of a complete classification of all possible shapes.

5. Conclusion

In this contribution, the effects of material distribution and overall architecture on the actuation patterns of a composite made of swellable and non-swellable materials constituents have been investigated. The space of possible actuation patterns can be restricted by symmetry considerations regarding the initial shape. For constant cross-sections, it is possible to achieve planar bending or twisting when the material distribution breaks some of the symmetry elements of the initial shape, preserving one mirror plane or one rotational axis. The observed actuation behaviour seems to depend on several geometrical parameters, which can be described empirically as phase ratio, topology, compactness and concavity of the cross-section as well as eccentricity. This bioinspired approach towards actuation enables the design space of biphasic actuators to be explored. Besides geometrical considerations, energies and internal stresses could also play a role and it would be interesting to look at the stress repartition inside the cross-section or to optimise the stored strain energy, which has not been attempted in the present work. The question whether asymmetric shapes can be decomposed into a set of symmetric shapes in order to predict their actuation patterns remains open, as well as the influences of defects on the material. This paper has been restricted to investigating only variations in architecture and material distribution within the 2D cross-section of a simple beam. Despite this extreme simplification, it has been found that the space of allowed movements is quite rich, including bending, twisting and curling. The study reported in this paper is clearly preliminary and much more remains to be investigated. For example, more complex material distributions (in 3D) [32] and shapes could enable further unexplored actuation movements. Moreover, it is not clear what the effect would be if the discrete multiphase materials would be replaced by graded material properties. It is quite likely that material optimisation methods could be of use for this problem [33]. Finally, it is important to stress that such systems need to be manufactured to be useful, which imposes further restrictions on the design space. But this initial study already shows that this simple bio-inspired approach may enable the design of artificial actuated materials with a wide span of potential applications.

The authors would like to thank Yael Abraham, Thomas Antretter, Rivka Elbaum, Matt Harrington, Davide Ruffoni and especially Ingo Burgert for stimulating discussions on actuation in plant systems.

References

[1] P. Fratzl: J. Roy. Soc. Int. 4 (2007) 637. PMid:17341452; PMCid:2373394; DOI:10.1098/rsif.2007.0218
[2] B. Bhushan: Philos. T. Roy. Soc. A. 367 (2009) 1445. PMid:19324719; DOI:10.1098/rsta.2009.0011
[3] J.W.C. Dunlop, Y.J.M. Brechet in: Materials Research Society Spring Meeting. 2009. San Francisco: MRS Symposium Proceedings.
[4] P.T. Martone, M. Boller, I. Burgert, J. Dumais, J. Edwards, K. Mach, N. Rowe, M. Rueggeberg, R. Seidel, T. Speck, Integr. Comp. Biol. (2010)
[5] P. Fratzl, F.G. Barth: Nature 462 (2009) 442. PMid:19940914; DOI:10.1038/nature08603
[6] I. Burgert and P. Fratzl: Philos. T. Roy. Soc. A. 367 (2009) 1541. PMid:19324722; DOI:10.1098/rsta.2009.0003
[7] R. Pfeifer, M. Lungarella, F. Iida: Science 318 (2007) 1088. PMid:18006736; DOI:10.1126/science.1145803
[8] R. Elbaum, L. Zaltzman, I. Burgert, P. Fratzl: Science 316 (2007) 884. PMid:17495170; DOI:10.1126/science.1140097
[9] R. Elbaum, S. Gorb, P. Fratzl: J. Struct. Biol. 164 (2008) 101. PMid:18625323; DOI:10.1016/j.jsb.2008.06.008
[10] I.M. Kulic, M. Mani, H. Mohrbach, R. Thaokar, L. Mahadevan: Proc. Roy. Soc. B. 276 (2009) 2243. PMid:19324799; PMCid:2677596; DOI:10.1098/rspb.2008.1685
[11] C. Dawson, J.F.V. Vincent, A.-M. Rocca: Nature 390 (1997) 668. DOI:10.1038/37745
[12] E. Reyssat, L. Mahadevan: J. Roy. Soc. Int. (2009)
[13] I. Burgert, M. Eder, N. Gierlinger, P. Fratzl: Planta 226 (2007) 981. PMid:17554550; DOI:10.1007/s00425-007-0544-9
[14] P. Fratzl, R. Elbaum, I. Burgert: Faraday Discuss. 139 (2008) 275. PMid:19049001; DOI:10.1039/b716663j
[15] L. Goswami, J.W.C. Dunlop, K. Jungnikl, M. Eder, N. Gierlinger, C. Coutand, G. Jeronimidis, P. Fratzl, I. Burgert: Plant J. 56 (2008) 531. PMid:18643995; DOI:10.1111/j.1365-313X.2008.03617.x
[16] N. Schreiber, N. Gierlinger, N. Putz, P. Fratzl, C. Neinhuis, I. Burgert: Plant J. 61 (2010) 854. PMid:20030750; DOI:10.1111/j.1365-313X.2009.04115.x
[17] Y. Forterre, J.M. Skotheim, J. Dumais, L. Mahadevan: Nature 433 (2005) 421. PMid:15674293; DOI:10.1038/nature03185
[18] A. Witztum, K. Schulgasser: J. Theor. Biol. 176 (1995) 531. DOI:10.1006/jtbi.1995.0219
[19] J.M. Skotheim, L. Mahadevan: Science 308 (2005) 1308. PMid:15919993; DOI:10.1126/science.1107976
[20] H. Lee, C. Xia, N.X. Fang: Proc. ASME. 13 (2008) 765.
[21] J.S. Randhawa, M.D. Keung, P. Tyagi, D.H. Gracias: Adv. Mater. 22 (2010) 407. PMid:20217729; DOI:10.1002/adma.200902337
[22] E. Hawkes, B. An, N.M. Benbernou, H. Tanaka, S. Kim, E.D. Demaine, D. Rus, R.J. Wood: Proc. Natl. Acad. Sci. USA. 107 (2010) 12441. PMid:20616049; PMCid:2906559; DOI:10.1073/pnas.0914069107
[23] M. Behl, M.Y. Razzaq, A. Lendlein: Adv. Mater. 22 (2010) 3388. PMid:20574951; DOI:10.1002/adma.200904447
[24] A.T. Sellinger, D.H. Wang, L.S. Tan, R.A. Vaia: Adv. Mater. 22 (2010) 3430. PMid:20354975; DOI:10.1002/adma.200904107
[25] M. Acet: Nat. Mater. 8 (2009) 854. PMid:19851320; DOI:10.1038/nmat2551
[26] B. Pokroy, S.H. Kang, L. Mahadevan, J. Aizenberg: Science 323 (2009) 237. PMid:19131625; DOI:10.1126/science.1165607
[27] A. Sidorenko, T. Krupenkin, A. Taylor, P. Fratzl, J. Aizenberg: Science 315 (2007) 487. PMid:17255505; DOI:10.1126/science.1135516
[28] P. Curie: J. Phys. Theor. Appl. 3 (1894) 393. DOI:10.1051/jphystap:018940030039300
[29] S. Janichen, P. Perner in: Structural, Syntactic, and Statistical Pattern Recognition, Proceedings 4109 (2006) 243.
[30] S. Timoshenko: J. Optic. Soc. Amer. 11 (1925) 233. DOI:10.1364/JOSA.11.000233

[31] M. Zupan, M.F. Ashby, N.A. Fleck: Adv. Eng. Mater. 4 (2002) 933. DOI:10.1002/adem.200290009
[32] K.K. Westbrook, H.J. Qi: J. Intell. Mater. Syst. Struct. 19 (2008) 597. DOI:10.1177/1045389X07077856
[33] S. Torquato: Annu. Rev. Mater. Res. 40 (2010) 101. DOI:10.1146/annurev-matsci-070909-104517

(Received November 18, 2010; accepted March 31, 2011)

Bibliography

DOI 10.3139/146.110517
Int. J. Mat. Res. (formerly Z. Metallkd.)
102 (2011) 6; page 607–612

ISSN 1862-5282

Correspondence address

Dr. John W. C. Dunlop
Max Planck Institute of Colloids and Interfaces,
Department of Biomaterials, Wissenschaftspark Potsdam-Golm
Am Mühlenberg 1, Raum 0.215, 14424 Potsdam, Germany
Tel: +49 331 5679420
Fax: +49 331 5679402
E-mail: John.Dunlop@mpikg.mpg.de

You will find the article and additional material by entering the document number **MK110517** on our website at *www.ijmr.de*

E.2 *Graded twister*

Similarly to subsection 6.2.1, the twist can be varied along the longitudinal direction by relaxing the assumption of translational invariance. In this subsection, we investigate an elongated rod-like object with a squared cross-section possessing a graded shear modulus (μ) along the longitudinal direction in the absence of *eigenstrain*. When this rod is twisted by external forces, the twist (τ) increases monotonically from the hard end (μ_{max}) to the soft end (μ_{min}). We make the connection to *twisters* and reveal the concept of a graded *twister*.

E.2.1 Experimental illustration

In fig. E.1, we see a graded and a uniform 3D printed rod-like object, where one end is fixed and the other end is rotated by approximately one turn ($\approx 360°$). We make the following observations:

1. In the uniform case, the twist is continuously distributed along the rod.
2. In the graded case, the twist is diminished near the hard end (left) and increased near the soft end (right) compared to the uniform case.

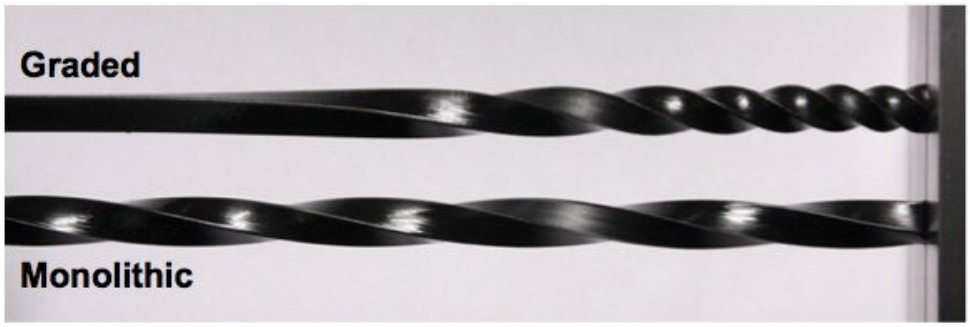

Figure E.1 – (Top) graded and (bottom) uniform 3D printed rod-like object, where one end is fixed (right) and the other end (left) is rotated by approximately one turn ($\approx 360°$). In the graded case, the hard end in one the left and the soft end is on the right. Image courtesy of James Weaver from the Wyss Institute.

E.2.2 Theoretical description

Let us model the graded *twister* from fig. E.1. The constitutive relation for a beam undergoing twisting is:

$$\tau = \frac{\mathrm{d}\theta}{\mathrm{d}z} = \frac{M_T}{\mu J}, \tag{E.1}$$

where τ is the twisting rate, θ the rotation angle between the material and geometrical frame, M_T the external twisting moment, μ the shear modulus and J the twisting inertia.

Uniform beam In the uniform case, the shear modulus is constant ($\mu = \mu_c$) and eq. E.1 can be integrated immediately:

$$\theta(z) = \frac{M_T}{\mu_c J} z. \tag{E.2}$$

With the boundary conditions $\theta\big|_{(z=0)} = 0$ and $\theta\big|_{(z=L)} = 2\pi$, we have:

$$M_T = 2\pi \frac{\mu_c J}{L}. \tag{E.3}$$

The rotation angle is then simply a linear function of the longitudinal coordinate (z):

$$\theta(z) = 2\pi\left(\frac{z}{L}\right), \quad \Longleftrightarrow \quad z(\theta) = L\left(\frac{\theta}{2\pi}\right). \tag{E.4}$$

Graded beam In the graded case, the shear modulus is a linear function of the longitudinal coordinate (z):

$$\mu(z) = \mu\big|_{(z=0)} + \frac{z}{L}\Delta\mu, \tag{E.5}$$

where $\Delta\mu = \mu\big|_{(z=L)} - \mu\big|_{(z=0)} = \mu_L - \mu_0$ is the difference between the hardest and the softest shear modulus. The constitutive equation eq. E.1 can be integrated:

$$\begin{aligned}
\theta(z) &= \int_0^z \frac{M_T}{\mu(s)J}\,\mathrm{d}s, \\
&= \frac{M_T L}{\Delta\mu J}\int_{\mu_0}^{\mu_0+\frac{z}{L}\Delta\mu}\frac{\mathrm{d}U}{U}, \\
&= \frac{M_T L}{\Delta\mu J}\ln(U)\Big|_{\mu_0}^{\mu_0+\frac{z}{L}\Delta\mu}, \\
&= \frac{M_T L}{\Delta\mu J}\ln\left(1+\frac{z\Delta\mu}{L\mu_0}\right).
\end{aligned} \tag{E.6}$$

With the boundary conditions $\theta\big|_{(z=0)} = 0$ and $\theta\big|_{(z=L)} = 2\pi$, we have:

$$M_T = 2\pi\frac{\Delta\mu J}{L\ln\left(1+\dfrac{\Delta\mu}{\mu_0}\right)}. \tag{E.7}$$

The rotation angle as a function of the longitudinal coordinate (z) is given by:

$$\theta(z) = 2\pi\frac{\ln\left(1+\dfrac{z\Delta\mu}{L\mu_0}\right)}{\ln\left(1+\dfrac{\Delta\mu}{\mu_0}\right)}, \quad \Longleftrightarrow \quad z = L\left(\frac{\mu_0}{\Delta\mu}\right)\left(\left(1+\frac{\Delta\mu}{\mu_0}\right)^{\frac{\theta}{2\pi}} - 1\right). \tag{E.8}$$

E.2.3 Numerical model

Using the finite-element method (section 4.3), we calculate the deformed configuration of graded beams with different shear modulus contrasts where one end is fixed and the other end is rotated by 360°. From fig. E.2, we observe that as the shear modulus contrast increases, the twist localizes more and more near the softer end.

Comparison between theoretical and numerical model By analyzing the deformed configuration given by the finite-element method (fig. E.2), we can see how the position where the rotation angle is a half-turn ($\theta = 180°$) changes as the shear modulus contrasts increases [2]. According to eq. E.8, the finite-element model and the theoretical approach lead to very similar results (fig. E.3).

2. We choose the angle $\theta = 180°$ arbitrarily and any other angle $0 < \theta < 2\pi$ would be also suitable.

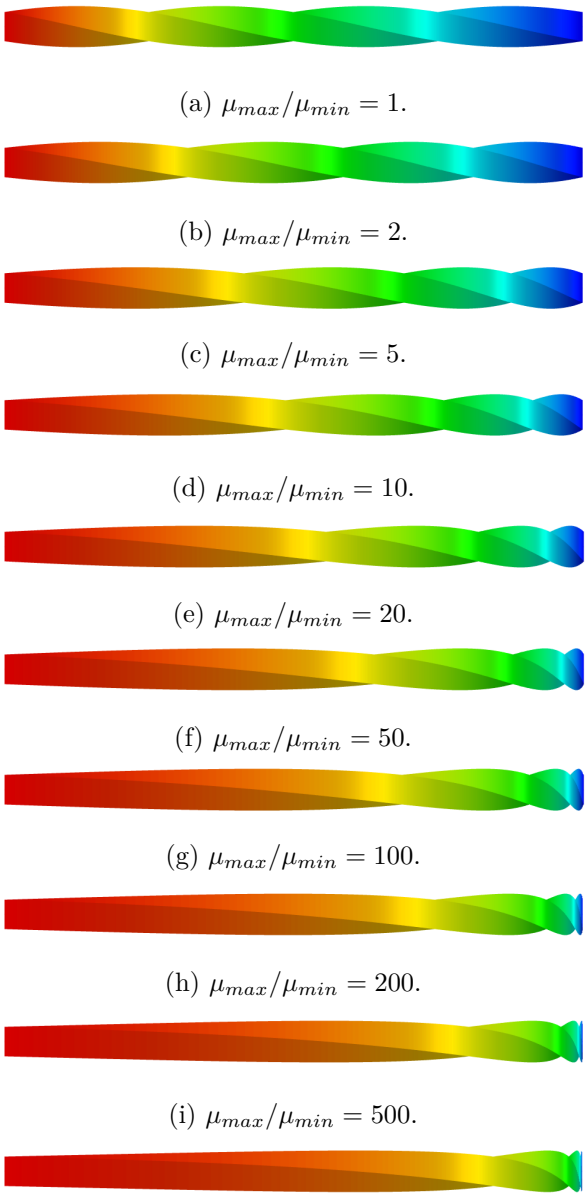

(a) $\mu_{max}/\mu_{min} = 1.$

(b) $\mu_{max}/\mu_{min} = 2.$

(c) $\mu_{max}/\mu_{min} = 5.$

(d) $\mu_{max}/\mu_{min} = 10.$

(e) $\mu_{max}/\mu_{min} = 20.$

(f) $\mu_{max}/\mu_{min} = 50.$

(g) $\mu_{max}/\mu_{min} = 100.$

(h) $\mu_{max}/\mu_{min} = 200.$

(i) $\mu_{max}/\mu_{min} = 500.$

(j) $\mu_{max}/\mu_{min} = 1000.$

Figure E.2 – Twisting of a graded beam with squared cross-section having a linearly varying shear modulus in the longitudinal direction when one end is fixed (left) and the other end is rotated by 360° (right). The different figures correspond to different shear modulus contrasts: (a) $\mu_{max}/\mu_{min} = 1$ (uniform), (b) $\mu_{max}/\mu_{min} = 2$, (c) $\mu_{max}/\mu_{min} = 5$, (d) $\mu_{max}/\mu_{min} = 10$, (e) $\mu_{max}/\mu_{min} = 20$, (f) $\mu_{max}/\mu_{min} = 50$, (g) $\mu_{max}/\mu_{min} = 100$, (h) $\mu_{max}/\mu_{min} = 200$, (i) $\mu_{max}/\mu_{min} = 500$, (j) $\mu_{max}/\mu_{min} = 1000$. The color represents the rotation of the cross-section: (red) 0°, (yellow) 90°, (green) 180°, (light blue) 270° and (dark blue) 360°. These figures were obtained using the finite-element method in Abaqus®.

E.2.4 Connection to *twisters*

Contrary to what is done throughout this thesis, the previous *morphing* pattern results from externally applied forces instead of internal *eigenstrain*. These have the benefit of being simpler

to produce experimentally [3] and are often simpler to analyze theoretically. Using the concept of impotent *eigenstrain*, the elastic strain distribution inside a *morphing* pattern resulting from some externally applied forces can be imposed as an *eigenstrain*, thus leading to this exact same pattern. In the case of torsion, the corresponding elastic strain distribution is mainly shear strains (subsubsection 3.1.2.3), which are more difficult to tune through material properties than extension strains. This is why we developed the *twisters*, where the differential *eigenstrain* can also be tuned along the longitudinal direction by varying the expansion properties.

The previous analysis shows how twisting can be tuned along a rod-like object by changing the shear modulus along the rod. From eq. E.1, we see that the shear modulus (τ) and the twisting rigidity (J) play symmetric roles, so changing the twisting rigidity along the rod should lead to the same graded twisting. In the case of *twister*, the differential *eigenstrain* ($\Delta\epsilon^*$) is another potential tuning parameter in addition to the shear modulus (τ) and the twisting rigidity (J).

$\Delta\mu$	$\frac{z}{L}\big\vert_{(\theta=\pi)}$
0	$\frac{1}{2} = 0.500$
1	$\frac{\sqrt{2}-1}{1} \approx 0.414$
4	$\frac{\sqrt{5}-1}{4} \approx 0.309$
9	$\frac{\sqrt{10}-1}{9} \approx 0.240$
19	$\frac{\sqrt{20}-1}{19} \approx 0.183$
49	$\frac{\sqrt{50}-1}{49} \approx 0.124$
99	$\frac{\sqrt{100}-1}{99} \approx 0.091$
199	$\frac{\sqrt{200}-1}{199} \approx 0.066$
499	$\frac{\sqrt{500}-1}{499} \approx 0.042$
999	$\frac{\sqrt{1000}-1}{999} \approx 0.031$

(a)

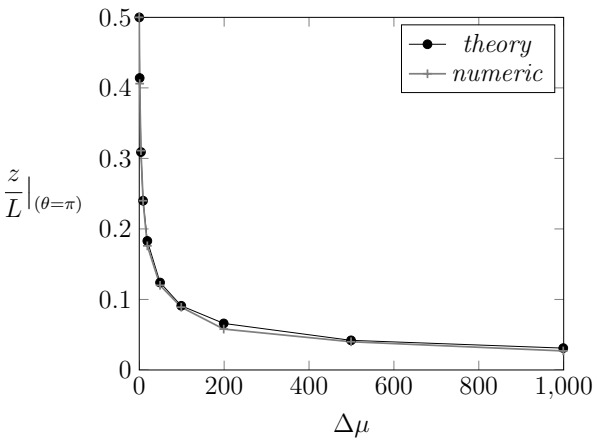

(b)

Figure E.3 – (Left) Using eq. E.8, we calculate the location along the rod where where the rotation angle is a half-turn ($\theta = 180°$) as a function of the shear modulus contrast. (Right) Analyzing fig. E.2, we can compare the finite-element results with the theoretical ones, which are very similar.

3. Externally applied forces are usually easy to impose, whereas manufacturing a graded structure requires an advanced multi-material printing machine.

Appendix F

Diffusion driven *morphers*

,

F.1 Shape-programmed folding of stimuli-responsive polymer bilayers [1]

ARTICLE

Shape-Programmed Folding of Stimuli-Responsive Polymer Bilayers

Georgi Stoychev,[†,‡] Svetlana Zakharchenko,[†,‡] Sébastien Turcaud,[§] John W. C. Dunlop,[§] and Leonid Ionov[†,*]

[†]Leibniz Institute of Polymer Research Dresden, Hohe Straße 6, D-01069 Dresden, Germany and Department of Biomaterials, [‡]Technische Universität Dresden, Physical Chemistry of Polymer Materials, 01062 Dresden, Germany, and [§]Max Planck Institute of Colloids and Interfaces, Am Mühlenberg 1, D-14424, Potsdam, Germany

ABSTRACT We investigated the folding of rectangular stimuli-responsive hydrogel-based polymer bilayers with different aspect ratios and relative thicknesses placed on a substrate. It was found that long-side rolling dominates at high aspect ratios (ratio of length to width) when the width is comparable to the circumference of the formed tubes, which corresponds to a small actuation strain. Rolling from all sides occurs for higher actuation, namely when the width and length considerably exceed the deformed circumference. In the case of moderate actuation, when both the width and length are comparable to the deformed circumference, diagonal rolling is observed. Short-side rolling was observed very rarely and in combination with diagonal rolling. On the basis of experimental observations, finite-element modeling and energetic considerations, we argued that bilayers placed on a substrate start to roll from corners due to quicker diffusion of water. Rolling from the long-side starts later but dominates at high aspect ratios, in agreement with energetic considerations. We have shown experimentally and by modeling that the main reasons causing a variety of rolling scenarios are (i) non-homogenous swelling due to the presence of the substrate and (ii) adhesion of the polymer to the substrate.

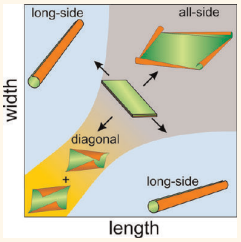

KEYWORDS: thermoresponsive · polymer · bilayer · tube · folding

Design of hollow 3D objects such as capsules and tubes is highly demanded for cell encapsulation, drug delivery and design of self-healing materials.[1] Most approaches for fabrication of capsules are based on the use of particles or fibers as templates, which are covered by functional materials. Hollow functional structures are, thus, formed after the removal of the core. Recently, the use of self-folding films that are able to form different 3D structures was suggested as a template-free alternative to the traditional template-based approaches.[2,3] The main advantage of self-folding films is the possibility to transfer a pattern, created on the surface of the unfolded film, into the inner and outer walls of the folded 3D structure.[4−6]

Inorganic and polymer-based bilayers are examples of self-folding films, which fold due to relaxation of internal stresses originated from dissimilar properties of the two layers, such as lattice mismatch, thermal expansion, or swellability. Inorganic-based self-folding films are promising for a variety of fields including transport,[7] nanooptics,[8] energy storage elements,[9] photovoltaic power applications,[10] optics,[11] and engineering of scaffolds,[12−15] as well as being suitable to investigate the role of confinement on cell behavior.[16] Polymer-based self-folding films, on the other hand, are particularly promising for biotechnological applications such as encapsulation of cells[17,18] and design of biomaterials.[19] These and other applications require precise control of the folding for fabrication of 3D objects with a defined shape. In particular, it was demonstrated that the resulting shape of the folded 3D object can be controlled by the shape of the original bilayer. For example, rectangular bilayers form tubes,[17] while star-like bilayers are able to form envelope-like capsules.[18]

Generally, the rolling of a rectangular bilayer may occur according to three different scenarios: long-side, short-side, and diagonal rolling (see Figure 1). The effects of film shape on the character of folding were experimentally investigated on examples of purely inorganic and composite polyaniline−inorganic bilayers. Smela *et al.* showed that short-side rolling was preferred in the case of free homogeneous actuation and that this preference increased with aspect ratio (ratio of length to width of rectangular pattern).[20] Li *et al.* experimentally demonstrated the opposite scenario[21] in the case where bilayers are progressively etched from a substrate, namely a preference for long-side rolling. They observed that when the tube circumference was much larger than the width, or the aspect ratio of the rectangle was high, rolling always occurred from the long side. When the tube circumference was much smaller than the width

* Address correspondence to ionov@ipfdd.de.

Received for review January 7, 2012 and accepted April 24, 2012.

Published online April 24, 2012
10.1021/nn300079f

1. Reprinted with permission from (Stoychev, Zakharchenko, et al. 2012). Copyright (2012) American Chemical Society.

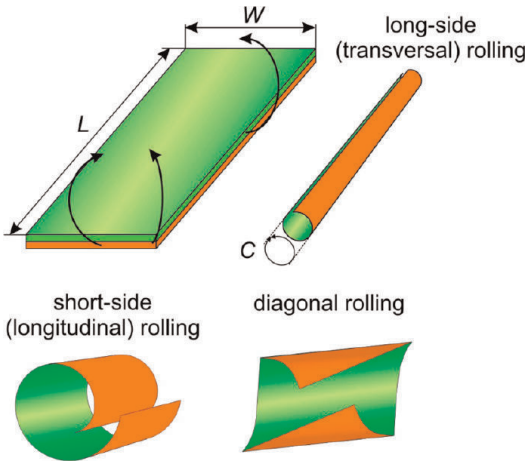

Figure 1. Scheme of rolling of a polymer bilayer according to different scenarios: short-side, long-side, and diagonal rolling.

and the aspect ratio of the rectangular bilayer was not very high, the rolling resulted in a mixed yield of long- and short-side rolling, as well as a "dead-locked turnover" shape. Short-side rolling occurred at small aspect ratios when the deformed circumference is close to the width. In these self-rolling systems, the active component undergoes relatively small volume changes or actuation strains, which are nearly homogeneous over the whole sample. Hydrogel films, which are also able to fold, demonstrate considerably different properties.[22−24] First, hydrogels undergo large volume changes (up to 10 times) upon swelling and contraction. Second, the swelling of a hydrogel is often kinetically limited: due to slow diffusion of water through a hydrogel, the parts that are closer to the edges swell first, while the parts that are closer to the center of the films swell later. Thus, the actuation profile inside the active layer is heterogeneous. In this paper we investigate the effects of shape, size, and rolling curvature on the direction of folding of rectangular polymer bilayers placed on a substrate, where the bottom component is a stimuli-responsive hydrogel.

EXPERIMENTAL OBSERVATIONS

Experimental Preparation. Two families of polymeric bilayers, made of an active and a passive layer, are studied. The passive component is either hydrophobic polycaprolactone (PCL) or random copolymer poly(methylmethacrylate-*co*-benzophenone acrylate) (P(MMA-BA)). The active component is a thermoresponsive hydrogel formed either by photo-cross-linked poly(*N*-isopropylacrylamide-*co*-acrylic acid-*co*-benzophenone acrylate) (P(NIPAM-AA-BA)) or by poly(*N*-isopropylacrylamide-*co*-benzophenone acrylate) (P(NIPAM-BA)). Thermoresponsive hydrogels swell and shrink at reduced and elevated temperature, respectively. The passive hydrophobic P(MMA-BA) and PCL layers restrict swelling of the active hydrogel. As a result, the bilayer made of these polymers does not uniformly expand/shrink but folds and unfolds due to swelling and collapse of the hydrogel layer.

P(NIPAM-AA-BA)/(P(MMA-BA) and P(NIPAM-BA)/PCL bilayers were prepared using photolithography, as described earlier.[17] First, we prepared two sets of patterned bilayers of P(NIPAM-AA-BA)/(P(MMA-BA), which differ in thickness (H) of the P(MMA-BA) layer, which results in different rolling curvature. One set formed narrow tubes with a diameter d = 20 μm ($H_{P(MMA-BA)}$ = 500 nm; $H_{P(NIPAM-AA-BA)}$ = 1200 nm), while the second set forms wider tubes with diameters in the range d = 70−90 μm ($H_{P(MMA-BA)}$ = 1200 nm; $H_{P(NIPAM-AA-BA)}$ = 1200 nm). Rectangular bilayers of different lengths (L = 100−1000 μm) and aspect ratios (ratio of length (L) to width (W), $A = L/W$ = 1−8) were fabricated using specially designed photomasks. After removal of the non-cross-linked polymer, the patterned bilayers were exposed to PBS solution (pH = 7.4) at room temperature. As a result, photo-cross-linked P(NIPAM-AA-BA) swelled, leading to rolling of the bilayer and formation of tubes. The folded films formed by each set of bilayers were then mapped by optical microscopy in order to assess the rolling radius as well as the deformation pattern (see Figures 2 and 3).

Experimental Results. It was found that the final diameter of the tube is independent of the size of the bilayer (L, W), but everything else being equal (Young modulus of active and passive layer as well as activation strain), it is solely controlled by the relative thickness of the active and passive layers[25] and, thus, is (almost) constant for each set of experiments. The direction of rolling strongly depends on the size and shape of the films as well as on the thickness of the active and passive layer (see Figure 4). We distinguished four general types of rolling: long-side rolling, diagonal rolling, short-side rolling, and mixed all-side rolling, which is a combination of the first three types. The character of preferential rolling is plotted as a function of the absolute values of width, length, and aspect ratio, as well as normalized values, which are obtained by dividing the length or width by the typical circumference of the rolled tube ($C = \pi d$, Figure 1).

Three types of rolling were observed when narrow tubes (d = 20 μm) are formed: long-side, diagonal, and all-side rolling (see Figure 4a). It must be noted that no short-side rolling was observed. The all-side rolling (see Figure 2, a1−3, b1−2) occurs when the width of the films considerably exceeds the circumference of rolling for aspect ratios of 1 or 2. A decrease of the width for an aspect ratio of 2 or more results in preferential long-side rolling (see Figure 2, b3, c1−3, d1−3), when the normalized length is more than 2. Depending on the ratio of width (W) to circumference (C), incompletely rolled tubes ($W/C < 1$), completely rolled tubes ($W/C \approx 1$), or doubled tubes ($W/C \geq 2$) are formed. A further decrease of the length leads to a mixture between

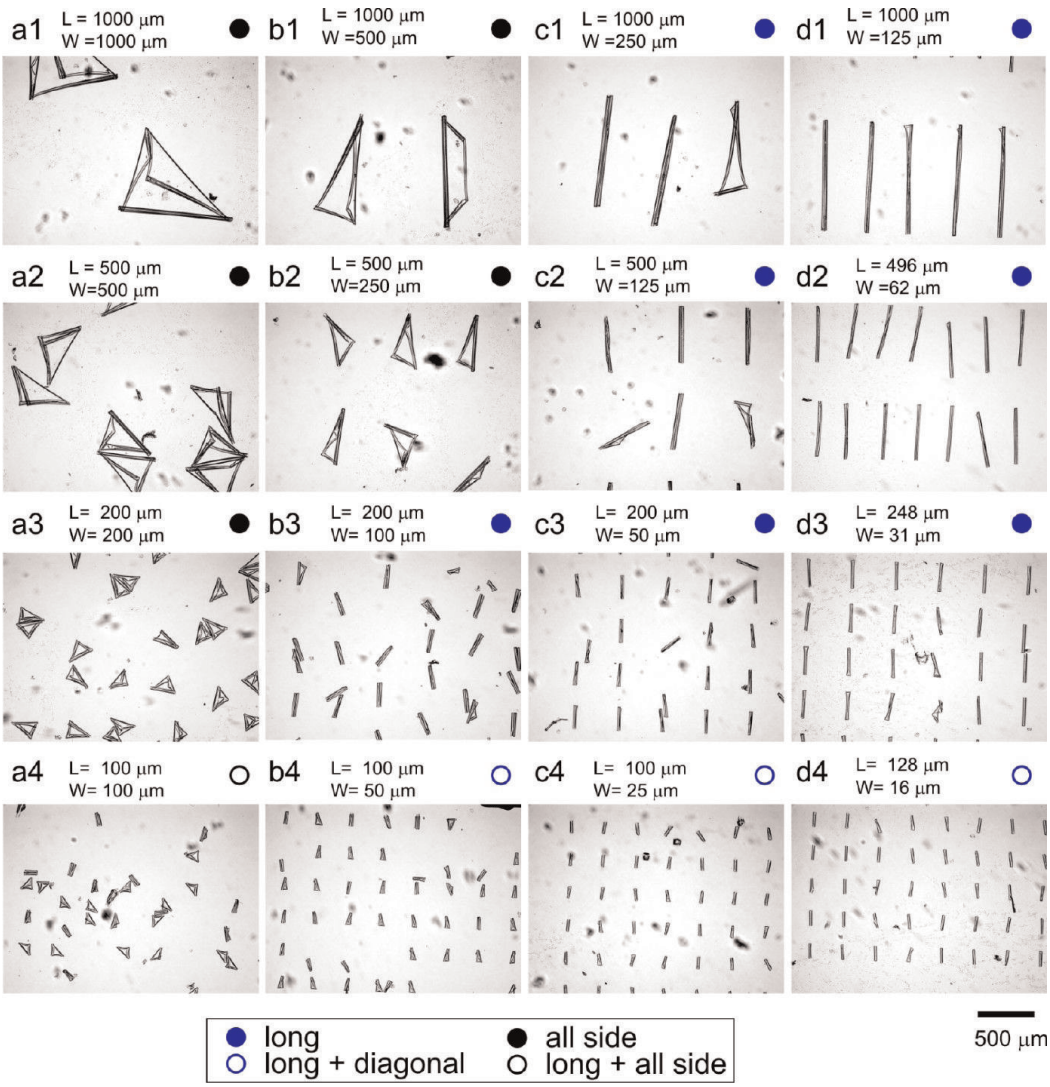

Figure 2. Microscopy snapshots of folded P(NIPAM-AA-BA)−P(MMA-BA) bilayers of different length (*L*) and width (*W*) that form narrow tubes of diameter $d = 20\ \mu m$; $H_{P(MMA-BA)} = 500$ nm; $H_{P(NIPAM-AA-BA)} = 1200$ nm.

long-side and diagonal or all-side rolling (see Figure 2, a4, b4, c4, and d4). The most promising parametric window for potential applications, such as microfluidics[24] and cell encapsulation,[17] is thus bilayers with an aspect ratio of 4 or more.

Different rolling behavior is observed when wide tubes ($d = 70-90\ \mu m$) are formed (see Figure 4b). First, the films with the highest aspect ratio slightly bend and almost do not roll because of the large circumference (see Figure 3, d1−4). Second, other bilayers roll either according to diagonal or all-side rolling scenarios. Diagonal rolling is observed in the cases of square films ($L/W = 1$) when two opposite corners bend toward each other (see Figure 3, a1−4). "Tick or check mark-like" structures (see for example Figure 3, c1, the film in the middle) in combination with diagonal rolling are observed in almost all cases at $L/W > 1$ when either adjacent or opposite corners bend toward each other. Bending from short sides was observed in combination with diagonal rolling only in one case (see Figure 3, b4).

The results obtained for narrow (Figure 2 and 4a) and wide (Figure 3 and 4b) tubes plotted as a function of normalized length and width are not fully identical. Figure 4b is shifted to larger values of *L*/*C*. The reason for this effect is not completely clear and could be due to effects related to heterogeneities in the swelling behavior, which are hard to fully consider. On the other hand, there is a clear correlation between the results given in Figure 4a and b, which is qualitatively summed up in Figure 4c. For example, all-side rolling is observed when both length and width considerably exceed the deformed circumference. Diagonal rolling is observed when $L = W$, and both are comparable to the circumference. Mixtures of diagonal rolling and the formation of "tick or check mark-like" structures (tube in the middle of Figure 3, c1) are observed when $L > W$ and both *L* and *W* are comparable to the circumference.

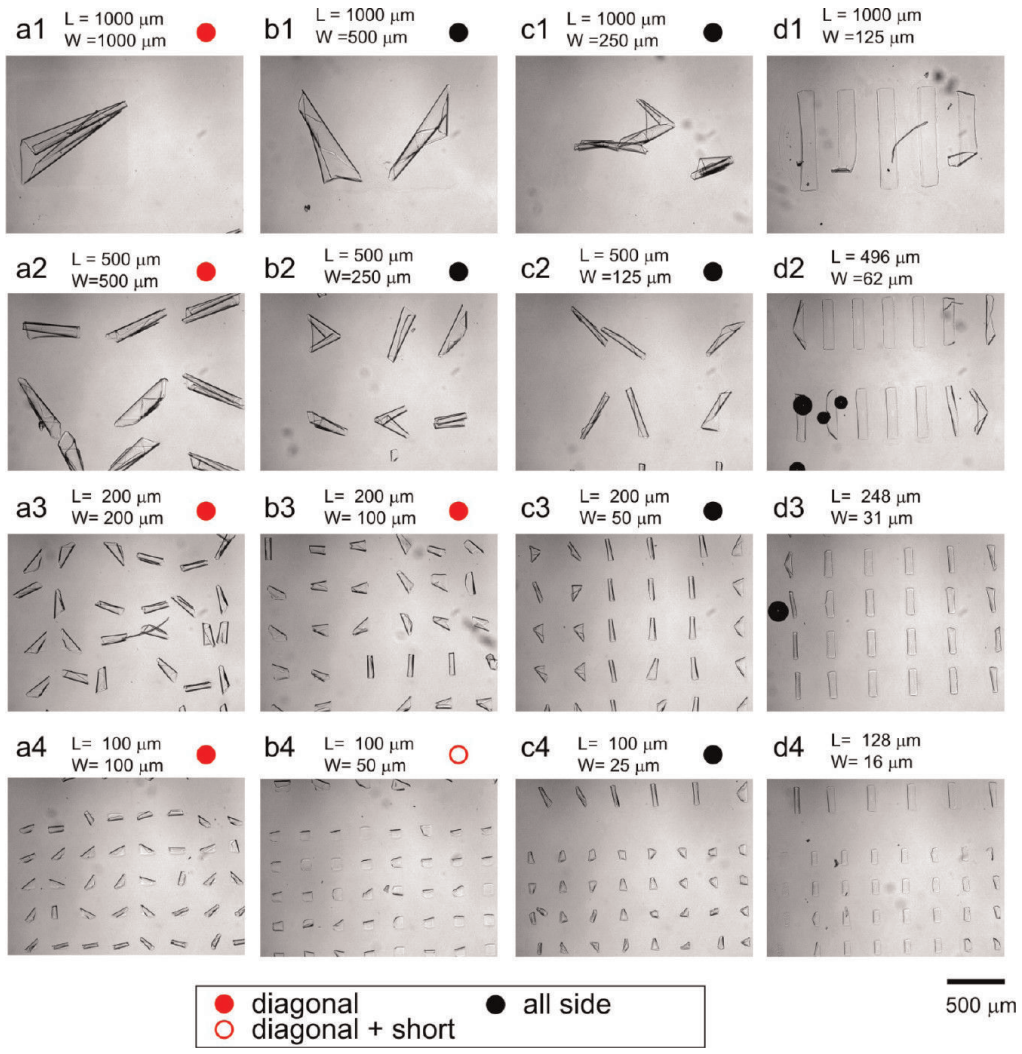

Figure 3. Microscopy snapshots of folded P(NIPAM-AA-BA)−P(MMA-BA) bilayers with different length (*L*) and width (*W*) that form wide tubes of diameter *d* = 70−90 μm; $H_{P(MMA-BA)}$ = 1200 nm; $H_{P(NIPAM-AA-BA)}$ = 1200 nm.

The long-side rolling takes place when the length considerably exceeds the deformed circumference ($L/C > 4$) and the aspect ratio is larger than 4. As a result, long tubes are formed, at least in the case of narrow tubes (d = 20 μm). In order to test the hypothesis that long tubes are formed when $L/C > 4$ and $W \approx C$ also in the case of wide tubes (d = 70−90 μm), we investigated rolling of 1800 μm × 300 μm large bilayer tubes ($H_{P(MMA-BA)}$ = 1200 nm, $H_{P(NIPAM-AA-BA)}$ = 1200 nm, W/C = 1.2; L/C = 7.5). Indeed, rolling resulted in preferential formation of long tubes (see Figure 4d), in agreement with our predictions.

Mechanism of Rolling. In order to clarify the variety of observed rolling scenarios, we experimentally investigated swelling and rolling of the bilayers. Rolling was investigated first using members of the second family of patterned bilayers formed by poly(*N*-isopropylacrylamide-*co*-benzophenone acrylate) and polycaprolactone with high aspect ratio (L/W = 6, H_{PCL} = 300 nm, $H_{P(NIPAM-BA)}$ = 750 nm).[17] Initially, the polymer films were immersed in warm water, where the active P(NIPAM-BA) hydrogel monolayer is shrunk. The temperature was gradually decreased, and rolling was observed. Diagonal rolling started from corners and stopped when two rolling fronts met each other (Figure 5a). Long-side rolling started later (Figure 5b) but eventually dominated, leading to a switching of the diagonally rolled corners to long-side rolled (Figure 5c,d). The formed double tubes were unrolled at elevated temperature (Supporting Information, Movie S1). The central part of the rolled bilayer, which has a shape of a line (Figure 5e), is still adhered to the substrate after rolling because the bilayer remains almost undeformed there. This adhesion area directs long-side rolling during the second cycle of temperature decrease and prevents short-side rolling. The second rolling, thus, proceeded similar to the first one: rolling starts from the corners and then switches to long-side rolling.

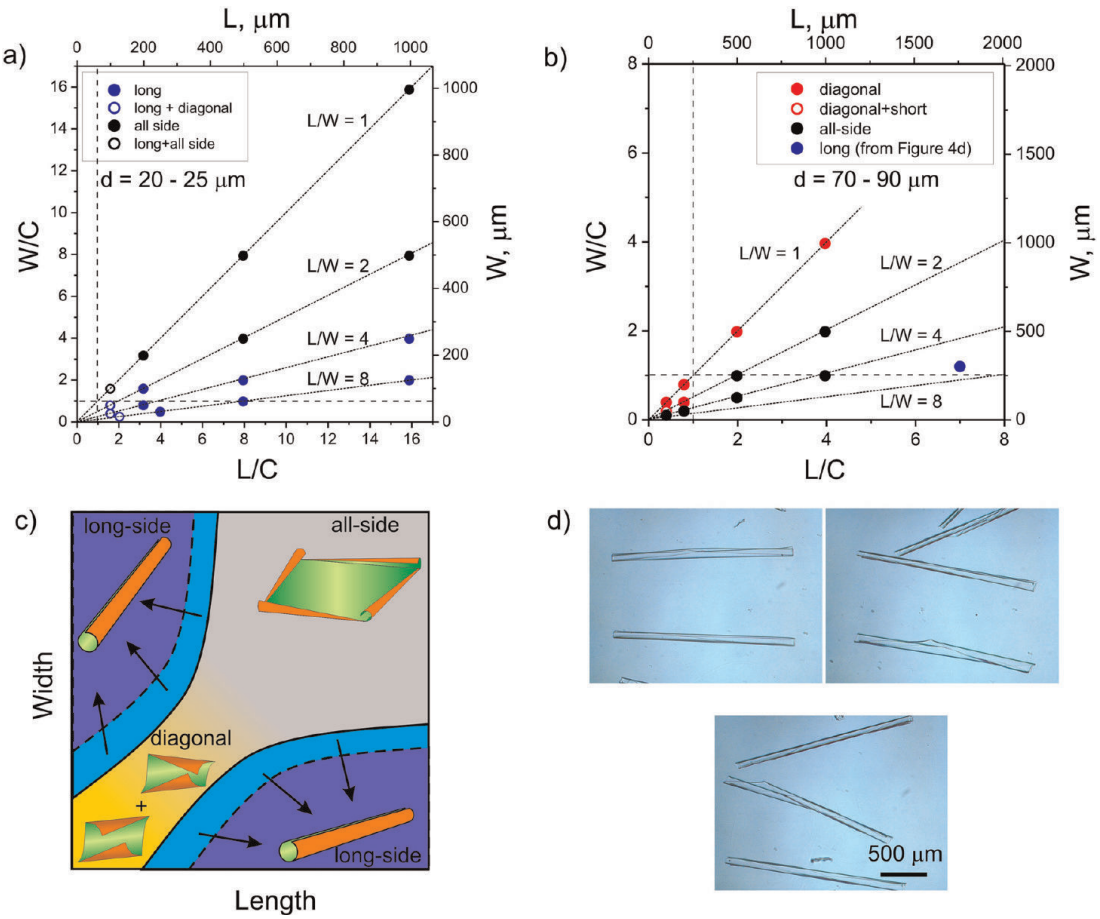

Figure 4. Dependence of preferential rolling direction of P(NIPAM-AA-BA)−P(MMA-BA) bilayers on the size and shape of the films when (a) narrow (d = 20 μm, $H_{P(MMA-BA)}$ = 500 nm; $H_{P(NIPAM-AA-BA)}$ = 1200 nm) and (b) wide (d = 70−90 μm, $H_{P(MMA-BA)}$ = 1200 nm; $H_{P(NIPAM-AA-BA)}$ = 1200 nm) tubes are formed. Dashed lines correspond to L/C = 1 and W/C = 1 (L and W are length and width of the film, respectively; C is the circumference of the rolled tube). (c) Schematic diagram of rolling scenario as a function of length and width. Arrows indicate how the diagram changes when circumference (C) increases. (d) Examples of wide tubes (d = 80 μm, $H_{P(MMA-BA)}$ = 1200 nm; $H_{P(NIPAM-AA-BA)}$ = 1200 nm) formed by rolling of 1800 μm × 300 μm large bilayers (corresponds to the blue point in part b).

In order to explain the fact that rolling starts from the corners, we experimentally investigated the swelling process. This was performed in a qualitative manner by observing changes in the interference pattern of white light with the bilayer during swelling. In order to avoid bending and folding of the bilayer during swelling, a very thin P(NIPAM-AA-BA) layer (H = 35 nm) under a thick P(MMA-BA) layer (H = 400 nm) was used. Due to the effect of interference of light, which is mirrored from the top and bottom surfaces of the bilayer, the changes of colors (see Figure 6) reflect changes in the film thickness. It is observed that the color of the films starts to change at the corners first, which confirms the assumption that edge-activation of the active layer due to slow water diffusion into the hydrogels is at the origin of the experimentally observed fact that rolling starts at corners. Thus, on the basis of the observations of rolling and swelling mechanisms, we can argue that diffusion determines folding in the first moments of folding, while adhesion seems to play a decisive role at later stages of folding.

THEORETICAL CONSIDERATIONS

Diffusion-Driven Actuation. The observed long-side folding of rectangular bilayers for some specific shape parameters contradicts the bending of bilayer actuators, which occurs along the short side.[20,25] However, this holds under the assumption that the active layer is homogeneously activated and that there is no interaction with a substrate. This is the case of a freely floating bilayer, where diffusion of water inside the hydrogel layer is not restricted by any substrate. It was confirmed that such freely floating bilayers undergo short-side rolling that is similar to the behavior of standard actuators (Figure 7a). As the studied bilayers are placed on a substrate, it is reasonable to assume that diffusion of water inside the active monolayer upon activation (T < T_critic) occurs primarily through its lateral sides. Additionally, not only does the substrate

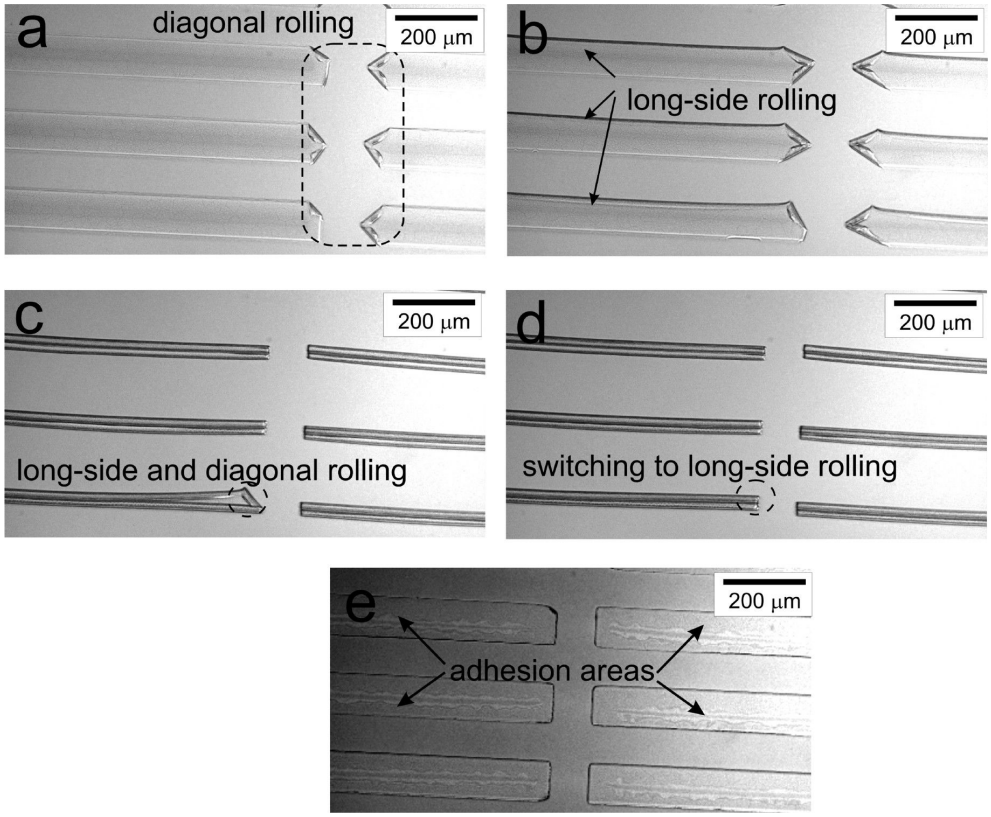

Figure 5. Time-resolved rolling of the P(NIPAM-BA)—PCL bilayer (H_{PCL} = 300 nm, $H_{P(NIPAM\text{-}BA)}$ = 750 nm, 930 μm × 90 μm); diameter of the tube d = 41 μm (a—e, supplementary Movie S1).

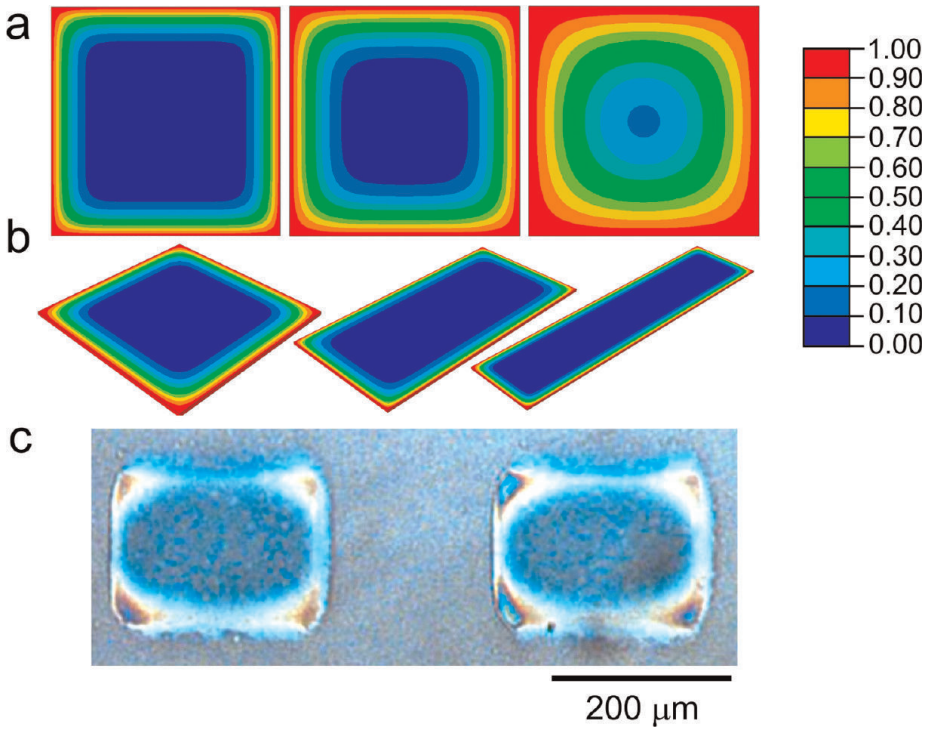

Figure 6. Color map of the calculated swelling (from 0 to 1) controlled by water diffusion in the active monolayer with a lateral constant boundary condition (blue is nonswollen) dependent on time (a) and shape (b) obtained by finite-element simulations as well as experimentally obtained microscopy snapshot of swollen P(NIPAM-BA)—PMMA bilayer ($H_{P(MMA\text{-}BA)}$ = 400 nm; $H_{P(NIPAM\text{-}AA\text{-}BA)}$ = 35 nm) after few seconds of swelling (c).

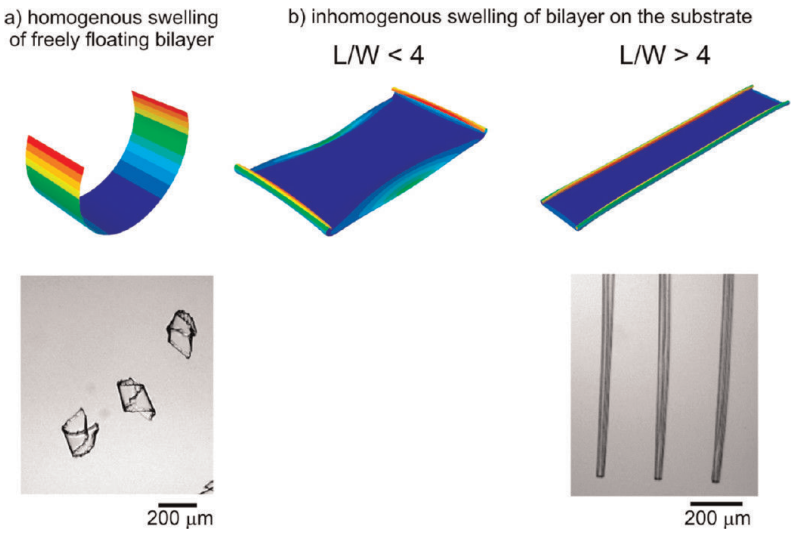

Figure 7. Simulation and experimentally observed folding of rectangular bilayers at different conditions: (a) freely floating rectangular bilayer (homogeneous swelling, supplementary Movie S2); (b) rectangular bilayer on substrate (inhomogeneous swelling, supplementary Movie S1).

confine diffusion, it also exerts adhesion forces to the bottom surface of the bilayer that impede actuation until a certain threshold of detachment forces is reached. This means that bending, which requires detachment of the substrate, occurs only for a sufficient activation strain. In particular, nonswollen areas do not bend.

Finite-Element Simulations. The diffusion pattern is assumed to obey a classical diffusion law (Fick's law) with a constant imposed boundary condition on the lateral sides of the active monolayer. Well known in one dimension, the two-dimensional diffusion pattern was obtained through a finite-element simulation using ABAQUS at different time points for different monolayer shapes (aspect ratio). Diffusion of water inside a hydrogel can be described as a first approximation by steady-state heat diffusion inside a medium with constant diffusivity. We used linear three-dimensional diffusion elements (DC3D8), in order to be able to apply the resulting activation field to actuate bilayers subsequently, and applied a constant boundary condition on the lateral surfaces. The solvent diffusion, however, is a very complex process that is quite difficult to fully describe because the boundary conditions of diffusion change as the film deforms and detaches from the substrate. We aimed to discuss diffusion in the very first moments of swelling, when the film starts to deform, as we believe that subsequent deformation of the film is largely determined by its starting deformation. The simulation allowed us to predict an inhomogeneous two-dimensional diffusion pattern that eventually becomes homogeneous after a sufficient time (see Figure 6a,b).

Subsequently, we applied the obtained thermal field at different time points to a bilayer of the same aspect ratio. Both layers of the bilayer are made of a linear elastic material with a normalized Young modulus of 1 and a Poisson ratio of 0.3. This crude simplification relies on the fact that the stiffness contrast between the active and the passive layer does not significantly affect the rolling radius of a bilayer.[25] The bottom layer possesses in-plane thermal expansion coefficients equal to 1, whereas the top layer is thermally inactive. In order to understand the influence of substrate adhesion, we imposed a fixed kinematical boundary condition at an internal rectangular bottom surface, scaled from the external shape. We used a fine mesh of first-order eight-node elements with reduced integration (C3D8R), which are able to follow the large displacements at reasonable cost. The deformed shape corresponding to an edge activation of the bilayer at a given time point in the diffusion process was calculated in a static step taking nonlinear geometric effects into account. Adaptive meshing techniques were used to avoid large distortions in mesh elements upon actuation. We compared the obtained results with the one obtained using the Riks method and found no discrepancy between the predicted deformed shapes. Surprisingly, convergence using a combination of adaptive meshing techniques on a fine mesh with a static nonlinear geometric step proved to be better than using the Riks method. This simple uncoupled model already shows that sharp activation strains near the edges combined with an internal constraint of the bottom layer produces interesting deformation patterns for different aspect ratios. In particular, the model predicts that short- and long-side rolling is more favorable at $L/W < 4$ and $L/W > 4$, respectively (see Figure 7b).

The appearance of all-side and diagonal rolling in experiments at smaller aspect ratios accounts for the fact that no preferential direction appears for bending

deformations. Also, imperfections of the material properties of the polymer film and substrate can be responsible for the observed symmetry-breaking.

Energetic Considerations. The fact that edge activation of a constrained bilayer leads to long-side rolling is also suggested by plate theory. The elastic energy of plate-like objects can be decomposed into a stretching and a bending term according to Föppl von Kármán plate theory,[26] in which the in-plane strains are integrated over the thickness taking into account the edge activation. This formulation describes accurately the elastic energy of a bilayer plate upon edge activation and can be solved numerically (this will be done in a subsequent paper). Another approach, which is less subtle, but that also leads to accurate results, is solving the 3D mechanical problem by a finite-element method. Essentially the problem can be described in the following way: we make an additive decomposition of the total strain in the active layer into an eigenstrain (or swelling strain) and an elastic strain $\varepsilon_{kl}^{T} = \varepsilon_{kl}^{eig} + \varepsilon_{kl}^{el}$. The eigenstrain is given as $\varepsilon_{ij}^{eig} = \alpha\delta_{ij}$, where δ_{ij} is the Kronecker delta tensor, and isotropic swelling is assumed in the current model. The amount of swelling depends on the swelling coefficient α, which in turn can vary spatially according to the solution of the diffusion equation. As the active layer is constrained by the passive layer, geometric incompatibilities result in elastic strains and thus stresses through Hooke's law, $\sigma_{ij} = E_{ijkl}\varepsilon_{kl}^{el}$. The final shape of the structure upon changes in the spatial distribution and magnitude of α is calculated by minimizing the elastic energy of the system. For further details of the finite-element method see, for example, ref 27. With the stretching term being linear in thickness, while the bending term is cubic, bending deformations are favored when the plate is sufficiently thin. Unlike in a beam-like bilayer, actuation triggers a biaxial expansion field inside the plate, which creates internal stresses in the long and in the short direction of the plate. Relaxation of internal stresses perpendicular to the edge of the bilayer will lead to bending, whereas relaxation of internal stresses parallel to the edge of the bilayer will produce stretching that will eventually lead to wrinkling, as in the edge of long leaves.[28] Because of the presence of the substrate, internal stresses perpendicular to the edge of the bilayer are more easily relaxed, leading to simple bending, while internal stresses parallel to the edge of the bilayer produce simple stretching. As the aspect ratio increases, it is thus less costly to relax stresses into bending on the long side than on the short side. This explains qualitatively why long-side rolling is observed as the aspect ratio increases.

Finite-element modeling and energetic considerations show that the experimentally observed appearance of long tubes for large aspect ratios and high activation strains are due to (i) non-homogenous swelling due to slow lateral diffusion, as well as (ii) adhesion of the bilayer to the substrate, constraining the deformations. Both these factors are caused by the specific arrangement of the experiment: (i) polymer bilayer is deposited on the substrate and (ii) active polymer is the bottom layer.

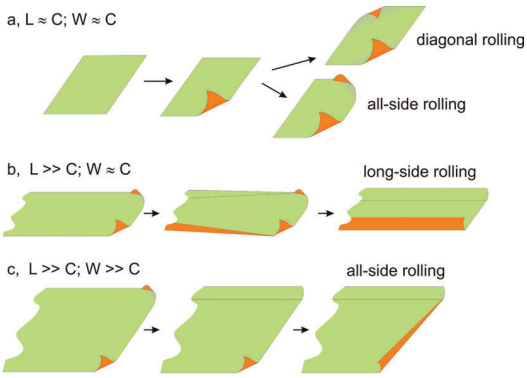

Figure 8. Schematic of rolling leading to diagonal rolling, long-side rolling, and all-side rolling.

Rolling Scenario. Finally, by considering modeling and experimental results, the following scenario of rolling of hydrogel-based polymer bilayer lying on a substrate is assigned. The rolling starts from the edges due to faster diffusion of water from the lateral surfaces, which then are able to detach from the substrate and to bend. Rolling can start either from two adjacent (for example Figure 3, d2, right lower polymer film, or Figure 3, b2, left upper film) or opposite edges (almost all polymer films in Figure 2, a2) or from all corners simultaneously, which is less probable if the bilayer is small due to the presence of imperfections and becomes energetically unfavorable once a sufficient actuation strain is reached. Rolling is almost immediately finished if the deformed circumference is comparable to the size of the bilayer. As a result, diagonally rolled tubes are formed if rolling starts from two opposite corners (Figure 8a), and "tick or check mark-like" structures (for example Figure 3, c1, the film in the middle) are formed if rolling starts from two adjacent corners.

A more complicated scenario is observed when the width of the films is smaller and the length is considerably larger than the deformed circumference. Rolling starts at the corners first, like before, but long-side rolling starts later (Figure 8b and Figure 5) and is energetically favored. Rolling along the short side is unfavorable because it implies more stored stretching energy along the long side. Further long-side rolling makes diagonally rolled corners unfavorable and leads to the switching of bent corners to a "long-side rolling" scenario. Depending on the width of the film compared to the deformed circumference, either an incompletely rolled tube is formed or the two long-side rolling fronts collide into a completely rolled or doubled tube.

If the deformed circumference is considerably smaller than the width and length of the films

(which implies a high activation strain), then rolling starts first from corners and then continues along all sides (Figure 8c). The rolling fronts do not collide until several revolutions are made, which were shown to be almost irreversible.[17] As a result, already rolled fronts are unable to unroll and irreversible all-side rolling is observed.

CONCLUSIONS

We investigated in detail folding of rectangular stimuli-responsive hydrogel-based polymer bilayers located on a substrate with different lengths, widths, and thicknesses. It was found that long-side rolling dominates at high aspect ratios (ratio of length to width) when the width is comparable to the circumference of the formed tubes. Rolling from all sides occurs when the width and length considerably exceed this circumference. Diagonal or all-side rolling is observed when the width and length are comparable to the circumference. Short-side rolling was observed very rarely and in combination with diagonal rolling. On the basis of both experimental observations and theoretical assumptions, we argued that bilayers placed on a substrate start to roll from corners due to quicker diffusion of water. Rolling from long-side starts later but dominates at high aspect ratio due to energetic considerations. We have shown experimentally and by finite-element modeling confirmed by theoretical considerations that the main reasons causing a variety of rolling scenarios are (i) non-homogenous swelling due to slow diffusion of water in hydrogels and (ii) adhesion of polymer to a substrate until a certain threshold. Moreover, non-homogenous swelling determines folding in the first moments, while adhesion plays a decisive role at later stages of folding.

The films that we investigated are fabricated on the microscale. On the other hand, the knowledge obtained in this work is applicable to thinner films to direct their folding in order to form tubes with diameter in the nano range. We believe that the obtained knowledge can be particularly helpful for the design of self-folding objects with highly complex shapes and provides an interesting model system for path-dependent actuation.

EXPERIMENTAL PART

Materials. *N*-Isopropylacrylamide (NIPAM, Aldrich), 4-hydroxybenzophenone (Fluka), polycaprolactone (M_n = 70 000–90 000, Aldrich), benzophenone (Aldrich), and acryloyl chloride (Fluka) were used as received. Methyl methacrylate (MMA, Alrich) was purified by filtration through an Al_2O_3 column before polymerization.

Synthesis of 4-Acryloylbenzophenone (BA). 4-Hydroxybenzophenone (20 g, 0.1009 mol), diisopropylethylamine (19.3 mL, 0.1110 mol), and 80 mL of methylene chloride were added into a 200 mL three-necked round-bottom flask fitted with an overhead stirrer, a thermometer, and an addition funnel with acroloyl chloride (9.02 mL, 0.1110 mol) solution in 20 mL of methylene chloride. The acroloyl chloride solution was added dropwise into the flask under cooling (0–5 °C) for *ca.* 3 h. The methylene chloride was removed by rotary evaporation. The residue was washed with 80 mL of 20% HCl and 80 mL of a saturated solution of sodium hydrocarbonate and dried over sodium sulfate. The solution was passed through a silica gel column with chloroform as the eluent. Chloroform was removed by rotary evaporator. Finally, 24.44 g (95%) of BA was obtained. ^{1}H NMR ($CDCl_3$, 500 MHz): 6.05 (dd, J_1 = 10.40, J_2 = 1.26, 1H), 6.34 (dd, J_1 = 10.40, J_3 = 17.34, 1H), 6.64 (dd, J_3 = 17.34, J_2 = 1.26, 1H), 7.27 (m, 2H), 7.49 (m, 2H), 7.59 (m, 1H), 7.80 (m, 2H), 7.86 (m, 2H).

Synthesis of P(NIPAM-BA). BA (0.02253 g, 0.089 mmol; 0.04551 g, 0.18 mmol; 0.11737 g, 0.47 mmol), NIPAM (1 g, 0.0885 mol), and azobisisobutyronitrile (AIBN) (0.01453 g, 0.089 mmol) were added in 10 mL test tubes. Components were dissolved in 6 mL of 1,4-dioxane and degassed with nitrogen for 30 min. Test tubes were tightly sealed and placed into a shaker (70 °C, 90 rpm) for 24 h. Then the P(NIPAN-BA) polymerization mixtures were cooled to room temperature and poured slowly into diethyl ether. Products were filtered and dried under vacuum.

Synthesis of P(MMA-BA). A 6.2803 g amount of MMA (62.72 mmol), 0.2405 g of BA (0.96 mmol), and 0.052 g of AIBN (0.31 mmol) were dissolved in 30 mL of toluene. The mixture was purged with nitrogen for 30 min. The polymerization was carried at 70 °C under a nitrogen atmosphere with mechanical stirring overnight. After cooling, the mixture was poured in 750 mL of diethyl ether, and the precipitate was filtered and dried under vacuum at 40 °C.

Preparation of Polymer Bilayers. In a typical experiment, poly(NIPAN-BA) was dip-coated from its ethanol solution on a silica wafer substrate. Polycaprolactone with 2–5 mass % of benzophenone or P(MMA-BA) was spin-coated from a toluene solution on poly(NIPAM-BA) film. The bilayer film was illuminated through a specially designed photomasks by a halogen lamp for 40 min to cross-link polymers. The illuminated film was rinsed in chloroform in order to remove polymers in nonirradiated areas.

Conflict of Interest: The authors declare no competing financial interest.

Acknowledgment. The authors are grateful to DFG (Grant IO 68/1-1) and IPF for financial support. We also thank Yves Bréchet for discussions about the FE simulations.

Supporting Information Available: Movies of long-side (Figure 5, S1) and short-side (Figure 7a, S2) rolling. This material is available free of charge *via* the Internet at http://pubs.acs.org.

REFERENCES AND NOTES

1. Esser-Kahn, A. P.; Odom, S. A.; Sottos, N. R.; White, S. R.; Moore, J. S. Triggered Release from Polymer Capsules. *Macromolecules* **2011**, *44*, 5539–5553.
2. Ionov, L. Soft Microorigami: Self-Folding Polymer Films. *Soft Matter* **2011**, *7*, 6786–6791.
3. Leong, T. G.; Zarafshar, A. M.; Gracias, D. H. Three-Dimensional Fabrication at Small Size Scales. *Small* **2010**, *6*, 792–806.
4. Randhawa, J. S.; Kanu, L. N.; Singh, G.; Gracias, D. H. Importance of Surface Patterns for Defect Mitigation in Three-Dimensional Self-Assembly. *Langmuir* **2010**, *26*, 12534–12539.
5. Luchnikov, V.; Sydorenko, O.; Stamm, M. Self-Rolled Polymer and Composite Polymer/Metal Micro- and Nanotubes with Patterned Inner Walls. *Adv. Mater.* **2005**, *17*, 1177–1182.
6. Cho, J. H.; Gracias, D. H. Self-Assembly of Lithographically Patterned Nanoparticles. *Nano Lett.* **2009**, *9*, 4049–4052.

7. Solovev, A. A.; Sanchez, S.; Pumera, M.; Mei, Y. F.; Schmidt, O. G. Magnetic Control of Tubular Catalytic Microbots for the Transport, Assembly, and Delivery of Micro-objects. *Adv. Funct. Mater.* **2010**, *20*, 2430–2435.
8. Smith, E. J.; Liu, Z.; Mei, Y. F.; Schmidt, O. G. System Investigation of a Rolled-Up Metamaterial Optical Hyperlens Structure. *Appl. Phys. Lett.* **2009**, *95*, 083104.
9. Bof Bufon, C. C. s.; Cojal González, J. D.; Thurmer, D. J.; Grimm, D.; Bauer, M.; Schmidt, O. G. Self-Assembled Ultra-Compact Energy Storage Elements Based on Hybrid Nanomembranes. *Nano Lett.* **2010**, *10*, 2506–2510.
10. Guo, X. Y.; Li, H.; Ahn, B. Y.; Duoss, E. B.; Hsia, K. J.; Lewis, J. A.; Nuzzo, R. G. Two- and Three-Dimensional Folding of Thin Film Single-Crystalline Silicon for Photovoltaic Power Applications. *Proc. Natl. Acad. Sci. U. S. A.* **2009**, *106*, 20149–20154.
11. Schwaiger, S.; Broll, M.; Krohn, A.; Stemmann, A.; Heyn, C.; Stark, Y.; Sticklerbhas, D.; Heitmann, D.; Mendach, S. Rolled-Up Three-Dimensional Metamaterials with a Tunable Plasma Frequency in the Visible Regime. *Phys. Rev. Lett.* **2009**, *102*, 163903.
12. Gracias, D. H.; Tien, J.; Breen, T. L.; Hsu, C.; Whitesides, G. M. Forming Electrical Networks in Three Dimensions by Self-Assembly. *Science* **2000**, *289*, 1170–1172.
13. Leong, T.; Gu, Z. Y.; Koh, T.; Gracias, D. H. Spatially Controlled Chemistry Using Remotely Guided Nanoliter Scale Containers. *J. Am. Chem. Soc.* **2006**, *128*, 11336–11337.
14. Randall, C. L.; Kalinin, Y. V.; Jamal, M.; Manohar, T.; Gracias, D. H. Three-Dimensional Microwell Arrays for Cell Culture. *Lab Chip* **2011**, *11*, 127–131.
15. Jamal, M.; Bassik, N.; Cho, J. H.; Randall, C. L.; Gracias, D. H. Directed Growth of Fibroblasts into Three Dimensional Micropatterned Geometries via Self-Assembling Scaffolds. *Biomaterials* **2010**, *31*, 1683–1690.
16. Huang, G. S.; Mei, Y. F.; Thurmer, D. J.; Coric, E.; Schmidt, O. G. Rolled-Up Transparent Microtubes as Two-Dimensionally Confined Culture Scaffolds of Individual Yeast Cells. *Lab Chip* **2009**, *9*, 263–268.
17. Zakharchenko, S.; Puretskiy, N.; Stoychev, G.; Stamm, M.; Ionov, L. Temperature Controlled Encapsulation and Release Using Partially Biodegradable Thermo-Magneto-Sensitive Self-Rolling Tubes. *Soft Matter* **2010**, *6*, 2633–2636.
18. Stoychev, G.; Puretskiy, N.; Ionov, L. Self-Folding All-Polymer Thermoresponsive Microcapsules. *Soft Matter* **2011**, *7*, 3277–3279.
19. Zakharchenko, S.; Sperling, E.; Ionov, L. Fully Biodegradable Self-Rolled Polymer Tubes: a Candidate For Tissue Engineering Scaffolds. *Biomacromolecules* **2011**, *12*, 2211–2215.
20. Alben, S.; Balakrisnan, B.; Smela, E. Edge Effects Determine the Direction of Bilayer Bending. *Nano Lett.* **2011**, *11*, 2280–2285.
21. Chun, I. S.; Challa, A.; Derickson, B.; Hsia, K. J.; Li, X. Geometry Effect on the Strain-Induced Self-Rolling of Semiconductor Membranes. *Nano Lett.* **2010**, *10*, 3927–3932.
22. Stuart, M. A. C.; Huck, W. T. S.; Genzer, J.; Muller, M.; Ober, C.; Stamm, M.; Sukhorukov, G. B.; Szleifer, I.; Tsukruk, V. V.; Urban, M.; *et al.* Emerging Applications of Stimuli-Responsive Polymer Materials. *Nat. Mater.* **2010**, *9*, 101–113.
23. Singamaneni, S.; McConney, M. E.; Tsukruk, V. V. Swelling-Induced Folding in Confined Nanoscale Responsive Polymer Gels. *ACS Nano* **2010**, *4*, 2327–2337.
24. Jamal, M.; Zarafshar, A. M.; Gracias, D. H. Differentially Photo-Crosslinked Polymers Enable Self-Assembling Microfluidics. *Nat. Commun.* **2011**, *2*, 527.
25. Timoshenko, S. Analysis of Bi-Metal Thermostats. *J. Opt. Soc. Am. Rev. Sci. Instrum.* **1925**, *11*, 233–255.
26. Audoly, B.; Pomeau, Y. *Elasticity and Geometry: from Hair Curls to The Non-Linear Response of Shells*; Oxford University Press: Oxford, 2010.
27. Zienkiewicz, O. C.; Taylor, R. L. *Finite Element Method for Solid and Structural Mechanics*, 6th ed.; Elsevier: New York, 2005.
28. Liang, H. Y.; Mahadevan, L. Growth, Geometry, and Mechanics of a Blooming Lily. *Proc. Natl. Acad. Sci. U. S. A.* **2011**, *108*, 5516–5521.

,

F.2 Hierarchical multi-step folding of polymer bilayers [2]

www.MaterialsViews.com

ADVANCED FUNCTIONAL MATERIALS
www.afm-journal.de

FULL PAPER

Hierarchical Multi-Step Folding of Polymer Bilayers

*Georgi Stoychev, Sébastien Turcaud, John W. C. Dunlop, and Leonid Ionov**

A highly complex multi-step folding of isotropic stimuli-responsive polymer bilayers resulting in a variety of 2D and 3D structures is reported. Experimental observations allow determination of empirical rules, which can be used to direct the folding of polymer films in a predictable manner. In particular, it is demonstrated that these rules can be used for the design of a 3D pyramid. The understanding and know-how attained in this study allow the very simple design of highly complex, self-folding 3D objects and open new horizons for 3D patterning, important for the design of microfluidic devices, biomaterials, and soft electronics.

1. Introduction

Nature offers an enormous arsenal of ideas for the design of novel materials with superior properties and interesting behavior. In particular, self-assembly and self-organization, which are fundamental to structure formation in nature, attract significant interest as promising concepts for the design of intelligent materials.[1] Self-folding stimuli-responsive polymer films are exemplary biomimetic materials[2] and can be viewed as model systems for bioinspired actuation. Such films, on one hand, mimic movement mechanisms in certain plant organs[3,4] and, on the other hand, are able to self-organize and form complex 3D structures.[5] These self-folding films consist of two polymers with different properties. Because of the nonequal expansion of the two polymers, these films are able to form tubes,[6,7] capsules[8] or more complex structures.[9] Similar to origami, the self-folding polymeric films provide unique possibilities for the straightforward fabrication of highly complex 3D microstructures with patterned inner and outer walls that cannot be achieved using other technologies.

There are two general approaches for the design of self-folding films. The first approach is based on the use of complexly patterned films, where locally deposited active materials form hinges.[10] Homogenous bilayer films are used in the second approach.[11] Because of the isotropy of the mechanical properties of the bilayer, the formed structures are hinge-free and have rounded shapes. Importantly, in all reported cases, folding runs in one step. On the other hand there are reports that folding in nature can have a very complex character, which strongly depends on the geometry and swelling path[12] that may result in multistep folding (development of curvature in different directions).[3] In this contribution, we demonstrate that the shape of isotropic polymer bilayers is able to direct folding in a sophisticated manner leading to even more complex hierarchical folding than in nature. In particular, films can undergo sequential folding steps by forming various 3D shapes with sharp hinges. By analyzing the folding patterns we elucidated empirical rules, cross-checked by analytical considerations and backed up with finite-element simulations, which allow the folding to be directed, leading to the design of specific 3D shapes. We also highlight the importance of path-dependency in the activation of the actuator, which enables to lock it in a local energy minimum, which can differ from the global one.

G. Stoychev, Dr. L. Ionov
Leibniz Institute of Polymer Research Dresden
Hohe Str. 6, D-01069 Dresden, Germany
E-mail: ionov@ipfdd.de
G. Stoychev
Technische Universität Dresden
Physical Chemistry of Polymer Materials
01062 Dresden, Germany
S. Turcaud, Dr. J. W. C. Dunlop
Department of Biomaterials
Max Planck Institute of Colloids and Interfaces
Am Mühlenberg 1, D-14424, Potsdam, Germany

DOI: 10.1002/adfm.201203245

2. Results and Discussions

For the experiments we used polymer films consisting of two layers of photo-crosslinked polymers: the active layer being a random thermoresponsive copolymer poly(N-isopropylacrylamide-co-acrylic acid) (P(NIPAM-AA) and the passive layer being poly-(methylmethycrylate) (PMMA) (**Figure 1**). The bilayer, prepared as described elsewhere,[7] is located on a silica wafer in such a way that the active and passive polymers are the bottom and top layers, respectively. The bilayer is undeformed in PBS 0.1 M pH = 7.4 environment at T > 70 °C and folding occurs after cooling below 70 °C (Figure 1).

Due to the relatively slow diffusion rate of water inside the P(NIPAM-AA) layer, actuation is driven by the progression of the diffusion front, along which the hydrogel starts to swell. This induces a path-dependency in the folding pattern as the bilayer is not homogeneously activated, but progressively swells as water diffuses from the lateral sides. The investigation of swelling was performed in a qualitative manner by observing the color change of the films which, due to light interference, reflects the change in optical path length (OPL) (**Figure 2**). The OPL varies as a function of the film thickness and refractive index, which in turn depends on the swelling degree.[13] The nonswollen elliptical and star-like films have a homogenous blue (Figure 2a) and reddish (Figure 2d) color, respectively. The difference in the color of both films is caused by their different

2. Reprinted with permission from (Stoychev, Turcaud, et al. 2013). Copyright (2013) WILEY-VCH.

ADVANCED FUNCTIONAL MATERIALS
www.afm-journal.de
www.MaterialsViews.com

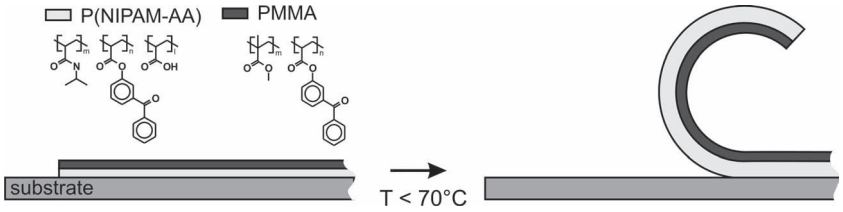

Figure 1. Scheme of folding of a bilayer polymer film consisting of two polymers: hydrophobic PMMA and thermoresponsive hydrogel P(NIPAM-AA).

starting thicknesses (Figure 2). The color of the films starts to change immediately after immersion in water at 25 °C, with the elliptical film becoming redder while the star-like film becomes green (Figure 2b,e). The changes of color in both cases start from the outer periphery of the bilayer film. As the active layer is confined between a water-impermeable silicon wafer and hydrophobic PMMA, this suggests that water can only penetrate inside the layer from the lateral sides.[14] The depth of water penetration along the perimeter of the film (activation depth) is uniform in both cases in the first moments of swelling. The differences in the swelling behavior between the two shapes appear after several seconds of incubation in water. The activation pattern depends on the external shape of the bilayers, with the position of the diffusion front (the activation depth) depending on the distance to the tissue border. This can been seen clearly in the differences of the activation patterns in the convex shapes like ellipse (Figure 2b), and concave ones like star (Figure 2d). For the star-like bilayers, the tips of the triangular-like arms swell faster than their base and their polygonal central part. This can be explained by the fact that after a certain time the diffusion fronts on either side of the arms intersect resulting in faster swelling. The experimental results show that the swelling starts from the periphery of the films and that the activation profile strongly depends on the shape of the film as confirmed by simple finite element simulations (see Figure 2c,f).

We next modeled and experimentally investigated the folding of circular/elliptical and star-like films. Modeling predicts that multiple wrinkles are formed along the perimeter of folding bilayer when it is edge-activated (Figure 2g). The spatial wavelength of the wrinkles is proportional to the activation depth (d) as observed in the wrinkles of leafs due to excessive radial edge-growth[15] and solved analytically in the context of geometrically nonlinear elasticity.[16] As the activation depth increases, the number of wrinkles decreases as P/d, where P is the perimeter of the shape (Figure 2h). The fact that there is both a gradient in radial- (edge-activation) and transversal direction (bilayer), results in a combination of wrinkling and bending, respectively (Figure 2g,h). In full agreement with the modeling predictions, experimental results show that the number of wrinkles decreases during folding (Figure 2i-l). Due to the transversal bending effect, the wrinkles actually evolve into local partial tubes as the activation depth increases. We observed that, at some point, the wrinkles stop to merge and their number remains constant. The probability of merging of two tubes depends on the angle (β, Figure 2h) between them. Experimentally, we found that the critical value of β below which merging of folded tubes was not observed is ca. 120–150°, which corresponds to 6–8 wrinkles when starting with a circular shape (inset in Figure 2h and Figure S3 in the Supporting Information). Based on these experimental observations we derived the first folding rule: "*Bilayer polymer films placed on a substrate start to fold from their periphery and the number of formed wrinkles/tubes decreases until the angle between adjacent wrinkles/tubes approaches 130°*".

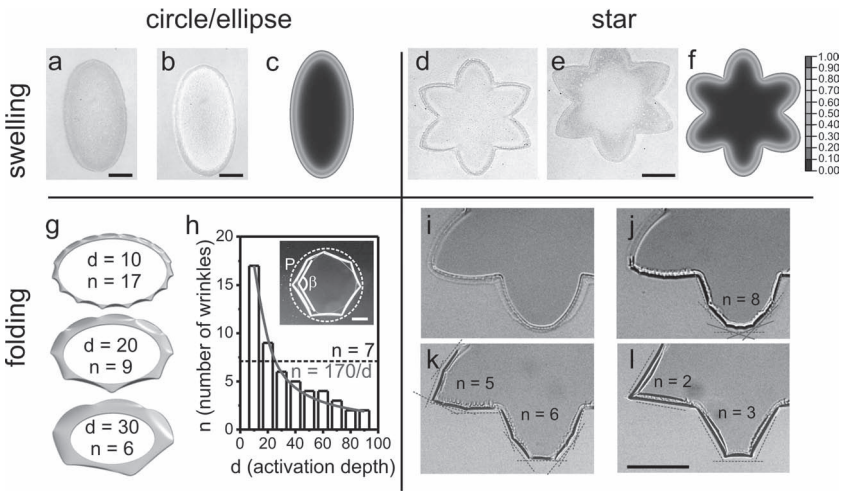

Figure 2. Swelling (upper panels) and first step of folding (lower panels) of circular/elliptical (left panels) and star-like (right panels) bilayer polymer films. a,b,d,e) Microscopy snapshots of swelling elliptical and star-like P(NIPAM-AA)/PMMA bilayers immediately after immersion in water (a,d) and after ca. 60 s incubation (b,e); c,f) Color map of the calculated swelling (from 0 to 1) controlled by water diffusion in the active monolayer with a lateral constant boundary condition (blue is non swollen) dependent on shape obtained by finite element simulations; g) Finite element simulations of wrinkling of a bilayer crown representing the activated edge in case of a circular shape; h) The number of wrinkles is inversely proportional to the actuation depth. Dashed line corresponds to the experimental observation of heptahedrons (inset) when folding is typically stopped in the case of circular shapes. The red line corresponds to n = 170/d. i–l) Two rays of six-ray star during wrinkling, decrease of number of wrinkles is observed. a, b) H_{PNIPAM} = 35 nm, H_{PMMA} = 400 nm; d,e) H_{PNIPAM} = 35 nm, H_{PMMA} = 500 nm; i–l) $H_{(PNIPAM-AA)}$ = 1200 nm, H_{PMMA} = 400 nm, scale bar is 200 μm.

After the number of wrinkles/tubes along the perimeter of the bilayer film stopped to change the bilayers are locked for some time until the subsequent folding step occurs. For example, the wrinkled semi-ellipse bends towards its base (**Figure 3**a). To explain the origin of the second step of folding we considered the geometry of the film after the first folding step. As mentioned, wrinkling of a bilayer leads to the formation of tubes along the perimeter of the film. Considering the fact that the rigidity of the tubes is higher than that of the undeformed films, the polygonal shapes are stiffened by this tube formation, and therefore possess a

www.MaterialsViews.com

ADVANCED FUNCTIONAL MATERIALS
www.afm-journal.de

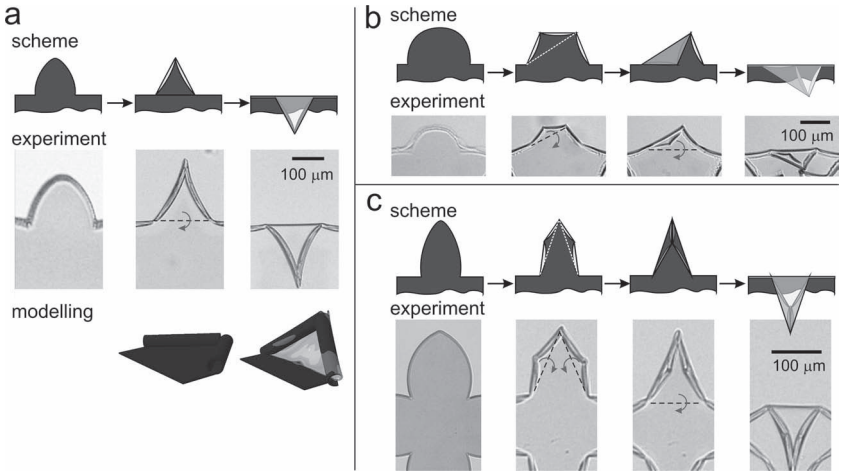

Figure 3. Schematic illustration, experimental observation, and modeling of the second step of folding of the elliptical arms depending on their shape. a) $H_{(PNIPAM-AA)}$ = 1200 nm, H_{PMMA} = 170 nm; b) ($H_{(PNIPAM-AA)}$ = 1200 nm, H_{PMMA} = 400 nm; c) $H_{(PNIPAM-AA)}$ = 900 nm, H_{PMMA} = 170 nm.

number of weak points located at the intersection of the tubes, i.e., at the vertices. These points act like hinges and folding is only observed along the lines connecting them (dashed line in Figure 3a). The formation of hinges during folding of isotropic bilayers, which to our knowledge has not been reported in the literature, is induced by the progressive activation from the lateral sides and the folded shapes are controlled by the initial shapes of the bilayers. This leads to the second rule of the folding: *"After the wrinkles along the perimeter of the film form tubes, further folding proceeds along the lines connecting the vertexes of the folded film"*.

In case there are more than two hinges in the film, a question arises: upon which connecting line will the folding occur? The number of hinges is largely determined by the shape of the semi-ellipses. The regular semi-ellipse, which has a triangular shape after the first step of folding, simply bends toward the base along the line connecting the two bottom vertexes (dashed line in Figure 3a). If the semi-ellipse is more rounded, it forms a trapezoid after the first-step of folding (Figure 3b). In the second step of folding, the trapezoid bends along one of the lines connecting the opposite top and bottom vertexes (dashed line in the second image from the left in Figure 3b). Next, the formed triangle bends towards its base along the line connecting the two bottom vertexes. The elongated semi-ellipse forms four folds after the first step of folding (Figure 3c). Interestingly, the semi-ellipse folds further along the lines connecting the vertexes at the base and the top vertex and no folding along the lines connecting neither the vertexes of the middle nor the ones at the base is observed. Looking at the evolution of the activation pattern through time (diffusion profile see Figure 2), we observe that the lines connecting the hinges can only be used if they are within the activated pattern (red). Thus, the third rule of the folding states: "*the folding goes along the lines which are closer to the periphery of the films*".

Six-ray stars demonstrate the formation of very complex structures (**Figure 4**). Notably simultaneous folding of all rays is observed very rarely and in most cases triangles (Figure 4g) were formed. We investigated the folding in a time-resolved manner in order to explain the formation of the triangles (**Figure 5**). Similar to the experiment demonstrated in Figure 2, wrinkles get longer and bend transversally into tubes (Figure 5b) thus increasing the rigidity of the ray. Next, one of the rays folds towards the center of the star (II in Figure 5c). Folding of this ray leads to the formation of a rigid semi-rolled tube, which is formed by the folded ray and the tubular shoulders of the adjacent rays (Figure 5c). The angle between the base of the folded ray and the shoulders of the neighboring arms is close to 180° (Figure 5c). In this configuration, the weak points located at the intersection between I–II and II–III has disappeared and rays I and III (Figure 5c) cannot bend anymore. As a result, only three remaining rays (IV, V, VI) can bend. If ray V folds, no additional rays can bend (Figure 4l). If ray IV folds (Figure 5d) ray V is blocked. Finally, ray VI can fold leading to the formation of a triangle (Figure 5e). The discussed principle can be easily applied to understand the formation of the other observed figures (Figure 4c–l, Supporting Information Figure S2 and Figure S3). In fact, several factors can be held responsible for the observed symmetry breaking (rays do not fold at the same time) such as inhomogeneities in the films and shape imperfections resulting in small deviations from the symmetric diffusion profile. Based on these experimental observations, one can derive the fourth folding rule: "*Folding of the rays may result in blocking of the neighboring rays if the angle between the base of the folded ray and the shoulders of the neighboring rays is close to 180°*".

Finally, we applied the derived rules for the design of truly 3D structures–pyramids. In fact, the reason why six-ray star formed flattened folded structures is their short arms and the hindering of folding of rays. Therefore, in order to fabricate pyramids we increased the relative length of the rays and changed the angle between them by decreasing their number (**Figure 6**a,b). The rays of the fabricated four-ray stars first wrinkle along their perimeter (Figure 6c, d). Four tubes are formed along the perimeter of each ray (first rule, Figure 6c), which then collapse two by two and form triangles (second rule, Figure 6d). Since the angle between the folds located on the shoulders of each ray is considerably smaller than 180°, the folding of rays is not self-interfering (forth rule) and all rays fold in the direction of the center of the star (third rule) thus forming a hollow pyramid (Figure 6e–g) that is supported by simulations (Figure 6h). In fact these rules are also applicable to other shapes such as rectangles. As an example we included two-step folding of rectangles (Supporting Information Figure S4).

We observed that, in general, folding rules are applicable to all thickness (we performed many experiments with different thicknesses). The difference between the thin and thick films are in minor. For example, we observe that when star-like thin fold than all six arms (Figure 4d,k) can fold inside because rigidity of the film is not that high. In the

ADVANCED FUNCTIONAL MATERIALS
www.afm-journal.de

www.MaterialsViews.com

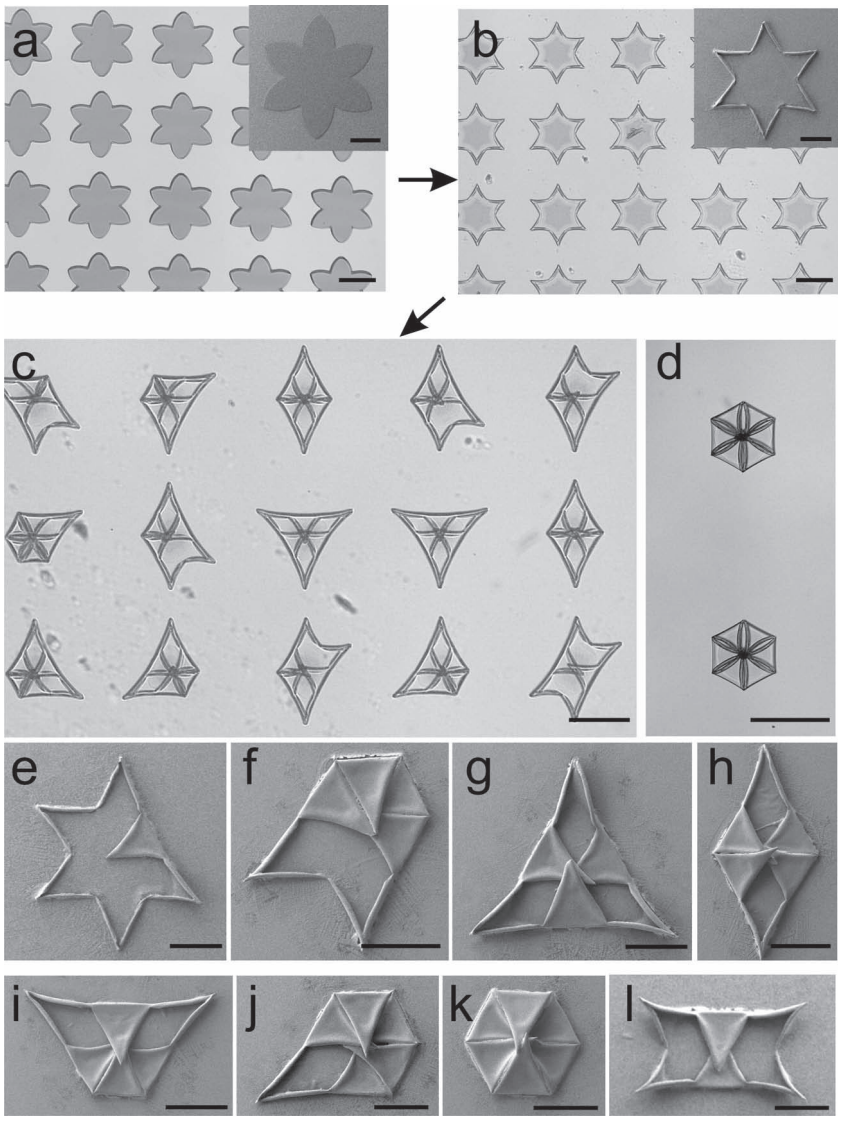

Figure 4. Examples of structures obtained by progressive edge-activation of six-ray star-like bilayers. a) Patterned bilayers; b) First step of actuation: wrinkles collapse into tubes; c–l) Second step of actuation: rays fold leading to several configurations depending on the order of folding. Scale bars are 200 µm, $H_{(PNIPAM-AA)}$ = 1200 nm, H_{PMMA} = 260 nm.

case of thick films, we typically observed folding of 3–4 arms (Figure 4g,l).

3. Conclusions

In conclusion, we investigated the actuation of patterned bilayers placed on a substrate. Due to the edge-activation of the bilayers, the observed deformed shapes differ from the classical ones obtained by homogeneous activation. We found that films can demonstrate several kinds of actuation behavior such as wrinkling, bending and folding that result in a variety of shapes. It was demonstrated that one can introduce hinges into the folded structure by proper design of the bilayer's external shape through diffusion without having to use site selective deposition of active polymers. Experimental observations lead us to derive four empirical rules backed up by theoretical understanding as well as simulations. We then demonstrated how those rules can be used to direct the folding of edge-activated polymer bilayers through a concrete example–the design of a 3D pyramid. We believe that the derived understanding and know-how will allow very simple design of highly complex, self-folding 3D objects and will open new horizons for 3D patterning which is highly important for the design of microfluidic devices, biomaterials, soft electronics, etc.

4. Experimental Section

Materials: *N*-isopropylacrylamide (NIPAM, Aldrich), 4-hydroxybenzophenone (Fluka), polycaprolactone (M_n = 70 000–90 000 Da, Aldrich), benzophenone (Aldrich) and acryloyl chloride (Fluka) were used as received. Methyl methacrylate (MMA, Aldrich) and acrylic acid were purified by filtration through Al_2O_3 column before polymerization.

Synthesis of 4-Acryloylbenzophenone (BA): 4-Hydroxybenzophenone (20 g, 0.1009 mol), diisopropylethylamine (19.3 mL, 0.1110 mol) and 80 mL of methylene chloride were added into 200 mL three-necked round-bottom flask fitted with an overhead stirrer, a thermometer, and an addition funnel with acroloyl chloride (9.02 mL, 0.1110 mol) solution in 20 mL of methylene chloride. The acroloyl chloride solution was added dropwise into the flask under cooling (0–5 °C) for ca 3 h. The methylene chloride was removed by rotary evaporation. The residue was washed with 80 mL of 20% HCl, 80 mL of saturated solution of sodium hydrocarbonate and dried over sodium sulphate. The solution was passed through a silica gel column with chloroform as the eluent. Chloroform was removed by rotary evaporator. Finally, 24.44 g (95%) of ABP was obtained. ^{1}H NMR ($CDCl_3$, 500 MHz): 6.05 (dd, J_1 = 10.40, J_2 = 1.26, 1H), 6.34 (dd, J_1 = 10.40, J_3 = 17.34, 1H), 6.64 (dd, J_3 = 17.34, J_2 = 1.26, 1H), 7.27 (m, 2H), 7.49 (m, 2H), 7.59 (m, 1H), 7.80 (m, 2H), 7.86 (m, 2H).

Synthesis of P(NIPAM-AA-BA): BA (0.28 g, 1,12 mmol); NIPAM (6 g, 51.57 mmol), AA (0.2556 g, 3.36 mmol), AIBN (0.01632 g, 0.38 mmmol) were added in 50 mL flask. Components were dissolved in 30 mL ethanol and degassed with nitrogen for 30 min. The mixture was purged with nitrogen for 30 min. The polymerization was carried at 70 °C under nitrogen atmosphere with mechanical stirring overnight. After cooling, the mixture was poured in 750 mL diethyl ether, the precipitate was filtered and dried in vacuum at 40 °C.

Synthesis of P(MMA-BA): 6.3 g MMA (62.7 mmol), 0.24 g BA (0.96 mmol) and 0.05 g AIBN (0.31 mmol) were dissolved in 30 mL of toluene. The mixture was purged with nitrogen for 30 min. The polymerization was carried at 70 °C under nitrogen atmosphere with mechanical stirring overnight. After cooling, the mixture was poured in 750 mL diethyl ether, the precipitate was filtered and dried in vacuum at 40 °C.

Preparation of Polymer Bilayers: In a typical experiment, poly-(NIPAN-BA) was dip-coated from its ethanol solution on silica wafer substrate. P(MMA-BA) was dip-coated from toluene solution on the

www.MaterialsViews.com

ADVANCED FUNCTIONAL MATERIALS
www.afm-journal.de

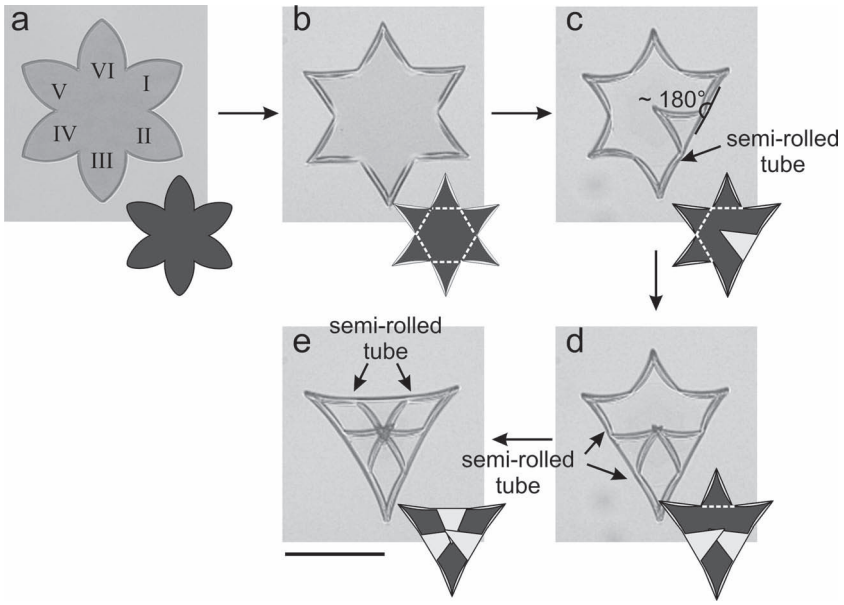

Figure 5. Microscopy snap-shots illustrating the mechanism of formation of triangles during actuation of a six-ray stars. Scale bar is 200 µm, $H_{(PNIPAM-AA)}$ = 1200 nm, H_{PMMA} = 170 nm.

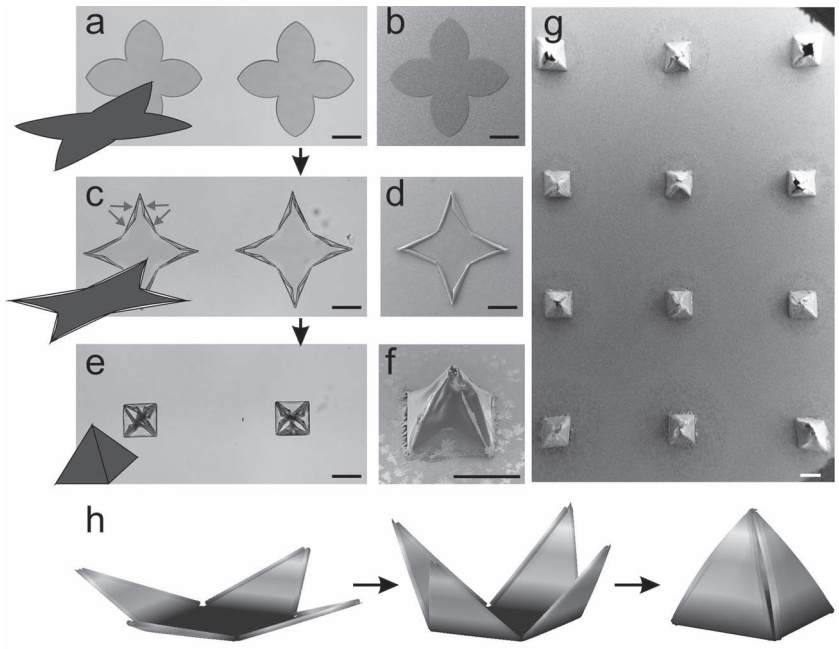

Figure 6. Sequential actuation of four-ray stars leads to the formation of pyramids. a,b) unactivated film; c,d) after wrinkling of the ray periphery into tubes, arrows indicate four wrinkles formed on each arm during first step of folding; e–g) after folding of rays leading to the formation of pyramids. Scale bar is 200 µm, $H_{(PNIPAM-AA)}$ = 1200 nm; H_{PMMA} = 260 nm. h) Simulated folding of four-arm star.

poly-(NIPAM-BA) film. The bilayer film was illuminated through a photomask (Toppan Photomasks inc.) by halogen lamp for 40 min to crosslink the polymers. The illuminated film was rinsed in chloroform in order to remove the polymers from non-irradiated areas. The prepared bilayers were then dried again in air before experiment and contained no water. The observation of bilayer was performed by Axiovert Zeiss Microscope using 5× and 10× air objectives.

Numerical Simulations: Simulations were performed in Abaqus v6.11 using the standard finite-element method. In order to simulate the diffusion process in the active layer we performed a 2D heat transfer analysis with imposed temperature on the free perimeter of the shapes (circle, semi-ellipsoid) and constant diffusive properties This resulted in a time-dependent temperature distribution that mimics the swelling process The resulting nodal temperatures at an early point in time were then applied to the corresponding 3D bilayer shapes having a mismatch in expansion properties (passive layer has 0 thermal expansion, while the active layer has in-plane expansion coefficients of 1). Due to symmetries only the relevant part of the bilayers were simulated in order to reduce computational costs. The resultant actuated shape was obtained through a geometrically nonlinear static step. For more detailed information see ref. [14]. Doing this, we assumed that diffusion-driven actuation follows a quasistatic process in which the timescales of diffusion and actuation are clearly separated. The progression of the diffusion front is slow (s) while the resultant mechanical actuation is fast (ms). This enabled us to consider the two phenomena separately thereby neglecting potential couplings between swelling and mechanical properties. Results are only qualitative, as the actual material characteristics of the hydrogels were not measured. However, the actuation pattern, and thus the number of wrinkles, only depends on the depth of the differential edge-activation named "activation depth" in this paper. This enabled us to predict and confirm the experimental actuation patterns with simple normalized properties.

Supporting Information

Supporting Information is available from the Wiley Online Library or from the author.

Acknowledgements

The authors are grateful to DFG (Grant IO 68/1-1) and IPF for financial support. The authors are grateful to K.-J. Eichhorn and R. Schulze (IPF) for assistance with ellipsometry.

Received: November 5, 2012
Published online: November 26, 2012

[1] a) A. Terfort, N. Bowden, G. M. Whitesides, *Nature* **1997**, *386*, 162; b) G. M. Whitesides, B. Grzybowski, *Science* **2002**, *295*, 2418.
[2] a) T. G. Leong, A. M. Zarafshar, D. H. Gracias, *Small* **2010**, *6*, 792; b) L. Ionov, *Soft Matter* **2011**, *7*, 6786.

ADVANCED FUNCTIONAL MATERIALS
www.afm-journal.de

www.MaterialsViews.com

[3] M. J. Harrington, K. Razghandi, F. Ditsch, L. Guiducci, M. Rueggeberg, J. W. C. Dunlop, P. Fratzl, C. Neinhuis, I. Burgert, *Nat. Commun.* **2011**, *2*, 337.
[4] a) J. W. C. Dunlop, R. Weinkamer, P. Fratzl, *Mater. Today* **2011**, *14*, 70; b) J. M. Skotheim, L. Mahadevan, *Science* **2005**, *308*, 1308; c) L. Mahadevan, S. Rica, *Science* **2005**, *307*, 1740.
[5] M. Jamal, A. M. Zarafshar, D. H. Gracias, *Nat. Commun.* **2011**, *2*, 527.
[6] S. Zakharchenko, E. Sperling, L. Ionov, *Biomacromolecules* **2011**, *12*, 2211.
[7] S. Zakharchenko, N. Puretskiy, G. Stoychev, M. Stamm, L. Ionov, *Soft Matter* **2010**, *6*, 2633.
[8] G. Stoychev, N. Puretskiy, L. Ionov, *Soft Matter* **2011**, *7*, 3277.
[9] A. Azam, K. Laflin, M. Jamal, R. Fernandes, D. Gracias, *Biomed. Microdevices* **2011**, *1*, 51.
[10] D. H. Gracias, V. Kavthekar, J. C. Love, K. E. Paul, G. M. Whitesides, *Adv. Mater.* **2002**, *14*, 235.
[11] G. S. Huang, Y. F. Mei, D. J. Thurmer, E. Coric, O. G. Schmidt, *Lab Chip* **2009**, *9*, 263.
[12] a) H. Y. Liang, L. Mahadevan, *Proc. Natl. Acad. Sci. USA* **2011**, *108*, 5516; b) H. Liang, L. Mahadevan, *Proc. Natl. Acad. Sci. USA* **2009**, *106*, 22049.
[13] a) I. Jung, J. S. Rhyee, J. Y. Son, R. S. Ruoff, K. Y. Rhee, *Nanotechnology* **2012**, *23*, 025708; b) J. Henrie, S. Kellis, S. M. Schultz, A. Hawkins, *Opt. Express* **2004**, *12*, 1464.
[14] G. Stoychev, S. Zakharchenko, S. Turcaud, J. W. C. Dunlop, L. Ionov, *ACS Nano* **2012**, *6*, 3925.
[15] M. Marder, E. Sharon, S. Smith, B. Roman, *Europhys. Lett.* **2003**, *62*, 498.
[16] B. Audoly, A. Boudaoud, *C. R. Acad. Sci., Ser. IIb: Mec.* **2002**, *330*, 831.

,

F.3 Cover of advanced functional materials [3]

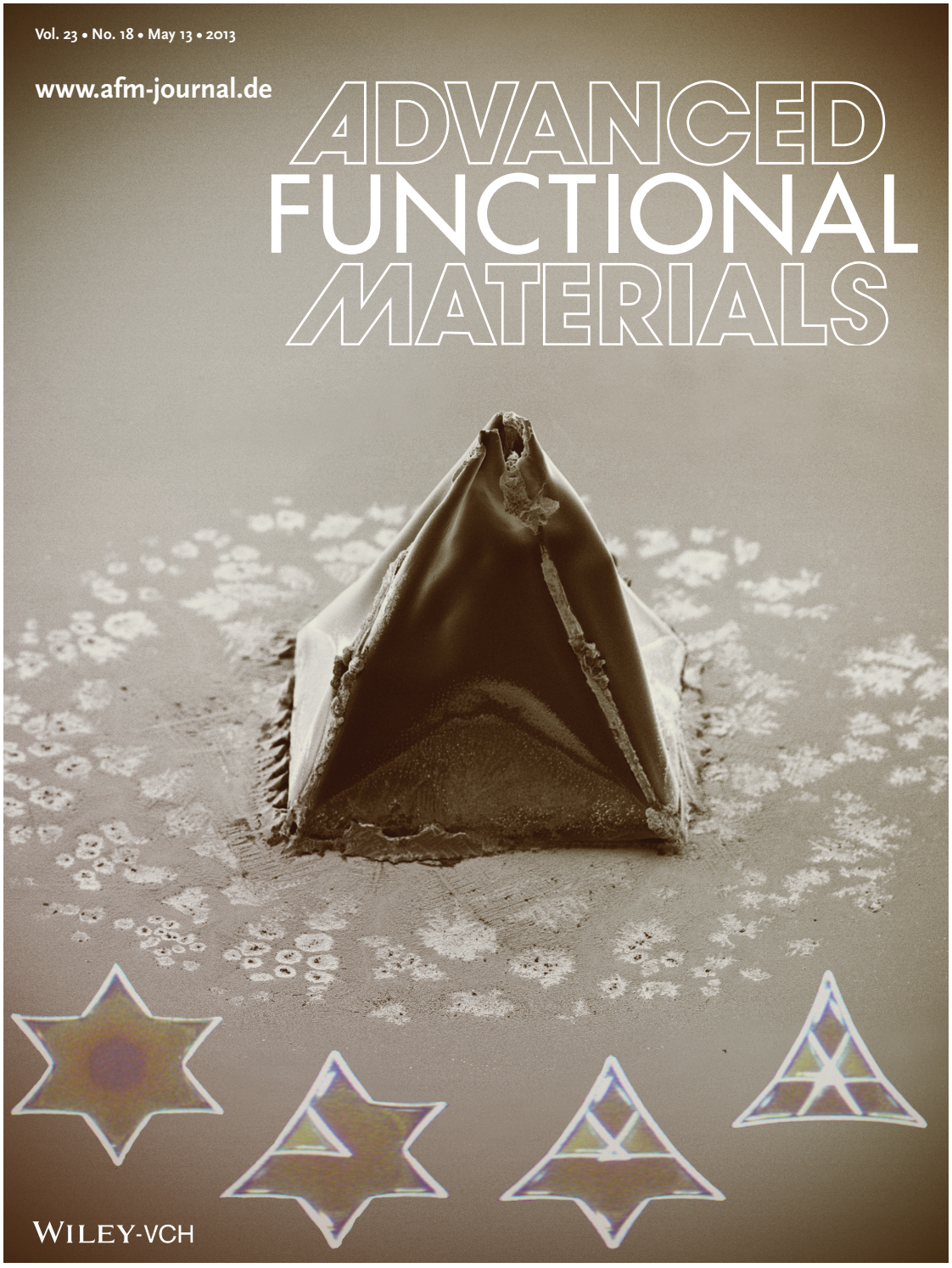

3. Reprinted with permission from (Stoychev, Turcaud, et al. 2013). Copyright (2013) WILEY-VCH.

Bibliography

Abraham, Yael et al. (2012). « Tilted cellulose arrangement as a novel mechanism for hygroscopic coiling in the stork's bill awn ». In: *Journal of The Royal Society Interface* 9.69, pp. 640–647.

Aharoni, Hillel et al. (2012). « Emergence of spontaneous twist and curvature in non-euclidean rods: application to Erodium plant cells ». In: *Physical review letters* 108.23, p. 238106.

Alben, Silas (2011). « Bending of bilayers with general initial shapes ». In: *Advances in Computational Mathematics*, pp. 1–22.

Alben, Silas, Bavani Balakrisnan, and Elisabeth Smela (2011). « Edge effects determine the direction of bilayer bending ». In: *Nano letters* 11.6, pp. 2280–2285.

Amar, Martine Ben, Martin Michael Müller, and Miguel Trejo (2012). « Petal shapes of sympetalous flowers: the interplay between growth, geometry and elasticity ». In: *New Journal of Physics* 14.8, p. 085014.

Armon, Shahaf et al. (2011). « Geometry and mechanics in the opening of chiral seed pods ». In: *Science* 333.6050, pp. 1726–1730.

Audoly, Basile and Arezki Boudaoud (2002). « Ruban à godets: an elastic model for ripples in plant leaves ». In: *Comptes Rendus Mecanique* 330.12, pp. 831–836.

— (2003). « Self-similar structures near boundaries in strained systems ». In: *Physical review letters* 91.8, p. 086105.

Audoly, Basile and Yves Pomeau (2010). *Elasticity and geometry*. Oxford Univ. Press.

Bell, Mrs RC and Jean Paul Richter (1970). *The notebooks of Leonardo da Vinci*. Vol. 1. Courier Dover Publications.

Benham, Craig J (1989). « Onset of writhing in circular elastic polymers ». In: *Physical Review A* 39.5, p. 2582.

Bergou, Miklós et al. (2008). « Discrete elastic rods ». In: *ACM Transactions on Graphics (TOG)* 27.3, p. 63.

Bertails, Florence et al. (2006). « Super-helices for predicting the dynamics of natural hair ». In: *ACM Transactions on Graphics (TOG)*. Vol. 25. 3. ACM, pp. 1180–1187.

Betts, Jonathan (1993). « John Harrison: inventor of the precision timekeeper ». In: *Endeavour* 17.4, pp. 160–167.

Bouaziz, Olivier, Yves JM Bréchet, and J David Embury (2008). « Heterogeneous and architectured materials: a possible strategy for design of structural materials ». In: *Advanced Engineering Materials* 10.1-2, pp. 24–36.

Boué, L et al. (2006). « Spiral patterns in the packing of flexible structures ». In: *Physical review letters* 97.16, p. 166104.

Brakke, Kenneth A (1992). « The surface evolver ». In: *Experimental mathematics* 1.2, pp. 141–165.

Bréchet, Yves JM and J David Embury (2013). « Architectured materials: Expanding materials space ». In: *Scripta Materialia* 68.1, pp. 1–3.

Bruno, Andrea et al. (2010). *Featuring Steel*.

Cerda, Enrique et al. (1999). « Conical dislocations in crumpling ». In: *Nature* 401.6748, pp. 46–49.

Charitat, Thierry and Bertrand Fourcade (1998). « Metastability of a circular o-ring due to intrinsic curvature ». In: *The European Physical Journal B-Condensed Matter and Complex Systems* 1.3, pp. 333–336.

Chebyshev, Pafnouti L (1878). « On the cut of clothes ». unpublished.

Chen, Zi, Qiaohang Guo, et al. (2012). « Nonlinear geometric effects in mechanical bistable morphing structures ». In: *Physical review letters* 109.11, p. 114302.

Chen, Zi, Carmel Majidi, et al. (2011). « Tunable helical ribbons ». In: *Applied Physics Letters* 98.1, p. 011906.

Chopra, Inderjit (2002). « Review of state of art of smart structures and integrated systems ». In: *AIAA journal* 40.11, pp. 2145–2187.

Chouaieb, Nadia, Alain Goriely, and John H Maddocks (2006). « Helices ». In: *Proceedings of the National Academy of Sciences* 103.25, pp. 9398–9403.

Curie, Pierre (1894). « Sur la symétrie dans les phénomènes physiques, symétrie d'un champ électrique et d'un champ magnétique ». In: *J. Phys. Theor. Appl.* 3.1, pp. 393–415.

Darwin, Charles (1865). « On the movements and habits of climbing plants. » In: *Journal of the Linnean Society of London, Botany* 9.33-34, pp. 1–118.

— (1888). *The movements and habits of climbing plants*. J. Murray.

Darwin, Charles and Francis Darwin (1897). *The power of movement in plants*. Appleton.

Dawson, Colin, Julian FV Vincent, and Anne-Marie Rocca (1997). « How pine cones open ». In: *Nature* 390.6661, pp. 668–668.

Demin, Dimitry and Sébastien Turcaud (2009). « Geometrical solutions of soap bubble clusters ». In: *Design Modeling Symposium 2009*. Ed. by Berlin Universität der Künste.

Dervaux, Julien and Martine Ben Amar (2008). « Morphogenesis of growing soft tissues ». In: *Physical review letters* 101.6, p. 068101.

Dervaux, Julien, Pasquale Ciarletta, and Martine Ben Amar (2009). « Morphogenesis of thin hyperelastic plates: a constitutive theory of biological growth in the Föppl–von Kármán limit ». In: *Journal of the Mechanics and Physics of Solids* 57.3, pp. 458–471.

Developers, Scipy (2014). *SciPy: Open source scientific tools for Python*. URL: `http://scipy.org/`.

Dias, Marcelo A, Levi H Dudte, et al. (2012). « Geometric mechanics of curved crease origami ». In: *Physical review letters* 109.11, p. 114301.

Dias, Marcelo A, James A Hanna, and Christian D Santangelo (2011). « Programmed buckling by controlled lateral swelling in a thin elastic sheet ». In: *Physical Review E* 84.3, p. 036603.

Dijksterhuis, Eduard Jan, Carry Dikshoorn, and Wilbur Richard Knorr (1987). *Archimedes*. Princeton University Press Princeton.

Donato, Cassia C, Marcelo AF Gomes, and Ricardo E de Souza (2002). « Crumpled wires in two dimensions ». In: *Physical Review E* 66.1, p. 015102.

— (2003). « Scaling properties in the packing of crumpled wires ». In: *Physical Review E* 67.2, p. 026110.

Dunlop, John WC and Yves JM Bréchet (2009). « Architectured structural materials: a parallel between nature and engineering ». In: *MRS Proceedings*. Vol. 1188. Cambridge Univ Press, pp. 1188–LL09.

Efrati, Efi, Yael Klein, et al. (2007). « Spontaneous buckling of elastic sheets with a prescribed non-Euclidean metric ». In: *Physica D: Nonlinear Phenomena* 235.1, pp. 29–32.

Efrati, Efi, Eran Sharon, and Raz Kupferman (2009). « Buckling transition and boundary layer in non-Euclidean plates ». In: *Physical Review E* 80.1, p. 016602.

Elbaum, Rivka, Stanislav Gorb, and Peter Fratzl (2008). « Structures in the cell wall that enable hygroscopic movement of wheat awns ». In: *Journal of structural biology* 164.1, pp. 101–107.

Elbaum, Rivka, Liron Zaltzman, et al. (2007). « The role of wheat awns in the seed dispersal unit ». In: *Science* 316.5826, pp. 884–886.

Eshelby, John D. (1957). « The determination of the elastic field of an ellipsoidal inclusion, and related problems ». In: *Proceedings of the Royal Society of London. Series A. Mathematical and Physical Sciences* 241.1226, pp. 376–396.

Euler, Leonhard (1952). *Methodus inveniendi lineas curvas maximi minimive proprietate gaudentes sive solutio problematis isoperimetrici latissimo sensu accepti*. Vol. 24. Springer.

Evangelista, Dennis, Scott Hotton, and Jacques Dumais (2011). « The mechanics of explosive dispersal and self-burial in the seeds of the filaree, Erodium cicutarium (Geraniaceae) ». In: *The Journal of experimental biology* 214.4, pp. 521–529.

Feynman, Richard (1981). *The pleasure of finding things out*. BBC Horizon. URL: `http://www.youtube.com/watch?v=FXiOg5-l3fk`.

Flynn, Cormac O and Brendan AO McCormack (2009). « A three-layer model of skin and its application in simulating wrinkling ». In: *Computer methods in biomechanics and biomedical engineering* 12.2, pp. 125–134.

Follett, Ken (1989). *The pillars of the earth*. Pan.

Forterre, Yoël et al. (2005). « How the Venus flytrap snaps ». In: *Nature* 433.7024, pp. 421–425.

Fratzl, Peter (2007). « Biomimetic materials research: what can we really learn from nature's structural materials? » In: *Journal of the Royal Society Interface* 4.15, pp. 637–642.

Fratzl, Peter and Friedrich G Barth (2009). « Biomaterial systems for mechanosensing and actuation ». In: *Nature* 462.7272, pp. 442–448.

Fratzl, Peter, Rivka Elbaum, and Ingo Burgert (2008). « Cellulose fibrils direct plant organ movements ». In: *Faraday discussions* 139, pp. 275–282.

Fratzl, Peter and Richard Weinkamer (2007). « Nature's hierarchical materials ». In: *Progress in Materials Science* 52.8, pp. 1263–1334.

Galileo, G, H Crew, and A de Salvio (1914). *Discourses and Mathematical Demonstrations Relating to Two New Sciences (1638)*.

Galloway, John (2002). « Helical imperative: paradigm of form and function ». In: *eLS*.

Geitmann, Anja and Joseph KE Ortega (2009). « Mechanics and modeling of plant cell growth ». In: *Trends in plant science* 14.9, pp. 467–478.

Gemmer, John and Shankar C Venkataramani (2013). « Shape transitions in hyperbolic non-Euclidean plates ». In: *Soft Matter* 9.34, pp. 8151–8161.

Gent, Alan N (1958). « On the relation between indentation hardness and Young's modulus ». In: *Rubber Chemistry and Technology* 31.4, pp. 896–906.

Genzer, Jan and Jan Groenewold (2006). « Soft matter with hard skin: From skin wrinkles to templating and material characterization ». In: *Soft Matter* 2.4, pp. 310–323.

Gerbode, Sharon J et al. (2012). « How the cucumber tendril coils and overwinds ». In: *Science* 337.6098, pp. 1087–1091.

Goethe, Johann Wolfgang (1790). « Die Metamorphose der Pflanzen ». In: *Goethes Naturwissenschaftliche Schriften* 6.

Gomes, Marcelo AF et al. (2008). « Plastic deformation of 2D crumpled wires ». In: *Journal of Physics D: Applied Physics* 41.23, p. 235408.

Goriely, Alain (2006). « Twisted elastic rings and the rediscoveries of Michell's instability ». In: *Journal of Elasticity* 84.3, pp. 281–299.

Goriely, Alain and Derek Moulton (2011). « Morphoelasticity: A theory of elastic growth ». In: *New Trends in the Physics and Mechanics of Biological Systems: Lecture Notes of the Les Houches Summer School: Volume 92, July 2009* 92, p. 153.

Goriely, Alain and Michael Tabor (1998). « Spontaneous helix hand reversal and tendril perversion in climbing plants ». In: *Physical Review Letters* 80.7, p. 1564.

Gracias, David H (2013). « Stimuli responsive self-folding using thin polymer films ». In: *Current Opinion in Chemical Engineering* 2.1, pp. 112–119.

Greenhill, A George (1881). *Determination of the greatest height consistent with stability that a vertical pole or mast can be made, and of the greatest height to which a tree of given proportions can grow*.

Guiducci, Lorenzo (2013). « Passive biomimetic actuators: the role of material architecture ». PhD thesis. Universität Potsdam.

Haeckel, Ernst (2013). *Kunstformen der Natur*. BoD–Books on Demand.

Han, Qing and Jia-Xing Hong (2006). *Isometric embedding of Riemannian manifolds in Euclidean spaces*. Vol. 130. American Mathematical Society.

Harlow, William M, WA Cote, and AC Day (1964). « The opening mechanism of pine cone scales ». In: *Journal of Forestry* 62.8, pp. 538–540.

Harner, Leslie L. (2013). *Selecting Controlled Expansion Alloys*. URL: `http://www.cartech.com/techarticles.aspx?id=1674/`.

Harrington, Matthew J et al. (2011). « Origami-like unfolding of hydro-actuated ice plant seed capsules ». In: *Nature communications* 2, p. 337.

Henderson, David W and Daina Taimina (2001). « Crocheting the hyperbolic plane ». In: *The Mathematical Intelligencer* 23.2, pp. 17–28.

Hibbett, Karlsson, and Sorensen (1998). *ABAQUS/standard: User's Manual*. Vol. 1. Hibbitt, Karlsson & Sorensen.

Hoberman, Chuck (2014a). *Toys*. URL: `http://www.hoberman.com/fold/main/index.htm`.

— (2014b). *Transformable design*. URL: `http://www.hoberman.com/`.

Hooke, Robert (1678). « Lectures de potentia restitutiva, or of spring explaining the power of springing bodies ». In: *Printed for John Martyn printer to the Royal Society, Bell in St. Paul's church-yard*.

Huang, Jiangshui et al. (2012). « Spontaneous and deterministic three-dimensional curling of pre-strained elastomeric bi-strips ». In: *Soft Matter* 8.23, pp. 6291–6300.

Huang, Minghuang et al. (2005). « Nanomechanical architecture of strained bilayer thin films: from design principles to experimental fabrication ». In: *Advanced Materials* 17.23, pp. 2860–2864.

Huntsman (2013). *A guide to thermoplastic polyurethanes*. URL: `http://www.huntsman.com/portal/page/portal/polyurethanes/Media%20Library/global/files/guide_tpu.pdf`.

Ichikawa, Kiyoshi (2001). *Functionally graded materials in the 21st century: a workshop on trends and forecasts*. Springer.

Ionov, Leonid (2013). « Biomimetic Hydrogel-Based Actuating Systems ». In: *Advanced Functional Materials* 23.36, pp. 4555–4570.

Isenberg, Cyril (1978). *The science of soap films and soap bubbles*. Courier Dover Publications.

Ismael, Jenann (1997). « Curie's principle ». In: *Synthese* 110.2, pp. 167–190.

Jia, Fei and Martine Ben Amar (2013). « Theoretical analysis of growth or swelling wrinkles on constrained soft slabs ». In: *Soft Matter* 9.34, pp. 8216–8226.

Jonkers, Henk M et al. (2010). « Application of bacteria as self-healing agent for the development of sustainable concrete ». In: *Ecological engineering* 36.2, pp. 230–235.

Keller, Joseph B (1980). « Tendril shape and lichen growth ». In: *Lect. Math. Life Sci* 30, pp. 257–274.

Kilian, Axel (2006). « Design exploration through bidirectional modeling of constraints ». In:

Kim Sung, Doris (2014). *Metal that breathes*. URL: `http://www.ted.com/talks/doris_kim_sung_metal_that_breathes`.

King, David A et al. (2009). « Trees approach gravitational limits to height in tall lowland forests of Malaysia ». In: *Functional Ecology* 23.2, pp. 284–291.

Kirchhoff, Gustav (1859). « Ueber das Gleichgewicht und die Bewegung eines unendlich dünnen elastischen Stabes. » In: *Journal für die reine und angewandte Mathematik* 56, pp. 285–313.

Klein, Yael, Efi Efrati, and Eran Sharon (2007). « Shaping of elastic sheets by prescription of non-Euclidean metrics ». In: *Science* 315.5815, pp. 1116–1120.

Koehl, MAR et al. (2008). « How kelp produce blade shapes suited to different flow regimes: A new wrinkle ». In: *Integrative and Comparative Biology* 48.6, pp. 834–851.

Korte, AP, EL Starostin, and GHM van der Heijden (2010). « Triangular buckling patterns of twisted inextensible strips ». In: *Proceedings of the Royal Society A: Mathematical, Physical and Engineering Science*, rspa20100200.

Krauss, Stefanie et al. (2013). « Self-repair of a biological fiber guided by an ordered elastic framework ». In: *Biomacromolecules* 14.5, pp. 1520–1528.

Landau, Lev Davidovich and Eugin M Lifshitz (1959). *Course of Theoretical Physics Vol 7: Theory and Elasticity*. Pergamon Press.

Le Bret, Marc (1984). « Twist and writhing in short circular DNAs according to first-order elasticity ». In: *Biopolymers* 23.10, pp. 1835–1867.

Li, Bo et al. (2012). « Mechanics of morphological instabilities and surface wrinkling in soft materials: a review ». In: *Soft Matter* 8.21, pp. 5728–5745.

Liang, Haiyi and L Mahadevan (2009). « The shape of a long leaf ». In: *Proceedings of the National Academy of Sciences* 106.52, pp. 22049–22054.

— (2011). « Growth, geometry, and mechanics of a blooming lily ». In: *Proceedings of the National Academy of Sciences* 108.14, pp. 5516–5521.

Liu, Zishun, Somsak Swaddiwudhipong, and Wei Hong (2013). « Pattern formation in plants via instability theory of hydrogels ». In: *Soft Matter* 9.2, pp. 577–587.

Loewy, Robert G (1997). « Recent developments in smart structures with aeronautical applications ». In: *Smart Materials and Structures* 6.5, R11.

Mandelbrot, Benoit B (1983). *The fractal geometry of nature*. Vol. 173. Macmillan.

Marder, M (2003). « The shape of the edge of a leaf ». In: *Foundations of Physics* 33.12, pp. 1743–1768.

Marder, M and N Papanicolaou (2006). « Geometry and elasticity of strips and flowers ». In: *Journal of statistical physics* 125.5-6, pp. 1065–1092.

Marder, M, E Sharon, et al. (2003). « Theory of edges of leaves ». In: *EPL (Europhysics Letters)* 62.4, p. 498.

Martin, Sebastian et al. (2010). *Unified simulation of elastic rods, shells, and solids*. Vol. 29. 4. ACM.

Martone, Patrick T et al. (2010). « Mechanics without muscle: biomechanical inspiration from the plant world ». In: *Integrative and comparative biology* 50.5, pp. 888–907.

McGinty, Bob (2014). *Finite Deformation Continuum Mechanics*. URL: `http://www.continuummechanics.org/cm/index.html`.

McLachlan, Robert (2014). *On the cut of clothes, by P. L. Tchebychef*. URL: `http://www.massey.ac.nz/~rmclachl/pseudosphere/tchebyshev.html`.

McMahon, Thomas A (1975). « The mechanical design of trees ». In: *Scientific American* 233, pp. 92–102.

McMillen, Tyler, Alain Goriely, et al. (2002). « Tendril perversion in intrinsically curved rods ». In: *Journal of Nonlinear Science* 12.3, pp. 241–281.

McNeel, Robert and Associates (2014a). *Grasshopper*. URL: `http://www.grasshopper3d.com/`.

— (2014b). *Rhinoceros*. URL: `http://www.rhino3d.com/`.

Menges, Achim (2014). *HygroScope: Meteorosensitive Morphology*. URL: `http://www.achimmenges.net/?p=5083`.

Michell, JH (1889). « On the stability of a bent and twisted wire ». In: *Messenger Math.* 11, pp. 181–184.

Mora, Thierry and Arezki Boudaoud (2006). « Buckling of swelling gels ». In: *The European Physical Journal E: Soft Matter and Biological Physics* 20.2, pp. 119–124.

Müller, Martin Michael, Martine Ben Amar, and Jemal Guven (2008). « Conical defects in growing sheets ». In: *Physical review letters* 101.15, p. 156104.

Mura, Toshio (1987). *Micromechanics of defects in solids*. Vol. 3. Springer.

Nardinocchi, P, L Teresi, and V Varano (2013). « The elastic metric: a review of elasticity with large distortions ». In: *International Journal of Non-Linear Mechanics* 56, pp. 34–42.

Nechaev, Sergei and Raphaël Voituriez (2001). « On the plant leaf's boundary,jupe à godets' and conformal embeddings ». In: *Journal of Physics A: Mathematical and General* 34.49, p. 11069.

Newton, I (1934). *Philosophiae Naturalis Principia Mathematica (1687), translated and reprinted by Cambridge Univ.*

Nietzsche, Friedrich Wilhelm (1886). *Jenseits von Gut und Böse*. Vol. 1988.

— (1887). *Die fröhliche Wissenschaft*. EW Fritzsch.

Niklas, Karl J (1994). *Plant allometry: the scaling of form and process*. University of Chicago Press.

Niordson, FI and JB Keller (1966). « The tallest column ». In: *J. Math. Mech* 16, pp. 433–446.

Novozhilov, Valentin Valentinovich (1999). *Foundations of the nonlinear theory of elasticity*. Courier Dover Publications.

Nyashin, Y, V Lokhov, and F Ziegler (2005). « Decomposition method in linear elastic problems with eigenstrain ». In: *ZAMM-Journal of Applied Mathematics and Mechanics/Zeitschrift für Angewandte Mathematik und Mechanik* 85.8, pp. 557–570.

Ottoni, Federica, Eva Coïsson, and Carlo Blasi (2010). « The Crack Pattern in Brunelleschi's Dome in Florence: Damage Evolution from Historical to Modern Monitoring System Analysis ». In: *Advanced Materials Research* 133, pp. 53–64.

Peraza-Hernandez, Edwin A et al. (2014). « Origami-inspired active structures: a synthesis and review ». In: *Smart Materials and Structures* 23.9, p. 094001.

Pérez, Fernando and Brian E. Granger (2007). « IPython: a System for Interactive Scientific Computing ». In: *Computing in Science and Engineering* 9.3, pp. 21–29. ISSN: 1521-9615. DOI: 10.1109/MCSE.2007.53. URL: http://ipython.org.

Pieranski, Piotr, Justyna Baranska, and Arne Skjeltorp (2004). « Tendril perversion-a physical implication of the topological conservation law ». In: *European journal of physics* 25.5, p. 613.

Piker, Daniel (2014a). *Kangaroo live physics engine*. URL: http://www.grasshopper3d.com/group/kangaroo.

— (2014b). *Pseudo-physical materials*. URL: http://spacesymmetrystructure.wordpress.com/2011/05/18/pseudo-physical-materials/.

— (2014c). *Space Symmetry Structure*. URL: http://spacesymmetrystructure.wordpress.com/.

Pollio, Vitruvius (1914). *Vitruvius: The Ten Books on Architecture*. Harvard university press.

Pottmann, Helmut (2007). *Architectural geometry*. Vol. 10. Bentley Institute Press.

Ramachandran, P. and G. Varoquaux (2011). « Mayavi: 3D Visualization of Scientific Data ». In: *Computing in Science and Engineering* 13.2, pp. 40–51. ISSN: 1521-9615.

Razghandi, Khashayar (2014). « Passive hydro-actuated unfolding of ice plant seed capsules as a concept generator for autonomously deforming devices ». PhD thesis. Technische Universität Berlin.

Razghandi, Khashayar et al. (2012). *Automobile objects*. URL: https://www.hu-berlin.de/pr/medien/publikationen/pdf/hu_wissen4.pdf.

Reissner, H (1931). « Eigenspannungen und Eigenspannungsquellen ». In: *ZAMM-Journal of Applied Mathematics and Mechanics/Zeitschrift für Angewandte Mathematik und Mechanik* 11.1, pp. 1–8.

Reyssat, E and L Mahadevan (2009). « Hygromorphs: from pine cones to biomimetic bilayers ». In: *Journal of The Royal Society Interface* 6.39, pp. 951–957.

— (2011). « How wet paper curls ». In: *EPL (Europhysics Letters)* 93.5, p. 54001.

Santangelo, Christian D (2009). « Buckling thin disks and ribbons with non-Euclidean metrics ». In: *EPL (Europhysics Letters)* 86.3, p. 34003.

Savin, Thierry et al. (2011). « On the growth and form of the gut ». In: *Nature* 476.7358, pp. 57–62.

Schleicher, S et al. (2011). « Bio-inspired kinematics of adaptive shading systems for free form facades ». In: *Proceedings of the IABSE-IASS Symposium, Taller Longer Lighter, London, UK*. Vol. 9.

Serikawa, Kyle A and Dina F Mandoli (1998). « An analysis of morphogenesis of the reproductive whorl of Acetabularia acetabulum ». In: *Planta* 207.1, pp. 96–104.

Sharon, Eran and Efi Efrati (2010). « The mechanics of non-Euclidean plates ». In: *Soft Matter* 6.22, pp. 5693–5704.

Sharon, Eran, Benoit Roman, Michael Marder, et al. (2002). « Buckling cascades in free sheets ». In: *Nature* 419.5, pp. 579–579.

Sharon, Eran, Benoit Roman, and Harry L Swinney (2007). « Geometrically driven wrinkling observed in free plastic sheets and leaves ». In: *Physical Review E* 75.4, p. 046211.

El-Shiekh, Aly, JF Bogdan, and RK Gupta (1971a). « The Mechanics of Bicomponent Fibers Part I: Theoretical Analysis ». In: *Textile Research Journal* 41.4, pp. 281–297.

— (1971b). « The Mechanics of Bicomponent Fibers Part II: Experimental Investigation ». In: *Textile Research Journal* 41.11, pp. 916–922.

Shim, Jongmin et al. (2012). « Buckling-induced encapsulation of structured elastic shells under pressure ». In: *Proceedings of the National Academy of Sciences* 109.16, pp. 5978–5983.

Skotheim, Jan M and L Mahadevan (2005). « Physical limits and design principles for plant and fungal movements ». In: *Science* 308.5726, pp. 1308–1310.

Spears, Kevin and Silas Alben (2008). « A cascade of length scales in elastic rings under confinement ». In: *Chaos* 18.4, p. 41109.

Spivak, Michael (1975). « Differential Geometry, volume 1–5 ». In: *Publish or Perish, Berkeley*.

Stamp, Nancy E (1984). « Self-burial behaviour of Erodium cicutarium seeds ». In: *The Journal of Ecology*, pp. 611–620.

Stoop, N, Falk K Wittel, and HJ Herrmann (2008). « Morphological phases of crumpled wire ». In: *Physical review letters* 101.9, p. 094101.

Stoop, Norbert et al. (2010). « Self-contact and instabilities in the anisotropic growth of elastic membranes ». In: *Physical review letters* 105.6, p. 068101.

Stoychev, Georgi, Sébastien Turcaud, et al. (2013). « Hierarchical Multi-Step Folding of Polymer Bilayers ». In: *Advanced Functional Materials* 23.18, pp. 2295–2300.

Stoychev, Georgi, Svetlana Zakharchenko, et al. (2012). « Shape-programmed folding of stimuli-responsive polymer bilayers ». In: *ACS nano* 6.5, pp. 3925–3934.

Studart, André R and Randall M Erb (2014). « Bioinspired materials that self-shape through programmed microstructures ». In: *Soft matter* 10.9, pp. 1284–1294.

Tesla, Nikola (1934). *Radio Power Will Revolutionize the World*. Modern Mechanix. URL: `http://blog.modernmechanix.com/radio-power-will-revolutionize-the-world/`.

Thompson, Darcy Wentworth et al. (1942). « On growth and form. » In: *On growth and form.*

Timoshenko, S et al. (1925). « Analysis of bi-metal thermostats ». In: *J. Opt. Soc. Am* 11.3, pp. 233–255.

Tobias, Irwin and Wilma K Olson (1993). « The effect of intrinsic curvature on supercoiling: predictions of elasticity theory ». In: *Biopolymers* 33.4, pp. 639–646.

Treloar, Leslie Ronald George (1975). *The physics of rubber elasticity*. Oxford University Press.

Turcaud, Sébastien et al. (2011). « An excursion into the design space of biomimetic architectured biphasic actuators ». In: *International Journal of Materials Research* 102.6, pp. 607–612.

Ueda, Yukio et al. (1975). « A new measuring method of residual stresses with the aid of finite element method and reliability of estimated values ». In: *Transactions of JWRI* 4.2, pp. 123–131.

Vasudevan, M and W Johnson (1961). « On multi-metal thermostats ». In: *Applied Scientific Research, Section B* 9.6, pp. 420–430.

Vincent, Julian FV, John D Currey, et al. (1980). *The mechanical properties of biological materials*. Cambridge University Press.

Wikipedia (2014). *Neri Oxman*. URL: `http://en.wikipedia.org/wiki/Neri_Oxman`.

Yang, Yang, Irwin Tobias, and Wilma K Olson (1993). « Finite element analysis of DNA supercoiling ». In: *The Journal of chemical physics* 98.2, pp. 1673–1686.

Yin, Jie. « Progress through Mechanics: Mechanics vs. Morphogenesis ». In:

Yin, Jie et al. (2008). « Stress-driven buckling patterns in spheroidal core/shell structures ». In: *Proceedings of the National Academy of Sciences* 105.49, pp. 19132–19135.

Zajac, EE (1962). « Stability of two planar loop elasticas ». In: *Journal of Applied Mechanics* 29.1, pp. 136–142.

Zakharchenko, Svetlana et al. (2010). « Temperature controlled encapsulation and release using partially biodegradable thermo-magneto-sensitive self-rolling tubes ». In: *Soft Matter* 6.12, pp. 2633–2636.